A tunable quantum gas for matter-wave interferometry and soliton experiments

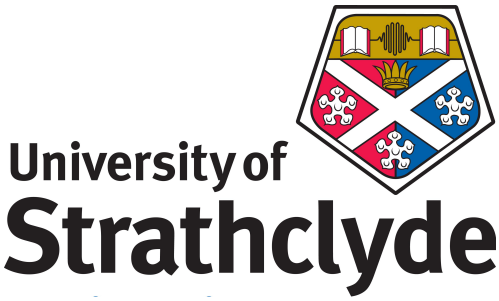

Andrea Di Carli

Experimental Quantum Optics and Photonics Group
Department of Physics and SUPA

University of Strathclyde

A thesis presented in the fulfilment of the requirements for the
degree of

Doctor of Philosophy

2019

Declaration of Authenticity and Author's Rights

This thesis is the result of the author's original research. It has been composed by the author and has not been previously submitted for examination which has led to the award of a degree.

Signed:

Date:

Abstract

The thesis reports on two strands of experiments in which we employ Bose-Einstein condensates of caesium atoms. Caesium provides favourable scattering properties due to a rich spectrum of magnetic Feshbach resonances at low fields. In particular, we take advantage of the tunability of the interaction strength to implement experiments to study matter-wave interferometry and solitons.

In a first series of experiments, we employ a magnetic levitation scheme and the tunability of caesium BEC to measure micro-g accelerations by using atomic interferometry, demonstrating free-evolution times of 1 s. We analyse the intrinsic effects of the curvature of our force field due to the magnetic levitation, and we observe the effects of a phase-shifting element in the interferometer paths.

In the second series of experiments, we exploit the tunability of our Bose-Einstein condensate to generate bright matter-wave solitons in quasi-1D geometry. We study the fundamental breathing mode frequency of a single matter-wave soliton by measuring its oscillation frequency as a function of the atom number and confinement strength and we observe signatures of the creation of second-order solitons.

Aside from introducing some general concepts of ultra-cold atomic collisions and BECs, I also present a brief overview of the experimental apparatus. This includes details of the vacuum setup, laser cooling, magnetic field coils and diagnostic procedures, and sequence for generating BECs of caesium atoms.

Acknowledgement

The achievement of my PhD would have not been possible without the contribution and the help of many extraordinary people that I met during these four years.

I want to dedicated a special thank to my first supervisor Dr. Elmar Haller. Elmar, you have been the best supervisor I could of asked for. You trusted me with the construction of the new experiment and you provided me your full support during these years. Most of my growth as experimental physicist is due to your dedication. You are an awesome and skilled scientist who is an incredible hard worker. I learned a lot from you. Outside the lab, you have been always willing to help me with any problem I encountered during my stay in Glasgow. I am infinitely grateful for your support.

Another special thank is devoted to my second supervisor Prof. Stefan Kuhr. You gave me the opportunity of joining your research group and allowing me to work with very talented people. Your precious advices and your enthusiasm have been the perfect ingredients for pushing me to do my best and for improving my self-confidence. I admire your clear way of explaining physics, it is simply fantastic.

I also would like to thank my lab mate Craig Colquhoun, who shared with me the good and bad times in the lab. You have been a huge help during these four years, which has been essential to my success. Your kindness is a quality that belongs to extraordinary man. You are a talented scientist, I wish you all the best in your career.

I thank Andrés Ulibarrena, Adrián Costa and Matthew Johnson who shared with me the best lunches in the best places in Glasgow, talking about politics, history, physics and meaning of life. We had nice weekends in which we prepared typical dishes from our home countries. I am appreciative of all of them.

I thank Dylan Cotta who hosted me during the first weeks in his flat and invited me to eat the best cous cous I ever had.

I thank all the members of the quantum gas microscope experiment, Bruno Peaudecerf, Manual Andia, Ilian Despard, Harikesh Ranganath, Matthew Brown and Arthur La Rooij for their help and suggestions along with all other members of the EQOP group. The group encourages collaboration and inspires a warm welcoming environment for all that have the pleasure of working here.

Questo dottorato è il punto di arrivo di un lungo percorso cominciato molto tempo fa. Molte persone hanno contribuito a sostenermi in maniera diretta o indiretta e a loro volgo i miei piu sentiti ringraziamenti.

Vorrei partire col ringraziare i miei nonni, paterni e materni, che mi hanno da sempre incentivato nell'intraprendere gli studi universitari oltreché nel finanzare gli stessi. Il vostro contributo è stato fondamentale senza di voi non sarei dove adesso sono. Ve ne sarò grato a vita.

Vorrei ringraziare mio padre che, quando ero poco piu che dodicenne, mi fece conoscere la fisica, la quale, col passare degli anni, diventò da semplice curiosità a passione. Ringrazio mia madre che mi ha costantemente spronato a dare del mio meglio oltrechè ad essermi vicina nei momenti più delicati. Un ringrazi-

amento speciale a mio fratello con ho condiviso gran parte della mia vita. Il tuo spirito impreditoriale è ammirevole sono sicuro che farai molta strada. Vi rigrazio inoltre per avermi fornito scorte di cibo (è importante mantenere una buona alimentazione).

Vorrei ringraziare i mei zii per avermi mostrato il loro interesse nella materia oggetto dei miei studi e per il loro supporto.

Ringrazio i miei amici Giulio Petrignani e Andrea Mainardi per essere riusciti a mantenere viva la nostra, ormai più che decennale, amicizia. Ringrazio i miei compagni di università Federico Amoroso e Edoardo Mazzi con i quali ho condiviso divertenti e amene serate in compagnia di una birra e del buon cibo.

Vorrei ringraziare tutte le persone che mi hanno incoraggiato e aiutato durante questo periodo, in particolare Stefania Broncano, Nancy Galeas e Marco Gabbrielli.

Dedico un ringraziamento speciale alla mia compagna, nonché futura moglie, Pamela Broncano. Il supporto e l'amore che quotidanamente mi dai riempiono la mia vita e la migliorano giorno dopo giorno. Tu conosci tutto di me, i miei punti di forza e le mie debolezze, sai darmi l'equilibrio e il sostegno anche quando non lo merito. Sei una compagna e una mamma meravigliosa.

Il dottorato non poteva che concludersi nel migliore dei modi rendendomi papà di un bellissimo e bimbo, Riccardo. Ti ringrazio Topino hai dato un piacevole senso alla mia vita.

Contents

Chapter 1

Introduction

In 1925, A. Einstein extended the statistical arguments introduced for photons by S. Bose [1] to massive particles and discovered a phase transition in which a macroscopic number of particles populate the ground state of the physical system [2]. This phenomenon was called Bose-Einstein condensation. Despite the initial skepticism about the real existence of Bose-Einstein condensation [3] in nature, F. London speculated in 1938 about a connection between Bose-Einstein condensation and the newborn phenomenon of superfluidity in liquid ^{4}He [4], which was discovered by P. Kapitza, J. F. Allen and D. Misener [5, 6]. However, this relationship was still not evident due to the strong interparticle interactions between helium atoms. In 1947 N. Bogoliubov employed the idea of Bose-Einstein condensation for the development of the theory of superfluidity for weakly interacting Bose gases [7]. A deeper understanding of the connection between Bose-Einstein condensation and superfluidity was provided by L. Landau, O. Penrose and L. Onsager with the introduction of the concept of off-diagonal long-range order [8–10], which is intimately related to the coherent behaviour of a Bose-Einstein condensate (BEC).

Despite remarkable theoretical advances for weakly interacting systems, strongly interacting superfluid ^{4}He was the principal subject of experimental investigation. In 1975, the proposal of laser cooling of neutral atoms by T. Hänsch and A. Schawlow [11], made an important advance towards the goal of a weakly interacting BECs. A few years later, the achievement of micro-kelvin temperatures

in vapour of alkali-metal atoms by laser cooling [12] in combination with the development of evaporative cooling [13] for hydrogen atoms, led to the realisation of Bose-Einstein condensation in 1995, for weakly interacting dilute gases of rubidium-87 [14], sodium-23 [15] and lithium-7 [16]. These pioneering experimental works were a milestone in quantum physics and they paved the way for the rich and prolific field of quantum gases. Since then, the coherent and the weakly interacting nature of Bose-Einstein condensates of alkali-metal atoms were intensively explored, leading to the demonstration of matter-wave interference [17,18], to the development of atom lasers [19,20], to the realisation of Josephson effects [21,22], to the observation of four wave mixing with matter waves [23], vortices [24,25], vortex lattices [26, 27], dark solitons [28, 29], bright solitons [30, 31]. In addition, BECs in optical lattice potentials are employed for studying and simulating strongly correlated quantum systems in condensed matter physics [32,33].

In this context, it is desirable to have a high degree of control of most of the parameters which characterise the system, in particular of the interatomic interaction strength. Among the other alkali-metal atoms, caesium offers very favourable scattering properties and a precise control of the interaction strength due to a rich spectrum of magnetic Feshbach resonances at low magnetic field strengths [34, 35]. In particular, caesium in the $|F = 3, m_F = 3\rangle$ state possesses a broad resonance at -12.8 G, which causes a smooth variation of the scattering length, permitting to tune the strength of the interactions over a wide range and with high precision. In addition, the zero crossing associated with this resonance is located at a relatively low magnetic field of 17.12 G in comparison with the other alkali-metal elements [30, 36–40]. This exceptional control on the interactions of caesium atoms was successfully exploited for the first proof of Efimov resonances in thermal clouds [42], for the suppression of collisional dephasing mechanisms in Bloch oscillations [43], for the first realisation of a super-Tonks-Girardeau gas [44] and for the creation of a metastable Mott-insulator state with attractive interactions [45]. Caesium is also the heaviest stable alkali element and possesses and a relatively large hyperfine splitting. These properties are convenient for reaching very low temperatures just by laser cooling [46–48].

Despite the advantages described above, caesium was the last stable alkali-metal atom to reach the quantum degeneracy regime [41], after long lasting attempts [49–51]. The main causes for this delay were exceptionally large two-body spin relaxation rates in the $|F = 4, m_F = 4\rangle$ state [50,52], and in the $|F = 3, m_F = -3\rangle$ state [49, 53, 55], and later an unexpected large three-body recombination rate in the state $|F = 3, m_F = 3\rangle$ [54]. Due to these intrinsic features, an uncommon procedure, based on the employment of optical traps combined with magnetic levitation and an offset field to tune interactions, was developed in 2002 by the group of R. Grimm in Innsbruck for reaching Bose-Einstein condensation [41].

The thesis focusses on two strands of experiments in which we exploited the favourable features of BEC of caesium. In the first series of experiments we employ a magnetic levitation scheme and the tunability of caesium BEC to measure micro-g accelerations by using atomic interferometry [56]. We also study the intrinsic effects of the curvature of our force field due to the magnetic levitation, and we observe the effects of a phase-shifting element in the interferometer paths. Also, we demonstrate expansion times of 1 s in a guiding dipole beam. In the second series of experiments we take advantage of the aforementioned zero crossing at 17.12 G to set the effective interaction between the atoms to attractive, allowing us to generate bright matter wave solitons in quasi-1D geometry. In particular, we study the fundamental breathing mode frequency of a single matter-wave soliton by measuring its oscillation frequency as a function of the atom number and confinement strength [57]. Furthermore, we observe strong indications of the creation of higher-order solitons, in particular the second-order soliton.

This thesis is structured as follows: in Chapter 2, I introduce the general concepts such as the scattering length, Feshbach resonances and Bose-Einstein condensation. Chapter 3 provides an overview on our experimental apparatus and on the cooling sequence for generating BECs of caesium. In Chapter 4, I report on the interferometric measurement of micro-g acceleration with levitated atoms, and in Chapter 5, I discuss the excitation modes of a bright matter-wave soliton. In the concluding Chapter 6, I draw the conclusion, and I present some ideas for

future works.

1.1 List of publications

The results presented in thesis have been published in the following articles:

- C. D. Colquhoun, A. Di Carli, S. Kuhr, and E. Haller, "Note: A simple laser shutter with protective shielding for beam powers up to 1 W", Rev. of Sci. Instrum. 89, 126102 (2018).
- A. Di Carli, C. D. Colquhoun, S. Kuhr, and E. Haller, "Interferometric measurement of micro-g acceleration with levitated atoms", New J. of Phys. 21, 053028 (2019).
- A. Di Carli, C. D. Colquhoun, G. Henderson, S. Flannigan, G.-L. Oppo, A. J. Daley, S. Kuhr, E. Haller, "Excitation modes of bright matter-wave solitons", Phys. Rev. Lett. 123, 123602 (2019).

Chapter 2

General concepts

In this chapter, I recall the basic theoretical concepts which are used frequently in the framework of this thesis. It is organised as follows: in Section 2.1, I describe the general theory describing collisions between ultra-cold atoms. In Section 2.2, I discuss and provide a brief explanation on the mechanism of magnetic Feshbach resonances. Section 2.3 illustrates the phenomenon of Bose-Einstein condensation and focuses on BECs in harmonic trapping potentials.

2.1 Collisions between ultra-cold atoms

This section reviews and summarises basic concepts of scattering theory which are essential in the description of interactions in dilute atomic gases in the low-energy regime. We are dealing with dilute gases and we can assume that two-body collisions prevail, simplifying considerably the scattering problem. An exhaustive treatment of the scattering theory can be found in textbooks [58–61], summer school lectures [62, 63] and a review paper [64].

2.1.1 Elastic collisions

Let us consider two distinguishable particles of mass m, with no internal degrees of freedom, which interact by means of the two-body potential $V(\mathbf{r})$, with $\mathbf{r}$ being the relative coordinate. In the reference frame of the centre of mass the Schrödinger equation describing the system is:

$$\left(\frac{\mathbf{p^2}}{2\mu} + V(\mathbf{r})\right)\psi_{\mathbf{k}}(\mathbf{r}) = E_{\mathbf{k}}\psi_{\mathbf{k}}(\mathbf{r})\,, \tag{2.1}$$

where $\mu = m/2$ is the reduced mass of the particles and $E_{\mathbf{k}} = \hbar^2\mathbf{k}^2/2\mu$ is the energy value of scattering state. Here, $\mathbf{k}$ is the wave number which in general is a vector.

At this point, one needs to find a solution of the previous equation and this is a complex task if we consider a general potential $V(\mathbf{r})$. For our purposes we can assume a spherically symmetric potential, $V(r)$, which has a finite range r_b. With this assumption, the asymptotic form, i.e for $r_b \ll r$, of the solution of equation 2.1 can be written as:

$$\psi_{\mathbf{k}}(\mathbf{r}) = e^{i\mathbf{k}\cdot\mathbf{r}} + f(k,\theta)\frac{e^{ikr}}{r}, \tag{2.2}$$

where the first term represents the incoming plane wave and the second describes the outgoing scattered wave as shown in Figure 2.1. Here, $k = |\mathbf{k}|$ is the modulus of the wave-number vector. The quantity $f(k,\theta)$ is called the scattering amplitude and takes in account all effects which are coming from the interaction between the two particles. Since we assumed a spherically symmetric potential, the scattering amplitude will depend on the scattering energy through k and on the direction

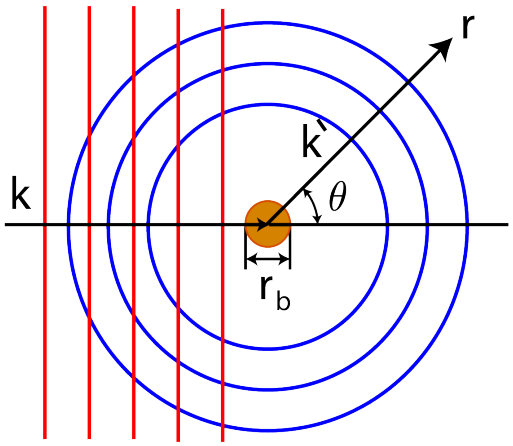

Figure 2.1: Representation of the scattering of an incoming plane wave with a wave vector $\mathbf{k}$, from a spherically symmetric potential $V(r)$ with a finite range r_b.

through the scattering angle θ between the incoming particle and the observation direction. It can easily be shown that it is possible from the scattering amplitude $f(k,\theta)$ to calculate the cross-section of the collision by integrating the scattering amplitude over the solid angle Ω:

$$\sigma_{\text{tot}}(k) = \int d\Omega \, |f(k,\theta)|^2. \tag{2.3}$$

This results is valid only for the scattering of two distinguishable particles. For identical particles the orbital component of the wave function must be symmetrical or antisymmetrical depending whether the particles are bosons or fermions. This fact leads to the following expression for the cross-section:

$$\sigma_{\text{tot}}(k) = \int d\Omega \, |f(k,\theta) \pm f(k,\pi-\theta)|^2, \tag{2.4}$$

with $0 \leq \theta \leq \pi/2$, where the plus sign refers to bosons and the minus sign to fermions.

2.1.2 Partial-wave decomposition

To carry out a more detailed analysis, it is possible to decompose the scattered wave functions into a radial part and into a set of spherical harmonic functions with different angular momenta, which are labelled by the orbital quantum number $l = 0, 1, 2, ...$ This way of expressing the wave function is called partial-wave expansion and each partial wave is named depending on the value of orbital quantum number i.e $l = 0$ is s-wave, $l = 1$ is p-wave, etc. For each partial wave it is possible to obtain a one-dimensional Schrödinger equation for the determination of radial wave functions $u_{k,l}(r)$

$$\left[\frac{d^2}{dr^2} + k^2 + \frac{l(l+1)}{r^2} + \frac{2\mu}{\hbar^2}V(r)\right] u_{k,l}(r) = 0, \tag{2.5}$$

where the additional term $l(l+1)/r^2$ represents the repulsive centrifugal barrier. At large distances, $r \gg r_b$, the interatomic potential becomes negligible and the asymptotic solution of the previous equation has the form

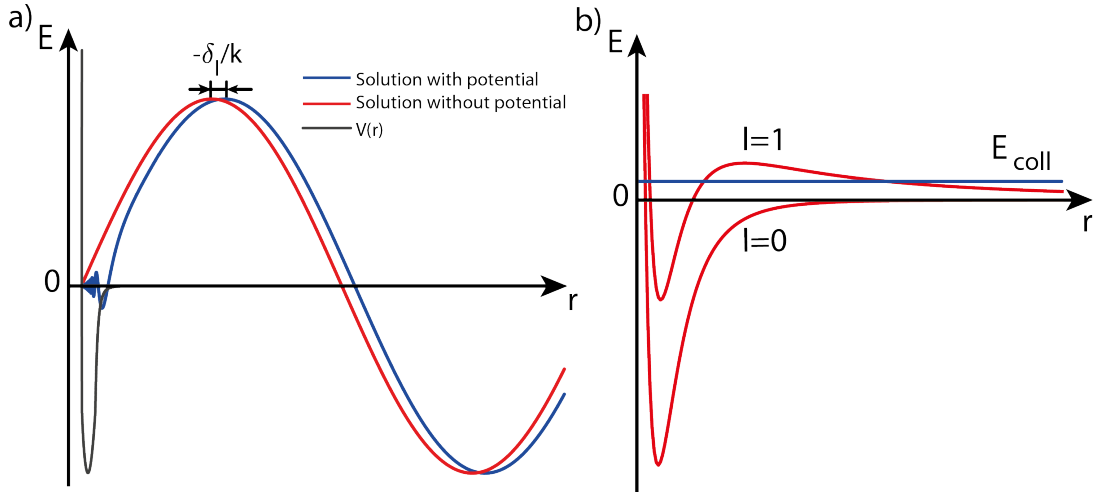

Figure 2.2: a) Comparison between the solutions of the radial wave function in the absence (red line) or in the presence (blue line) of the interatomic potential (grey line). For distances which are bigger than the characteristic potential range the main effect of the potential is to add a phase shift δ_l on the partial wave. b) Effective radial potentials experienced by two colliding atoms for angular momentum values of $l = 0$ and $l = 1$ (red curves). In particular for $l = 1$ the presence of a potential barrier can be noticed. For low enough collisional energies (blue line) this barrier suppresses the phase shift contribution of partial waves with $l > 0$.

$$u_{k,l}(r) \sim A_l \sin\left(kr - \frac{\pi l}{2} + \delta_l(k)\right), \tag{2.6}$$

which is analogous to the free wave solution except for a phase shift $\delta_l(k)$, which takes into account the effects of the inter-atomic potential on the reflected outgoing wave, and for an amplitude term A_l, which in general depends on the orbital quantum number l. We can thus express the scattering amplitude in terms of the phase shifts $\delta_l(k)$ of the partial waves:

$$f(k,\theta) = \sum_{l=0}^{\infty} \frac{2l+1}{k\cot\delta_l(k) - ik} P_l(\cos\theta), \tag{2.7}$$

where $P_l(\cos\theta)$ are the Legendre polynomials. The cross-section of the scattering is given by

$$\sigma_{\text{tot}}(k) = \frac{4\pi}{k^2} \sum_{l=0}^{\infty} (2l+1)\sin^2\delta_l(k). \tag{2.8}$$

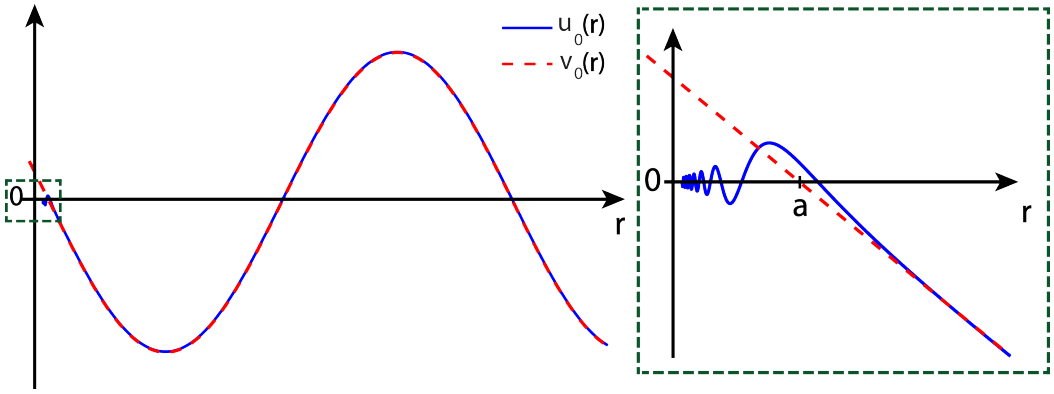

Figure 2.3: Differences between the solution $u_0(r)$ and the extended solution $v_0(r)$ for low energies. The extended solution matches totally the full solution for large distances and approximates it for r which tends to zero. For small values of r, expanded view in dashed box, the zero crossing of the extended wave function represents the geometrical interpretation of scattering length a. In this particular case the scattering length is positive but it can also assume negative values.

For identical particles, only even (bosons) or odd (fermions), values of the orbital quantum number l contribute to the computation of the scattering amplitude and the cross-section.

2.1.3 Scattering length

We are interested in the collision properties of bosons at very low collisional energies, usually below 100 μK, which are lower than the centrifugal barrier[1] as depicted in Figure 2.2b. Thus, we can neglect the phase shift $\delta_l(k)$ derived from the partial waves with $l > 0$ and consider only the s-wave contribution to the scattering amplitude. In this limit we can thus focus on equation 2.5 with $l = 0$. We know that for distances r large compared to the range of the potential the solution $u_{k,0}(r)$ behaves as $\sin[kr + \delta_0(k)]$ [61]. Let us denote with $v_{k,0}(r)$ the function that extends, for all r, the asymptotic form of the full solution $u_{k,0}(r)$, i.e $v_{k,0}(r) = A\sin[kr + \delta_0(k)]$. If we expand the extended solution $v_{k,0}(r)$ around $kr = 0$ we obtain:

$$v_k \sim A(\sin\delta_0(k) + kr\cos\delta_0(k)) \propto (r - a), \tag{2.9}$$

[1]For caesium the energy needed for overcoming the centrifugal barrier is about 190 μK [65].

where we have defined the scattering length a

$$a = -\lim_{k\to 0} \frac{\tan \delta_0(k)}{k}. \tag{2.10}$$

The scattering length has a simple geometrical interpretation: it is the point of intersection of the extended wave function $v_{k,0}(r)$ with the r axis that is the closest to the origin for k or E that goes to zero, as show in Figure 2.3. The scattering length can assume either positive or negative values and this corresponds respectively to an effective repulsion or attraction between the atoms [61]. It is possible to write the scattering amplitude and the cross section for bosons in terms of the scattering length a:

$$f(k) = -\frac{a}{1 - ika} \tag{2.11}$$

$$\sigma_{\mathrm{B}}(k) = \frac{8\pi a^2}{1 + k^2 a^2}. \tag{2.12}$$

As can easily be noted from the previous equations, the scattering length is the only relevant parameter to describe the collision process in the low-energy limit, although its value depends crucially on the exact potential $V(r)$. In particular, the presence of a bound state which is immediately close to the continuum has a considerable effect on the scattering length making it very large and positive if the bound state is below or large and negative if it is above [61, 62].

Generally, in order to study the macroscopic behaviour of the dilute gas at low temperatures, one can neglect the real potential and consider the scattering length as a given experimental parameter. Furthermore, it is possible to introduce a so called pseudopotential:

$$V_{\mathrm{pseudo}}(\mathbf{r}) = \frac{4\pi\hbar^2 a}{m}\delta(\mathbf{r})\frac{\partial}{\partial r}(r...), \tag{2.13}$$

which reproduces exactly, for arbitrary k, the result for the scattering amplitude reported in equation 2.11. The pseudopotential $V_{\mathrm{pseudo}}(\mathbf{r})$, in the limit of small

values of ka, can be approximated by the delta potential [61, 62]:

$$V_{\mathrm{d}}(\mathbf{r}) = g\delta(\mathbf{r}), \tag{2.14}$$

with:

$$g = \frac{4\pi\hbar^2 a}{m}. \tag{2.15}$$

2.2 Feshbach resonances

This section is devoted to an introduction and a brief explanation of the physics of the so-called Feshbach resonances. Feshbach resonances were investigated initially in the contexts of nuclear physics by H. Feshbach [66, 67] and of atomic physics by U. Fano [68] for the study of the resonance phenomena that originate from the coupling of a discrete state to the scattering state. In the framework of ultra-cold gases, Feshbach resonances have been considered in references [69, 70] which first pointed out the possibility of using an external magnetic field for changing the sign and magnitude of the scattering length of the atoms. The first experimental demonstration of a magnetically induced Feshbach resonance in ultra-cold atoms was provided by W. Ketterle's group in 1998 [36]. Since then, these resonances have become a crucial tool for the study of collapse of BECs [71–73], soliton generation [30, 31], molecule formation [74, 75], for exploration of the crossover from molecular BEC to a BCS superfluid of weakly bound Cooper pairs in fermi gases [76–78], and very recently for the creation and investigation of the Bose polaron in BEC [79].

2.2.1 Description of a magnetic Feshbach resonance

We give a general picture on the underlying physics of a Feshbach resonance. Further details on this topic can be found in the review article [80]. The typical mechanism that gives rise to a Feshbach resonance is depicted in Figure 2.4. A pair of atoms is prepared in the scattering state, also called *incident channel*, with a corresponding collision energy E_{coll}. The atoms will experience a background

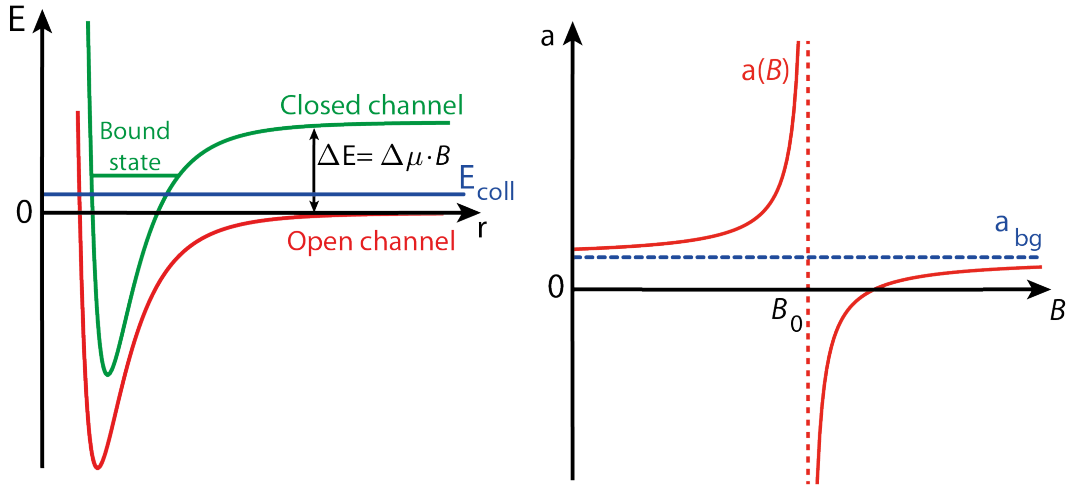

Figure 2.4: Representation of a two-channel magnetic Feshbach resonance: the open channel potential (red line) sets the background scattering length a_{bg} as shown in the left plot (dashed blue line), a closed channel which has a bound molecular state and a different magnetic moment (green line) can couple to the incident channel (blue line). The detuning between the energy of the bound state and the scattering state can be varied by applying an external magnetic field. The value of the scattering length a is affected by the presence of bound state in the closed channel as shown on the left plot. At the resonance point, i.e B_0, the scattering length diverges.

potential $V_{\rm bg}(r)$, called *open channel*, which, in the asymptotic limit, lies below the incident channel. We denote with $V_{\rm c}(r)$, named *closed channel*, the molecular potential that the atoms would feel if they were in a different internal state. We also assume that this potential lies above the incident channel in the asymptotic limit, and possesses at least a bound molecular state near the threshold of the open channel. If the incident and closed channel are coupled together, a Feshbach resonance appears whenever the collision energy of the scattering state in the open channel approaches the bound molecular state of the closed channel. In particular, in the case that the closed channel has a different magnetic moment from the open channel, the two potentials can be varied by the amount $\Delta E = \Delta\mu \cdot B$ by applying an external magnetic field B. The presence of such a resonance affects the value of the scattering length a, which can be expressed as a function of the magnetic field B by the formula [81]:

$$a(B) = a_{\rm bg}\left(1 - \frac{\Delta B}{B - B_0}\right). \tag{2.16}$$

Here a_{bg}, called background scattering length, is the value of scattering length when the bound state is far from resonance, B_0 represents the position of the resonance, and Δ is the width of the resonance which depends on the coupling strength between the two channels. The typical behaviour of the scattering length is shown in Figure 2.4: it diverges nearby the resonance position B_0 and tends towards the value a_{bg} for magnetic field values B far from B_0. Associated with a Feshbach resonance there is the zero crossing point which occurs at $B = B_0 + \Delta B$. This point is fundamental since it allows to switch the sign of the interactions.

2.2.2 Feshbach resonances in caesium

Caesium is characterised by a rich spectrum of Feshbach resonances and molecular states. The richness of collision properties is due mainly to strong relativistic interactions such as magnetic spin-spin interaction and second order spin-spin interaction [80]. The first intensive investigations on Feshbach resonances of caesium atoms have been performed by the group of S. Chu [34, 82, 83] in which more than 60 Feshbach resonances were discovered at relatively low magnetic field ($B < 250\,\mathrm{G}$). These early results led to the construction of accurate theoretical models of the mutual potential of two caesium atoms [34, 84, 85]. Following experimental works [86–88] have found good agreement with these models. Recently, new Feshbach resonances, for caesium in its absolute ground state, have been discovered in the high magnetic field region between 450 G and 1000 G and have been used for the improvement of the previously mentioned theoretical models [35].

Figure 2.5 shows the magnetic field dependence of the scattering length for caesium atoms, in the absolute ground state $|F = 3, m_F = 3\rangle$, in the range we are interested in for our experiment. A broad resonance located at around -12.8 G causes a smooth variation of the scattering length. This allows us to tune the scattering length with high precision. An interesting point is the magnetic field value in which the scattering length is zero. This point is at 17.12 G and has been precisely measured by minimising the interaction-induced dephasing of Bloch oscillations [43]. The zero crossing is particularly useful because it

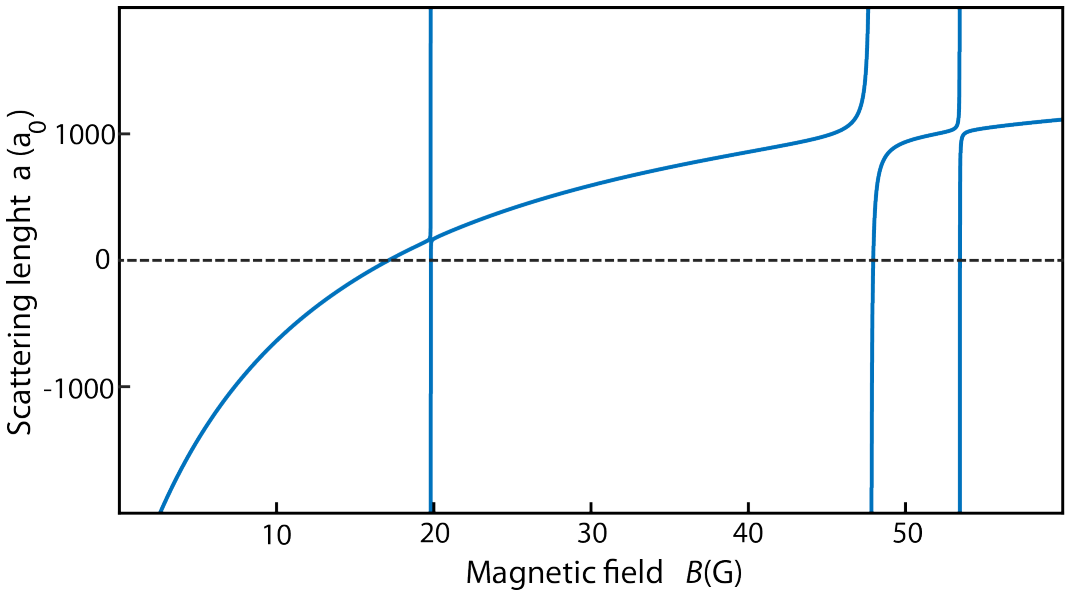

Figure 2.5: Scattering length a, in Bohr radii, a_0, versus magnetic field B for the $|F = 3, m_F = 3\rangle$ state of caesium. A broad Feshbach resonance positioned at $-12.8\,\mathrm{G}$ causes a smooth variation of the scattering length and allow us to fine tune it for a wide range of scattering length values. At the zero crossing the value of the slope is $67.5\,\mathrm{a_0/G}$. Further narrow resonances are located $19.8\,\mathrm{G}$, $47.9\,\mathrm{G}$ and $53.4\,\mathrm{G}$.

permits to change sign of the scattering length and this is what we will need later for studying Bose-Einstein condensates in the regime of attractive interaction. Additional narrow resonances are positioned at $19.8\,\mathrm{G}$, $47.9\,\mathrm{G}$ and $53.4\,\mathrm{G}$ [35,86].

2.3 Theory of Bose-Einstein condensation

The phenomenon of Bose-Einstein condensation derives from the indistinguishability of identical particles. In particular, for bosons, the assumption that the wave function of the total system must be symmetric by exchange of atoms in a pair of particles affects the statistical behavior of a Bose gas. A qualitative description starts by considering the relevant length scales which describe the system [61]. The spatial density of the gas n sets the mean interparticle distance $d = n^{-\frac{1}{3}}$ whereas the temperature T of the gas enters in the expression of the so

called thermal deBroglie wavelength defined by

$$\lambda_{\mathrm{dB}}(T) = \sqrt{\frac{2\pi\hbar^2}{mk_BT}}, \tag{2.17}$$

where k_{B} is the Boltzmann constant and m is the mass of the particle. If we take in account the interactions between the particles of the gas, the significant length scale is set by the range of the potential r_b. For large temperatures with $\lambda_{\mathrm{dB}} \ll r_b \ll d$, the collisions between the particles involve many partial waves and their trajectories can be regarded as classical and the equilibrium is described by a Maxwell-Boltzmann (MB) distribution. By cooling the atomic ensemble, when $r_b \ll \lambda_{\mathrm{dB}} \ll d$, quantum effects manifest in the collisions, as described previously, but, essentially, the Bose gas is still described by a MB distribution. By further lowering the temperature or, equivalently, by increasing the spatial density of the Bose gas, the thermal deBroglie wavelength approaches the mean interparticle distance. Here the particles start to show wave-like behaviour and effects of the quantum statistic due to indistinguishability are more evident. Such a phenomenon has the feature of a phase transition and occurs for a critical temperature T_{c} or critical density n_{c}. Well below T_{c} or well above n_{c} all the particles populate macroscopically the ground state and the system behaves like a giant matter wave.

2.3.1 Formal definition of a BEC

This simplified picture can be represented in a more quantitative and formal way. According to Leggett [89, 90], a rigourous and general definition of a BEC has been given by Penrose and Onsager [10]. Let us consider a system of N interacting boson particles. We introduce the single-particle density matrix $\rho(\mathbf{r}', \mathbf{r}; t)$ defined as

$$\rho(\mathbf{r}', \mathbf{r}; t) = N \sum_i p_i \int d\mathbf{r}_2 d\mathbf{r}_3 ... d\mathbf{r}_N \Psi_i^*(\mathbf{r}', \mathbf{r}_2, ..., \mathbf{r}_{\mathrm{N}}; t) \Psi_i(\mathbf{r}, \mathbf{r}_2, ..., \mathbf{r}_{\mathrm{N}}; t), \tag{2.18}$$

where $\Psi_i(\mathbf{r}, \mathbf{r}_2, ..., \mathbf{r}_N; t)$ is a many-body normalised wave function which is symmetric under the exchange of any pair of particles and p_i represent the probability to find the system in the pure state $\Psi_i(\mathbf{r}, \mathbf{r}_2, ..., \mathbf{r}_N; t)$. The single-particle density matrix $\rho(\mathbf{r}', \mathbf{r}; t)$ satisfies the eigenvalue equation

$$\int d\mathbf{r}' \rho(\mathbf{r}', \mathbf{r}; t) \varphi_i(\mathbf{r}', t) = n_i(t) \varphi_i(\mathbf{r}, t), \tag{2.19}$$

where the function $\varphi_i(\mathbf{r}, t)$ represents the single-particle wave function and $n_i(t)$ is the occupation number of the single-particle state $\varphi_i(\mathbf{r}, t)$. The functions $\varphi_i(\mathbf{r}, t)$ are well defined in the general case of non uniform and interacting systems of particles and do not need to be eigenfunctions of the single-particle Hamiltonian. They also provide a basis for rewriting the single-particle density matrix in the diagonalised form:

$$\rho(\mathbf{r}', \mathbf{r}; t) = \sum_{i=0}^{\infty} n_i(t) \varphi_i^*(\mathbf{r}'; t) \varphi_i(\mathbf{r}, t). \tag{2.20}$$

From the previous equation it is now straightforward to define a BEC as the condition in which one of the single particle states, usually the ground state, is macroscopically occupied. In other words, a BEC occurs when the population in one state, denoted by N_0, is of the order of the total particle number N, whereas the other single particle states have a occupation of order one. This definition of a BEC[2] is particularly suitable because of its connection with the concept of coherent matter waves usually associated with a BEC. Suppose the system is in the BEC regime, it is convenient to write equation 2.20 in the separated form

$$\rho(\mathbf{r}', \mathbf{r}; t) = N_0 \varphi_0^*(\mathbf{r}') \varphi_0(\mathbf{r}) + \sum_{i=1}^{\infty} n_i \varphi_i^*(\mathbf{r}') \varphi_i(\mathbf{r}). \tag{2.21}$$

This expression highlights that the state of the atomic ensemble can be regarded as composed by a coherent matter wave, represented by the macroscopic occupied single particle state $\varphi_0(\mathbf{r})$, and an incoherent component, described by sum of dif-

[2]Other definitions make use of the concept of off-diagonal long-range order [91] and spontaneous symmetry breaking [97]. Further discussions on this topic can be found in [90, 92].

ferent single states $\varphi_i(\mathbf{r})$ which are characterised by unity occupation and relative random phases. If now we consider values of $\mathbf{r}$ and $\mathbf{r}'$ such that their distance is of the order of the deBroglie wavelength λ_{dB}, it is reasonable to expect that the incoherent component will interfere destructively, giving a small contribution whereas the condensate wave function contribution will still be non-negligible:

$$\rho(\mathbf{r}', \mathbf{r}; t) \sim N_0 \varphi_0^*(\mathbf{r}') \varphi_0(\mathbf{r}), \qquad |\mathbf{r}' - \mathbf{r}| \gg \lambda_{\mathrm{dB}}, \tag{2.22}$$

showing that in the BEC regime, matter behaves as a coherent wave. Experimental confirmation of the coherent nature of a BEC has been given by many ground-breaking experiments [17, 18, 93–95]. We will exploit the coherence properties of BECs for the experiment on the interferometric measurement of micro-g acceleration with levitated atoms.

2.3.2 BEC in harmonic potentials

Additional quantitative details can be provided by analysing the standard case of a non-interacting Bose gas in a harmonic potential. Here, I discuss the essential results whereas for a thorough treatment I refer the reader to the following textbooks [96, 97] and review article [98]. In the framework of the grand canonical ensemble, the average particle occupation number n_i of the single-particle state $\varphi_i(\mathbf{r})$, associated with the energy E_i, is given by:

$$n_i = \frac{1}{e^{\beta(E_i - \mu)} - 1}, \tag{2.23}$$

where $\beta = 1/k_{\mathrm{B}}T$ and μ is the chemical potential. The chemical potential is a constant which is fixed by the normalisation condition $N = \sum_{i_0} n_i$. In the case of our interest, i.e. the harmonic trapping potential

$$V_{\mathrm{ext}} = \frac{1}{2} m\omega_x^2 x^2 + \frac{1}{2} m\omega_y^2 y^2 + \frac{1}{2} m\omega_z^2 z^2, \tag{2.24}$$

it is possible to find the critical temperature T_c in which the BEC transition occurs [97]:

$$T_c = 0.94 \frac{\hbar \omega_{ho}}{k_B} N^{\frac{1}{3}}, \tag{2.25}$$

where $\omega_{ho} = (\omega_x \omega_y \omega_z)^{\frac{1}{3}}$ i.e., the geometrical average of the oscillator angular frequencies. Well below the critical temperature T_c, in the limit of $T = 0$, the atoms will populate macroscopically the single-particle ground state of the harmonic potential which is given by [97]:

$$\varphi_0(\mathbf{r}) = \left(\frac{m\omega_{ho}}{\pi\hbar}\right)^{\frac{1}{4}} \exp\left[-\frac{m}{2\hbar}\left(\omega_x x^2 + \omega_y y^2 + \omega_z z^2\right)\right], \tag{2.26}$$

whereas the density distribution becomes $n(\mathbf{r}) = N\varphi_0(\mathbf{r})$. The characteristic length scale of the condensate is fixed by the average harmonic oscillator length:

$$a_{ho} = \sqrt{\frac{\hbar}{m\omega_{ho}}}. \tag{2.27}$$

So far we have not considered the interactions between the particles in the description. At temperatures T which are well below the critical temperature T_c, the relevant length scales are set by the mean inter-particle distance d and by the range of the interactions r_b which in the limit low-energy collision we have shown to be the scattering length a. In general, the scattering length can assume either small or large values compared to the mean inter particle distance, we are interested in the weakly interacting regime defined by the condition:

$$|a| \ll d \qquad \text{or equivalently} \qquad n|a|^3 \ll 1. \tag{2.28}$$

The Hamiltonian of a system of N interacting bosons in an external potential $V_{ext}(\mathbf{r})$ is given by [61]:

$$H = \sum_{i=1}^{N}\left[-\frac{\hbar^2}{2m}\nabla_i^2 + V_{ext}(\mathbf{r}_i)\right] + \frac{1}{2}\sum_{i=1}^{N}\sum_{j=i}^{N} V(\mathbf{r}_i - \mathbf{r}_j), \tag{2.29}$$

where $V(\mathbf{r}_i - \mathbf{r}_j)$ is a generic two-body potential. At $T = 0$ we assume that

the system is in the BEC regime, therefore all the bosons will occupy the single particle state $\varphi(\mathbf{r})$. The total wave function will be thus:

$$\Phi_{\mathrm{N}}(\mathbf{r}_1, \mathbf{r}_2, ..., \mathbf{r}_{\mathrm{N}}, t) = \prod_{i=1}^{N} \varphi(\mathbf{r}_i, t). \tag{2.30}$$

By using a variational approach analogous to the least action principle and considering that in the limit of low energy the interparticle potential is given by $V(\mathbf{r}) = g\delta(\mathbf{r})$, it is possible to derive the so called Gross-Pitaevskii equation (GPE) [90, 97]:

$$i\hbar\frac{\partial}{\partial t}\Psi(\mathbf{r}, \mathbf{t}) = \left[-\frac{\hbar^2}{2m}\nabla^2 + V_{\mathrm{ext}}(\mathbf{r}, t) + g|\Psi(\mathbf{r}, \mathbf{t})|^2\right]\Psi(\mathbf{r}, \mathbf{t}), \tag{2.31}$$

where $\Psi(\mathbf{r}, \mathbf{t}) = \sqrt{N}\varphi(\mathbf{r}, t)$ is the so called order parameter[3] and it is normalized to the total particle number N:

$$\int |\Psi(\mathbf{r}, \mathbf{t})|^2 d\mathbf{r} = N. \tag{2.32}$$

The GPE was discovered by Gross and Pitaevskii [99, 100] in 1961 and later successfully employed for the description of the superfluid properties of weakly interacting trapped BECs [98]. For time independent external potentials we can seek solutions of the form $\Psi(\mathbf{r}, \mathbf{t}) = \psi(\mathbf{r})e^{-i\mu t/\hbar}$ and substitute it in equation 2.31. We thus obtain:

$$\left[-\frac{\hbar^2}{2m}\nabla^2 + V_{\mathrm{ext}}(\mathbf{r}) + g|\psi(\mathbf{r})|^2\right]\psi(\mathbf{r}) = \mu\psi(\mathbf{r}), \tag{2.33}$$

where μ is the chemical potential. The solution of the previous equation, in the general case, must be found numerically. However, it is possible to find an explicit solution when the energy of the harmonic oscillator $\hbar\omega_{\mathrm{ho}}$ is smaller than the interaction energy per particle. In this case, which is equivalent to the condition $Na/a_{\mathrm{ho}} \gg 1$, we can neglect the kinetic term in equation 2.33, the

[3] This nomenclature derives from considering the Bose-Einstein condensation a phase transition in which then appears a spontaneous symmetry breaking and thus a process that can be described in the framework of the Landau theory of phase transitions.

Thomas-Fermi approximation (TFA), and obtain the following solution for the wave function:

$$\psi(\mathbf{r}) = \begin{cases} \sqrt{\frac{\mu - V_{\text{ext}}(\mathbf{r})}{g}} & \text{if} \quad \mu > V_{ext}(\mathbf{r}) \\ 0 & \text{otherwise.} \end{cases} \tag{2.34}$$

From this solution we obtain that the particle density $n(\mathbf{r}) = |\psi(\mathbf{r})|^2$ has the shape of an inverted parabola with a peak given by:

$$n_{\text{pk}} = \frac{\mu}{g}, \tag{2.35}$$

and vanishes when the condition $\mu = V_{\text{ext}}(\mathbf{r})$, is satisfied. Such condition defines the so called Thomas-Fermi radii R_i with $i = x, y, z$ which are:

$$R_i = a_{\text{ho}} \left(\frac{15Na}{a_{\text{ho}}} \right)^{\frac{1}{5}} \frac{\omega_{\text{ho}}}{\omega_i}. \tag{2.36}$$

From the normalisation condition given by equation 2.32, it is possible to provide an explicit expression for the chemical potential:

$$\mu = \frac{\hbar\omega_{\text{ho}}}{2} \left(\frac{15Na}{a_{\text{ho}}} \right)^{\frac{2}{5}}. \tag{2.37}$$

The TFA describes very well the behaviour of the wave function when its variation is such that the kinetic energy can be neglected. This assumption is no longer valid in the proximity of the Thomas-Fermi radii where the TFA predicts the formation of sharp edges instead of a smoother decay. The natural length for which the wave function decays, also called the healing length, is obtained by equating the kinetic energy and the interaction energy of equation 2.33 and is given by [97]:

$$\xi = \sqrt{\frac{\hbar^2}{2mgn_{\text{pk}}}}. \tag{2.38}$$

Chapter 3

Experimental apparatus and BEC sequence

This chapter describes the experimental apparatus and the sequence we employ for the generation of a Bose-Einstein condensate of caesium. For achieving Bose-Einstein condensation, a vacuum chamber, lasers for cooling, magnetic fields, diagnostic procedures as well as computer control of the experimental sequence, are needed. Since we started the project with empty optical tables, the construction of the whole experimental apparatus and the optimisation of the sequence took a considerable part of my doctoral work. The work was performed collaboratively with my colleague Craig Colquhoun and I will refer to his PhD thesis for further details on our experimental apparatus and on the cooling sequence [101].

The chapter is structured as follows: Sections 3.1 to 3.3 provide an overview of the vacuum setup, the laser setup, and the magnetic coils. In Section 3.4, we discuss our diagnostic methods, such as the imaging setup, microwave spectroscopy, and our computer control system. In Section 3.5, we describe our experimental sequence to generate a BEC, which starts with a two-dimensional magneto-optical trap (2D+MOT), which acts as a bright source of cold atoms for the 3D-MOT cooling stage. The atoms are further cooled by degenerate Raman sideband cooling, and then magnetically levitated. The cold cloud is captured by a large-volume dipole trap, and its density is increased by a small-volume dipole trap. Finally, the atoms are cooled to quantum degeneracy by evaporative cooling.

3.1 Vacuum setup

An experiment with ultracold atoms needs to be performed in a vacuum chamber in order to minimise the destructive collisions between the atoms and the background gas. Our vacuum setup is based on a two-chamber design with two glass cells, as shown in Figure 3.1. Glass cells are used instead of a stainless steel chamber in order provide improved optical access and to reduce eddy currents.

The high-pressure section on the right in Figure 3.1 is the 2D-MOT chamber and it consists of a caesium oven and an epoxy-glued glass cell. The oven is a bellow, which contains an ampoule with 5 g of caesium. The bellow is connected to the glass cell by a valve, which is used to regulate the amount of caesium effusing into the chamber. The glass cell, manufactured by Japan Cell, has external dimensions of 50 mm × 50 mm × 150 mm, and has anti-reflection coating at a wavelength of 852 nm on its internal and external surfaces. A pressure of 10^{-8} mbar in this part is provided by an ion pump (Agilent VacIon 8 L/s).

In the low-pressure section on the left in Figure 3.1 (main chamber) all cooling stages that lead to the BEC are performed. It consist of an un-coated, optically-contacted glass cell (Japan Cell) with external dimensions of 50 mm × 50 mm × 150 mm, and of a double cube with four glass windows that can be used to steer the atomic beam coming from the 2D+MOT section. The cube is connected to a titanium sublimation pump and to an ion pump (Agilent VacIon Plus 55), which are used to reach a pressure of 5×10^{-11} mbar.

The two sections are connected by a differential-pumping tube, which allows a differential pressure of at least four orders of magnitude to be supported, and acts as a geometrical filter for the atomic beams. A central valve is employed to separate the two sections when the experiment does not run. The pressures in the two sections are monitored by two pressure gauges. In order to reduce stray magnetic fields, each ion pump is shielded by μ-metal casing. Further details on the preparation of the vacuum setup can be found in the PhD thesis of Craig Colquhoun [101].

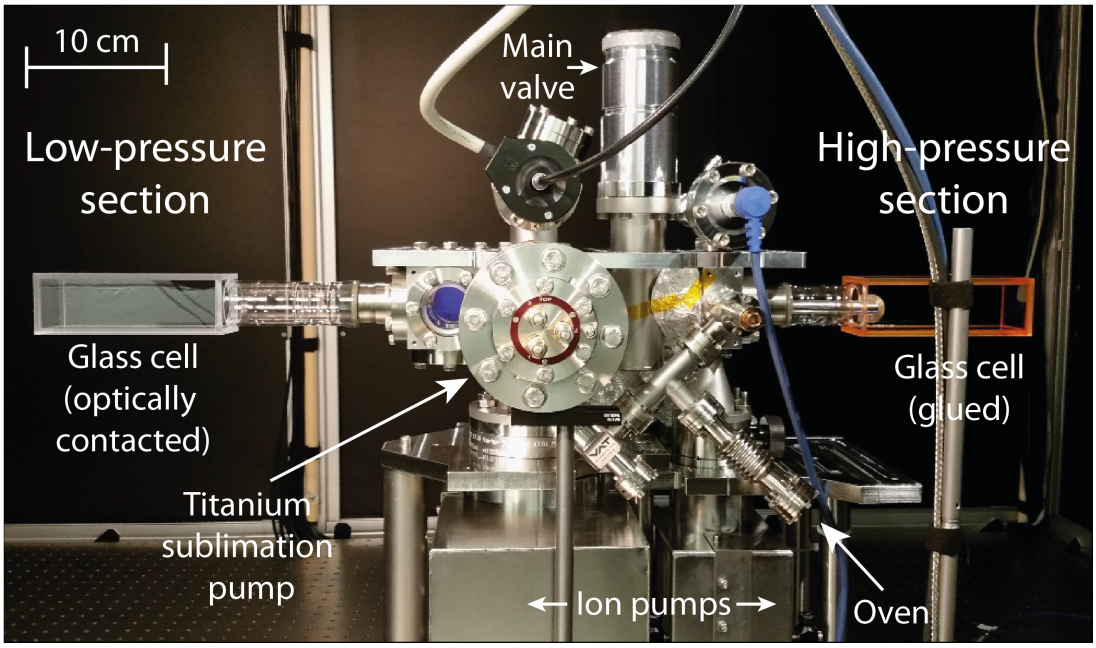

Figure 3.1: Vacuum setup consisting of two chambers with two glass cells. On the right: high-pressure section, consisting of a caesium oven and an epoxy-glued glass cell. On the left: low-pressure section, consisting of an un-coated, optically-contacted glass cell and of a double cube with four glass windows. Ion pumps and a titanium sublimation pump keep the low pressures in the sections.

3.2 Laser cooling setup

This section describes the diode laser setup that we use to drive the cooling and imaging transitions of caesium-133. It is based on a master-slave configuration using polarisation spectroscopy for frequency stabilization [102, 103] and tapered amplifiers to increase the output power. Our laser frequencies are on the D2-line with a wavelength of 852 nm. As shown in Figure 3.2, two sets of frequencies are employed, which are close to the hyperfine transitions $|F = 4\rangle \rightarrow |F' = 5\rangle$ and $|F = 3\rangle \rightarrow |F' = 3\rangle$ to drive cycling transitions and to repump the atoms.

The light driving the cycling transition for the magneto-optical traps is red-detuned with respect to the $|F = 4\rangle \rightarrow |F' = 5\rangle$ transition. We use a detuning of 10 MHz and 20 MHz from the cycling hyperfine transition for the 2D+MOT and 3D-MOT respectively. To allow for a larger detuning for an optical molasses and a compressed MOT, we employ an offset-locking scheme to control the frequency of the 3D-MOT light over a range of 90 MHz. In addition, light for absorption imaging is also resonant to the cycling transition and the light to generate the

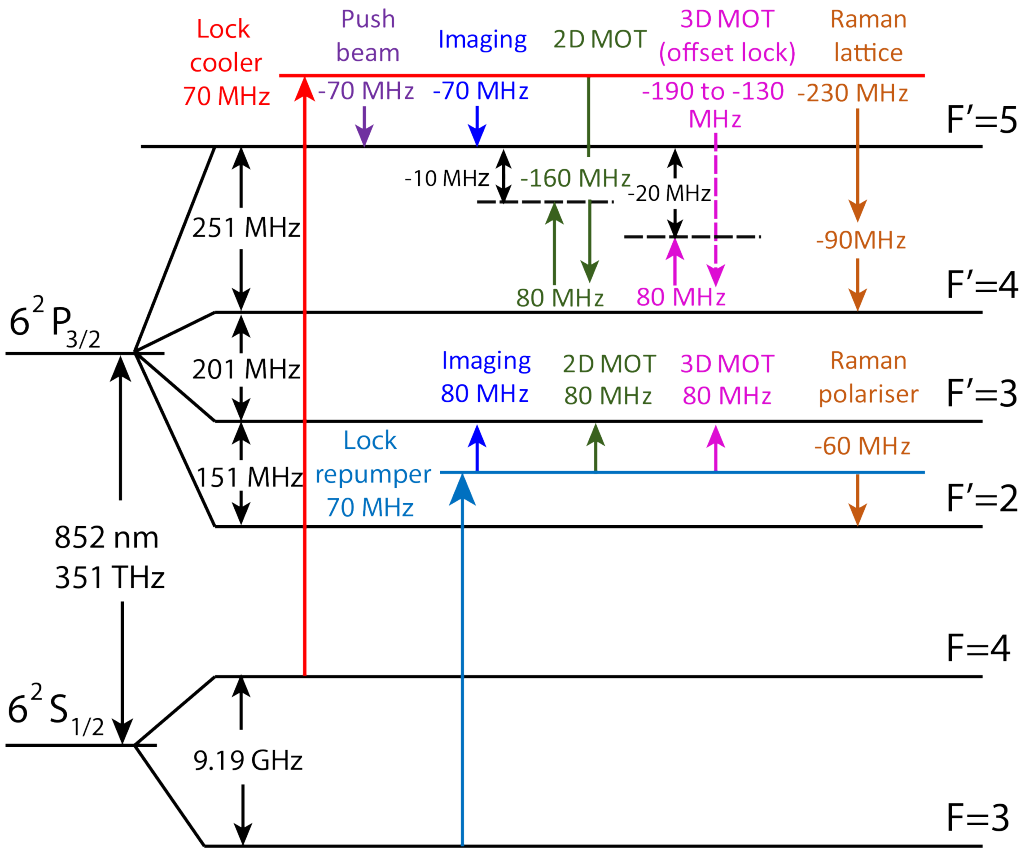

Figure 3.2: Diagram of the transitions and light detunings used for the various cooling stages of caesium atoms. The figure is adapted from [104].

lattice for degenerate Raman sideband cooling is resonant with the $|F = 4\rangle \rightarrow |F' = 4\rangle$ transition.

Although the light of the MOT is far detuned by 251 MHz from the next possible transition, $|F = 4\rangle \rightarrow |F' = 4\rangle$, there is a small but non-negligible probability to excite atoms to the hyperfine state $|F' = 4\rangle$ from which the atoms can emit a photon by spontaneous emission and decay into the state $|F = 3\rangle$. Atoms in this state are no longer resonant with the cooling transition $|F = 4\rangle \rightarrow |F' = 5\rangle$ and a second laser system is necessary to repump the atoms back into the cooling cycle. Due to the small probability for decay to the $|F = 3\rangle$ state, this laser has relatively low power of a few milliwatts.

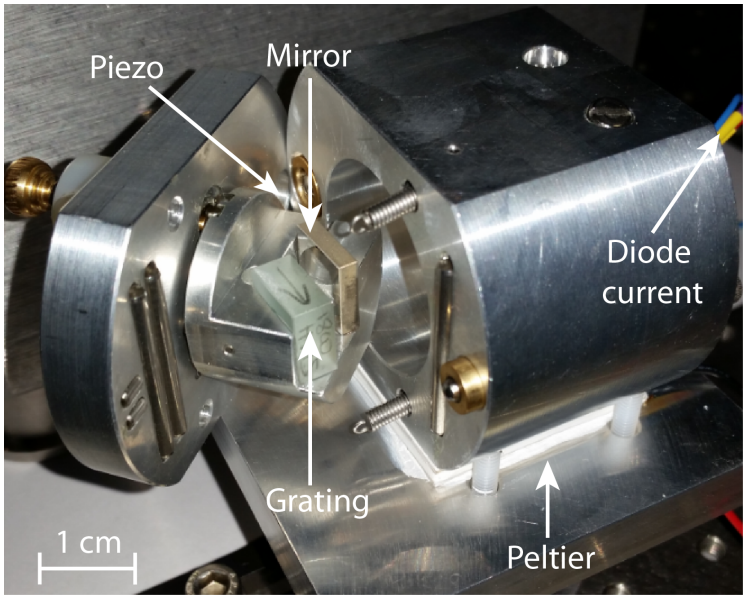

Figure 3.3: External cavity diode laser used as master laser.

3.2.1 Master lasers

In order to operate a MOT efficiently, a narrow-band, frequency-stabilized source of light source is required with a linewidth below 1 MHz. Typically, free running laser diodes provide a wider linewidth of tens of MHz, and the presence of current and thermal fluctuations, and other sources of noise, lead to a drift of the light frequency.

A broad linewidth of the diode can be reduced by using an external cavity diode laser (ECDL). We employ an ECDL in the so-called Littrow configuration, based on the design described in [105], in which a holographic grating is used to reflect a small amount of the laser emission back into the laser diode, thus forming an external cavity. The retro-reflected beam forces the laser diode to emit radiation at frequency modes allowed by the external cavity. We vary the laser frequency by changing the current, the temperature and the angle of the grating. The laser is mounted on a Peltier element that is used to stabilise and change the temperature, which is monitored by a thermistor. A piezoelectric transducer is used to finely adjust the grating. The ECDL is shown in Figure 3.3. The whole system is controlled by electronic PID regulators for current and temperature (MOGLABS DLC202).

Current and thermal fluctuations and drifts, and mechanical vibrations lead to a change of the frequency of the light, and an active stabilization that locks the frequency on to a reference point is needed. The reference point is given by a well-defined atomic transition obtained by means of polarization spectroscopy [102, 103]. The experimental setup for the polarization spectroscopy is shown in Figure 3.4. A σ^+-polarized light beam, called pump beam, passes through a cell containing caesium vapor. Because of the selection rules with $\Delta m_F = \pm 1$, on resonance, the pump beam will optically pump the atoms toward increasing m_F-states causing a non-uniform population distribution in the different magnetic sub-levels. A second and weaker counter-propagating, linearly-polarized beam, called probe beam, is overlapped with the pump beam. Considering that linearly polarized light can be written as a superposition of σ^+ and σ^-, the probe beam will experience a different index of refraction for the two orthogonal components σ^+ and σ^-, due to the anisotropy in the atoms population induced by the pump. This leads to a phase shift between the two components of the polarization, which induces a rotation of the polarization plane of the light. This rotation is measured by setting the polarization of the probe beam to 45° and by using a polarizing beam splitter (PBS) and a differential photodiode to measure the difference between the signals as shown in Figure 3.4.

3.2.2 Slave laser and tapered amplifier

The two master lasers generate an output power of approximately 40 mW, which is insufficient for the MOT and the Raman cooling. To amplify the light, we use two slave lasers, each capable of generating a maximum output power of 150 mW for cooling and repumping transitions. Both slave lasers are temperature and current controlled by PID controllers and are locked to the frequencies of the master lasers by means of injection seeding. We send a small amount of light ($< 400\,\mu$W) from the master laser into the diode of the slave laser, which forces the diode to adopt frequency and polarization of the master laser. The light of the slave lasers is again amplified by two commercial tapered amplifiers (TA) (Thorlabs TPA850P10), generating light for the 2D-MOT, 3D-MOT and the

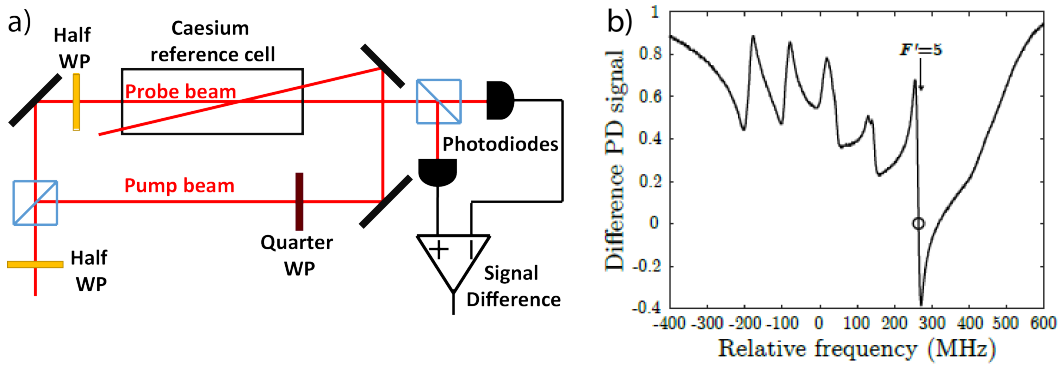

Figure 3.4: a) Scheme of polarization spectroscopy. b) Spectrum of the polarisation absorption spectroscopy associated to the cooling laser. The locking point (circle) is at the zero crossing of the signal difference and corresponds to the $|F = 4\rangle \rightarrow |F' = 5\rangle$ transition. The second figure is taken from [101].

lattice for the degenerate Raman sideband colling. Both TAs provide an output power of about 1 W. We continuously monitor the frequencies of the slave lasers and tapered amplifiers by a commercial Fabry-Perot cavity (Thorlabs SA210-8B). A detailed scheme of the whole laser setup is shown in Figure 3.5.

3.3 Magnetic fields

A precise control over the magnetic fields is indispensable to produce BECs. In our experiment we need magnetic field gradients, which are employed for the 2D+ and 3D MOTs and for the levitation of the atoms, offset fields for tuning the interactions, as well as shim coils for stray field corrections and fast magnetic field control. As described in Section 3.1, our vacuum setup is divided into the 2D+MOT chamber and a main chamber, and our coil design follows a similar arrangement. Here, we provide only a general overview of the magnetic fields (further details can be found in [101]).

3.3.1 2D+MOT coils

For creating the two dimensional quadrupole field in the 2D+MOT chamber, we employ two pairs of rectangular coils, which are made from 0.8 mm diameter copper wire in 14 layers from the centre, with 10 windings per layer. The inner

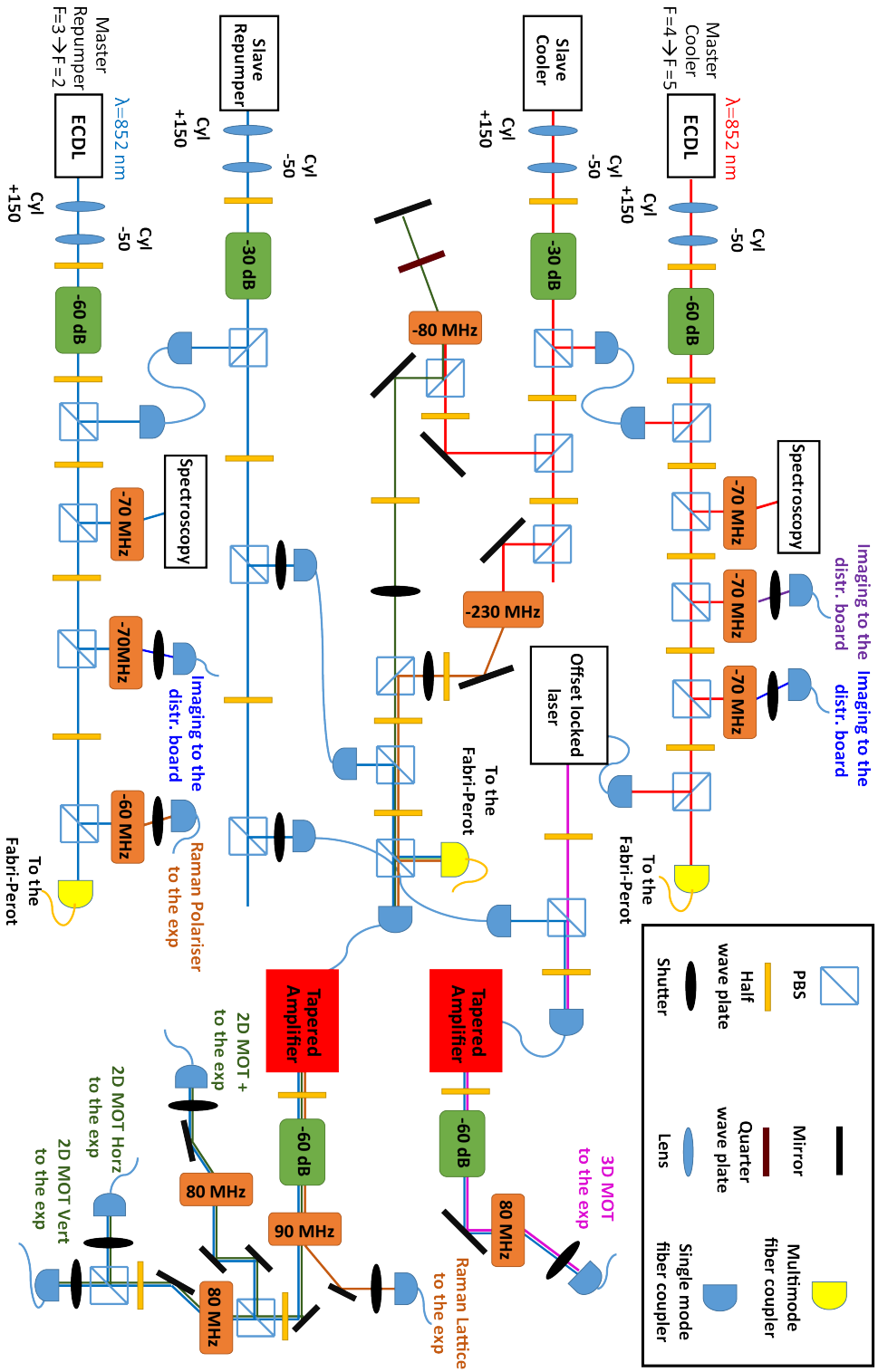

Figure 3.5: Detailed scheme of the cooling laser setup. ECDLs provide stable and narrow-band laser frequencies. A small amount of light from the ECDLs seeds two slave lasers, which are amplified by tapered amplifiers. Each lasing device is protected from back reflections by optical isolators. Acoustic-optic modulators are intensively employed for shifting the light frequency by a few tenths of MHz.

dimensions of each coil are 30 mm × 150 mm. The coils are supported by a 3D-printed mount of a graphite compound (3D-Alchemy), as shown in Figure 3.6 a. The gradient coils and the shim coils are glued to the inner and outer sides of the support, Figure 3.6 b. The gradient coils are driven by a power supply (TENMA 72-10495) in a counter-propagating current configuration, allowing us to generate magnetic field gradients of about 10 G/cm with current of 1 A.

3.3.2 Main coils

In the main chamber we perform all the cooling stages that lead to Bose-Einstein condensation. Magnetic fields for the 3D MOT, for the levitation and for tuning the interactions are provided a by single pair of coils. Each coil is divided in 7 independently controllable sections in order to have a good flexibility. They are made of rectangular copper wire with dimension of 2 ×1 mm. The coils have an inner diameter of 12 cm and are separated by a mutual distance of approximately 6 cm. They are mounted on a non-metallic 3D-printed support (Duraform) in order to minimise eddy currents. The coils can generate a heating power of up to 6 kW, and require water cooling. Our cooling design uses water channels in the enclosure of the coils, in combination with thin copper sheets, which serve as heat sinks to transfer heat from the inside of the coils to the water channel, Figures 3.6c,d.

We employ two switch-mode power supplies to drive the coils (Delta Elektronika SM120-50, SM7020-D) providing maximal currents of 50 A and 20 A for the generation of a homogeneous magnetic field and a field gradient, respectively. As will be explain in Chapter 4, a precise control of the gradient field is crucial for levitating the atoms. We control the currents with a feedback loop that consists of a current transducer, to measure the current, and a PID controller, which drives a MOSFET to regulate the current.

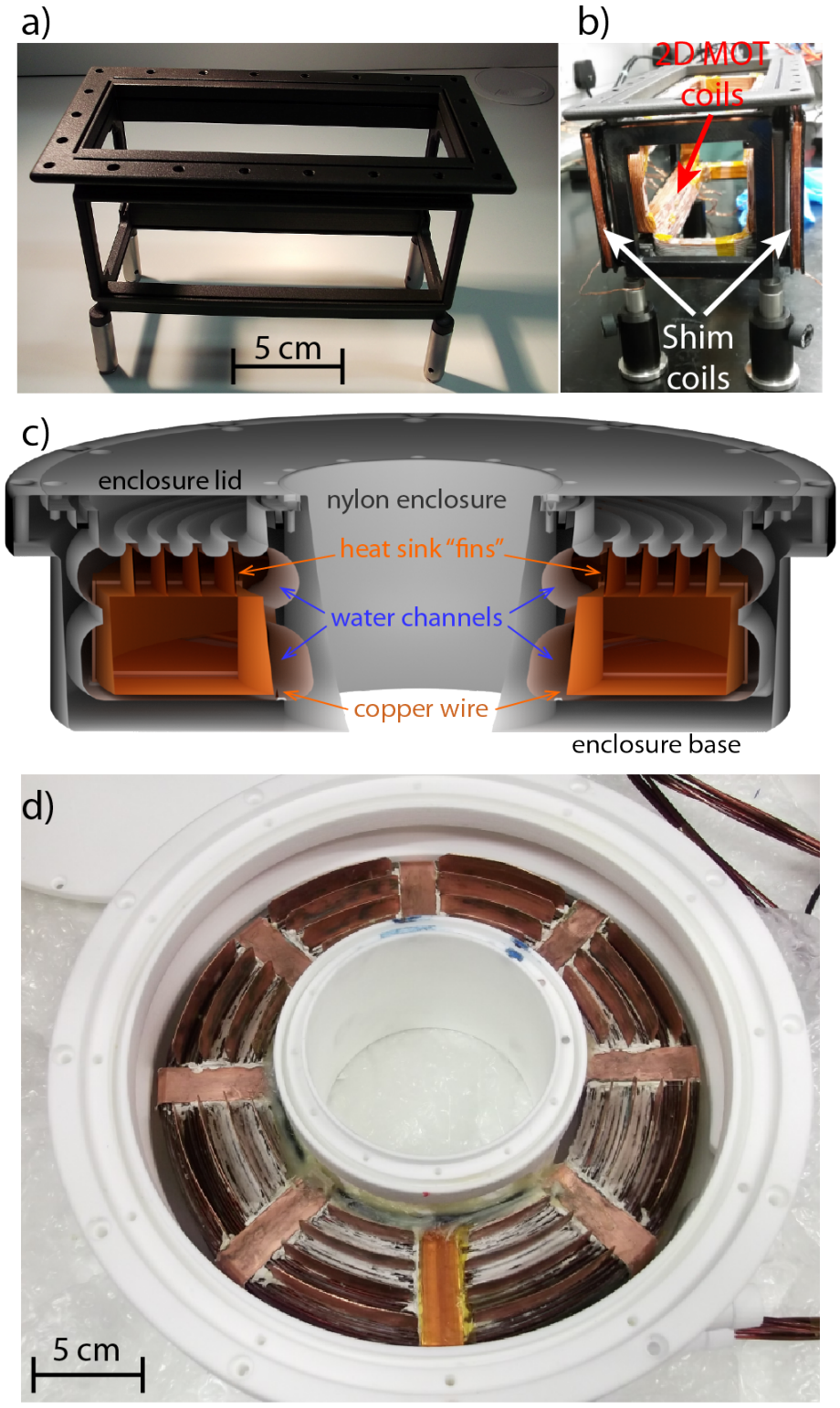

Figure 3.6: a) 3D-printed support for 2D-MOT coils. b) Gradient coils and shim coils glued onto the mount. c) Cross section of the main coil, to illustrate the design of water channels in the non-metallic enclosure and the layout of the copper sheets. d) Main coils in the nylon enclosure before being closed and sealed.

3.4 Diagnostic and computer control

In this section, I summarise the procedures we use for measuring the physical properties of our cold cloud, for diagnosing magnetic fields in our main chamber and for controlling the experimental sequence.

3.4.1 Imaging

In our experiment, we use absorption imaging to detect the spatial distribution of the atomic cloud. We illuminate the atoms with a resonant light pulse and image the shadow of the cloud onto a camera [106]. Assuming that the imaging beam propagates along the y axis with an initial intensity profile $I_0(x,z)$, the light intensity $I(x,z)$ that reaches the camera on the x,z plane is given by [107]:

$$I(x,z) = I_0(x,z)e^{-D(x,z)}, \tag{3.1}$$

where $D(x,z)$ is the optical density, which is

$$D(x,z) = D_0(x,z)\frac{1}{1+\frac{I}{I_{\text{sat}}}+\frac{4\Delta^2}{\Gamma^2}} \tag{3.2}$$

$$\text{with} \qquad D_0(x,z) = \sigma_0 \int n(x,y,z)dy. \tag{3.3}$$

Here I_{sat} is the saturation intensity for caesium, Δ is the detuning from the imaging transition, Γ is the line width of the transition, σ_0 is the absorption cross section and $n(x,y,z)$ the cloud density distribution. In our imaging setup, we use linearly polarised light[1] that is resonant, $\Delta = 0$, with the $|F=4\rangle \rightarrow |F'=5\rangle$ transition, Figure 3.2, and we set the intensity of the imaging beam such that $I/I_{\text{sat}} \ll 1$ to work in the linear regime. We extract the atom number by taking a picture of the beam intensity profile with the atom cloud, $I(x,z)$, and without the atom cloud, $I_0(x,z)$. By inverting equation 3.1, we obtain the number of

[1]For linearly polarised light the absorption cross-section σ_0 is calculated from the average of the Clebsch-Gordan coefficients over all m_F Zeeman sub-levels leading to $\sigma_0 = 0.1945\lambda^2$, where λ is the wavelength of the imaging beam [108]. We chose to use linearly polarised light because the imaging process is robust against small magnetic field fluctuation and it is well suited to our experimental configuration.

atoms from the ratio between $I(x, z)$ and $I_0(x, z)$. A typical imaging sequence consists of releasing the atoms from the cooling or trapping beams and letting them expand with the levitation field on for few tens of milliseconds. In this stage the offset field is set close to 17.2 G to minimise interaction effects during the expansion. Then, we switch off the levitation and offset field and let the atoms fall for 5 ms. The images are taken at zero magnetic field and the measured time for the magnetic field to settle close zero is below 3 ms. Subsequently, we send a pulse of repumping and resonant light of a duration of 100 μs to image the atomic cloud. After the first image, we wait about 100 ms and we take the image of the beam intensity profile.

We employ two horizontal imaging setups in which one is used for imaging large clouds, for instance of the MOT, and the other one for imaging small clouds, for instance BECs. For a large field of view, we employ, in the 4-f configuration, a sequence of $f = 300$ mm and $f = 100$ mm lenses with a diameter of 25.4 mm, which set a diffraction limited resolution of 10 μm and a magnification of 1/3, and a CCD camera (Allied Vision Manta G-125B). For a stronger magnification, we use a sequence of $f = 75$ mm (diameter of 25.4 mm), and $f = 150$ mm doublet lenses (diameter of 50.8 mm), which set a diffraction limited resolution of 2.5 μm (4 μm smallest measured size of a BEC) and a magnification of 2, and a CMOS camera (MatrixVision BlueFox3-1012bG).

3.4.2 Microwave spectroscopy

Microwave spectroscopy provides a sensitive tool to diagnose magnetic fields. It relies on the differential Zeeman shifts of atomic hyperfine states in a magnetic field, leading to magnetic field-dependent transition frequencies. In our case, we perform microwave spectroscopy between $|F = 3\rangle$ and $|F = 4\rangle$ hyperfine levels, which are separated by 9.19 GHz.

For implementing microwave spectroscopy, we use a frequency generator, which produces frequencies up to 2.7 GHz (Marconi2031), set to an output of about 2.3 GHz. The signal is sent to a frequency doubler (Mini-Circuits ZX90-2-36-S+), then to two amplifiers (Mini-Circuits ZX60-6013E-S+ and ZX60-V62+)

and to a second frequency doubler (Mini-Circuits ZX90-2-50-S+). The generated signal is at 9.2 GHz and is amplified by other two amplifiers (Mini-Circuits ZX60-183A-S+ and Kuhne PA8501000). The signal is eventually sent to a microwave horn, which is positioned below the main chamber at a distance of about 15 cm from the trap center.

3.4.3 Computer control

We require a precise control of digital and analogue signals with a time resolution of 10 μs. The signals are used to regulate currents and laser pulses during our experimental sequence.

Our hardware is based on two digital boards (National Instruments NI-6534), two analog boards (National Instruments NI-6733) and a digital-analog board (National Instruments NI-6723). In total, we have 40 analog channels, which output voltages in the range of -10 V to +10 V, and 64 digital outputs, which generate TTL signals, all with a time resolution of 10 μs.

The NI cards are controlled by a dedicated PC and a server program that was developed in C++. In order to have an intuitive user interface, we employ a separated PC to program the experimental sequence in MATLAB and transmit the timing information via network to the hardware server program. Our MATLAB interface allows us to set predefined parameters, such as timings and wave forms, by means of a graphical user interface (GUI).

3.5 BEC generation sequence

As mentioned in the introduction, the first successful cooling sequence for the generation of BECs of caesium was developed in Innsbruck [41] and our sequence is based on that pioneering work. In addition, we enhance atom numbers and loading durations by using a 2D-MOT setup and large-volume dipole traps.

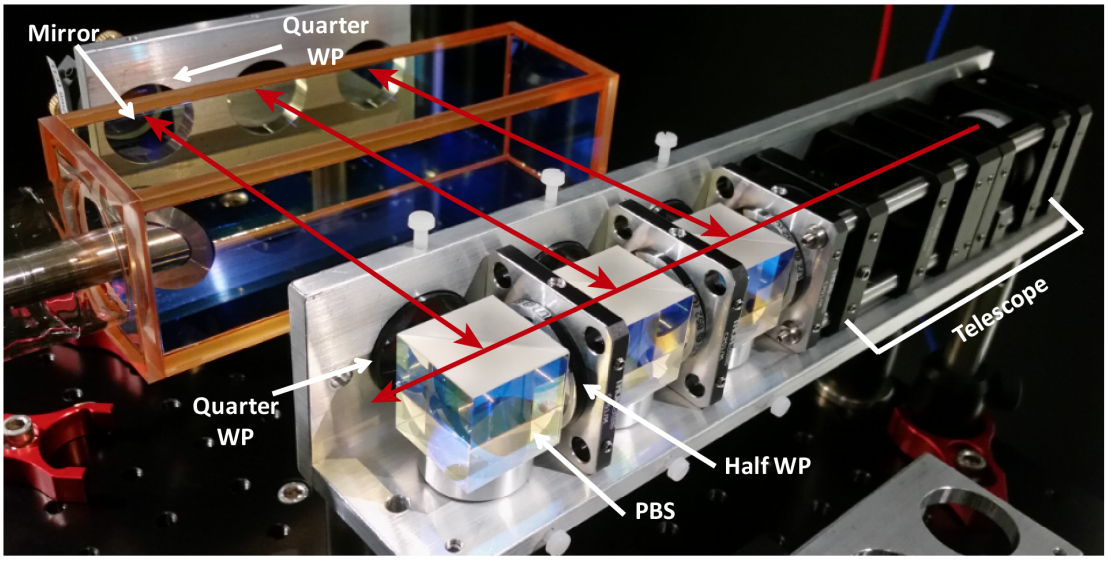

Figure 3.7: Optical setup of the 2D+MOT consisting of a cage-mounted telescope and three polarizing beam splitters with half-wave plates and quarter-wave plate at the input and output port respectively. The transversal beams are retro-reflected by mirrors mounted on mirror mounts, which are fixed on the aluminium bracket.

3.5.1 2D and 3D MOT

Magneto-optical trapping is the most common technique for confining and cooling atoms down to the micro-Kelvin regime. In our experiment, we use a 2D-MOT as a source of a cold atomic beam and a 3D-MOT as an initial cooling stage for cooling and trapping of atoms in our main chamber. Magneto-optical traps employ the dissipative force, generated by red-detuned and counter-propagating light beams, to slow and cool down the atoms while a magnetic quadrupole field generates a position-dependent force, which provides a spatial confinement [109, 110].

Our sequence starts by cooling atoms in the 2D-MOT section. Here, the atoms are cooled in the two transversal dimensions by means of three 25 mm size retro-reflected beams in a σ^++σ^- configuration and trapped transversally by two pairs of anti-Helmoltz coils as described in Section 3.3.1. As illustrated in Figure 3.7, the transversal beam is magnified up to a diameter of a 25.4 mm by a cage-mounted telescope, and three vertical and horizontal MOT-beams are derived by polarizing beam splitters. A half-wave plate at the input port of each

PBS is used to regulate the power, and a quarter-wave plate at each output port is employed to generate circularly polarised light. Every component is mounted on an aluminium bracket designed to keep the optical system as compact as possible. Three mirrors, which are mounted on mirror mounts, are used to retro-reflect the beams. We use the same design for the vertical direction. A total light power of 180 mW is used, and the optimised magnetic field gradient is close to 5 G/cm.

In order increase the atomic flux, we adopted a slightly modified version called 2D+MOT [111] where two counter-propagating laser beams are added along the longitudinal direction. The beams have a diameter of 25 mm and a power of about 1.5 mW. One of the beams enters from the back of the glass cell whereas the other enters from the side and is reflected along the longitudinal axis by a gold-plated mirror glued onto the differential pumping tube, Figure 3.7. In the center of the gold-plated mirror, a small exit hole (4 mm) allows the atoms to be transferred into the main chamber. Such transfer is accomplished by using a resonant light beam, also called push beam, which has a diameter of 2 mm and a power of about 400 μW.

In the main chamber, the atoms are captured by a 3D-MOT, which consists of three pairs of counter-propagating laser beams and a quadrupole magnetic field. We use a single polarization-maintaining optical fiber to deliver the laser light containing the cooling and repumping frequencies for the 3D-MOT. The laser beam is magnified up to almost 25 mm diameter by a telescope and split into six MOT-beams with an optical power of 80 mW. The optical setup for the splitting of the beams is built on the back of the main breadboard in order to save space. As shown in Figure 3.8, the six beams are directed towards the glass cell by mean of six periscopes.

In our 3D-MOT, a maximal atom number was determined for optimized parameters of 12 G/cm for the magnetic-field gradient, and a red detuning of 20 MHz for the cooling light. The initial loading rate of our 3D-MOT is 7×10^9 atoms/s, which sets a lower bound on the atom flux from the 2D+MOT. After almost 3 s of loading time, we reach a saturated cloud of more than 9×10^9 atoms. The measured temperature of the cloud is about 260 μK, which is obtained by absorbtion

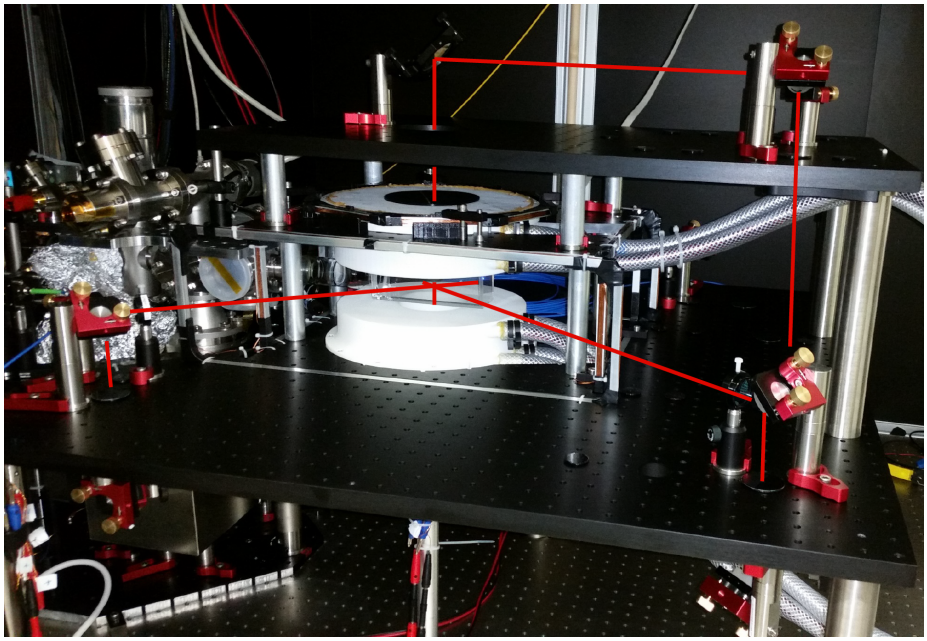

Figure 3.8: 3D MOT optical setup in which three pairs of laser beams are directed towards the centre of the main chamber by periscopes.

imaging in time of flight.

In order to increase the phase-space density[2], we compress the cloud by detuning the cooling light to -90 MHz from the $|F = 4\rangle \rightarrow |F' = 5\rangle$ transition with a linear ramp of a duration of 4 ms. The gradient and total optical power are kept constant. After the compression phase we reach a temperature of about 42 μK.

3.5.2 Degenerate Raman sideband cooling

Degenerate Raman sideband cooling is a powerful cooling scheme, which has been employed for achieving sub-μK temperatures [48, 112, 113] and, recently, for generating BEC without evaporative cooling [114]. In our case, it allows us to reach temperatures around $1\,\mu$K and at the same time to polarise the atoms into the $|F = 3, m_F = 3\rangle$ state. Our design is based on references [48, 113] which consists of four lattice beams and a single polarising beam. Here, we describe the essential features of this cooling scheme.

In summary, once the atoms are released from the 3D MOT, the lattice light,

[2]The phase-space density is defined as PSD $= n\lambda_{\mathrm{dB}}^3$, where n is the peak density

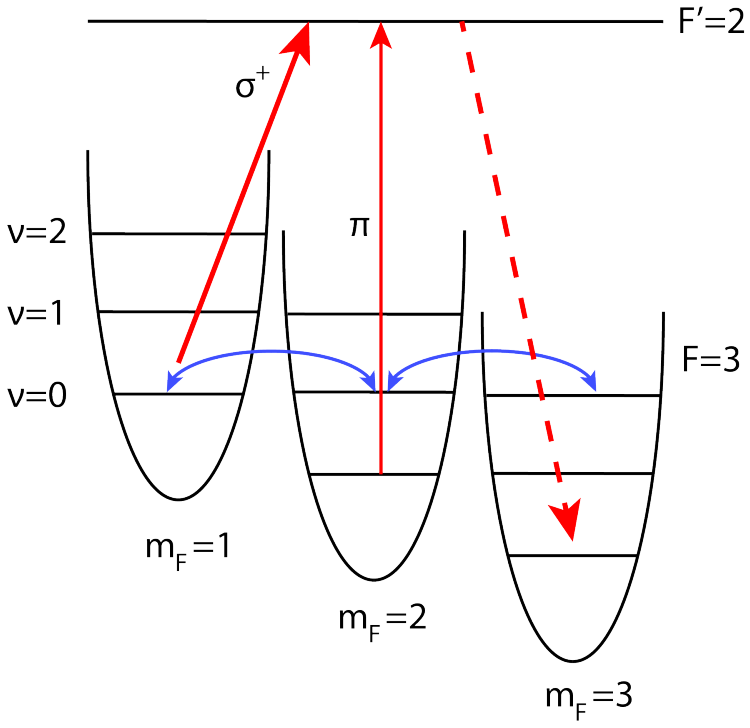

Figure 3.9: Scheme of the degenerate Raman sideband cooling. The blue arrows represent two-photon transitions, induced by the lattice light, that couple Zeeman states with degenerated vibrational levels. The red arrows show the absorbtion (full line) and the emission (dashed line) σ^+ polarized light, which provides optical cooling. In addition, the employment of linearly polarised light permits the atoms to be transferred out of the dark state.

which is resonant with the $|F = 4\rangle \rightarrow |F' = 4\rangle$ transition, pumps the atoms quickly into the $|F = 3\rangle$ state. At this stage, the atoms populate the highly excited vibrational trap levels of the lattice. The vibrational levels are coupled by the lattice light, which is now -9.19 GHz detuned from the $|F = 4\rangle \rightarrow |F' = 4\rangle$ transition, and drives coherent Raman transitions between these states. At the same time, a weak magnetic field shifts the levels $|m_F = k + 1, \nu = l + 1\rangle$ and $|m_F = k, \nu = l\rangle$, where ν denotes the vibrational quantum number, so that they are degenerate. The cooling cycle can be described as follows: in a first step, an atom starting in the level $|m_F = k + 1, \nu = l + 1\rangle$ is transferred to the level $|m_F = k, \nu = l\rangle$ by a Raman transition; in a second step a σ^+-polarised beam excites the atom from the $|m_F = k, \nu = l\rangle$ level into the $|F' = 2\rangle$ state, where it decays by emitting an incoherent σ^+-photon into the $|m_F = k + 1, \nu = l\rangle$ level [3]

[3]The vibrational level $\nu = l$ does not change during the absorbtion and spontaneous emission

as shown in Figure 3.9. In addition, a small amount of linearly polarised light allows to transfer atoms in the $m_F = 2$ state to the dark state $m_F = 3$. This can be accomplished by adjusting the horizontal magnetic fields by means of a pair of shim coils.

In the experimental sequence, we load the atoms into the lattice by ramping up the light intensity in 2 ms with a linear ramp. Each lattice beam has a diameter of 1.5 mm and a final optical power of about 25 mW. For the given lattice beam parameters, we found optimal cooling for a weak magnetic field of 100 mG. The polarising beam has a diameter of 2 mm and a final optical power of about 2 mW. This beam is 7 MHz blue detuned respect to the $|F = 3\rangle \rightarrow |F' = 2\rangle$ transition in order to account for the ac-Stark shift induced by the lattice light. Since the cooling efficiency depends crucially on the polarisation of the polarising beam, we use a combination of two half-wave plates and a quarter-wave plate for setting the polarisation. After 3 ms of degenerate Raman sideband cooling we, have 3×10^8 atoms in the $|F = 3, m_F = 3\rangle$ state, at temperature of just below 1μK.

3.5.3 Magnetic levitation

Unlike the other alkali-metal atoms, caesium atoms need to be in the lowest Zeeman state $|F = 3, m_F = 3\rangle$ to reach quantum degeneracy. This state is collisionally stable, but it is a high-field seeker state, with the disadvantage that magnetic traps cannot be used. Moreover, caesium is the heaviest alkali-metal atom and experiences a relatively strong gravitational attraction, which requires optical traps with large laser powers for compensation. In order to suppress the gravitational force, we apply a vertical magnetic field gradient, which levitates the atoms. By assuming that the atomic magnetic dipole follows the magnetic field adiabatically, i.e for slow-varying magnetic fields, the magnetic potential U_{mag} experienced by an atom can be written as

$$U_{\text{mag}} = \mu_B g_F m_f \left|\mathbf{B}\right|, \tag{3.4}$$

of the photon when the atoms in the lattice are in the Lamb-Dicke regime.

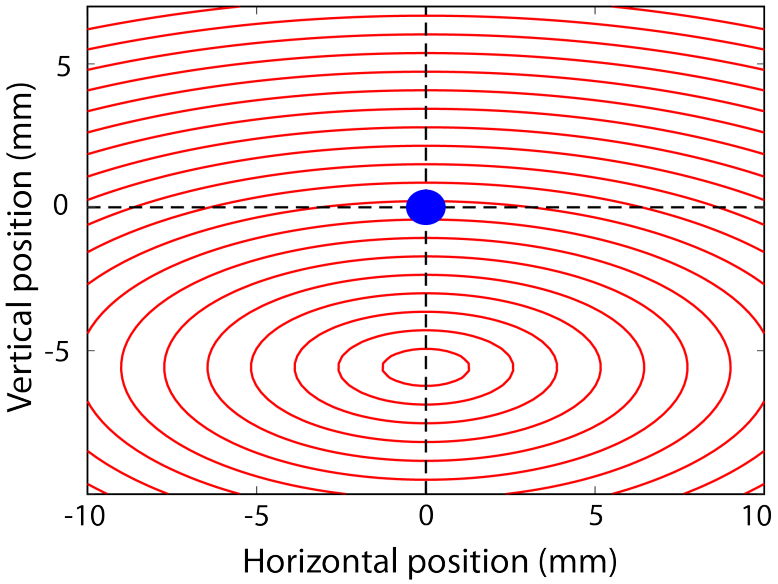

Figure 3.10: Calculated magnetic field strength for a magnetic field gradient $\partial_z B$ of 31 G/cm and for an offset field B_0 of 17 G. The lines have a spacing of 2 G.

where μ_B is the Bohr magneton, g_f is the gyromagnetic factor related to the hyperfine level F and m_f the magnetic quantum number. In our case, the total magnetic field $\mathbf{B}$ is the sum of a quadrupole field, which generates a vertical gradient $\partial_z B$, and a positive offset field B_0 oriented along the vertical direction, which allows for interaction tuning. The total magnetic field strength in the vertical plane is illustrated in Figure 3.10.

The gravitational potential for a caesium atom is $U_{\text{gra}} = mgz$, where g is the gravitational acceleration. The value of the magnetic field gradient, which counteracts the gravitational acceleration is

$$\frac{\partial B_z}{\partial z} = \frac{mg}{\mu_B g_F m_f}, \tag{3.5}$$

which is 31.1 G/cm for or caesium in the $|F = 3, m_F = 3\rangle$ state.

As consequence of the solenoidal nature of the magnetic field, i.e $\nabla \cdot \mathbf{B} = 0$, the presence of a vertical magnetic gradient leads to a magnetic field gradients along the horizontal directions, which results in an outwards horizontal force. The potential deriving from this horizontal force can be expressed in the form of

a harmonic expulsive potential [65]

$$U_{\text{hor}} = U_0 - \frac{1}{2} m\alpha^2 r^2, \tag{3.6}$$

where $r = \sqrt{x^2 + y^2}$ is the horizontal displacement of the atoms from the origin and α is the anti-trapping angular frequency, which in the case of levitated atoms is [65]

$$\alpha = g\sqrt{\frac{m}{3\mu_B B_0}}. \tag{3.7}$$

From equation 3.6, the equations of motion for an atom at initial position $r(0)$ with a initial speed of $v_r(0)$ are [65]

$$r(t) = r(0)\cosh(\alpha t) + \alpha^{-1} v_r(0)\sinh(\alpha t) \tag{3.8}$$

$$v_r(t) = v_r(0)\cosh(\alpha t) + \alpha r_0 \sinh(\alpha t). \tag{3.9}$$

As we will discuss in Chapter 4, such anti-trapping potential will be an important limiting factor in our interferometric measurements with levitated atoms.

In the experimental sequence, the levitation field needs to be switched on quickly after the Raman cooling to avoid the atoms' acceleration which would lead to the heating of the cloud. By employing a 400 V discharge capacitor, which drives a short current pulse in the inner-most section of the main coil, we manage to levitate the atoms and to keep its position while the levitation field is ramped up to 31.1 G/cm with a linear ramp of a duration of 5 ms. At the same time an offset field of about 40 G is applied to shift the center of the quadrupole field and to control the collision rate via magnetic Feshbach resonances.

3.5.4 Reservoir and dimple traps

After Raman cooling, we have a cold levitated atom cloud that needs to be confined. We employ far-detuned optical dipole traps to provide a conservative potential which allows us to capture the atoms with minimal heating of the cold cloud. Here, we summarise the basic physical mechanism underlying conservative potentials generated with laser light. Further details about optical dipole traps

for neutral atoms can be found in the review article [115].

In synthesis, the oscillating electric field E of a laser light induces an oscillating electric dipole d in a neutral atom at the same driving angular frequency ω, such that $d = \alpha(\omega)E$. Here, $\alpha(\omega)$ is the atomic polarisability, which in general is a complex quantity. The induced oscillating dipole interacts again with the electric field of the laser light, resulting in the dipole potential $V_{\text{dip}} = 1/2\,\langle dE\rangle$, where $\langle\cdot\rangle$ denotes a time average, which is proportional to the intensity I of the laser field. For an atom which has a transition energy of $\hbar\omega_0$ with a natural linewidth of Γ, the dipole potential $V_{\text{dip}}(r)$ and the photon scattering rate Γ_{sc} are related to the real and imaginary part of $\alpha(\omega)$, respectively. They are given by [115]:

$$V_{\text{dip}}(\mathbf{r}) = -\frac{3\pi c^2\Gamma}{2\omega_0^3}\left(\frac{1}{\omega_0-\omega}+\frac{1}{\omega_0+\omega}\right)I(\mathbf{r}), \tag{3.10}$$

and

$$\Gamma_{\text{sc}}(\mathbf{r}) = -\frac{3\pi c^2\Gamma\omega^3}{2\hbar\omega_0^6}\left(\frac{1}{\omega_0-\omega}+\frac{1}{\omega_0+\omega}\right)^2 I(\mathbf{r}). \tag{3.11}$$

In the case of caesium, the above formulae have to account for the D_1 and D_2 transitions by introducing an effective transition frequency [115]

$$\omega_{\text{eff}} = \frac{1}{3}\omega_1 + \frac{2}{3}\omega_2 = 2\pi \times 256\,\text{THz}, \tag{3.12}$$

and an effective natural linewidth

$$\Gamma_{\text{eff}} = \frac{1}{3}\Gamma_1 + \frac{2}{3}\Gamma_2 = 2\pi \times 5.00\,\text{MHz}. \tag{3.13}$$

In all the trapping stages of the experiment, we use beams with a Gaussian intensity profile, i.e [115]

$$I(r,z) = \frac{2P}{\pi w^2(z)}\exp\left(-2\frac{r^2}{w^2(z)}\right) \quad \text{with} \quad w(z) = w_0\sqrt{1+\left(\frac{z}{z_R}\right)^2}, \tag{3.14}$$

where r is the coordinate in the radial direction, z is the coordinate along the beam propagation axis, P is the beam power, w_0 the beam waist at the focus, and $z_R = \pi w_0^2/\lambda$ is the Rayleigh length. Here, λ represents the wavelength of the

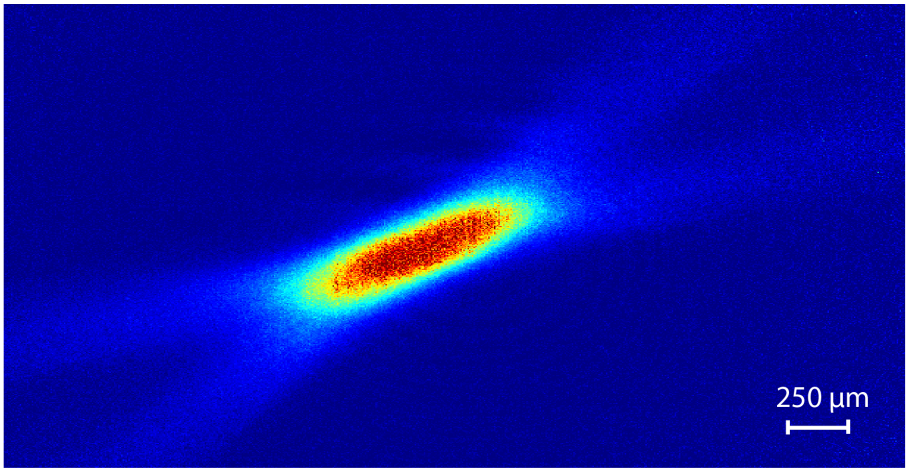

Figure 3.11: Absorbtion image of a cold cloud of about 3 $\times 10^7$ atoms after being released from the large volume dipole trap.

laser light.

In the experimental sequence, once the atoms are released from the Raman lattice and then levitated, the cold cloud is loaded within 40 ms into a large and shallow optical dipole trap which is formed by two crossed horizontal beams at a wavelength of 1070 nm. The laser light is provided by an Ytterbium fiber laser with a maximum power of 200 W (IPG Photonics, YLR-LP-200), which is split by a polarising plate and focussed such that each beam has a maximum power of 100 W and a waist of 800 μm at the centre of the main chamber, corresponding to 25 μK trapping potential depth. After a hold time of 200 ms, we have about 3.8×10^7 atoms at a temperature of about 9 μK, Figure 3.11.

The large beam waists of the reservoir trap provide a large capture volume for the atoms, but they prevent efficient and fast evaporative cooling. Instead, immediately after the loading of the reservoir trap, two tightly focused beams in a crossed configuration, also named dimple, are employed to locally increase the phase space density of the cold cloud [116, 117]. Our dimple beams consist of a vertical and a horizontal beam with waists of 90 μm and 50 μm, respectively. Both beams are derived from a 50 W fiber amplifier (Nufern NUA-1064-PD-0050-DO) seeded by a Nd:YAG laser (Coherent Mephisto), which provides light at a wavelength of 1064 nm with a line width below 10 kHz. The dimple beams are

ramped up in 2 ms to 120 mW for the horizontal beam, and to 260 mW for the vertical beam and kept at these powers for 100 ms while the reservoir trap is at the maximum power.

Subsequently, we ramp down the reservoir beams in 1300 ms while the offset field is reduced to 23 G in order to control three-body losses and to keep a good thermalisation rate. After 100 ms of plain evaporation in the dimple trap, we have about 1.1×10^6 atoms at a temperature of 1 μK, corresponding to a phase space density of about 10^{-6}, which are good condition for starting the forced evaporative cooling.

3.5.5 Forced evaporation and BEC

We employ three stages of forced evaporation to reach quantum degeneracy. Each stage consists of a linear ramp of the intensities of the dipole beams, and a ramp of the magnetic field. In the first stage, we ramp down the intensity of the horizontal and vertical dipole beams to 30 mW and 70 mW respectively in 500 ms. At the same time we set the offset field at 21 G $a_{\text{off}} = 210a_0$ for three-body collision losses minimisation [41, 42]. At this stage we have a thermal cloud of 8×10^5 at a temperature of about 230 nK, which correspond to a phase space density of about 0.53.

In the second stage, a 1 s-duration linear ramp that decreases the beam power to 10 mW (horizontal) and 26 mW (vertical) allows us to reach the phase transition from a thermal gas to a BEC, as can be seen in the appearance of a bimodal distribution, Figure 3.12. We have 5×10^5 atoms at a temperature of approximately 60 nK.

Eventually, a third final linear ramp lowers the beams power to 1 mW (horizontal) and 8 mW (vertical) in 3 s allowing us to obtain a BEC of about 2.0×10^5 with a condensate fraction of $N/N_0 = 0.48$ at temperature of about 10 nK.

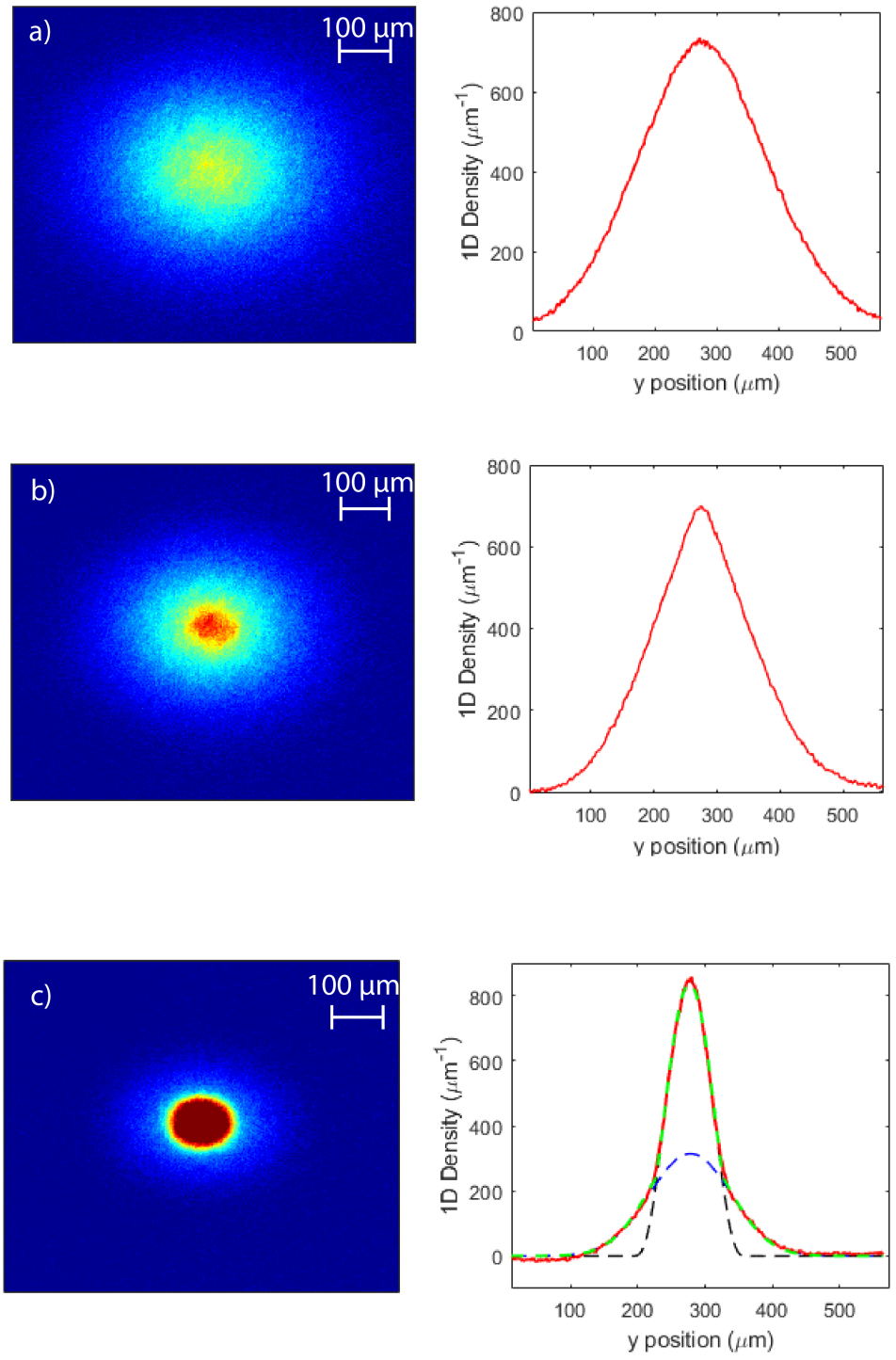

Figure 3.12: Absorbtion images of the density distribution of the atom cloud after free expansion of 50 ms at different stages of the evaporation. a) After the first evaporation stage the atoms are still thermal. b) After the second ramp, the cloud reaches the phase transition. The integrated density profile starts to show a bimodal distribution. c) BEC with thermal fraction after the last evaporation stage. Red line: integrated density profile. Blue dashed line: Gaussian fit of the thermal cloud. Black dashed line: parabola fit, TFA, of the BEC fraction. Green dashed line: Bimodal distribuction resulting from the combination of the two previous fits.

Chapter 4

Interferometric measurement of micro-g acceleration with levitated atoms

The chapter is an extension of the article A. Di Carli, C. D. Colquhoun, S. Kuhr, and E. Haller, "Interferometric measurement of micro-g acceleration with levitated atoms", New J. of Phys. **21**, 053028 (2019). The article can be found in Appendix C and is cited as Ref. [56].

4.1 Introduction

In the last decades, atomic interferometry has been employed successfully for precise measurements of the local gravitational acceleration [118, 119], for sensing rotations [120–122] and inertial forces [123–125]. Furthermore, atomic interferometers have found application in both applied, such as gravimetry and gradiometry [126–128], and fundamental physics, such as measurements of the fine structure constant [131, 132], Newton's gravitational constant [133–135], constraints on dark energy [136] and forces exerted by black-body radiation [137].

Analogous to optical interferometers, in atom interferometers, the matter wave is split into two or more parts, then the parts evolve independently along different paths. The atoms accumulate relative phase shifts depending on the interaction

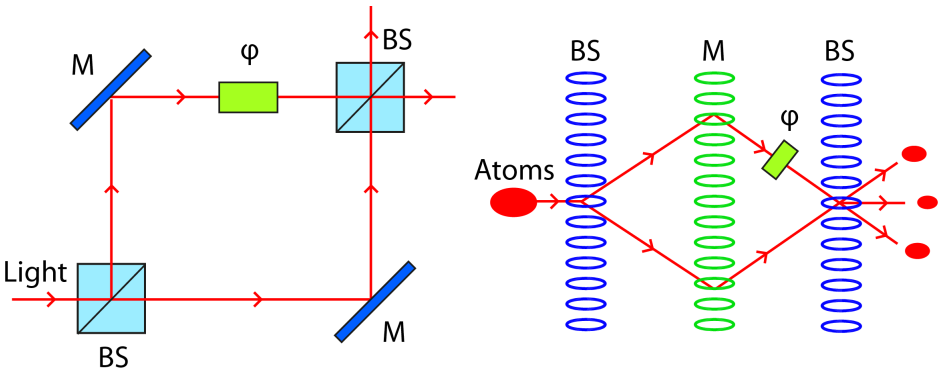

Figure 4.1: Analogy between an optical and an atom interferometer. In both cases, the optical and matter waves are split by a beam splitting element (BS) and, after a free evolution, reflected by a mirror element (M). Eventually, the waves are recombined by another beam splitting element (BS). The interference pattern that forms after the recombination depends on the relative phase shift φ accumulated along the total interferometric sequence. Figure inspired by [174].

with a local potential and eventually are recombined to form an interference pattern as shown in Fig. 4.1. A comprehensive review on atom interferometry is given in [156].

Most atom interferometers use cold thermal atom clouds as sources of matter waves for sensing inertial forces [118, 120]. Recent experiments also employ Bose-Einstein condensates for atom interferometry [146–150]. BECs, as described in Chapter 2, provide coherent, low dispersive and very bright sources of cold atoms which are capable to enhance the visibility of the interference pattern very close to 100% [151]. Although at first glance the high density of the BEC might improve the sensitivity of an atom interferometer, it is its Achilles' heel. The presence of interaction-induced dephasing [152] might lead to uncontrolled phase shifts caused by density fluctuations and strongly limit the interferometer's signal-to-noise ratio. The effect of atom-atom interactions is considerably stronger for trapped BEC interferometers [129, 130, 146], whereas it is negligible for expanded BECs [148, 150, 153, 154].

For inertial quantities, it is widely known that the sensitivity of atom interferometers increases with the space-time area enclosed by the arms of the interferometer [155]. In general, the area depends on the interrogation time of the interferometer and is limited by Earth's gravitational acceleration in most Earth-

based experimental setups. Several strategies have been adopted to increase interferometer sensitivity, such as large-momentum transfer (LMT) [157–159] for increasing the area spanned by the interferometer, or atomic fountains [160], drop towers [161, 162], parabolic fights [163, 164] and space facilities [165, 166] for increasing the interrogation time.

In this chapter, I will describe an experiment in which we use magnetic levitation as a different approach to extend the evolution time in Earth-based laboratories. Compared to the other aforementioned methods for extending the free evolution time, our experimental setup is significantly simpler and smaller. We utilize magnetic levitation to create and to interferometrically measure milli-g and micro-g acceleration of BECs in free expansion, and we show that the negligible center-of-mass motion of levitated atoms facilitates a direct study of phase-shifting elements in the interferometer paths. We employ BECs as sources of cold atoms for increasing the performance of the interferometer. In addition, we study the advantages and limitations of using magnetic levitation and demonstrate that it can be employed to reach an expansion time of 1 s, which is comparable to current drop-tower experiments [162].

The chapter is organised as follows: Section 4.2 provides an overview of our experimental setup. Section 4.3 motivates and illustrates the techniques we use for implementing atomic splitters and mirrors whereas in Section 4.4, we illustrate the interferometer scheme and provide the expression of the phase shift accumulated along the interferometer sequence. In Section 4.5, we present the results of the measurements achieved with our levitated interferometer. Small changes to the magnetic levitation gradient allow us to create marginal accelerations of milli-g (Section 4.5.1) and micro-g (Section 4.5.2). An additional laser beam in one of the interferometer paths constitutes a phase-shifting element, presented in Section 4.5.3. In Section 4.6 we estimate possible sources of noise and systematic errors. In Section 4.7, we measure features of the magnetic field distribution, such as the transversal curvature of the force field. Finally, using a combination of low interaction strength, low trapping frequencies, and magnetic levitation we demonstrate long expansion and observation times in Section 4.8.

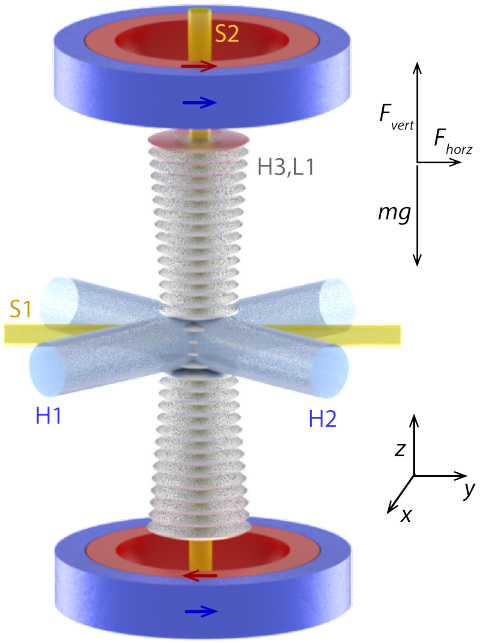

Figure 4.2: Sketch of the experimental apparatus. Magnetic field coils to control the offset field B_0 (blue, outer coils) and the vertical gradient of the magnetic field $\partial_z B$ (red, inner coils). Laser beams with small beam waists (S1, S2) and large beam waists (H1, H2, H3) trap the atoms, and a lattice L1 is used to split the wave packet during the interferometer sequence. Figure published in [56].

4.2 Description of the experimental apparatus

The experimental apparatus needed for performing the experiment is shown Figure 4.2. The part of the setup employed for magnetic-field generation consists of one pair of coils with co-propagating currents (blue, outer pair of coils), and one pair with counter-propagating currents (red, inner pair of coils). They are used for generating the offset field B_0 and the magnetic levitation field $\partial_z B$ respectively. Additional pairs of independently controlled shim coils are used for fine tuning.

The optical section consists of two crossed dipole beams (S1, S2), a vertical lattice beam (L1) and three large-waist dipole beams (H1, H2, H3). The beams S1 and S2 are employed for the evaporative cooling and the handling of the BEC after its generation, L1 is used to split and reflect the wave packet during the interferometer sequence and H1-H3 are employed for the long-expansion experiment.

The sequence for the generation of the BEC has been described in detail in chapter 3. We start with BECs of 2.5×10^5 atoms in the crossed laser beams S1 and S2 with trap frequencies $\omega_{x,y,z} = 2\pi \times (23.5, 17.7, 15.4)$ Hz. The atoms are in the absolute ground state $|F = 3, m_f = 3\rangle$ at a scattering length of $a = 210\, a_0$. We further reduce interactions by tuning the scattering length to $65\, a_0$ and by removing atoms by forced evaporation with a non-levitating magnetic field gradient. The starting condition for the interferometry measurements is a BEC of approximately 8×10^4 atoms corresponding to a peak density of about $6 \times 10^{13}\,\mathrm{cm}^{-3}$.

4.3 Splitting and reflection of a BEC

In analogy with optical interferometers, atom interferometers need some basic elements which split and reflect coherently the atomic wave function. Coherent splitting and reflection of matter waves can be accomplished by employing nanostructures, such as transmission gratings [138], double slits [139] and atom holograms [140], or by exploiting the mechanical force imprinted onto the atom by the light, like absorption from a travelling wave [141], stimulated Raman transitions [142] and optical standing waves [143–145].

In our experiment we use optical standing waves, also called optical gratings or lattices, for splitting and reflecting BEC whose center-of-mass is initially at rest. One advantage of using optical gratings instead of other methods that use resonant light is that the momentum states of the matter waves are changed whereas the internal states of the atoms are left unchanged. This leads to the suppression of noise effects caused by uncontrolled phase shifts relative to the different magnetic moments of the internal states in a homogeneous magnetic field. Other advantages are the suppression of incoherent photon scattering, which prevents the heating of the cold cloud, and the possibility of imparting large momentum to the matter wave without significant losses [157].

The effect of a light grating on matter was studied in the early stages of the quantum theory in 1933 by Kapitza and Dirac [168] where they showed that a

beam of electrons is partially diffracted from a standing wave of light by stimulated Compton scattering. This effect has been called Kapitza-Dirac scattering. Kapitza-Dirac scattering was later demonstrated for atomic beams [144] and BECs [169] in the limit of short light pulse durations and strong atom-light interaction and is used as a fundamental tool for splitting ultracold atom clouds. The basic physical mechanism relies on the coherent absorption and emission of off-resonant photons from the optical grating by the atoms [156, 167]. When an atom absorbs or emits a photon it exchanges a linear momentum equal to $p = \pm\hbar k$, where k is the photon wave number. In a standing wave, due to symmetry reasons, the atom can only be excited in the $\pm 2n\hbar k$ momentum states. The characteristic energy associated with the absorbtion or emission of a photon by the atom is called the recoil energy and is given by:

$$E_r = \frac{\hbar^2 k^2}{2m}, \tag{4.1}$$

where m is the mass of the atom. For caesium atoms and for a lattice light with a wavelength of 1064 nm, the value of one recoil energy is $E_r = h \times 1325\,\mathrm{Hz}$.

An optical standing wave is typically generated by a couple of counter-propagating laser beams. The resulting AC Stark potential for the atoms can be written as [170]

$$V(x,t) = V_0(t)\cos^2(kx), \tag{4.2}$$

where $V_0(t)$ is the lattice depth. In general, the potential is time dependent and is proportional to the intensity of the laser beam. The equation which describes a BEC in an optical lattice is thus

$$i\hbar\frac{\partial}{\partial t}\psi_p(x,t) = \left[-\frac{\hbar^2}{2m}\frac{\partial^2}{\partial x^2} + V_0(t)\cos^2(kx)\right]\psi_p(x,t), \tag{4.3}$$

where the effects of interactions have been omitted because the timescale associated with the peak chemical potential of the released BEC is usually longer than the timescale of a typical splitting pulse. By considering a single square pulse of duration t_p, which is shorter than the typical oscillation time in the lattice

well, $t_{ho} = 2\pi/\omega_{ho}$ with $\omega_{ho} = \sqrt{4VE_r}/\hbar$ [170], we can neglect the motion of the atoms during the pulse and thus the kinetic term in equation 4.3. In this so called Raman-Nath regime or thin grating regime, the general solution for atoms at rest is given by [167, 170]

$$\psi(x,t) = e^{-i\frac{\beta t}{2t_p}} \sum_{n=-\infty}^{\infty} (-i)^n J_n\left(\frac{\beta t}{2t_p}\right) \psi_{2n\hbar k}(x,t), \tag{4.4}$$

where $\beta = V_0 t_p/\hbar$ represents the pulse area, n is an integer number and J_n corresponds to the n-th Bessel function. From the given solution, it is clear that only even momentum states of the atoms are excited, thus recovering the intuitive picture given earlier. The population of the n-th momentum state after a pulse duration t_p is

$$P_n = J_n\left(\frac{\beta}{2}\right). \tag{4.5}$$

It would be desirable to use a single pulse for transferring all atoms from $|p = 0\hbar k\rangle$ to momentum states $|p = \pm 2\hbar k\rangle$ and vice versa, which would implement a 50 : 50 beam splitter. Unfortunately, this is not possible and composite pulses are needed as shown in [146, 149, 171, 172], where efficiencies above 99% were accomplished. In our experiment we adopt the composite pulse, shown in Figure 4.3, that is a combination of square sub-pulses in which the two side sub-pulses are characterised by the same duration t_s and intensity I_s whereas the central sub-pulse is characterised by a duration t_c and intensity I_c. More details about the splitting-recombination pulse used in this experiment are given in [173–175]. Here, we limit ourself to optimise the pulse parameters experimentally.

The second element that we need to implement for our interferometer scheme is an atomic mirror which inverts the motion of the two wave packets, allowing us to close the interferometer arms. In terms of quantum states, the optical grating transfers atoms from the $|\pm 2\hbar k\rangle$ state to the $|\mp 2\hbar k\rangle$ state imparting thus a momentum of $\Delta p = \pm 4\hbar k$. We implement the inversion with a Gaussian shaped light pulse, which is characterised by an intensity maximum $I_{\max}$ and a 1/e duration of t_G.

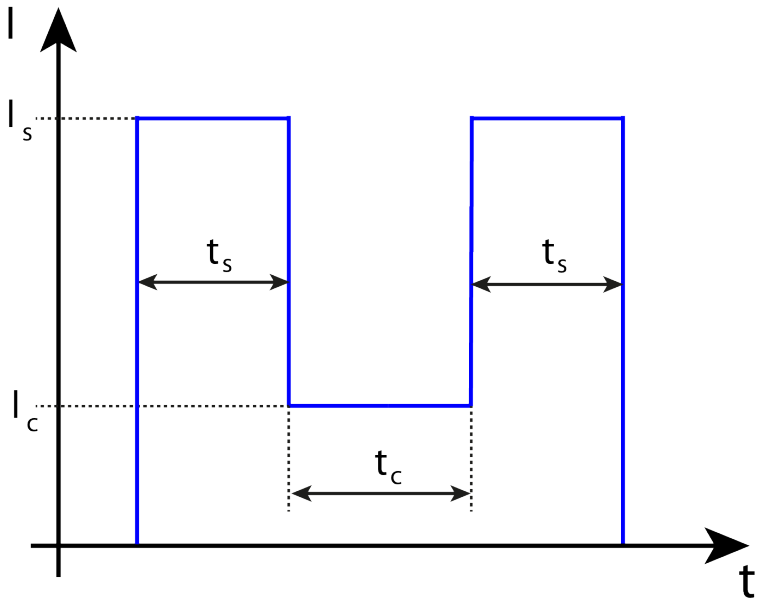

Figure 4.3: Time-dependent intensity and characteristic durations of the composite light pulse employed for the high efficiency splitting and recombination of the BEC. The two side sub-pulses are characterised by the same duration t_s and intensity I_s. The central sub-pulse has a duration of t_c and intensity of I_c.

4.4 Interferometer sequence and phase shift

Our interferometer setup and pulse sequence are based on references [146,149,171] and illustrated in Figure 4.4. The BEC is split by a first pulse into two wave packets with opposite momenta $\pm 2\hbar k$. The wave packets propagate freely for an evolution time, T_1, under the effect of the gravitational potential $U_{\text{gra}}(z) = mgz$ and the magnetic potential $U_{\text{gra}}(z) = \mu_B m_f g_f B(z)$, where $B(z)$ can be written as $B(z) = B_0 + \partial_z B z$. In a second step, we apply a Gaussian pulse that reflects the wave packets and we let them evolve for an evolution time T_2. A third pulse, which is identical to the first pulse, is used for recombining the two wave packets. The result of this pulse sequence are three wave packets with momenta $p_0 = 0$, $p = \pm 2\hbar k$.

In optical and matter wave interferometry, the interference pattern depends crucially on the accumulated phase shift of the wave packets during their evolution, and the measured quantity is typically inferred from the shape and time evolution of the interference pattern. The signal of the interferometer sequence described above has an oscillatory behaviour in the relative population of the mo-

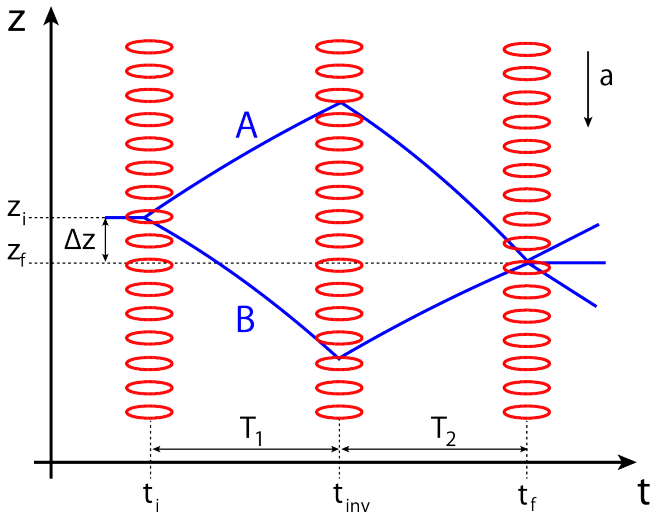

Figure 4.4: Scheme of the interferometer sequence. The sequence starts with a BEC initially at rest, at the vertical position z_i. The BEC is split by a first light pulse at t_i, in two wave packets. The wave packets evolve along two classical paths A and B, which are affected by the reflection pulse, at t_{inv}, and by total acceleration a. Eventually, the wave packets are recombined by a light pulse, at t_f, at the final position z_f. The free evolution times are denoted with T_1 and T_2. The difference between the final and initial position is Δz.

mentum modes, resulting in a probability P_0 to find an atom in the p_0 momentum mode of the following form:

$$P_0 = P_m + \frac{C}{2}\cos(\Delta\Phi_{\text{tot}}), \tag{4.6}$$

where C is the interference contrast, P_m is the offset of the interference signal and $\Delta\Phi_{\text{tot}}$ is the total phase difference accumulated during the whole interferometric sequence. In our experiment, P_0 is determined from the ratio between the atom number in the p_0 mode and the total atom number in all momentum modes.

Our goal is to measure the centre-of-mass acceleration, a_c, of a BEC, using the phase difference between the wave packets during the interferometer sequence. As shown in Figure 4.4, our interferometer has an upper arm (A) and a lower arm (B). The phase difference, $\Delta\Phi$, which is accumulated during the interferometer evolution, is proportional to the difference between the action $S_{\Gamma A}$ computed along the classical path ΓA and the action $S_{\Gamma B}$ computed along the classical path

ΓB [149, 176], namely

$$\Delta\Phi = \frac{S_{\Gamma A} - S_{\Gamma B}}{\hbar}. \tag{4.7}$$

The the action S_Γ is defined as

$$S_\Gamma = \int_{t_i}^{t_f} dt L_\Gamma, \tag{4.8}$$

where L_Γ is the Lagrangian of the system, defined as the difference between the kinetic energy and the potential energy, and evaluated along the path for which the action is stationary. In our case the Lagrangian can be written as:

$$L = \frac{1}{2}mv^2 - (mgz - \mu_B m_f g_f B(z)). \tag{4.9}$$

We use the energetically lowest Zeeman sub-state of caesium atoms with $m_f = 3$ and $g_f = -1/4$. Based on the Euler-Lagrange equation, we write the equation of motion

$$ma_c = \frac{3}{4}\mu_B \partial_z B - mg, \tag{4.10}$$

where the center-of-mass acceleration, a_c, results from the difference between the gravitational force and the magnetic levitation force. The thorough calculation of the phase difference due to the external potentials in the previous Lagrangian $\Delta\phi_{\text{ext}}$ can be found in [175], with a final result of

$$\Delta\phi_{\text{ext}} = 4ka_c \left(T_2^2 - T_1^2\right). \tag{4.11}$$

In our interferometer scheme, the free evolution times T_1 and T_2 are equal, making the contribution of the external potentials U_{gra} and U_{mag} towards $\Delta\Phi$ equal to zero. This is also valid for vanishing a_c, namely when there is a perfect balance between the gravitational acceleration and the magnetic levitation acceleration. It is useful to recall that the value of the magnetic gradient which cancels the gravitational acceleration for a cesium atom is $\partial_z B = 4mg/(3\mu_B) = 31.1$ G/cm.

Additional phase contributions arise from the interaction between the optical standing wave and the cloud of atoms during the splitting, the reflection and the

recombination pulse [149, 176]. Since the phase value of a standing wave is space dependent, a spatial displacement Δz, as shown in Figure 4.4, is proportional to a phase difference, $\Delta\Phi_L$, leading to the simple relation [149]

$$\Delta z = \frac{\Delta\Phi_L}{2k_L} \tag{4.12}$$

During the total interferometer evolution time $\Delta T = T_1 + T_2 + T_{\text{pulse}}$, the center-of-mass of the BEC is displaced by

$$\Delta z = \frac{1}{2} a_c \Delta T^2. \tag{4.13}$$

We can thus write the phase difference due to the optical standing wave as

$$\Delta\Phi_L = 2k_L \frac{1}{2} a_c \Delta T^2. \tag{4.14}$$

The total phase difference is therefore given by

$$\Delta\Phi_{\text{tot}} = \Delta\Phi_{\text{ext}} + \Delta\Phi_L + \Phi_0 = 2k_L \frac{1}{2} a_c \Delta T^2 + \Phi, \tag{4.15}$$

where the phase term Φ_0 has been introduced to account for phase shifts due to the initialization process, noise such as lattice vibrations [164], and for interaction effects [148]. A typical experimental sequence is shown in Figure 4.5. The splitting and recombination pulses are optimised experimentally for durations of $60\,\mu s$, $110\,\mu s$, and $60\,\mu s$, and lattice intensities of $6.6\,E_r$, $0.2\,E_r$, and $6.6\,E_r$. We achieve a splitting efficiency of 96% of the atoms in the $\pm 2k_L\hbar$ modes. The limiting factor is given by the thermal component of our BEC. As mentioned earlier, the reflection pulse has a Gaussian intensity shape and we find that a maximum of $17\,E_r$ and a 1/e duration of $35\,\mu s$ maximise the reflection efficiency for the atoms. Our efficiency of the inversion pulse is 83%, which is much lower than the efficiency of the splitting pulse, and atoms in other momentum modes are clearly visible in Figure 4.5. This lower efficiency may be due to the velocity selectivity of the inversion pulse and due to the velocity difference of the accelerated wave packets.

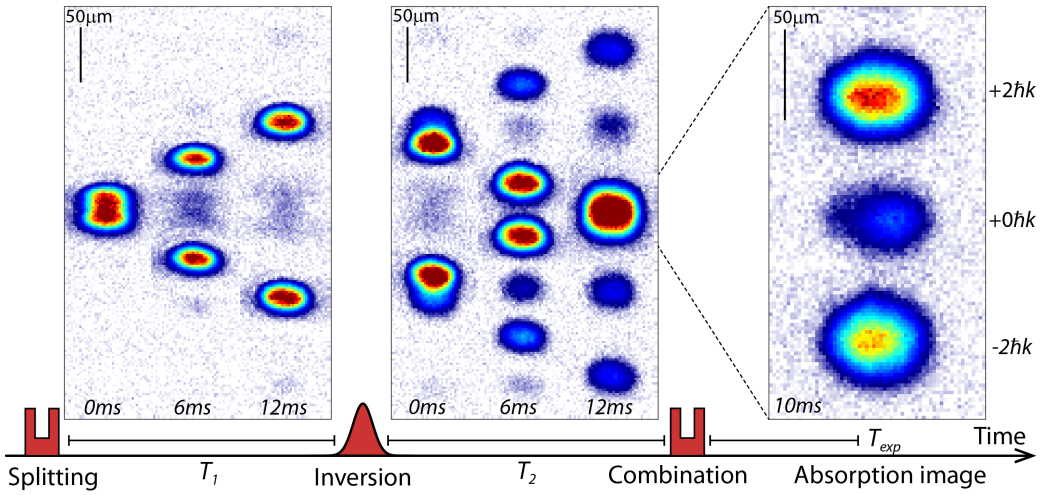

Figure 4.5: Interferometer scheme. Average of three absorption images of the matter waves after the splitting and the inversion pulses (left to right: $T_1 = T_2 =$ 0 ms, 6 ms, 12 ms), and after the recombination pulse and an expansion time of 10 ms. All images are taken after an additional time-of-flight of 1ms. Figure published in [56].

4.5 Interferometric measurement of the acceleration

4.5.1 Milli-g detection

In the previous section, we demonstrated that the total vertical acceleration of the centre-of-mass of our BEC depends on our magnetic field gradient. We are thus able to apply small forces to the atoms by changing the levitation current I_{lev} which is defined as the coil current with a cancellation of magnetic and gravitational accelerations. Experimentally, we determine I_{lev} by minimising position drifts of the BEC during free levitated expansion.

Once the BEC is prepared, we increase the current I in the gradient coils with a linear ramp of duration of 75 ms to the ratios I/I_{lev} of 1.003, 1.001, and 1.0003. We then release the BEC from the optical trap and apply the interferometer sequence described in Section 4.4. The current imbalance results in a small upwards acceleration of the BEC, which is measured with our interferometer scheme. Figures 4.6 a-c show the measurements of P_0 for varying evolution times ΔT. As expected, we observe sinusoidal oscillations of P_0 and we employ equation 4.6

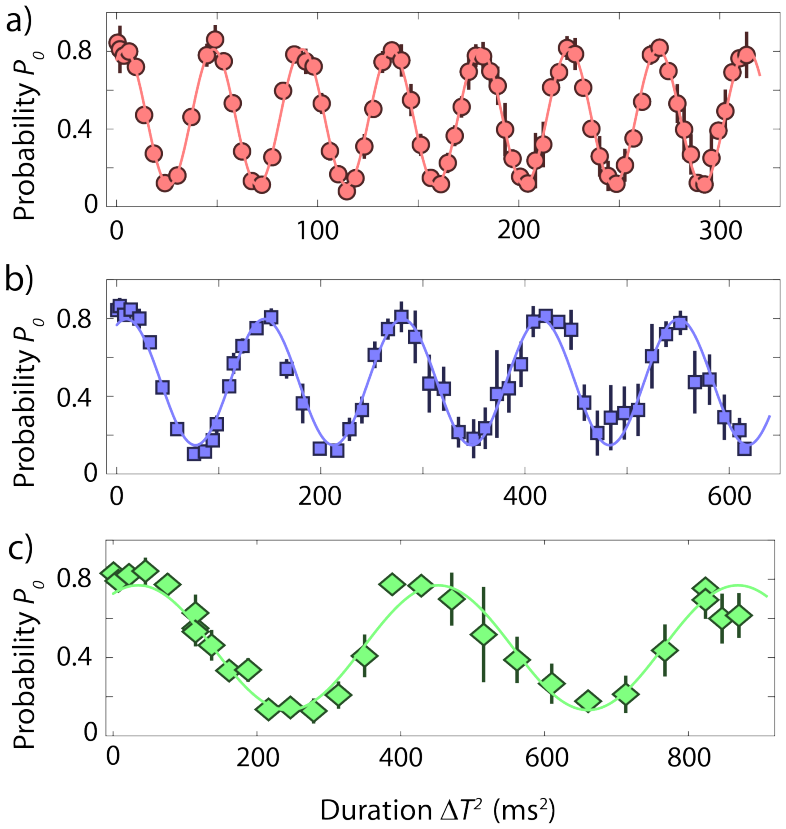

Figure 4.6: Interferometric measurement of milli-g accelerations. a-c) Probability of observing atoms in the $p_0 = 0 \times k_L$ momentum mode for increasing duration ΔT and gradient coil currents I/I_{lev} of a) 0.003, b) 0.001, c) 0.0003. Solid lines represent fits to the data points using equation 4.6. Error bars indicate one standard deviation of the data points. Figure published in [56].

for fitting the data (solid lines) and extracting the values of the acceleration a_c, Figure 4.7.

An independent measurement of a_c, based on the free motion of the BEC, is provided for comparison. We measure the shift of the center-of-mass position for an expansion time T_{exp} of an untrapped BEC in our magnetic-field gradients. The acceleration a_c is given by the free fit parameter (blue diamonds in Figure 4.7). We find excellent agreement within two standard deviations between the two methods. However, the sensitivity of the free-expansion measurement is limited by the observation time. Although our levitation scheme allows for very long observation times, as described extensively in Section 4.8, it also induces a horizontal dispersion of the BEC in free space, which will be discussed in Section 4.7.

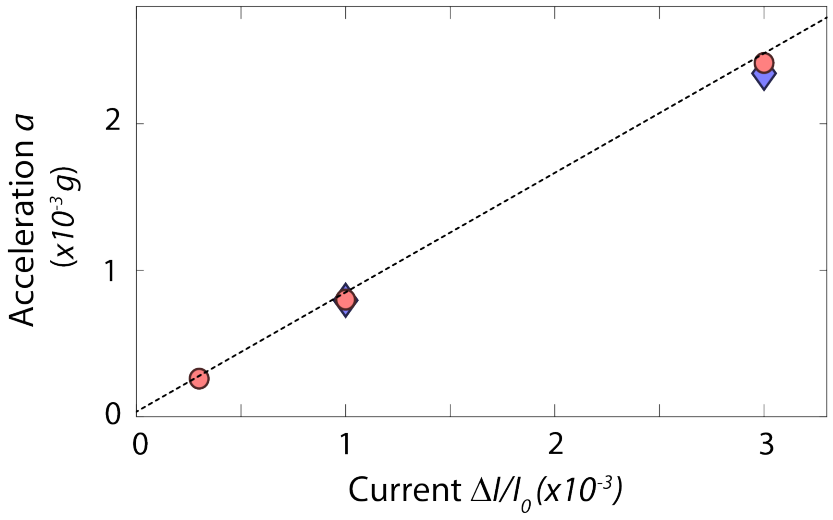

Figure 4.7: Comparison of the acceleration measurement with the interferometer scheme (red circles) and by the center-of-mass motion (blue diamonds). Figure published in [56].

Here, we limit the observation time to 200 ms, which allows us to measure the acceleration for $I/I_{\mathrm{lev}} = 1.001$, 1.003, but not for 1.0003. The measurement results in Figure 4.7 have relative uncertainties of approximately 4% for the free expansion measurement and 0.5% for the interferometric approach.

4.5.2 Micro-g detection

In a second measurement, we utilize the interferometer scheme to minimise the forces on the atoms. We vary the currents in our shim coils and I_{lev} with the goal to maximise the oscillation period of P_0 (red circles Figure 4.8a). For optimal current values, we observe a slow drop of the value of P_0 from approximately 0.75 to 0.45 over $\Delta T^2 \approx 1600\,\mathrm{ms}^2$. This reduction is not necessarily caused by a residual acceleration of the wave packets, as it can also originate from dephasing mechanisms that are discussed in Section 4.6. However, fitting $P_0(t)$ with equation 4.6 provides an upper limit to the acceleration experienced by the atoms. We determine an upper limit for the acceleration of the atoms of $a_{\mathrm{c}} = 70(10)\times10^{-6}\,g$ which is to the best of our knowledge, the smallest absolute value for an acceleration that is measured directly with ultracold-atom interferometry.

4.5.3 Phase-shifting element detection

Compared to fountain experiments, the center-of-mass motion of our wave packets is contained within a small spatial region of a few hundreds of micrometers, and it is straightforward to add additional phase-shifting elements in the path of the wave packets. As a result, it is possible to use the levitated interferometer scheme to analyse additional potentials for the atoms with high precision. We demonstrate this approach by adding a horizontal laser beam (wavelength 1064 nm, waist 40 μm, power 29 μW) approximately 50 μm above the initial position of the atoms (Figure 4.8b). This beam creates a Gaussian dipole potential with a depth of approximately 3 nK, and it introduces a differential phase shift between the upper and lower wave packets which can be detected by the interferometer. In addition to a measurement of the AC Stark shift of the light field as in reference [177], our setup facilitates the study of the spatial dependence of the potential.

The effect of the laser beam on $P_0(t)$ is clearly visible in Figure 4.8a when comparing the data sets with the beam (blue squares) and without the beam (red circles). For increasing pulse duration T_1, the upper wave packet passes twice through the laser beam and it samples increasing spatial sections of the potential. We adjusted the power of the beam to create a single oscillation of the phase for a wave packet that fully transverses the beam, resulting in a minimum of $P_0(t)$ at an evolution time $T_1 = 7$ ms in Figure 4.8a.

Constant propagation velocities of the wave packets during the evolution times T_1 and T_2 make it easy to relate the time to the position of the atoms. We use a numerical model to integrate the phase shift of the upper wave packet in the dipole potential of the laser beam over the interferometer path $z(t)$ and include the unperturbed phase shift as measured in Section 4.5.2. Fitting the model parameters to our data set (blue line Figure 4.8a), we determine a beam position of 45(1) μm, a waist of 37(4) μm and a beam power of 25(3) μW, which are in excellent agreement with the independently measured values.

Our model neglects the spatial extent of the wave packets and we determine the phase shift at the center-of-mass position, whereas our experimental sequence

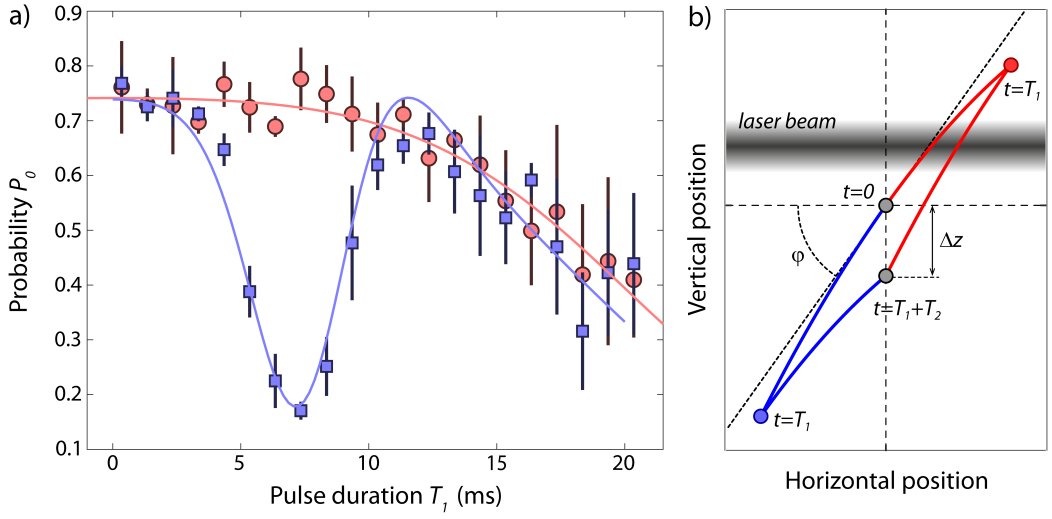

Figure 4.8: Interferometric measurement of micro-g accelerations and phase shifts due to a laser beam. a) Probability of observing atoms in the $0\hbar k_L$ momentum mode vs T_1 for minimized acceleration of the atoms (red circles) and for an addition laser beam in the path of the upper wave packet (blue squares). Error bars indicate one standard deviation of the data points. b) Illustration of the position of the wave packets and the additional laser beam during the pulse sequence. Angles and axes are not to scale in the illustration. Figure published in [56].

averages over local phase shifts within the upper matter wave packet. Local phase shifts result in density variations in the profiles of the momentum modes in our absorption images, but measuring the total atom number in the momentum modes provides only the average phase shift of the wave packet.

4.6 Estimation of systematic effects

We estimate possible sources of measurement errors, fluctuations and dephasing mechanisms. Fluctuations of a homogeneous magnetic field will only slightly change the interaction strength of our BEC, but deviations of the magnetic-field gradient can induce additional accelerations and alter the measurement result. In our setup, small deviations of the magnetic field gradient can occur as the wave packets move during an interferometer sequence away from the original position with optimized levitation. We estimate from our numerical magnetic field simulation that our coil design causes a relative increase of the field gradient

of 2×10^{-6} for a vertical position shift of $50\,\mu$m. In addition, the quadratic Zeeman effect induces another deviation of the levitation force of 6×10^{-6} for the same position shift. As a result, the upper and lower wave packets experience a position-dependent acceleration, which increases the separation of the wave packets before the inversion pulse, and which reduces the convergence after the inversion pulse. Similar to our measurements in Section 4.7, we would expect the final displacement of the wave packets to cause horizontal fringes in the absorption images, which we do not observe. As a result, we conclude that the vertical force gradients are negligible for the time scales of our interferometer.

In addition, the position-dependent magnetic field strength causes an almost linear change of the scattering length of approximately $\pm 10\,a_0$ over $50\,\mu$m. As a result, the atoms in the upper wave packet experience a stronger interaction and faster phase evolution than the atoms in the lower wave packet. Assuming constant densities and a linear change of the scattering length, we would expect the phase shift between the wave packets to increase with ΔT^2, and it would be difficult to distinguish this effect from a phase evolution due to acceleration. However, in our setup the wave packets expand after release and the densities decrease strongly over a timescale of $1/\omega_{x,y,z} \approx 10\,$ms. The position-dependent scattering length would result in a change of the oscillation frequencies within 10-15 ms in Figure 4.6a-c, which we do not observe, and we conclude that the phase shift due to a position-dependent scattering length is below our sensitivity for this measurement.

Fluctuations of the acceleration of the BEC can be caused by time-dependent changes of B_0 and $\partial_z B$, either due to external magnetic fields or due to the finite stability of the currents in our coils. We determine a current reproducibility of 1.4×10^{-6} by measuring the standard deviation of the current during the interferometer sequence over 60 consecutive cycles. For each cycle, the current measurement averages over 80 ms. We believe that the current reproducibility will eventually set the limiting precision for our interferometric measurements with levitated atoms. While it is in principle possible to increase the current reproducibility by 1-2 orders of magnitude by improving our current regulation

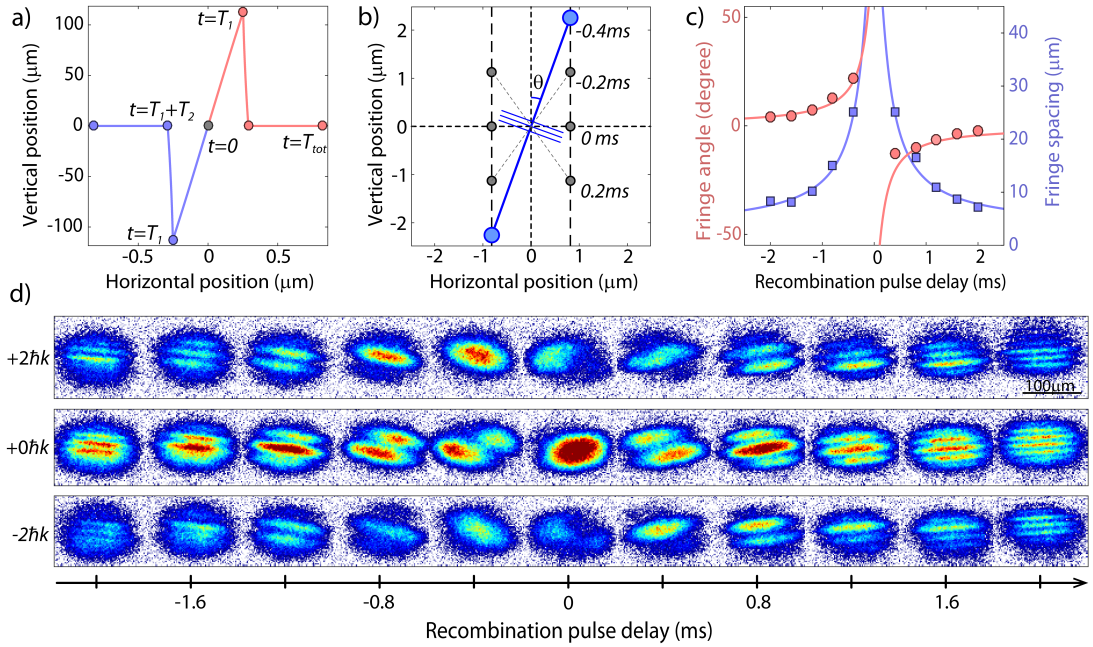

Figure 4.9: Effect of the force field curvature on the interference pattern. a) Calculated interferometer path of the center-of-mass positions of the levitated wave packets with $\delta t = 0\,\mathrm{ms}$. b) Center-of-mass positions of the two wave packets for δt = -0.4 ms (blue), -0.2 ms, 0 ms, +0.2 ms (grey). Blue parallel lines indicate the orientation of the interference pattern. c) Fringe angles (red circles) and fringe spacings (blue squares) vs. the delay δt of the recombination pulse, inferred from the data in (d). Solid lines show our fit results for eq. 4.20. d) Absorption images for varying δt between -2.0 ms and 2.0 ms in steps of 0.4 ms. Common parameters are $\alpha = 2\pi \times 3.29\,\mathrm{Hz}$, $\varphi = 0.108°$, $T_1 = 20\,\mathrm{ms}$, T_{exp}=30 ms. Figure published in [56].

electronics, it would be very hard to reach the precision of atomic fountain experiments, which are of the order of $\Delta g/g \sim 10^{-9}$ [119]. Nonetheless, we believe that magnetic levitation schemes will provide a valuable technological addition for precision measurements with ultracold atoms. Reducing gravitational acceleration to micro-g effectively removes the center-of-mass motion of the atoms, and it allows for a direct measurement of phase-shifts due to additional elements in the interferometer path, as demonstrated in the previous section.

4.7 Effects of spatial curvature of the force field

Our magnetic field configuration does not only provide a vertical magnetic field gradient to levitate the atoms, but it also generates a weak, horizontal anti-trapping potential. This potential is a result of the spatial curvature of our quadrupole-like distribution of the magnetic field. In this section, we demonstrate that the anti-trapping potential causes an additional interference pattern which can be employed to measure the anti-trapping frequency or the angle between the lattice beam and the vertical field axis.

It is useful to recall some results on the levitating magnetic field given in Chapter 3. In the quadrupole approximation, the horizontal magnetic field and magnetic force experienced by the atom are given by [41, 178, 179]

$$B_{\mathrm{horz}}(r) = B_0 + \frac{2}{9}\frac{m^2}{\mu_B}\frac{g^2}{B_0}r^2, \tag{4.16}$$

$$F_{\mathrm{horz}}(r) = m\alpha^2 r, \tag{4.17}$$

where $r = \sqrt{x^2 + y^2}$ is the horizontal displacement of the atoms from the origin and $\alpha = g\sqrt{m/(3\mu_B B_0)}$. The quadratic scaling of $B_{\mathrm{horz}}(r)$ with r results in a weak, outwards-directed force in the horizontal plane. This anti-trapping effect can be associated with frequency α, and it causes a weak, position-dependent acceleration with a time-dependent horizontal position $r(t)$ and horizontal velocity $v_r(t)$ [75]:

$$\begin{aligned} r(t) &= r(0)\cosh(\alpha t) + \alpha^{-1} v_r(0)\sinh(\alpha t) \\ v_r(t) &= v_r(0)\cosh(\alpha t) + \alpha r_0 \sinh(\alpha t) \\ z(t) &= v_z(0)t + z(0). \end{aligned} \tag{4.18}$$

For this calculation we assume perfect levitation and linear vertical motion $z(t)$ during the interferometer sequence.

In an experimental setup there will always be a small angle φ between the

lattice beam L1 and the vertical axis of the magnetic field, and a splitting pulse will always imprint a small velocity component $v_r(0) = (\hbar k_L/m)\sin(\varphi)$ along the horizontal direction. Consequently, a small horizontal displacement due to $v_r(0)$ results in an outwards-directed force on the wave packets in the anti-trapping potential, and in a finite horizontal displacement at the end of the interferometer sequence as illustrated in Figure 4.9a. The horizontal distance between the wave packets is typically two orders of magnitude smaller than the vertical displacement during the interferometer sequence, and both distances become comparable only in the proximity of the recombination pulse and during the expansion time. We illustrate the positions of the wave packets in Figure 4.9b for small delay times of the recombination pulse $\delta t = T_2 - T_1$ with $T_1 = 20\,\mathrm{ms}$. Depending on δt, the orientation of the blue line connecting the wave packets changes from almost vertical for $\delta t = \pm 0.4\,\mathrm{ms}$ to horizontal for $\delta t = 0\,\mathrm{ms}$. We define an angle θ, which is chosen to be positive clockwise and in the interval $[-90°, 90°]$, to indicate the orientation of the line, and we define $d(\delta t)$ to be the distance between the two wave packets.

In analogy to Young's double slit experiment [17,162], the interference pattern of two wave packets at distance $d(\delta t)$ shows a fringe spacing d_F of

$$d_\mathrm{F} = \pi\hbar t/(md) + d_0. \tag{4.19}$$

Here, t is the total duration of the interferometer sequence with $t = T_1 + T_2 + T_\mathrm{pulse} - \delta t + T_\mathrm{exp}$, and $d_0 \geq 0$ is a constant phase shift that depends on the initial conditions such as the density distribution [180–182]. In our absorption images of the interfering wave packets for constant times T_1, T_exp and varying delay δt (Figure 4.9d), interference fringes with varying separation d_F and angle θ are clearly visible for all momentum modes $p_0, p_\pm$.

From the evolution of the fringes as a function of time delay δt, we infer properties of the curvature α and the angle φ. We simultaneously fit the fringe spacing in equation 4.19 and the fringe angle θ with $\theta(\delta t) = \arctan(z(\delta t)/r(\delta t))$. Here $z(\delta t)$ and $r(\delta t)$ are the vertical and horizontal positions of the wave pack-

ets for varying δt. We integrate the center-of-mass motion of the wave packets in equation 4.18 with starting conditions $r(0) = z(0) = 0$ over all steps of the interferometer sequence to determine $z(\delta t)$ and $r(\delta t)$

$$\begin{aligned} z(\delta t) =& - v_z(0)\delta t \\ r(\delta t) =& \frac{v_r(0)}{\alpha}\cosh(\alpha T_{\text{exp}})\Big[\sinh(\alpha T_1)\cosh(\alpha(T_1+\delta t)) + \\ & \qquad (\cosh(\alpha T_1)-1)\sinh(\alpha(T_1+\delta t))\Big] + \\ & \frac{v_r(0)}{\alpha}\sinh(\alpha T_{\text{exp}})\Bigg(\Big[\sinh(\alpha T_1)\sinh(\alpha(T_1+\delta t)) + \\ & \qquad (\cosh(\alpha T_1)-1)\cosh(\alpha(T_1+\delta t))\Big] + 1\Bigg). \end{aligned} \tag{4.20}$$

Equations 4.20 contain two free parameters, the anti-trapping frequency α and the lattice angle φ, which can both be used to fit our data points in Figure 4.9c. We choose to constrain α and vary φ during the fitting procedure, as it is experimentally difficult to determine the laser beam angle with milliradian precision, and we independently measured α by observing center-of-mass oscillations of BECs in optical dipole traps. The fit results, represented by solid lines in Figure 4.9c, show good agreement with our data points, and we measure a lattice angle of $\varphi = 0.108(7)^\circ$ for $\alpha = 2\pi \times 3.29(5)\,\text{Hz}$.

Note that α scales with $1/\sqrt{B_0}$ in equation 4.16, and we can use larger values for B_0 to reduce the anti-trapping effect, e.g. by tuning the interaction strength with a broad magnetic Feshbach resonance at 800 G [35]. However, it will be difficult to reduce α significantly due to its square-root dependence on B_0. Instead, it is easier to compensate the anti-trapping effect with an additional dipole trap, as demonstrated in the next section.

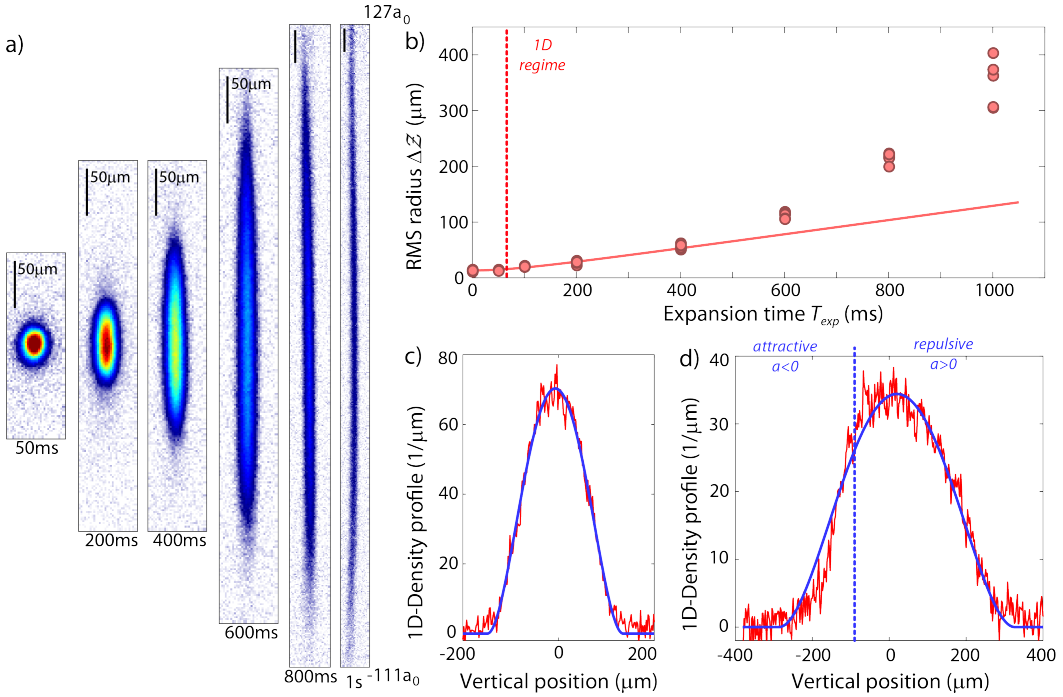

Figure 4.10: Long expansion times. a) Average of 6-8 absorption images for each expansion time: $T_{\mathrm{exp}} = 50, 200, 400, 600, 800, 1000\,\mathrm{ms}$. Note that the scaling of the images changes as indicated by the $50\,\mu$m scale bar in each picture. b) RMS-widths of the integrated 1D-density distribution vs. expansion time. c,d) 1D-density profiles and fits (blue lines) for expansion times of c) 400 ms and d) 600 ms. Figure published in [56].

4.8 Long expansion times: exploiting micro-g acceleration

In this section, we demonstrate that magnetic levitation allows us to extend the expansion time of a BEC to 1 s. Typical expansion times for falling BECs are on the order of tens of milliseconds, often limited by the detection area of the imaging system, by the gravitational acceleration and by the expansion velocity of the gas. Usually, the expansion velocity of a quantum gas is not caused by the temperature of the gas but by repulsive interaction during the initial spreading. The current record for long observation times under milli-g acceleration is 1 s [161] with an expansion energy of 9 nK. The experiment was performed in a drop tower, and ballistic expansion was observed over approximately 500 ms, limited by stray magnetic fields.

In our experiment, we can reduce the interaction energy of the BEC by tuning the scattering length close to $0\,a_0$ by means of a magnetic Feshbach resonance (Figure 2.5). Further reduction of the expansion energy has been demonstrated by rapidly changing the scattering length from a positive value to $0\,a_0$ during trap release [178], but we refrain from using this trick to avoid excitations of the BEC during release. Our horizontal magnetic field curvature (Section 4.7) introduces another limitation. During long observation times, the BEC expands horizontally into regions with a lower magnetic field gradient, causing a position-dependent sag of the density profile. In addition, small fluctuations of the horizontal magnetic field can break the symmetry and introduce slow horizontal drifts. We suppress both effects by keeping a vertical laser beam (H3 in Figure 4.2a) on during the expansion time, thus observing free expansion only in the vertical direction.

In detail, we reduce the trap frequency by slowly transferring the atoms from a crossed dipole trap of beams S1 and S2 to a crossed dipole trap of beams H1, H2, and H3 with final trap frequencies of $\omega_{x,y,z} = 2\pi \times (3.2, 3.4, 2.1)\,\mathrm{Hz}$, a scattering length of $15\,a_0$ and atom numbers of approximately 1.1×10^4. Excitations of the BEC during the transfer are suppressed by smooth changes of the potential with a total transfer duration of 4 s. After an additional settling time of 1 s we switch off the horizontal beams H1 and H2 and study the expansion of the BEC in the vertical beam H3. The vertical trapping frequency of the laser beam H3 is approximately 25 mHz, and the resulting fractional reduction of the expansion width after 1 s is 6×10^{-4}, which is far below our measurement sensitivity for the width of the BEC.

The expansion of the BEC in the vertical direction is clearly visible on absorption images (Figure 4.10a) for expansion times 0 to 1000 ms, and horizontally-integrated 1D density profiles for expansion times of 400 ms and 600 ms are given in Figure 4.10c and d. Although the trapped BEC is initially only weakly confined with almost symmetric trap frequencies, it changes dimensionality during the expansion process in the vertical beam. The density of the BEC decreases strongly during the vertical expansion, and the chemical potential becomes smaller than the transversal harmonic oscillator energy $\hbar\omega_{x,y}$ as required for a quasi-1D de-

scription [186]. As a result, we do not expect a shape-preserving spreading of the density distribution for a 1D expansion because the BEC passes through various interaction regimes as its density decreases [183, 184]. For illustration, we show a fit to the upper 80% of the 1D-density profiles $n(z)$ for the "3D cigar"-regime [185] (Figure 4.10c), but we refrain from a complete analysis of the density profiles, which is beyond the scope of this thesis. Instead, we quantify the width of the expanding BEC with the root-mean-square (RMS) radius $\Delta\mathcal{Z} = \left(\frac{1}{N}\int n(z)(z-\bar{z})^2\right)^{1/2}$ to provide an estimate of the expansion velocity (red circles Figure 4.10b). Here, $\bar{z}$ is the center-of-mass position of the atoms. We observe an initial interaction driven expansion and a ballistic flight for $T_{\mathrm{exp}} \leq 400\,\mathrm{ms}$ with an RMS expansion velocity of $v_{\mathrm{rms}} = 0.128(5)\,\mathrm{mm/s}$ and a corresponding kinetic energy of $mv_{\mathrm{rms}}^2/2 = \frac{1}{2}\,k_B \times 260(20)\,\mathrm{pK}$. We note that this is the expansion energy of the BEC component, but not the initial temperature of the trapped quantum gas.

Similar to reference [161], we find an accelerated expansion for longer expansion times, $T_{\mathrm{exp}} > 500\,\mathrm{ms}$. We expect that the dominant source of the accelerated expansion is the curvature of our levitation gradient due to the quadratic Zeeman effect and due to our coil design, as discussed in Section 4.5.2. However, the density profiles of the atoms on the absorption images indicate two other contributions. We observe small radial bending of the expanding cloud for long expansion times after release from the trap in the guiding beam H3 (see image $T_{\mathrm{exp}} = 1\,\mathrm{s}$ in Figure 4.10a). This bending effect can be caused by a non perfect alignment of guiding beam H3 along the vertical gradient direction and can distort the radially integrated density distribution. In addition, we observe asymmetric 1D density profiles $n(z)$ for $T_{\mathrm{exp}} > 500\,\mathrm{ms}$ (Figure 4.10d). The profiles show a slower expansion velocity for the lower part of the cloud than for the upper part. We assume that this effect is caused by the position-dependent scattering length due to our magnetic field gradient. The zero crossing of a is indicated in Figure 4.10d by a dashed blue line. We find small position fluctuations for long expansion times $T_{\mathrm{exp}} > 400\,\mathrm{ms}$ of the BEC due to the finite current stability for the magnetic field gradient (Section 4.5.2). For illustration, we re-centered the center-of-mass

position in the absorption images for the averaging process in Figure 4.10a, but all other data in Figure 4.10b-c results from the analysis of individual absorption images.

4.9 Conclusions

In conclusion, we employed an atom interferometer with BECs with tuneable interaction and magnetic levitation to demonstrate absolute acceleration measurements in the micro-g regime and we used the negligible center-of-mass motion of levitated atoms to study the position-dependent phase-shift of the dipole potential of a focused laser beam. Moreover, we demonstrated expansion times of 1 s for a BEC, which is comparable to current drop-tower experiments, and we used an extrapolation method for the fringe patterns to study the curvature of a force field that acts perpendicular to our interferometer setup. In our setup, limitations were provided by magnetic-field fluctuations due to the current regulation, and by position-dependent interactions and magnetic-field gradients. Although the sensitivity of our interferometer setup with levitated atoms is significantly lower than the sensitivity of atomic fountain experiments, we believe that levitation schemes provide interesting features with the prospect of technical applications. Cancelling gravitational acceleration offers the possibility to combine long observation times with compact interferometer setups. Interesting applications for our setup are the measurement of local variations of electric and magnetic fields, and of mean-field effects due to atomic interactions.

Chapter 5

Excitation modes of bright matter-wave solitons

This chapter is an extension of the article A. Di Carli, C. D. Colquhoun, G. Henderson, S. Flannigan, G.-L. Oppo, A. J. Daley, S. Kuhr, E. Haller, "Excitation modes of bright matter-wave solitons", Phys. Rev. Lett. **123**, 123602 (2019). The article can be found in Appendix D and is cited as Ref. [57].

5.1 Introduction

Bright solitons are one-dimensional (1D) non-linear waves that preserve their shape during the propagation in a homogeneous potential and, except for a change in the relative phase shift, during their mutual collisions [187]. They appear in various fields such as non-linear optics [188, 189], where they found also application in broadband long-distance communications [189], particle physics [190], fluid dynamics [191, 192], geophysics [193, 194] and biophysics [195, 196].

Bose-Einstein condensates with attractive interactions can also display solitary dispersion properties which arise from the interplay between the zero-point kinetic energy, which tends to disperse the matter-wave, and the attractive mean field interaction, which tends to increase the BEC's density [197]. Attractive BECs are not always stable against collapse, as demonstrated in [71, 73, 198–201], and stable ground states are only allowed for a restricted set of parameters. The

stability condition for harmonically trapped BECs is set by the dimensionless parameter [96, 97]:

$$k_c = \frac{N|a|}{a_{ho}}. \tag{5.1}$$

Typical values of k_c are of the order of unity and depend on the trapping geometry. Such values have been the subject of numerous theoretical, both numerical [202–205] and variational [206–208], studies, which employed the full Gross-Pitaevskii equation (3D-GPE), equation 2.31. Experimental investigation of k_c was performed in [72].

Strictly speaking, solitons propagate in a one-dimensional (1D) geometry. Due to the intrinsic three-dimensional nature of our world it is not possible to realise a pure one-dimensional system working with attractive BECs. However, it is possible to circumvent this limitation by introducing the concept of a quasi-one-dimensional system [209]. The general idea for creating low-dimensional systems with quantum gases consists of "freezing" the degrees of freedom by making them energetically inaccessible. In this way the system is kept in the ground state along the restricted directions while it can evolve freely along the others. In the case of harmonically trapped quantum gases, quasi-one-dimensional regimes can been accomplished by confining it in a cylindrically, symmetric trapping potential such that the energy associated with the transversal confinement $\hbar\omega_r$ is larger than all the other characteristic energies of the system namely the chemical potential μ and the longitudinal trapping energy $\hbar\omega_z$ or, equivalently, such that the transversal harmonic oscillator length a_r is smaller than the healing length ξ of the condensate and the transversal harmonic oscillator length a_z [186, 210]. In this limit, the BEC is well described by the one-dimensional Gross-Pitaevskii equation (1D-GPE), equation 5.7, or by an effective one-dimensional equation which accounts for small 3D effects, the so called non-polynomial Schrödinger equation (NPSE), equation 5.6.

As stated in the definition, bright solitons are also properly defined when the potential along the propagation direction is homogeneous so that the 1D-GPE reduces to the non-linear Schrödinger equation (NSE), equation 5.8. BECs are usually generated in harmonic trapping potentials although box potentials have

been recently achieved [211]. The presence of a harmonic potential breaks the integrability of the system preventing the realisation of a real soliton. Nevertheless, stable ground states forming in a harmonic potential still posses soliton-like behaviour under propagation and collisions [205, 212, 213]. Such non-linear waves are sometimes named bright solitary waves (BSW) [205, 212, 213], and this definition is also extended to stable attractive BECs in which 3D effects are not negligible [205, 214, 215]. Here, we do not make this distinction and we will use the term bright matter-wave soliton in a broad sense.

Experimentally, bright matter-wave solitons have been created in cigar shaped potentials by quenching the particle interaction in a BEC from repulsive to attractive, in the case of confining [30, 216] and expulsive [31, 217, 218] harmonic potentials. Moreover, several dynamical properties of bright matter-wave solitons, such as, formation of soliton trains by modulational instabilities [219, 220], mutual collisions [221], reflection from a barrier [222], excitations following the collapse of attractive BECs [216], quadrupole oscillations of attractive BECs in three dimensions (3D) [223], have been investigated. Moreover, BEC solitons have been proposed, and later successfully employed, for enhancing the performance of atom interferometers [224–226]. Although the aforementioned experiments have improved considerably the understanding of solitons in BECs, the experimental investigation of the excitation modes of a single bright matter-wave soliton is still missing.

In this chapter, I will describe an experiment in which we study the fundamental breathing mode of a single soliton by measuring its oscillation frequency and the time evolution of its density profile. In our experiment bright matter-wave solitons are created by quenching the interactions of our BEC from repulsive to attractive in combination with a rapid reduction of the longitudinal confinement. By mismatching the quench parameters, we excite the breathing modes of the emerging soliton, allowing us to study its breathing frequency as a function of atom number and harmonic confinement. We compare the experimental results with numerical simulations of the 1D-GPE and of the NPSE, as well as, with analytical expressions derived from a variational model. In addition, we observe

signatures of higher-order matter-wave solitons. Higher-order solitons are exact solutions of the NSE and can be interpreted as stable excitations with a periodic and coherent evolution of the density profile and phase, or as a bound state of overlapping modes [208, 232]. We generate higher-order solitons by matching the initial size of the BEC before an interaction quench to values close to those required for second- and third-order solitons.

The chapter is structured as follows: in Section 5.2 we introduce the equations that describe BEC in the quasi-1D limit and that are used for numerical simulations whereas in Section 5.3 we illustrate the variational model, which is employed to derive an analytical expression of the breathing oscillation frequencies. Section 5.4 provides an overview of the experimental apparatus and Section 5.5 describes how we generate bright matter-wave solitons experimentally. In Section 5.6 we present measurements of the solitons's breathing oscillation frequencies as a function of the atom number and of the longitudinal trapping confinement. Finally, in Section 5.7, we report about observation of higher-order matter-wave solitons.

5.2 From 3D-GPE to 1D-GPE

As mentioned in the introduction, matter-wave bright solitons are typically generated in a cylindrically shaped trapping potential in which the transversal trapping frequency ω_r is greater than the longitudinal trapping frequency ω_z. By substituting the definition of the order parameter, $\Psi(\mathbf{r},\mathbf{t}) = \sqrt{N}\varphi(\mathbf{r},t)$, in equation 2.31 and considering the cylindrical symmetry of the system, the 3D-GPE can be rewritten in the following form:

$$i\hbar\frac{\partial}{\partial t}\varphi(\mathbf{r},t) = \left[-\frac{\hbar^2}{2m}\nabla^2 + \frac{1}{2}m(\omega_r^2 r^2 + \omega_z^2 z^2) + gN\left|\varphi(\mathbf{r},t)\right|^2\right]\varphi(\mathbf{r},t), \tag{5.2}$$

where $r^2 = x^2 + y^2$. Several approaches can be followed for reducing the dimensionality of the 3D-GPE [96, 97, 227]. Here, we sketch the method used by Salasnich et al [228] who derived an effective one-dimensional equation that also

takes into account three-dimensional effects. The 3D-GPE can be obtained by imposing the stationary condition on the action $\delta S = 0$ with S defined by [228]:

$$S = \int dt d\mathbf{r}\, \varphi^*(\mathbf{r},t) \left[i\hbar\frac{\partial}{\partial t} + \frac{\hbar^2}{2m}\nabla^2 - V_{ext}(\mathbf{r}) - \frac{gN}{2}\left|\varphi(\mathbf{r},t)\right|^2 \right] \varphi(\mathbf{r},t). \tag{5.3}$$

When the chemical potential of the condensate μ is comparable with the energy of the transversal harmonic oscillator $\hbar\omega_r$ it is reasonable to assume the following ansatz [228]

$$\varphi(\mathbf{r},t) = f(z,t) \times \frac{1}{\sqrt{\pi}\sigma(z,t)} \exp\left[-\frac{(x^2+y^2)}{2\sigma(z,t)^2} \right], \tag{5.4}$$

where $f(z,t)$ represents a slowly varying wave function along the longitudinal axis and $\sigma(z,t)$ represents a Gaussian width with an axial degree of freedom that takes interaction effects into account. By substituting the above ansatz in the definition of the action and deriving the Euler-Lagrange equation for $f(z,t)$ and $\sigma(z,t)$ we obtain the following equation for σ [228]:

$$\sigma^2 = a_r^2\sqrt{1+2aN\left|f\right|^2}, \tag{5.5}$$

where $a_r = \sqrt{\hbar/m\omega_r}$ represents the transversal harmonic oscillator length. The time evolution for f follows [228]:

$$\begin{aligned} i\hbar\frac{\partial}{\partial t}f = \Bigg[&-\frac{\hbar^2}{2m}\frac{\partial^2}{\partial z^2} + V_{ext}(z) + \frac{gN}{2\pi a_r^2}\frac{\left|f\right|^2}{\sqrt{1+2aN\left|f\right|^2}} \\ &+ \frac{\hbar\omega_r}{2}\left(\frac{1}{\sqrt{1+2aN\left|f\right|^2}} + \sqrt{1+2aN\left|f\right|^2} \right) \Bigg] f. \end{aligned} \tag{5.6}$$

The last equation is called the non-polynomial Schrödinger equation (1D-NPSE). It has been employed successfully, e.g., for the description of the dynamics of a bright soliton in an expulsive potential [229], the tunneling and nonlinear self-trapping in a Josephson junction [21] and the formation of trains of solitons [220]. In the limit of weak interactions, $Na|f|^2 \ll 1$, the 1D-NPSE reduces to the well

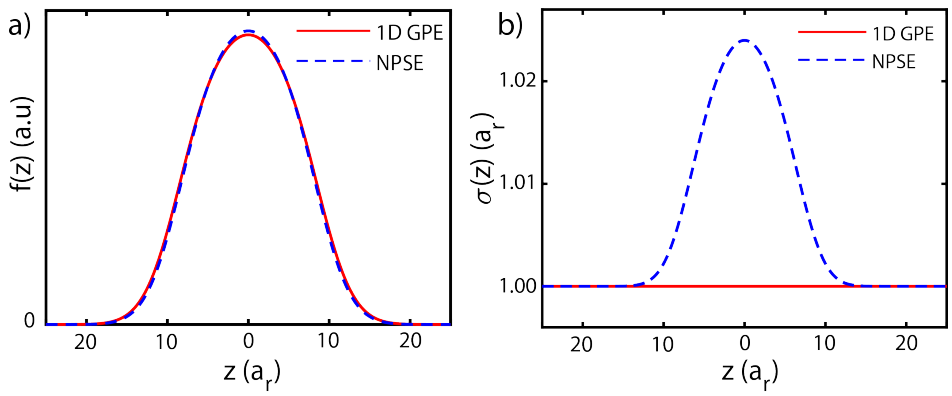

Figure 5.1: a) Comparison between the numerically computed ground state wave function for 1D GPE (red line) and the NPSE (blue dashed line) for a harmonic, longitudinal trapping potential. b) Gaussian ground state in the transversal direction. Parameters used: $\omega_z = 2\pi \times 5\,\mathrm{Hz}$, $\omega_r = 2\pi \times 95\,\mathrm{Hz}$, $N = 1500$, $a = 6\,a_0$.

known 1D Gross-Pitaevskii equation [96]

$$i\hbar\frac{\partial}{\partial t}f = \left[-\frac{\hbar^2}{2m}\frac{\partial^2}{\partial z^2} + V_{ext}(z) + \frac{gN}{2\pi a_r^2}|f|^2\right] f. \tag{5.7}$$

The 1D-GPE describes an effective one-dimensional BEC with a constant radial component, e.g. $\sigma = a_r$. In Figure 5.1a the comparison is shown between the ground state wave function computed employing the 1D GPE (red line) and the NPSE (blue dashed line) for a longitudinal harmonic potential and for parameters which are similar to those used in the experiment. The wave function computed with the NPSE shows a slightly higher peak[1] compared to the 1D-GPE wave function. This is due to the fact that the NPSE allows the interactions to partially expand the BEC along the radial direction, Figure5.1b, keeping the overall wave function more compact. The code for solving the ground state wave functions employs the Split-Step Fourier Method in imaginary time propagation and has been taken and adapted from [230].

In the case of absence of the external longitudinal potential $V_{ext}(z) = 0$, the 1D-GPE reduces to the so called non-linear Schrödinger equation (NLSE) [96,97]:

$$i\hbar\frac{\partial}{\partial t}f = \left[-\frac{\hbar^2}{2m}\frac{\partial^2}{\partial z^2} + \frac{gN}{2\pi a_r^2}|f|^2\right] f, \tag{5.8}$$

[1]The relative difference between the two peak densities is about 0.02.

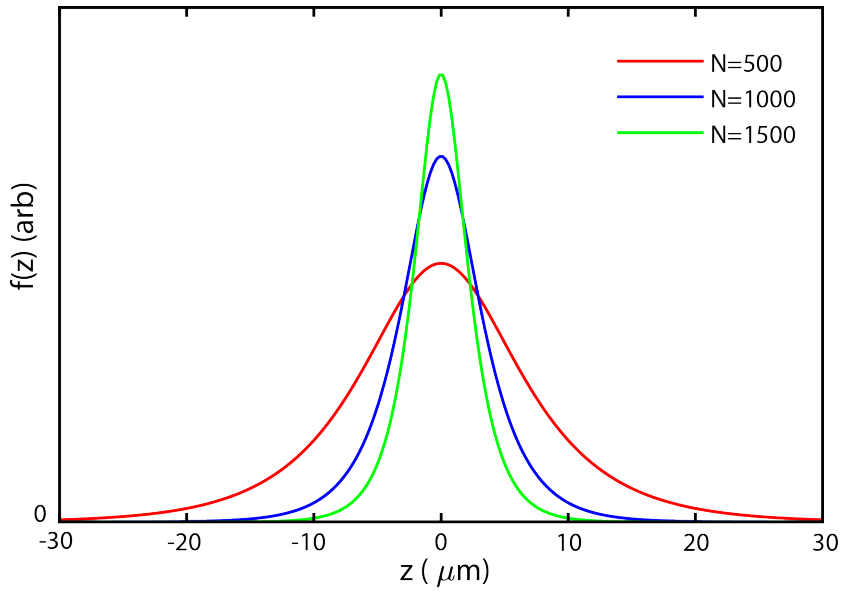

Figure 5.2: Soliton profiles for different atom number, calculated using equation 5.9. Parameters used: $\omega_r = 95\,\mathrm{Hz}$, $a = -5\,a_0$.

which is a well known equation in the context of non linear optics [189]. In the case of a BEC with attractive interactions $a < 0$ the NLSE possesses an analytic solution, derived for the first time by Zakharov and Shabat in [231], which describes a shape preserving object, called a soliton, that has, in the static situation, the following form [96, 97]:

$$f(z) = \frac{1}{\sqrt{2\xi}} \mathrm{sech}\left(\frac{z}{\xi}\right), \tag{5.9}$$

where $\xi = a_\perp^2 / (|a|N)$ represents the characteristic spatial extension of the soliton and corresponds to the healing length at its peak density. Typical soliton profiles are shown in Figure 5.2 for various atom numbers. For increasing atom number and thus mean field attractive interaction the soliton width decreases. It is worth noticing that both the 1D-GPE (equation 5.7) and the NLSE (equation 5.8) do not support BEC collapse due to the fact that in 1D the dispersive term is always able to counterbalance the effect of the attractive mean field.

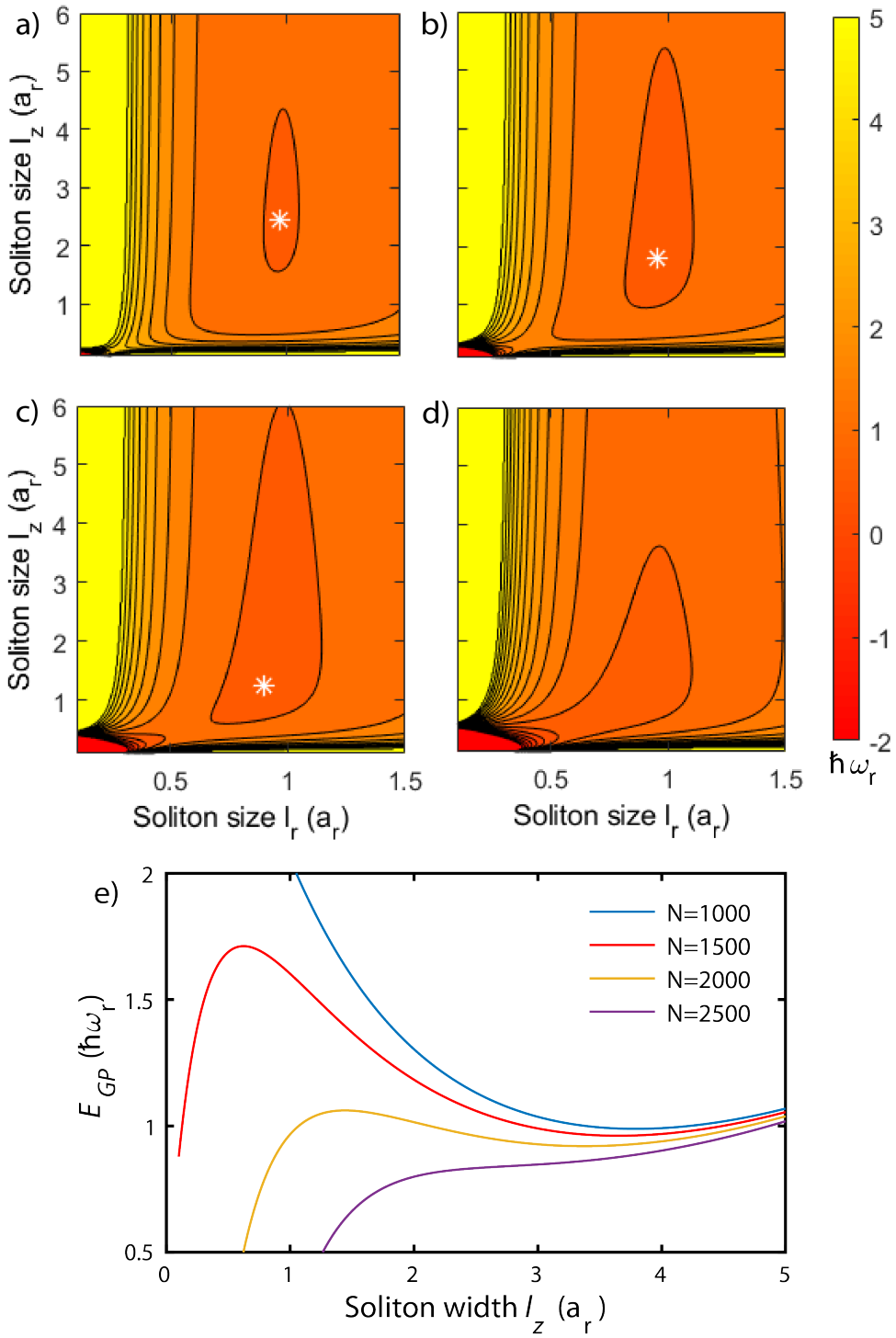

Figure 5.3: a)-d) Energy surfaces defined by equation 5.12, in units of $\hbar\omega_r$, respectively for $N = 1000$, $N = 1500$, $N = 2000$, $N = 2500$ atoms. The white asterisk indicates the local minimum of the energy surface. e) Scaled energy per particle, E_{GP}, along the path of lowest energy as a function of the longitudinal soliton width l_z. Common parameters are $\omega_r = 95\,\mathrm{Hz}$, $a = -5\,a_0$.

5.3 Variational model

The equations 5.6 and 5.7 given in the previous section provide the correct framework for a numerical simulation of our experimental conditions. However, numerical simulations alone do not provide an intuitive and qualitative understanding of the model we want to study. Variational methods provide an intuitive and accurate model for exploring static and dynamic properties of bright solitary matter-waves [205–208]. In this section the variational model of references [205, 208] will be presented and will be used to provide a simple expression for the breathing frequencies of bright matter-wave soliton in the limit of weak interactions.

For a cylindrical cigar-shaped potential the energy functional of equation 5.2 is given by [205, 208]:

$$E[\psi] = \int d^3\mathbf{r} \left[\frac{\hbar^2}{2m} |\nabla\psi(\mathbf{r})|^2 + \frac{1}{2} m(\omega_r^2 r^2 + \omega_z^2 z^2) |\psi(\mathbf{r})|^2 + \frac{gN}{2} |\psi(\mathbf{r})|^4 \right]. \quad (5.10)$$

The ansatz for a solitonic solution in a 3D cigar-shaped trap is [205, 208]:

$$\psi(r,z) = \frac{1}{\sqrt{2l_z}} \mathrm{sech}\left(\frac{z}{l_z}\right) \times \frac{1}{\sqrt{\pi l_r}} \exp\left(-\frac{r^2}{2l_r^2}\right), \quad (5.11)$$

where l_r, l_z correspond, respectively, to the transverse and longitudinal widths. The functional is minimized with respect to the parameters l_r, l_z. By performing the integral in equation 5.10 with the above ansatz and by rescaling the variables with the transversal frequency ω_r, the following equation for the scaled energy is obtained [208]:

$$\varepsilon_{GP} = \frac{1}{2\gamma_r^2} + \frac{\gamma_r^2}{2} + \frac{1}{6\gamma_z^2} + \frac{\pi^2}{24}\lambda^2\gamma_z^2 + \frac{\alpha}{3\gamma_r^2\gamma_z}, \quad (5.12)$$

with $\varepsilon_{GP} = E_{GP}/\hbar a_r$, $\gamma_r = l_r a_r$, $\gamma_z = l_z a_r$, $\lambda = \omega_z/\omega_r$, $\alpha = Na/a_r$. The energy surface which arises from the previous equation is shown in Figure 5.3 a-d, for trapping and interaction parameters similar to those used in the experiment, as a function of the atom number N. A local minimum exists for atom numbers below a critical value (white asterisk, Figure 5.3 a-c), with a combination of widths l_r, l_z

that provide a stable configuration for the BEC. Above the critical atom number, the energy has a minimum when both the widths are zero, and the BEC collapses. Figure 5.3e shows the scaled energy per particle along the path of lowest energy as a function of the longitudinal width l_z. Collapse is prevented by an energy barrier formed by the kinetic energy. For increasing atom number, this barrier is gradually reduced by the interaction energy until the local minimum vanishes. By differentiating equation 5.10 with respect to the two normalised widths and by equating to zero the two deriving equations, the parameters of the local energy minimum can be found by solving the system of equations [208]:

$$-\gamma_r^{-3} + \gamma_r - \frac{2}{3}\alpha\gamma_r^{-3}\gamma_z^{-1} = 0 \tag{5.13}$$

$$-\frac{\gamma_z^{-3}}{3} + \frac{\pi^2}{12}\lambda^2\gamma_z - \frac{\alpha}{3}\gamma_r^{-2}\gamma_z^{-2} = 0. \tag{5.14}$$

In general, the previous system of equations does not provide an analytical solution and must be solved numerically. In the limit of weak interactions and strong transversal confinement $\hbar\omega_r \gg \mu$, the condensate populates the ground state of the transversal harmonic oscillator. In this regime we can set $\gamma_r = 1$ in previous equations, and the minimum of the energy is found by solving equation 5.14. Also, considering attractive interactions $\alpha = -|\alpha| = -\sqrt{\zeta}$ we obtain the equation [208]:

$$\frac{\pi^2}{4}\lambda^2\gamma_z^4 + \sqrt{\zeta}\gamma_z - 1 = 0. \tag{5.15}$$

In reference [208] the previous equation has been solved in the case of expulsive potential $\omega_z^2 < 0$. Here we provide the solution in the case of a trapping potential $\omega_z^2 > 0$:

$$\gamma_z^* = \frac{F}{\sqrt{\zeta}}, \tag{5.16}$$

with

$$F = -\sqrt{\frac{G}{2}} + \frac{1}{2}\sqrt{-2G + \frac{4\sqrt{2}}{\pi^2\sqrt{G}}\left(\frac{\zeta}{\lambda}\right)^2}, \tag{5.17}$$

where

$$G = \frac{\Delta}{\pi^{\frac{4}{3}}}\left(\frac{\zeta}{\lambda}\right)^{\frac{4}{3}} - \frac{4}{3\pi^{\frac{2}{3}}}\frac{1}{\Delta}, \left(\frac{\zeta}{\lambda}\right)^{\frac{2}{3}}, \tag{5.18}$$

with

$$\Delta = \sqrt[3]{1 + \sqrt{1 + \frac{64\pi^2}{27}\left(\frac{\lambda}{\zeta}\right)^2}}. \tag{5.19}$$

In order to find the oscillation frequencies, equations of motion for the variational parameters are needed. By performing a Lagrangian variational analysis, such equations are [208]:

$$\ddot{\gamma}_r = \gamma_r^{-3} - \gamma_r + \frac{2\alpha}{3\gamma_z}\gamma_r^{-3} \tag{5.20}$$

$$\left(\frac{\pi^2}{12}\right)\ddot{\gamma}_z = \frac{\gamma_z^{-3}}{3} - \frac{\pi^2}{12}\lambda^2\gamma_z + \frac{\alpha}{3\gamma_r^2}\gamma_z^{-2}, \tag{5.21}$$

where the time derivative is with respect to the normalised time $\tau = \omega_r t$. We assume that the quench will excite breathing motion along the z direction only. Again, by setting $\gamma_r = 1$ in the previous equations we obtain:

$$\left(\frac{\pi^2}{12}\right)\ddot{\gamma}_z = \frac{\gamma_z^{-3}}{3} - \frac{\pi^2}{12}\lambda^2\gamma_z + \frac{\alpha}{3}\gamma_z^{-2}. \tag{5.22}$$

In the case of small deviations from the equilibrium position (minimum of the energy landscape), we can write the solution as $\gamma_z = \gamma_z^* + \delta\gamma_z$, where γ_z^* is the minimum given by equation 5.16 and $\delta\gamma_z$ is a small deviation. A linear expansion of equation 5.22 leads to the following expression for the longitudinal breathing angular frequency:

$$\omega_B = \omega_r\sqrt{\frac{12}{\pi^2}\left(\gamma_z^{*-4} + \frac{\pi^2}{12}\lambda^2 + \frac{2\alpha}{3}\gamma_z^{*-3}\right)}. \tag{5.23}$$

5.4 Experimental sequence

The experimental sequence starts with a levitated BEC of 2.5×10^5 atoms with a condensate fraction of approximately 70% and a scattering length of $a = 210\,a_0$. As described in Chapter 3, the BEC is generated in a crossed optical dipole trap formed by the horizontal and vertical laser beams L_H and L_V as shown in Figure 5.4a.

The solitons in our setup are confined to a quasi-1D geometry with almost

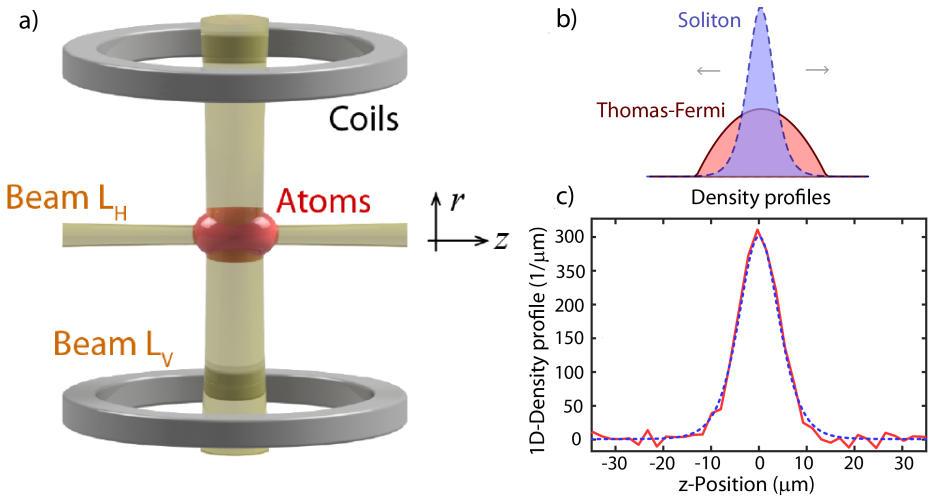

Figure 5.4: a) Sketch of the experimental setup with laser beams L_H, L_V. b) Thomas-Fermi density profile for a BEC (solid red line) and a soliton density profile (dashed blue line). c) Integrated density profile of the absorption image for t = 60 ms (red line) and fitted profile by using the function $A(\mathrm{sech}(z/B))^2$ (dotted blue line). Figures published in [57].

free propagation along the horizontal direction and strong radial confinement of $\omega_r = 2\pi \times 95\,\mathrm{Hz}$ provided by laser beam L_H. In quasi-1D geometry, the critical dimensionless parameter k_c, defined in equation 5.1, can be rewritten as $k_c = N|a|/a_r$ with $k_c = 0.67$ [205]. For our typical experimental scattering length of approximately $-5\,a_0$, this corresponds to a critical atom number of 2500. As a result, we need to strongly reduce the atom number to avoid collapse, modulation instabilities [30] and three-body losses [220] for a deterministic and reproducible creation of the soliton. We remove atoms with a small additional magnetic-field gradient, which pushes the atoms over the edge of the optical dipole trap. Our precise control of magnetic-field strengths allows us to reduce the atom number down to 200 atoms, with a reproducibility of ±100 for 600 atoms and ±350 for 4500 atoms, measured as the standard deviation of the atom number in 50 consecutive runs, Figure 5.5. A removal period of 4 s and smooth ramps of the magnetic-field strength are necessary to minimise excitations of the BEC. Following the removal procedure we measure residual fluctuations of the width of the BEC below 3.5%.

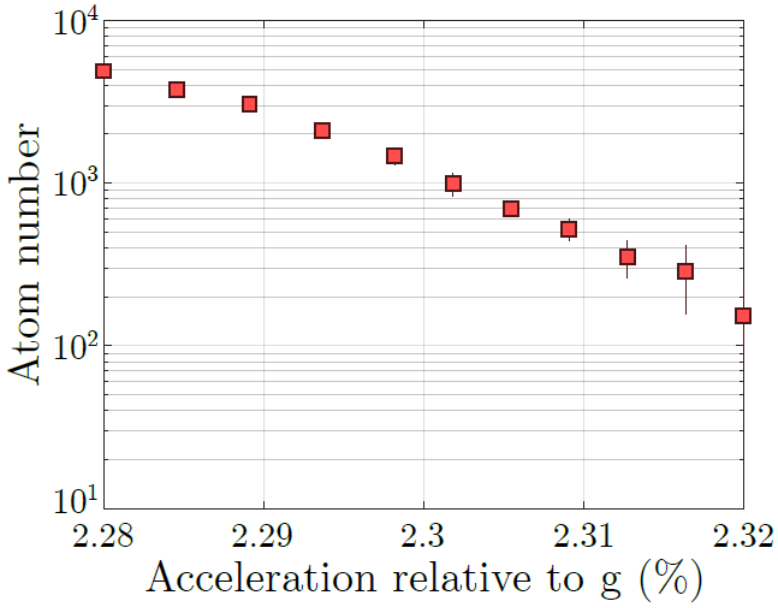

Figure 5.5: Atom number as a function of the percentage of the gravitational acceleration experienced by the atom in the trap. Figure taken from [101].

5.5 Soliton generation via quench

We generate the matter-wave soliton with a quench of the scattering length towards attractive interaction ($a_i \rightarrow a_f$), and by a reduction of the longitudinal trap frequencies ($\omega_{z,i} \rightarrow \omega_{z,f}$). When changing a and ω_z independently, the quenches excite inward- and outward motion, respectively. Usually it is desirable to minimize the excitations of the soliton by matching the initial Thomas-Fermi density profile of the BEC closely to the density profile of the soliton, as illustrated in Figure 5.4b and by adjusting the quench parameters. However, we deliberately mismatch the quench parameters from those employed for generating a stable soliton to create breathing oscillations of the soliton in order to study its self-trapping potential. The cloud size $l_z(t)$ at a hold time t after the quench is measured by fitting the function $A(\mathrm{sech}(z/B))^2$, with fit parameters A and B, to the density profiles, Figure 5.4c. The density profiles are determined from absorption images after a free expansion time of 16 ms (Figure 5.6a).

The response of the atomic cloud to the different steps of the quench protocol is presented in Figure 5.6b. We first quench only the longitudinal confinement for $N \approx 1700$ atoms from $\omega_{z,i} = 2\pi \times 5.8(2)$ Hz to $\omega_{z,f} = 2\pi \times 4.3(2)$ Hz in 4 ms

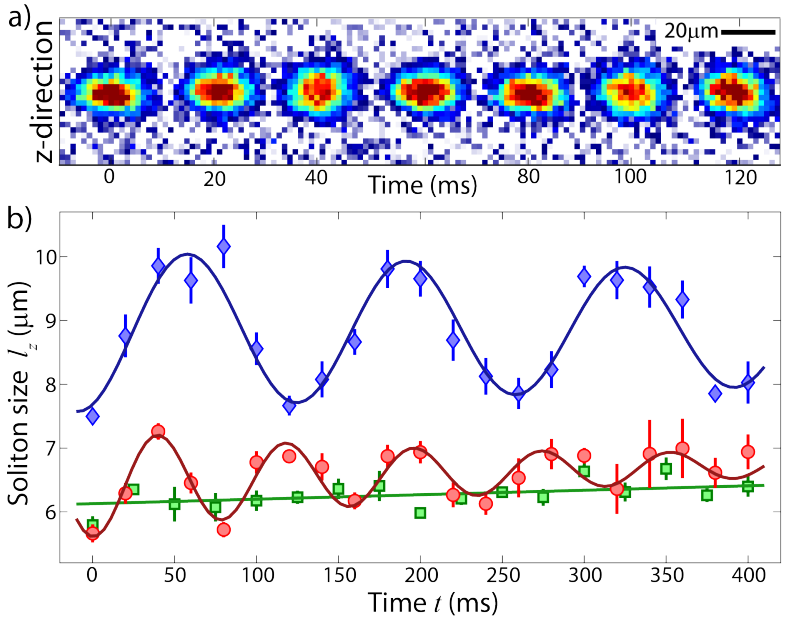

Figure 5.6: a) Absorption images after an expansion time of 16 ms (taken from data set with red circles in b). b) Oscillations of a quantum gas with $N \approx 1700$ after various quenches with a final trap frequency $\omega_{z,f} = 2\pi \times 4.3(2)$ Hz. Blue diamonds: quench of only ω_z excites breathing oscillations of a BEC; Red circles: additional interaction quench to $a_f = -5.4a_0$ to excite breathing oscillations of a soliton; Green squares: optimized quench parameters to minimize the breathing amplitude of the soliton. The uncertainty intervals indicate ± 1 standard error. Solid lines are damped sinusoidal fits. Figure published in [57].

while keeping the interaction strength constant $a_i = +7\,a_0$ (blue diamonds in Figure 5.6b). The BEC starts an outwards motion with an oscillation frequency of $\omega_{\mathrm{BEC}} = 2\pi \times 7.5(1)$ Hz $\approx \sqrt{3}\ \omega_{z,f}$, which is well expected for a BEC in the Thomas-Fermi regime [44, 185]. In a second quench protocol, we additionally quench the interaction strength to $a_f = -5.4\,a_0$ (green squares in Figure 5.6b). In order to minimise excitations of the soliton, we set $\omega_{z,i} = 2\pi \times 11.2(2)$ Hz to match the width of the BEC to the expected size of the soliton. As a result, we observe almost dispersionless solitons with a linear increase of l_z of $0.7(3)\,\mu m/s$ (green line in Figure 5.6b). Finally, we deliberately mismatch the size of the BEC with $\omega_{z,i} = 2\pi \times 8.5(1)$ Hz, and generate small amplitude oscillations of the soliton with a frequency of $\omega_{sol} = 2\pi \times 12.8(4)$ Hz (red circles in Figure 5.6b). This breathing frequency of the soliton is significantly larger than any possible breathing frequency of a BEC, and larger than the breathing frequency of non-

interacting atoms of $2\omega_{z,f} = 2\pi \times 8.6(3)$ Hz. We observe no discernible oscillation in the radial direction after the quenches.

5.6 Measurement of the breathing frequency of a soliton

We demonstrate that the breathing frequency, ω_{sol}, depends on the interaction strength, a property typical of the nonlinear character of the soliton. The interaction term in the 1D-GPE depends on the product Na, and we expect that the variation of scattering length and atom number have equivalent effects on ω_{sol}. We choose to change N, since the initial removal process is independent of the interaction quench, and it allows us to study the breathing frequency without changing the quench protocol and without excitations of additional modes. We measure the breathing frequency, ω_{sol}, for varying N with fixed parameters $\omega_{z,i} = 2\pi \times 5.8(2)$ Hz, $\omega_{z,f} = 2\pi \times 4.3(2)$ Hz, $a_i = +7\,a_0$, $a_f = -5.4\,a_0$, $\omega_r = 2\pi \times 95$ Hz (see red circles in Figure 5.7). The values of ω_{sol} decrease for lower N, and they approach the breathing frequency $2\omega_{z,f}$ for non-interacting atoms in a harmonic trap (dashed gray line).

We compare our experimental data points to numerical and variational models. For a numerical simulation of the 1D-GPE and NPSE, we use the ansatz in equation 5.9 to calculate the starting conditions, and we determine the breathing frequency from a spectral analysis of the time evolution of the wave function (blue triangles in Figure 5.7). The simulations were done in collaboration with the local theoretical group, lead by A. Daley and G.-L Oppo. Numerical simulations were performed by Grant Henderson and Stuart Flannigan [57]. In addition, we compare the data with the analytical approximation for the breathing frequency (Figure 5.7 red line) provided by equation 5.23. We find that the models agree well with the trend of the measurements of ω_{sol}, although our experimental data points are systematically lower for large N than our theoretical predictions. We speculate that this is due to non-harmonic contributions to the energy of the soliton on the breathing oscillations for finite oscillation amplitudes.

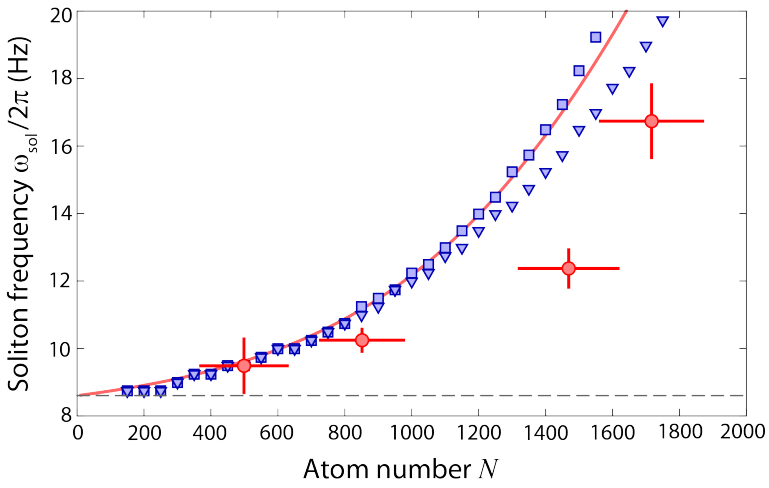

Figure 5.7: Dependence of the soliton breathing frequency ω_{sol} on the atom number N. Quench parameters $\omega_{z,i} = 2\pi \times 5.8(2)\,\mathrm{Hz}$, s$\omega_{z,f} = 2\pi \times 4.3(2)\,\mathrm{Hz}$, $a_i = +7a_0$, $a_f = -5.4a_0$, $\omega_r = 2\pi \times 95\,\mathrm{Hz}$. Red circles: experimental data, the uncertainty bars for the atom number indicate the standard deviation of N over the first 100 ms of each frequency measurement. Blue triangles: numerical simulation of the 1D-GPE. Blue squares: numerical simulation of the NPSE. Red line: analytical approximation from equation 5.23. Dashed gray line: oscillation frequency of a non-interacting gas, $2\omega_{z,f}$. Figure published in [57].

To determine the influence of the trapping potential, we measure the variation of ω_{sol} as we reduce the longitudinal trapping frequency $\omega_{z,f}$. Smaller values of $\omega_{z,f}$ result in larger equilibrium sizes of the soliton, and we need to reduce the initial trap frequencies $\omega_{z,i}$ to keep the oscillation amplitudes comparable during the measurements. The typical difference between $\omega_{z,i}$ and $\omega_{z,f}$ is approximately 3 Hz. Two regimes can be identified in Figure 5.8 where the soliton frequency changes with varying the trap frequencies $\omega_{z,f}$. For large values of $\omega_{z,f}$ the trap dominates the breathing of the soliton and ω_{sol} approaches twice the trap frequency $2\omega_{z,f}$. For small values of $\omega_{z,f}$, interactions dominate the breathing of the soliton and ω_{sol} reaches a constant value. This offset of the breathing frequency is a result of the "self-trapping" potential of a free soliton.

Again, we compare the experimental results with our theoretical models (see red line in Figure 5.8) and the numerical simulations of the 1D-GPE (see blue band in Figure 5.8 for simulations between $N = 1300$ and $N = 1500$. Numerical simulations were performed by Grant Henderson and Stuart Flannigan [57]). The simulations predict a lower breathing frequency for the free soliton than the

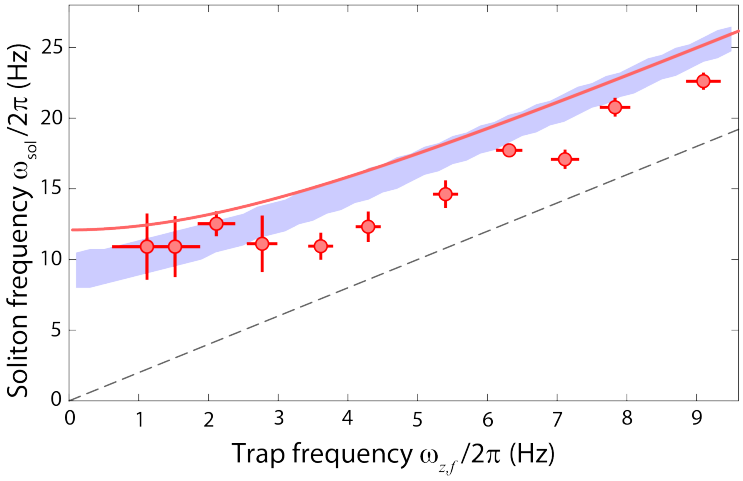

Figure 5.8: Dependence of the soliton breathing frequency ω_{sol} on the trap frequency ω_z for $a_f = -5.4a_0$. Red circles: experimental data points for $N \approx 1450$. Blue area: simulation of the 1D-GPE for $N = 1300$ to 1500. Red line: analytical approximation from equation 5.23. Dashed gray line: $2\omega_{z,f}$. Figure published in [57].

analytical approximation, but all curves are within the uncertainly range of the experimental data.

5.7 Observation of higher-order bright matter-wave solitons

5.7.1 Wave functions for higher-order solitons

Breathing oscillations of the soliton width are not the only possible excitation modes of solitons. The existence of higher-order solitons has been predicted in 1974 by Satsuma and Yajima for the dimensionless non-linear Schrödinger equation [232]

$$i\frac{\partial}{\partial\tau}b = \frac{1}{2}\frac{\partial^2}{\partial\zeta^2}b + |b|^2 b, \tag{5.24}$$

and observed later in non-linear optics [188,234]. Higher-order solitons arise from the evolution of the non-normalised soliton solution

$$b(\zeta, \tau = 0) = A\mathrm{sech}(\zeta) \tag{5.25}$$

when A is equal to an integer number and they can be interpreted as stable excitations with periodic oscillations of the density profile and phase or as a bound state of n strongly overlapping solitons [208].

Later, similar effects were proposed for bright matter-wave solitons [208, 233], where it was suggested that nth-order solitons can be generated by a rapid increase of the attractive interaction strength by a factor n^2, with n representing an integer number. This relies on the fact that the constant A in equation 5.25 is related to the initial l_i and the post-quench l_f characteristic lengths by [208]

$$A = \sqrt{\frac{l_i}{l_f}}, \tag{5.26}$$

where $l = a_r^2/(2aN)$. In the homogeneous case, the second-order soliton has the following analytic expression [208] (see also Appendix A)

$$f(z,t) = \frac{1}{2\sqrt{l_f}} e^{i\frac{\hbar t}{128ml_f^2}} \left[\frac{\cosh(\frac{3z}{8l_f}) + 3e^{i\frac{\hbar t}{16ml_f^2}} \cosh(\frac{z}{8l_f})}{\cosh(\frac{z}{2l_f}) + 4\cosh(\frac{z}{4l_f}) + 3\cos(\frac{\hbar t}{16ml_f^2})} \right], \tag{5.27}$$

which has an oscillation period of

$$T = 32\pi m l_f^2/\hbar. \tag{5.28}$$

Essentially, an n^{th}-order soliton forms for a sech-shaped wave function with an initial size $l_z^{(n)}$ that is the n^2 multiple of the healing length l_z, i.e. $l_z^{(n)} = n^2\ l_z$. Similarly, our simulations of the 1D-GPE show that higher-order solitons can be created for an increased initial size of the wave packet, Figure 5.9. Large initial soliton sizes lead to the periodic formation of local maxima and minima of the density profile. Striking characteristics of the time evolution are the periodic development of a sharp central peak with side wings for the second-order soliton (Figure 5.9a,b), and the periodic formation of a broad double-peak structure for the third-order soliton (Figure 5.9c,d). Sizes and interaction quenches that do not fulfil the previous conditions lead to a "shedding" of the atomic density in the $z-$direction, as will later see in the experiments in Section 5.7.2. The wave

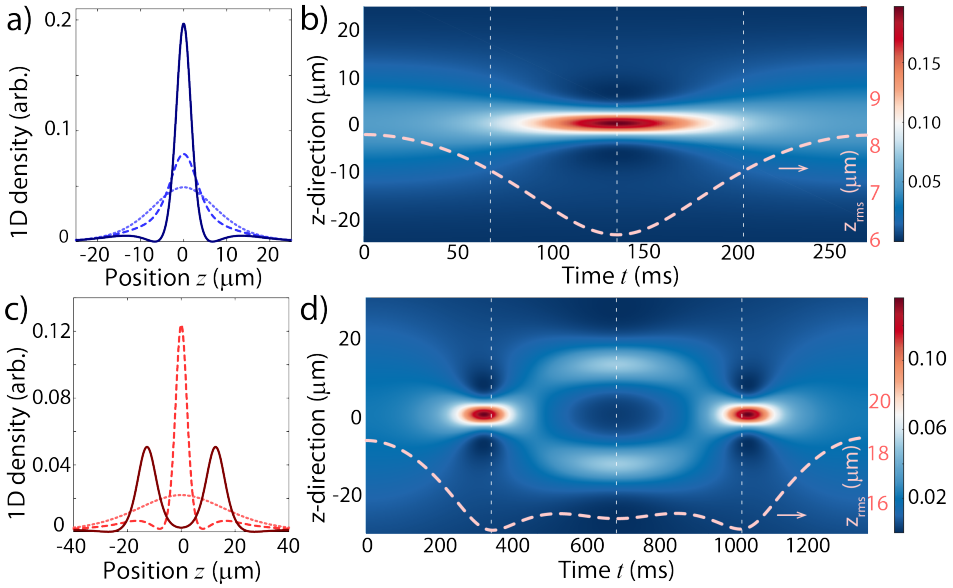

Figure 5.9: Simulation of higher-order solitons in the 1D-GPE. Temporal snapshots a) and temporal evolution b) of the atomic density profile of an $n = 2$ soliton for $N = 1800$, $a = -3.7\,a_0$, $l_z^{(2)} = 10.2\ \mu\text{m} = 4l_z^{(1)}$, and an oscillation period of $T_2 = 271\,\text{ms}$. Temporal snapshots c) and temporal evolution d) of the atomic density profile of an $n = 3$ soliton for the same values of N, a, but with $l_z^{(3)} = 22.8\ \mu\text{m} = 9l_z^{(1)}$, and with a period $T_3 = 1373\,\text{ms}$. The density profiles in a) and c) are plotted at $t = 0$ (dotted lines), $t = 1/4T$ (dashed lines), $t = 1/2T$ (solid lines). The dashed lines in b) and d) display the temporal evolution of the size of the soliton wavepacket z_{rms} (right scale). Figure published in [57].

packet oscillates and loses particles until its size and shape match the next (lower n) higher-order soliton [232].

5.7.2 Observation of second-order bright matter-wave solitons

We apply two different quench protocols to study the evolution of strongly excited solitons. In the first protocol, we apply a strong quench to a repulsive BEC whereas in the second, we create a soliton by a first quench followed by second quench of the scattering length by approximately a factor 4, as suggested in [208]. Depending on the initial size and the quench parameters, we observe shedding and fragmentation of the wave packet, and we measure oscillation frequencies that indicate the creation of higher-order solitons. To demonstrate the effect of a strong quench of an elongated BEC, we prepare a BEC containing $N \approx 3000$

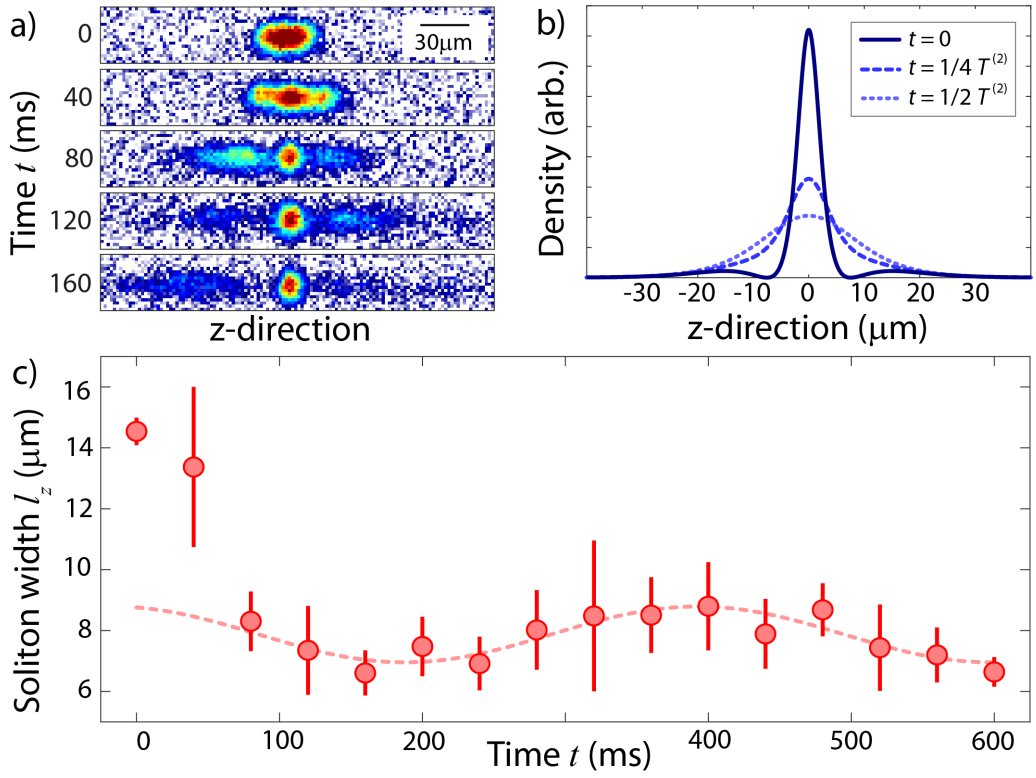

Figure 5.10: Time evolution after a strong quench of interactions and trap frequency. a) Absorption images at time t after the quench and after 11 ms of free expansion. b) 1D-GPE simulation of the density profiles for a second-order soliton with 1100 atoms, $a_f = -5.3\,a_0$, and with an oscillation period $T^{(2)}$ of 432 ms. c) Time evolution of the measured width l_z of the central wave packet (red circles), sinusoidal fit with period 420(30) ms (dashed red line). The uncertainty intervals indicate ± 1 standard deviation . Figure published in [57].

atoms in a cylindrical dipole trap with $\omega_r = 2\pi \times 86$ Hz and $\omega_{z,i} = 2\pi \times 4.9(2)$ Hz at an initial scattering length of $a_i = 56\,a_0$. Then we increase a_i and reduce $\omega_{z,i}$ before slowly ramping a and ω_z to $-5.3\,a_0$ and $2\pi \times 0.0(6)$ Hz in 13 ms, while keeping ω_r constant. Our quench induces an initial spreading of the wave packet, followed by a strong shedding of atoms and, finally, in the formation of a soliton that contains $N \approx 1100$ atoms (Figure 5.10a). We determine soliton width and find a slow oscillation of $l_z(t)$ with a frequency of $2\pi \times 2.4(2)$ Hz (Figure 5.10c). This frequency is significantly smaller than the expected breathing frequency of first-order solitons, $2\pi \times 6.0$ Hz, and it matches well to the expected frequency of $2\pi \times 2.3$ Hz for second-order solitons in equation 5.28.

Observing shedding and oscillations agrees well with the predictions for higher-

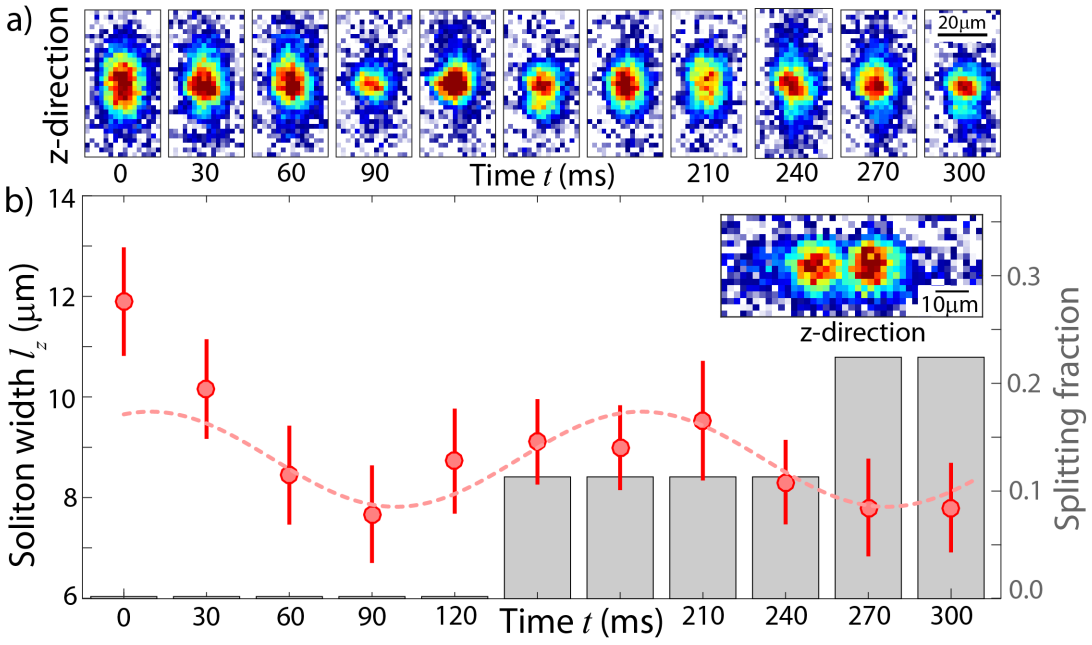

Figure 5.11: Second-order soliton and splitting after the double-quench. a) Absorption images at time t after the quench and after 7 ms of free expansion. b) Time evolution of the measured width l_z of the central wave packet (red circles), sinusoidal fit with period 180(20) ms (dashed red line). The histogram counts the fraction of images showing a splitting of the wave function (9 repetitions per time step). Inset: absorption image of a split matter-wave for $t = 210$ ms. Figure published in [57].

order solitons within the 1D-GPE [232], however, we find a strong dependence on details of the quench parameters, such as the quench duration, the initial atom number and the final values of the longitudinal trapping frequency and scattering length. We also implement the double-quench protocol, which consists of creating a stable soliton with a first quench followed by second quench of the scattering length. We start by preparing a BEC at an initial scattering length of $a_i = 29\,a_0$, with atom number and trapping parameters similar to those used in the previous protocol. To generate a stable soliton, we quench the scattering length a_i and the longitudinal trapping frequency, respectively, to $a_f = -0.8\,a_0$ and $\omega_f = 2\pi \times 1.4(2)$ Hz in 15 ms. After a settling time of 25 ms, we apply a second quench in 2 ms of only the interaction strength to $a_f = -4.6\,a_0$. Starting with approximately 2200 atoms, we observe no shedding but a small loss of 300 atoms during the first 60 ms. The density distributions (Figure 5.11a) resemble the expected profiles for a second-order soliton (Figure 5.10b) and the width

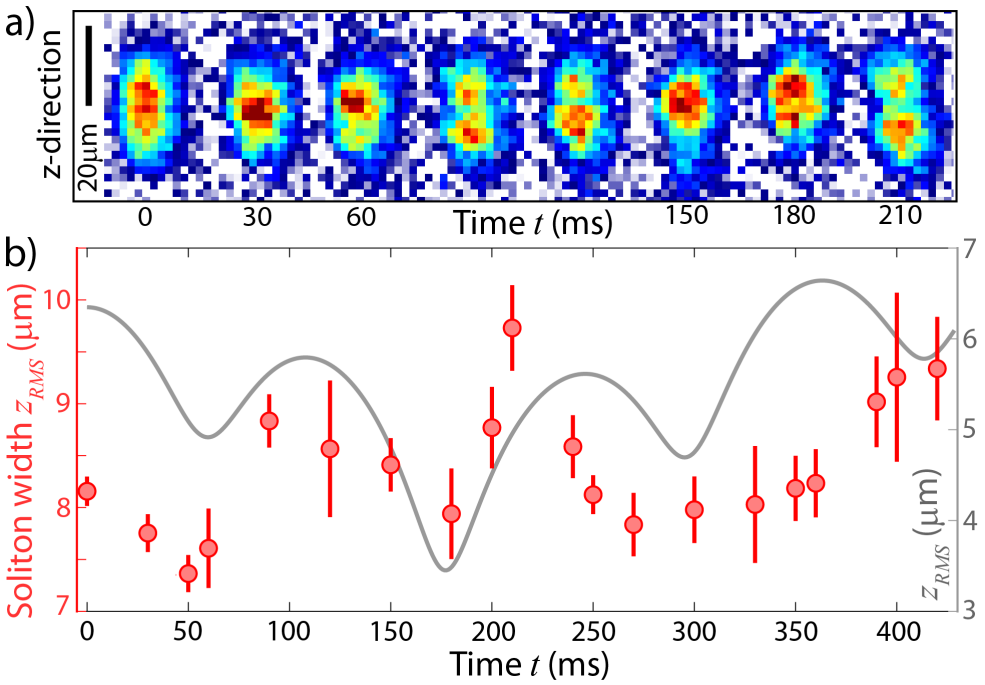

Figure 5.12: Attempt to observe a third-order solitons. a) Absorption images after 6ms of expansion time for different evolution times t. b) Evolution of the second-moment z_{rms}. Error bars indicate ± 1 standard errors. The solid lines show numerical simulations with the 1D-GPE model for the evolution of z_{rms} (see Supplementary material in [57]). Figure published in [57].

of the wave packet oscillates with a frequency of $2\pi \times 5.6(6)$ Hz (Figure 5.11b), which matches the expected frequency of $2\pi \times 5.2$ Hz for second-order solitons ($2\pi \times 13.2$ Hz for the first-order).

For both measurements (Figure 5.10c, 5.11b), a small percentage of absorption images show the splitting of the soliton into two fragments (inset Figure 5.11b). Due to the destructive nature of our absorption images it is difficult to follow the evolution of the same matter-wave soliton and to provide an explanation on the cause of the splitting process. A double-peak structure in the density profile can indicate fragmentation due to classical or quantum effects, or simply an insufficient technical control of our quench parameters. The percentage of images which show a splitting of the wave packet increases for longer evolution times, and we indicate the fraction in Figure 5.11b with a histogram.

5.7.3 Attempt to observe a third-order soliton

We also tried to generate a third-order soliton by a strong quench of a BEC. We start by preparing a BEC with $N \approx 1800$ atoms and by adjusting its initial size by setting the initial trap frequency and scattering length to $\omega_{z,i} = 6.0(2)\,\mathrm{Hz}$ and $a_i = 10\,a_0$, respectively. Then we quench both the longitudinal trapping frequency and the scattering length to $\omega_{z,f} = 2\pi \times 0.6(5)\,\mathrm{Hz}$, and $a_f = -6.7\,a_0$. The result of this quench is illustrated in Figure 5.12 in which the absorption images show the formation of a double-peak structure that indicates the presence of a third-order soliton. We quantify the periodic change of the soliton shape by evaluating the second moment z_{rms} of the density distribution $\eta(z,t)$, i.e.

$$z_{rms}(t) = \left(\frac{1}{N}\int \eta(z,t)(z-\bar{z})^2 dz\right)^{1/2}, \tag{5.29}$$

where $\bar{z}$ is the mean position of the wave packet, and compare it with a numerical simulation of the 1D-GPE (Figure 5.12a grey line). The time evolution of $z_{rms}(t)$ exhibits a local maximum for the double peak structure of the third-order soliton, Figure 5.12a. However, the experimental data do not agree with the numerical simulation of the 1D-GPE. In particular, the second moment z_{rms} measured in the experiment is systematically smaller than that expected from the simulation and the general trend predicted from the 1D-GPE is not matched by the experimental data. We suspect that deviation may be caused by finite quench duration, by a residual trapping potential, or by our imaging resolution.

5.8 Conclusions

In conclusion, we experimentally investigated the excitation modes of bright matter-wave solitons in a quasi-one-dimensional geometry. The solitons were created by quenching the interactions from repulsive to attractive and the longitudinal confinement of a BEC. A mismatch of quench parameters allowed the excitation of breathing modes of a soliton. We determined its breathing frequency as a function of atom number N and longitudinal confinement ω_z. Moreover, we

observed signatures of the generation of second-order solitons by measuring their oscillation period. We also observed the shedding and splitting of the soliton wave function, and showed absorption images that hint to possible creation of a third-order soliton.

Chapter 6

Conclusions and outlook

During the course of my PhD I built the experimental setup, which took the best part of two years. We implemented and optimised all the stages for the generation of Bose-Einstein condensate of caesium. As a result, our system can routinely produce BECs of 2.0×10^5 atoms. We employed our tunable caesium BECs for performing two strands of experiments which formed the key part of my thesis.

In the first series of experiments, we used a magnetic levitation scheme for measuring micro-g accelerations by means of atom interferometry. In this context, we discussed the limitations of the levitation scheme due to the curvature of the force field, and due to field fluctuations caused by our current regulation. In the second series of experiments, we generated bright matter-wave solitons by taking advantage of a zero crossing of a broad Feshbach resonance. We studied the breathing mode of a single bright matter-wave soliton in quasi-1D geometry by measuring its oscillation frequency as a function of the atom number and longitudinal confinement. Furthermore, we reported on the observation of the $N = 2$ higher-order soliton and its decay.

6.1 Outlook

We are currently performing experiments in which we employ the vertical magnetic field gradient to map the field-dependent s-wave scattering length $a(B)$ to position space. This approach opens the possibility to explore the dynamics of

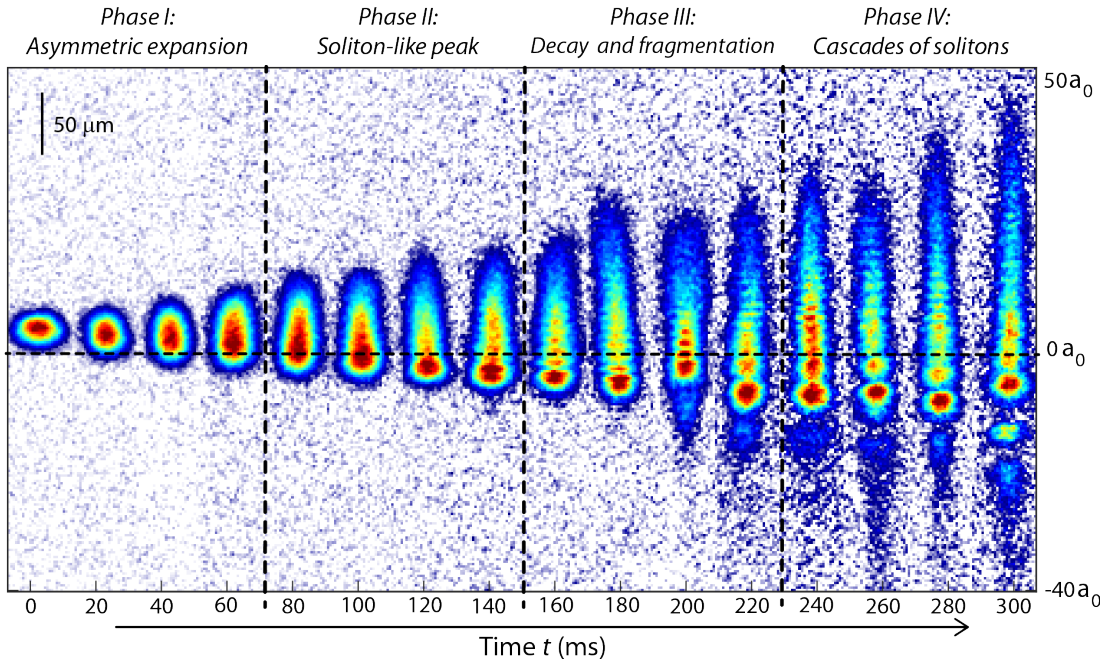

Figure 6.1: Absorption images of expanding and levitating BECs in a vertical dipole trap in spatially varying scattering length a over an evolution time of 300 ms.

BECs with position-dependent interactions, also called collisionally inhomogeneous matter-wave [235]. First theoretical investigations studied the adiabatic compression of a bright matter-wave soliton due to time- and space-dependent s-wave scattering lengths [236]. Later, the combination of magnetic Feshbach resonances and magnetic-field gradients was proposed for the generation of collisionally inhomogeneous matter waves [235]. In this context, compression [235], dynamical trapping and transmission of matter-wave solitons were predicted [237]. Other theoretical proposals exploited optical Feshbach resonances for realising BECs with space-dependent interactions [238–241]. So far, collisionally inhomogeneous BECs have been experimentally realised by using optical Feshbach resonances [242, 243], but inelastic light-induced collisions caused loss and heating of the quantum gas. Our experimental system facilitates magnetic Feshbach resonances and magnetic-field gradients, and is well suited for the implementation of some of the above mentioned proposals [235, 237].

For magnetic-field values which are sufficiently far from the Feshbach resonance, it is possible to express locally the spatial dependence of the scattering

length a as a linear function of the vertical position z, i.e $a = \bar{a}_0 + \Delta a\, z$. Here $\bar{a}_0$ and Δa represent the offset and the spatial gradient of the scattering length respectively. In the case $\Delta a\, d/\bar{a}_0 \ll 1$, where d represents the characteristic length scale of the matter-wave, the expanding BEC experiences an adiabatic variation of the scattering length as discussed in [235, 237]. It is interesting to probe the regime of a strong scattering-length gradient which violates the above condition. In particular, matter-waves, which expand simultaneously into regimes with attractive and repulsive interactions, are intriguing. Figure 6.1 shows preliminary expansion measurements of a BEC close to the zero crossing of the scattering length. The BEC first expands asymmetrically in a vertical dipole trap, and then forms a soliton on the attractive side of the crossing. The soliton decays and induces density modulations in the quantum gas. Currently, we are investigating the mechanism underlying the formation and the decay of the initial soliton.

The decay of bright matter-wave solitons is an active field of theoretical research. As the role of quantum noise is strongly debated [244–249], we are planning to study solitons with small atom numbers. So far, experimentally generated bright matter-wave solitons contain a few hundreds of atoms [30, 222]. In this regime, solitons can still be described within a mean-field theory by the Gross-Pitaevskii equation. Recently, excitation modes of higher-order solitons have been proposed for testing various theoretical models beyond GPE, such as the multi-configurational time-dependent Hartree method for bosons [244, 245], truncated Wigner methods and positive-P phase-space representations [246, 247], numerical Bethe ansatz [248] and time-evolving block decimation [249]. We plan to perform experiments with the goal of testing the above mentioned theoretical models.

Appendix A

Matching 1D-GPE with the Satsuma-Yajima model

The aim of this section is to find the correspondence between the 1D-GPE and the dimensionless non-linear Schrödinger equation used by Satsuma and Yajima in 1974 [232] in which, for the first time, the analytic solution for the second order $N = 2$ higher order soliton has been found. However, such a solution has been given in dimensionless units and the connection with the physical units that appear in the 1D-GPE is needed. Although the explicit solution in terms of the 1D-GPE units has been already given by L. Carr and Y. Castin in 2002 [208], we found it useful to make explicitly the full derivation.

We start by recalling the 1D-GPE (see eq. 5.7 in Chapter 5):

$$i\hbar\frac{\partial}{\partial t}f(z) = \left[-\frac{\hbar^2}{2m}\frac{\partial^2}{\partial z^2} + V_{ext}(z) + \frac{gN}{2\pi a_r^2}|f(z)|^2\right] f(z), \tag{A.1}$$

where $V_{ext}(z)$ is a general external potential, $g = 4\pi\hbar^2 a/m$ and $a_r = \sqrt{\hbar/m\omega_r}$. The wave function $f(z)$ satisfies the normalisation condition:

$$\int_{-\infty}^{\infty} dz|f(z)|^2 = 1, \tag{A.2}$$

which implies that its physical dimension is $[f] = 1/\sqrt{L}$ with L representing length. In order to obtain a bright soliton solution, the atom-atom interactions must be attractive i.e the value of the scattering length is negative $a < 0$. For convenience we will use the absolute value of the scattering length $|a|$ and write

explicitly the minus sign in the equation. Moreover, in the Satsuma-Yajima model the external potential is set to zero. We can thus simplify eq. A.1 and write:

$$i\hbar\frac{\partial}{\partial t}f = \left[-\frac{\hbar^2}{2m}\frac{\partial^2}{\partial z^2} - \frac{|g|N}{2\pi a_r^2}|f|^2\right] f. \tag{A.3}$$

The characteristic length that emerges naturally by equating the kinetic and interaction energy is:

$$\frac{\hbar^2}{ml^2} = \frac{4\pi\hbar^2 aN}{2\pi m a_r^2}\frac{1}{l}, \tag{A.4}$$

which leads to

$$l = \frac{a_r^2}{2aN}. \tag{A.5}$$

We define the new dimensionless variable in the following way:

$$\zeta = \frac{z}{l}. \tag{A.6}$$

In order to maintain the correct normalisation need to scale the integral of f as well, leading to the following relations:

$$dz = l d\zeta \tag{A.7}$$

$$\int_{-\infty}^{\infty} l d\zeta \left|\frac{F(\zeta)}{\sqrt{l}}\right|^2 = \int_{-\infty}^{\infty} d\zeta \, |F(\zeta)|^2 = 1, \tag{A.8}$$

where we have imposed:

$$f(z) \equiv \frac{F(\zeta)}{\sqrt{l}}. \tag{A.9}$$

This implies that every time we scale a length in the 1D-GPE we need to redefine the wave function in a similar way to eq. A.9. The 1D-GPE becomes:

$$i\hbar\frac{\partial}{\partial t}F = -\frac{\hbar^2}{2ml^2}\frac{\partial^2}{\partial \zeta^2}F - \frac{\hbar^2}{ml^2}|F|^2 F. \tag{A.10}$$

By rewriting it as:

$$i\frac{ml^2}{\hbar}\frac{\partial}{\partial t}F = -\frac{1}{2}\frac{\partial^2}{\partial \zeta^2}F - |F|^2 F, \tag{A.11}$$

and defining the normalised time as:

$$\tau = \frac{\hbar}{ml^2}t, \tag{A.12}$$

we get

$$i\frac{\partial}{\partial\tau}F = -\frac{1}{2}\frac{\partial^2}{\partial\zeta^2}F - |F|^2F. \tag{A.13}$$

By setting $u = F^*$, we obtain

$$i\frac{\partial}{\partial\tau}u = \frac{1}{2}\frac{\partial^2}{\partial\zeta^2}u + |u|^2u. \tag{A.14}$$

The integral of $|u|^2$ is

$$\int_{-\infty}^{\infty} d\zeta |u(\zeta)|^2 = \int_{-\infty}^{\infty} d\zeta |F(\zeta)|^2 = 1. \tag{A.15}$$

Satsuma-Yajima solutions are not normalised, their ansatz is

$$b(\epsilon, \theta = 0) = A\,\mathrm{sech}(\epsilon), \tag{A.16}$$

where A is a real number. The integral of the modulus square of the ansatz is:

$$\int_{-\infty}^{\infty} d\epsilon |b(\epsilon)|^2 = A^2 \int_{-\infty}^{\infty} d\epsilon\,\mathrm{sech}^2(\epsilon) = 2A^2 \tag{A.17}$$

As pointed out in reference [208], the value of A can be connected with a quench of the parameters of the physical system. We start from some given initial conditions which set the characteristic length l_i. The ground state solution of equation A.14 is

$$u(\zeta_i) = \frac{1}{\sqrt{2}}\,\mathrm{sech}\zeta_i, \tag{A.18}$$

which corresponds to the normalised solution of eq. A.16 with $N = 1$, i.e $b^{A=1}(\zeta_i) = \sqrt{2}u(\zeta_i)$. We quench now one of the parameters of the system and this leads to the final characteristic length l_f which is related to the initial one by the relation $l_i = ql_f$, where q is a real number that accounts for the magnitude of the quench, implying that the scaled variables will satisfy the relation $\zeta_f = q\zeta_i$. We now

evaluate the integral of the ground state with respect to the final dimensionless variable ζ_f:

$$\int_{-\infty}^{\infty} d\zeta_f \operatorname{sech}^2(\zeta_i) = \int_{-\infty}^{\infty} d\zeta_f \operatorname{sech}^2(\zeta_f/q) = 2q. \tag{A.19}$$

By equating A.19 with A.17 we obtain that:

$$A = \sqrt{\frac{l_i}{l_f}}. \tag{A.20}$$

The above relation is important because it suggests how a higher-order soliton can be generated. For instance, for an $N = 2$ higher-order soliton the quench should satisfy $l_i = 4l_f$ which, as suggested in [208], can be accomplished by quenching the scattering length by a factor 4.

We still need to rewrite eq. A.14 with the normalisation given in eq.A.16. By multiplying equation A.14 by $(2A^2)^{\frac{3}{2}}$ and by defining the function

$$a = \sqrt{2A^2}u, \tag{A.21}$$

we get:

$$i2A^2\frac{\partial}{\partial\tau}a = 2A^2\frac{1}{2}\frac{\partial^2}{\partial\zeta^2}a + |a|^2a. \tag{A.22}$$

The function a is scaled to match the square modulus integral of eq A.16:

$$\int_{-\infty}^{\infty} d\zeta|a(\zeta)|^2 = 2A^2\int_{-\infty}^{\infty} d\zeta|u(\zeta)|^2 = 2A^2. \tag{A.23}$$

Let us scale again the 'spatial' variable by defining:

$$\epsilon = \frac{\zeta}{2A^2}. \tag{A.24}$$

With this change of variable we need to keep the integral of the modulus square of a constant. Since $d\zeta = 2A^2d\epsilon$ we have:

$$\int_{-\infty}^{\infty} 2A^2d\epsilon|\frac{b(\epsilon)}{\sqrt{2A^2}}|^2 = \int_{-\infty}^{\infty} d\epsilon|b(\epsilon)|^2 = 2A^2, \tag{A.25}$$

where we have defined the function $b(\epsilon)$:

$$a = \frac{b(\epsilon)}{\sqrt{2A^2}}. \tag{A.26}$$

Equation A.22 can be rewritten as:

$$i(2A^2)^2 \frac{\partial}{\partial \tau} b = \frac{1}{2} \frac{\partial^2}{\partial \epsilon^2} b + |b|^2 b. \tag{A.27}$$

By defining:

$$\theta = \frac{\tau}{(2A^2)^2}, \tag{A.28}$$

we get the dimensionless non-linear Schrödinger equation of reference [232]:

$$i \frac{\partial}{\partial \theta} b = \frac{1}{2} \frac{\partial^2}{\partial \epsilon^2} b + |b|^2 b \tag{A.29}$$

with the correct normalisation of the function b:

$$\int_{-\infty}^{\infty} d\epsilon |b(\epsilon)|^2 = 2A^2. \tag{A.30}$$

A second-order soliton is defined when $A = 2$, and the corresponding analytical solution of eq. A.29 is [232]:

$$b(\epsilon, \theta) = 4e^{-i\theta/2} \left[\frac{\cosh(3\epsilon) + 3e^{-4i\theta} \cosh(\epsilon)}{\cosh(4\epsilon) + 4\cosh(2\epsilon) + 3\cos(4\theta)} \right]. \tag{A.31}$$

From eq. A.28, eq. A.24 and eq. A.26, we can rewrite eq.A.31 as:

$$a(\zeta, \tau) = \sqrt{2} e^{-i\frac{\tau}{128}} \left[\frac{\cosh(\frac{3\zeta}{8}) + 3e^{-i\frac{\tau}{16}} \cosh(\frac{\zeta}{8})}{\cosh(\frac{\zeta}{2}) + 4\cosh(\frac{\zeta}{4}) + 3\cos(\frac{\tau}{16})} \right]. \tag{A.32}$$

By recalling the definition of u, eq. A.21, and that $F = u^*$ we obtain:

$$F(\zeta, \tau) = \frac{1}{2} e^{i\frac{\tau}{128}} \left[\frac{\cosh(\frac{3\zeta}{8}) + 3e^{i\frac{\tau}{16}} \cosh(\frac{\zeta}{8})}{\cosh(\frac{\zeta}{2}) + 4\cosh(\frac{\zeta}{4}) + 3\cos(\frac{\tau}{16})} \right]. \tag{A.33}$$

Finally, from eq. A.12, eq. A.9, and eq. A.6, we recover the expression for $A = 2$

in the physical units of the 1D-GPE given in [208]:

$$f(z,t) = \frac{1}{2\sqrt{l}} e^{i\frac{\hbar t}{128ml^2}} \left[\frac{\cosh(\frac{3z}{8l}) + 3e^{i\frac{\hbar t}{16ml^2}} \cosh(\frac{z}{8l})}{\cosh(\frac{z}{2l}) + 4\cosh(\frac{z}{4l}) + 3\cos(\frac{\hbar t}{16ml^2})} \right]. \tag{A.34}$$

From the previous equation the oscillation period associated with a second order soliton is:

$$T = \frac{32\pi ml^2}{\hbar}. \tag{A.35}$$

In conclusion, we obtained the analytical expression of the second-order soliton and of its oscillation period in terms of the physical units that appear in the 1D-GPE.

Appendix B

Publication: A simple laser shutter with protective shielding for beam powers up to 1 W

Note: A simple laser shutter with protective shielding for beam powers up to 1 W

Craig D. Colquhoun, Andrea Di Carli, Stefan Kuhr, and Elmar Haller[a)]
Department of Physics, SUPA, University of Strathclyde, Glasgow G4 0NG, United Kingdom

(Received 22 August 2018; accepted 10 November 2018; published online 5 December 2018)

We present the design of an inexpensive and reliable mechanical laser shutter and its electronic driver. A camera diaphragm shutter unit with several sets of blades is utilized to provide fast blocking of laser light and protective shielding of the shutter mechanism up to a laser beam power of 1 W. The driver unit is based on an Arduino microcontroller with a motor-shield. Our objective was to strongly reduce construction effort and expenditure by limiting ourselves to a small number of modular parts, which are readily available. We measured opening and closing durations of less than 800 μs, and a timing jitter of less than 25 μs for the fastest set of blades. No degradation of the shutter performance was observed over $5{\cdot}10^4$ cycles.
https://doi.org/10.1063/1.5053212

Mechanical optical shutter units have become indispensable in modern optics laboratories to provide a time-dependent extinction of laser light. Depending on the application, a multitude of desirable properties can be identified, such as low extinction ratios, fast switching times, low time jitter, high reliability, high repetition rates, small sizes, or long operation lifetimes.

Commercial products are currently available that fulfil most of those design requirements at high costs,[1] but laboratories often need dozens of shutter units and commercial solutions can quickly become unaffordable. As a result, many experimental groups have developed their own shutter designs with varying design goals and technical approaches,[2] e.g., based on loudspeakers,[3] computer hard drives,[4] or piezoelectric devices.[5,6]

In this article, we present the design of a mechanical shutter and its driver unit with two design objectives. The first objective is to strongly reduce construction effort and costs while preserving fast switching times and a high reliability. We do so by limiting ourselves to a small number of modular parts which are readily available.[7,8] The shutter unit utilizes a small diaphragm shutter with multiple blades as is normally used in compact digital cameras, and the driver unit is based on an Arduino microcontroller with a motor-shield.[8] The second design objective is a protection mechanism that facilitates the blocking of laser beams up to a continuous power of 1 W. We implement the protection with a shielding blade that reflects the laser light.

Details and additional materials for the construction are available in the supplementary material. Here, we give an outline to the design of the shutter blades, the driver unit, the microcontroller software, and the enclosure of the shutter. An experimental characterisation of the switching time, the jitter, and the reliability is provided.

Figure 1 illustrates the design of the **shutter blades**. The shutter contains three sets of blades—a light pair of blades B1 that close from opposite sides of the aperture in a "scissor" motion, overlapping in the centre and blocking light; a sturdy filter blade B2 originally intended to attenuate the light in a camera; and an unused blade with a hole which only limits the aperture size B3. We utilize blades B1 for fast switching operations and blade B2 for protection and dispersive reflection of laser light. Typically, the blades of small diaphragm shutters are optimized for low weight and friction, and they start to bend or melt when absorbing laser powers of more than 50 mW. We managed to increase the beam power up to 1 W[9] by adhering a small strip of aluminum foil to filter blade B2 that dispersively reflects the laser light and dissipates heat. By our

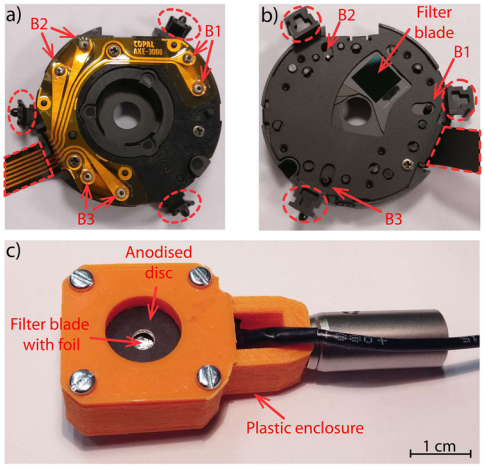

FIG. 1. Images of the (a) back and (b) front of the shutter before modifications and (c) within its 3D-printed enclosure. Red dashed lines indicate removed parts, and red arrows point toward the (a) connection terminals of the solenoids and (b) sliders of the shutter blades. The labels indicate that the connection terminals and sliders attach to scissor blades B1, filter blade B2, and unused aperture blade B3.

[a)]Electronic mail: elmar.haller@strath.ac.uk

design, most of the reflected light is trapped in the enclosure of the shutter.

The positions of the blades are controlled by small solenoids with independent connection terminals as indicated by red arrows in Fig. 1(a). The shutter blades are bistable without any springs or other self-restoring elements, and a short current pulse of ±200 mA for a duration of 3 ms is sufficient to flip the position. The final state of the shutter is determined by the direction of the current. For simplicity, we typically connect both blades, B1 and B2, in series by soldering thin wires to the connection terminals, but an independent control of the blades is used for the purpose of testing the shutter for this note.

The **shutter driver** consists of an Arduino microcontroller with a motor-shield (Fig. 2). The microcontroller monitors a digital (TTL) input signal that indicates the state of the shutter—a low (high) signal corresponds to a closed (open) state. The detection of a signal change triggers the short current pulse of the motor-shield with the required current direction to flip the blades. An operation of both solenoids in series requires a supply voltage of 5–6 V for the motor-shield to generate the correct current pulse. It is possible to supply the shield by the regulated 5 V output of the Arduino microcontroller, but a direct connection to the main power supply is advisable for the simultaneous control of 4 shutters units. For convenience, we added to the circuit a toggle switch to open the shutter manually, and a light emitting diode (LED) to indicate the shutter status. We intentionally limited the circuit to include only essential elements, and all components except for the microcontroller can be integrated into the front panel without the need of an additional circuit board.

Our **microcontroller software** is provided in the supplementary material. The tasks of the program are the tracking of the shutter status, the detection of a change of the TTL input signal, and the control of the motor-shield. Timer interrupts are included for the parallel control of several shutter units. The use of interrupts allows us to generate current pulses of well-defined duration without blocking the program flow. We measured a response delay between the input signal and the current pulse of 230(30) μs for a simultaneous use of 4 shutters units.

A plastic **enclosure** is used for the shutter unit to reduce the coupling of vibrations. The casing is 3D-printed using fused deposition modeling of polylactide (PLA) plastic. We sandwich the shutter between rubber "O" rings and a black anodised aluminum disc with a small hole of 4 mm diameter to further dampen vibrations. The disc reduces possible backscattering from the aluminum foil adhered to the shutter blades, and it prevents a melting of the casing material due to a misaligned laser beam. The corresponding computer-aided design (CAD)-model files of the enclosure can be found in the supplementary material.

The final part of this note describes an experiment to benchmark the speed, time jitter, and robustness of the shutter and driver unit. We used a photodiode[10] and an oscilloscope to measure the power of a laser beam after it propagated through the shutter. Timings for the shutter and for the acquisition oscilloscope were provided by an NI-multifunction IO device.[11] The shutter aperture is 4 mm in diameter, and the laser beam was collimated with a $1/e^2$ waist of 1.1 mm. As opposed to our normal operation, we connected each shutter blade to the shutter driver separately to study the timed opening and closing of the blades independently of one another. The intensity profiles of 500 consecutive opening and closing cycles were recorded and analyzed (Fig. 3). No degradation was detected over the course of $5{\cdot}10^4$ additional cycles.

Figure 3 shows the photodiode signal for a time t after the trigger signal to (a) open or (b) close the shutter with scissor blades B1 (blue) and filter blade B2 (red). The photodiode voltage is normalized for each data set to the signal of an open shutter. We determine an opening delay between the trigger and an increase to 5% of the full photodiode signal of 2.29(2) ms and 3.71(3) ms for blades B1 and B2. The opening durations, measured by an increase from 5% to 95% of the total signal, is 790(10) μs and 1.51(3) ms for the two sets of blades. The closing procedure is slightly faster with a closing delay of 2.73(2) ms and 2.71(3) ms and a closing duration of 573(7) μs and 1.46(2) ms for blades B1 and B2, respectively. Opening and closing delays are longer than the electronic response time, and we expect most of the delay time to be used to overcome

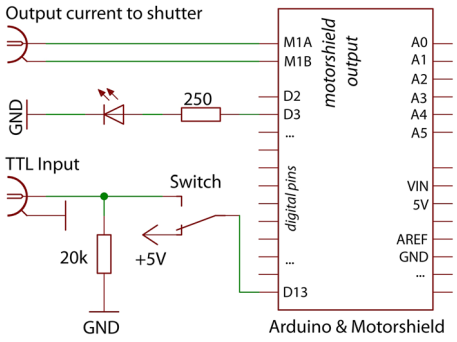

FIG. 2. Circuit diagram of the shutter controller. The design is based on an Arduino microcontroller with a motor-shield. We added a toggle switch to open the shutter manually by bypassing the TTL input signal, and an LED to indicate the status of the shutter blades. One motor-shield facilitates the simultaneous control of 4 shutter units.

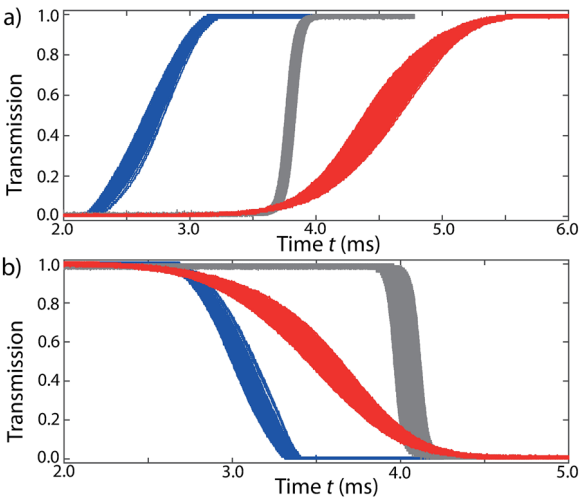

FIG. 3. Transmission signals of the two blades being (a) opened and (b) closed. The red (blue) lines show the transmission throughout the operation of filter blade B2 (scissor blades B1). The gray lines show the operation of B2 for a reduced beam waist (see text). The time scale indicates the delay time t after the change of the TTL input signal.

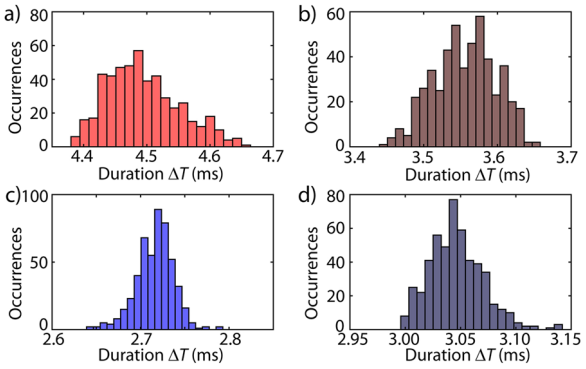

FIG. 4. Histograms of opening times for the transmission signals. (a) half-opening times and (b) half-closing times of filter blade B2. (c) half-opening times and (d) half-closing times of scissor blades B1.

friction and to separate the overlapping blades. We presume that the scissor blades are faster than the filter blade because they close in from both sides and meet in the centre of the aperture, thus traveling half the distance. Both blades have a velocity of approximately 1.2 m/s.

Another important property to characterise a shutter is the reproducibility of operation times. The histograms in Fig. 4 show the variation of the half-opening and half-closing times, i.e., the time ΔT to reach 50% of the total beam power after a change of the trigger signal. Our histograms display a low jitter time with no significant outliers. Filter blade B2 shows a positive (negative) skew of the distribution for the opening (closing) process with standard deviations of 60 μs (40 μs). The distributions of the timing of scissor blades B1 show the opposite skews with the standard deviations of 21 μs (24 μs). We speculate that this skewing is due a position dependent variation of the friction between blades, and the details of the skewing might vary from device to device. The difference in opening and closing times for the same blade might be due to a small misalignment between the center of the shutter aperture and the laser beam.

For a better comparison with other publications, we reduce the $1/e^2$-waist of the beam to 140 μm and repeat the measurements. 500 data sets for the opening and closing of blade B2 are represented by gray lines in Fig. 3. The reduced beam waist results in a reduction in the time taken for the photodiode signal to change between 5% and 95% of the total signal. For blades B1 (B2), we measure an opening duration of 137(7) μs [220(5) μs] and a closing duration of 100(4) μs [155(5) μs], which are in agreement with previous measurements and with the scaling of the beam waist.

In conclusion, we implemented and benchmarked a simple and robust shutter design based on a diaphragm shutter with multiple pairs of blades. A lightweight pair of blades is utilized for fast shutter operation while being protected by a slower and sturdier blade. The shutter can operate up to a continuous laser beam power of 1 W. For the opening and closing of fast blades B1, we measured delays of less than 3 ms, opening and closing durations of less than 800 μs (140 μs for the smaller waist) and a timing jitter of less than 25 μs. Our design goal for the shutter and driver units was to strongly reduce construction effort and costs while preserving robustness and high power operation.

Please see supplementary material for the software of the microcontroller and for the CAD-model files for the casing of the shutter.

We acknowledge the financial support by the EU through the Collaborative Project QuProCS (Grant Agreement No. 641277). A.D.C. acknowledges the financial support by EPSRC and SFC via the International Max-Planck Partnership. This work was supported in part by the EPSRC Programme Grant DesOEQ (Grant No EP/P009565/1).

[1]Examples for commercial products: Vincent Associates, ES6B Laser Shutter, VED24 Shutter Driver, or Thorlabs, SHB025 Shutter.
[2]S. Martínez, L. Hernández, D. Reyes, E. Gomez, M. Ivory, C. Davidson, and S. Aubin, Rev. Sci. Instrum. **82**, 046102 (2011).
[3]K. Singer, S. Jochim, M. Mudrich, A. Mosk, and M. Weidemüller, Rev. Sci. Instrum. **73**, 4402 (2002).
[4]L. Maguire, S. Szilagyi, and R. Sholten, Rev. Sci. Instrum. **75**, 3077 (2004).
[5]C. S. Adams, Rev. Sci. Instrum. **71**, 59 (2000).
[6]W. Bowden, I. R. Hill, P. E. G. Baird, and P. Gill, Rev. Sci. Instrum. **88**, 016102 (2017).
[7]Images show the Q1 diaphram shutter used for digital cameras ES65, ES70, ES71 by Samsung. This shutter and similar shutters by other manufacturers are available on ebay and aliexpress.
[8]Arduino Mega Microcontroller, and Arduino Motor-Shield by Adafruit, version 1. Inexpensive units can be found on ebay and aliexpress.
[9]Test conditions: power 1 W, wavelength 1064 nm, duration 1 hour.
[10]Photodiode, Thorlabs PDA100A-EC, bandwidth 2.4 MHz.
[11]I/O-Device, National Instruments USB-6366.

Appendix C

Publication: Interferometric measurement of micro-g acceleration with levitated atoms

New Journal of Physics
The open access journal at the forefront of physics

Deutsche Physikalische Gesellschaft DPG
IOP Institute of Physics

Published in partnership with: Deutsche Physikalische Gesellschaft and the Institute of Physics

OPEN ACCESS

RECEIVED
9 November 2018

REVISED
27 March 2019

ACCEPTED FOR PUBLICATION
23 April 2019

PUBLISHED
22 May 2019

PAPER

Interferometric measurement of micro-*g* acceleration with levitated atoms

A Di Carli, C D Colquhoun, S Kuhr and E Haller

University of Strathclyde, Department of Physics, Scottish Universities Physics Alliance (SUPA), Glasgow G4 0NG, United Kingdom

E-mail: elmar.haller@strath.ac.uk

Keywords: interferometry, BEC, metrology, acceleration measurement

Abstract

The sensitivity of atom interferometers is usually limited by the observation time of a free falling cloud of atoms in Earth's gravitational field. Considerable efforts are currently made to increase this observation time, e.g. in fountain experiments, drop towers and in space. In this article, we experimentally study and discuss the use of magnetic levitation for interferometric precision measurements. We employ a Bose–Einstein condensate of cesium atoms with tuneable interaction and a Michelson interferometer scheme for the detection of micro-*g* acceleration. In addition, we demonstrate observation times of 1s, which are comparable to current drop-tower experiments, we study the curvature of our force field, and we observe the effects of a phase-shifting element in the interferometer paths.

1. Introduction

Precision measurements with matter waves have shown tremendous advances over the last decades. In particular, atomic matter wave interferometers demonstrated a ground-breaking increase of the measurement precision of inertial effects, such as rotation [1, 2] and acceleration [3, 4]. In addition, atomic matter wave interferometers have been used to determine the fine-structure constant [5], Newton's gravitational constant [6, 7], and constraints on dark energy [8]. Similar to optical interferometers, atom interferometers split a matter wave into two parts, evolve the parts independently along different paths, and finally recombine the waves to form an interference pattern [9]. The interference pattern depends on the accumulated phase shift of the wave packets during the independent evolution, and the measured quantity is typically inferred from the shape and time evolution of the pattern. The sensitivity of interferometers increases with the accumulated phase shift, which again depends on the evolution time [10]. However, the evolution time of a free falling atom cloud is limited by Earth's gravitational acceleration in most experimental setups, and considerable efforts are made to increase the duration, e.g. in fountain experiments [11], drop towers [12, 13], parabolic flights [14, 15] and in space [16].

In this article, we employ magnetic levitation as a different method to extend the evolution time in earthbound laboratories. Magnetic levitation relies on the use of magnetic forces to cancel the gravitational acceleration and to levitate the particles in space. The method is well established for experiments with ultracold atoms [17–19], and its experimental implementation, i.e. using a pair of current-carrying coils, is significantly simpler and smaller than an atomic fountain apparatus or a drop-tower experiment. Here, we study the advantages and limitations of magnetic levitation for matter wave interferometry with the motional states of Bose–Einstein condensates (BECs), and we demonstrate that magnetic levitation can be employed to reach an expansion time of 1s, which is comparable to current drop-tower experiments [12]. Furthermore, we utilize magnetic levitation to create and to interferometrically measure micro-*g* acceleration in free expansion, and we show that the negligible center-of-mass motion of levitated atoms facilitates a direct study of phase-shifting elements in the interferometer paths.

Other interferometer schemes use external trapping potentials to prevent the gravitational acceleration by channelling the wave packets along magnetic [20, 21] and optical [22, 23] waveguides. External guiding and

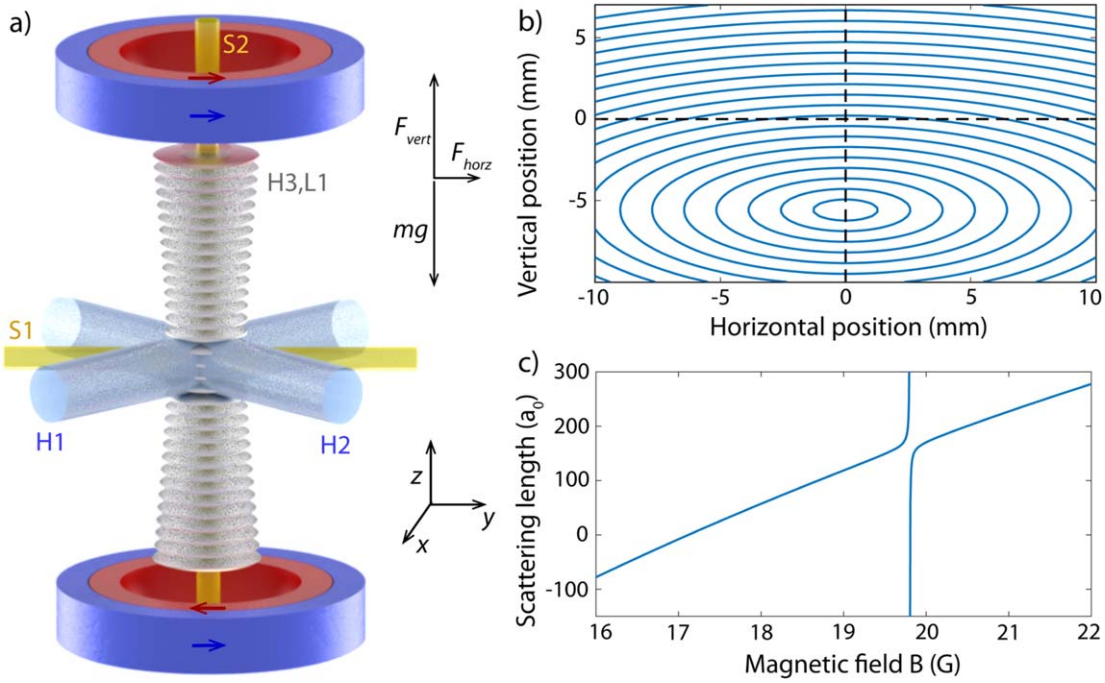

Figure 1. Experimental setup. (a) Magnetic field coils to control B_0 (blue, outer coils) and $\partial_z B$ (red, inner coils). Laser beams with small beam waists (S1, S2) and large beam waists (H1, H2, H3) trap the atoms, and a lattice L1 is used to split the wave packet during the interferometer sequence. Top and bottom coils have an inner diameter of 12 cm and a vertical separation of 6 cm. (b) Numeric simulation of the total magnetic field $|B(y, z)|$ for $\partial B/\partial z = 31.1$ G cm^{-1} and $B_0 = 17.4$ G, field lines indicate a magnetic field strength of 2–40 G. (c) Zero crossing of the scattering length at 17.1 G due to a broad Feshbach resonance for cesium atoms.

trapping potentials allow for equally long observation times [24], however, they introduce additional challenges. External potentials can cause spatially varying phase shifts and undesired excitations of the wave packets [23, 24], which limit the measurement precision. Our levitation scheme avoids trapping potentials along the gravitational axis, and it facilitates a tuneable scattering length for future studies of interaction effects in atom interferometers.

This article is structured as follows: section 2 provides an overview of our experimental setup, magnetic levitation scheme, and the use of a magnetic Feshbach resonance to control the interaction strength of cesium atoms. Section 3 is used to illustrate the interferometer scheme, and in section 4 we evaluate our measurement precision. Small changes to the magnetic levitation gradient allow us to create marginal accelerations of milli-g (section 4.1) and micro-g (section 4.2). An additional laser beam in one of the interferometer paths constitutes a phase-shifting element in section 4.3. In section 5, we measure features of the magnetic field distribution, such as the transversal curvature of the force field. Finally, using a combination of low interaction strength, low trapping frequencies, and magnetic levitation we demonstrate long expansion and observation times in section 6.

2. Magnetic levitation scheme and experimental apparatus

Our experimental apparatus is designed to independently control two parameters of the magnetic field. The magnetic field strength $B_0 = |\mathbf{B}(x, y, z)|$, at the position of the atoms ($x = y = z = 0$ mm) is used to tune atomic interactions by means of a broad magnetic Feshbach resonance for cesium atoms in the strong-field-seeking Zeeman state $|F = 3, m_F = 3\rangle$. We reduce the effects of interaction by setting B_0 to 17.4 G with an s-wave scattering length, a, of approximately 65 a_0 during the interferometer sequences (figure 1(c)), where a_0 is Bohr's radius. The second controlled parameter is the vertical gradient of the magnetic field, $\partial_z B$, which can be adjusted to exert a vertical pull on the atoms and cancel the gravitational acceleration. Due to the Zeeman effect, cesium atoms in the given state experience a vertical force that is proportional to the magnetic field gradient, $F_{\text{vert}} = \frac{3}{4}\mu_B \partial_z B$. For a mass m of a cesium atom, the levitation gradient can be calculated as $\partial_z B = 4\text{mg}/(3\mu_B) = 31.1$ G cm^{-1} [19, 25]. Here, μ_B represents the Bohr magneton and g the gravitational acceleration.

Our coil configuration is based on established designs [18, 19, 25]. It consists of two vertical coils above and below the atoms (inner diameter 12 cm, separation 6 cm), with 5 independently controllable sections. We generate B_0 and $\partial_z B$ by means of two vertical pairs of coil sections with co- and counter-propagating currents (outer and inner sections in figure 1(a)). Pairs of shim coils on each axis at distances of approximately 20 cm

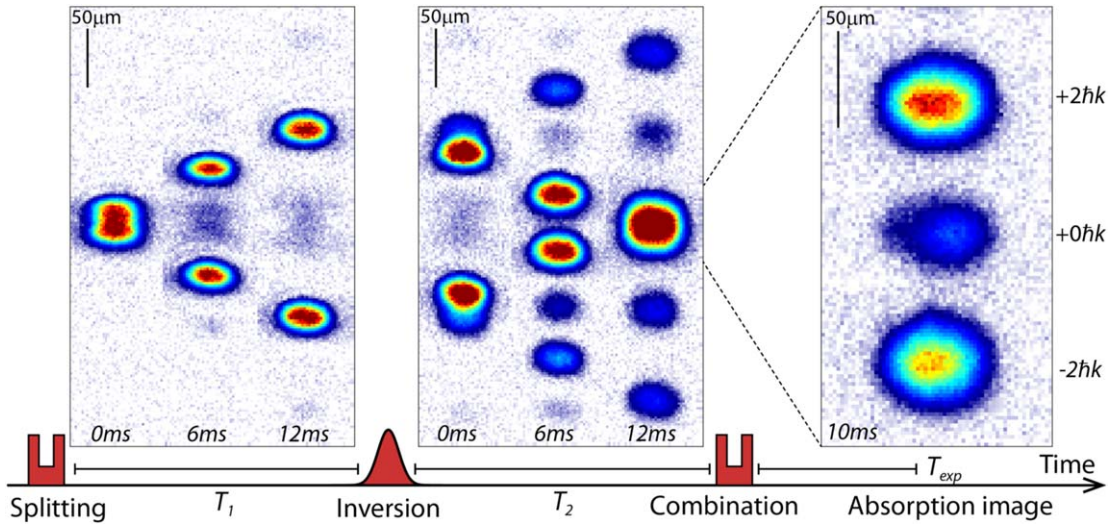

Figure 2. Interferometer scheme. Average of three absorption images of the matter waves after the splitting and the inversion pulses (left to right: $T_1 = T_2 = 0, 6, 12$ ms), and after the recombination pulse and an expansion time of 10 ms. All images are taken after an additional time-of-flight of 1 ms.

from the atoms allow for additional fine control of the magnetic field. Figure 1(b) shows the total magnetic field strength $B(y, z)$ in the vertical plane as calculated by a numerical simulation of our coils with finite wire elements. The field can be approximated by a magnetic quadrupole field with a shifted minimum at a few millimetres below the atom cloud. Experimentally, we determine B_0 by microwave spectroscopy and we optimize the levitation gradient $\partial_z B$ by varying the levitation current $I_{\rm lev}$ and minimizing position drifts of a BEC during free levitated expansion. Additional effects due to horizontal field curvature and limitations of the levitations scheme for precision measurements are discussed in section 5.

The matter waves of our interferometer are provided by Bose–Einstein condensates. In our setup, 2×10^9 cesium atoms are loaded from a 2D+ magneto optical trap (MOT) into a 3D MOT within 3 s. The atoms are cooled by degenerate Raman sideband cooling [26], and then sequentially transferred into two pairs of crossed optical dipole traps, the first with wavelength 1070 nm, total power 200 W, waists 700 μm, and the second with wavelength $\lambda = 1064.495(1)$ nm, power 400 mW, waists 90 μm (labels S1, S2 in figure 1(a)). Bose–Einstein condensation is reached after 6 s of evaporative cooling, and the density distribution of the atoms is detected by means of resonant absorption imaging after a variable time of levitated expansion and after 1 ms of unlevitated time-of-flight. One cooling cycle has a duration of 15 s and it is similar to [25].

We generate BECs of 2.5×10^5 atoms in the Zeeman sub-state $|F = 3,\ m_F = 3\rangle$ at a scattering length of $a = 210\ a_0$, trapped in the crossed laser beams S1, S2 with trap frequencies of $\omega_{x,\,y,\,z} = 2\pi\times(23.5,17.7,15.4)$ Hz. To reduce interactions during the interferometric measurement, we tune the scattering length to 65 a_0 and remove atoms by forced evaporation with a non-levitating magnetic field gradient. The BECs for the interferometer measurements in this work consist of approximately 8×10^4 atoms with a thermal fraction below 5%. Vibrational isolation and damping of the optical table is achieved by a pneumatic isolation system (Newport S-2000A).

3. Interferometer scheme

We employ a Michelson interferometer scheme that is based on three Kapitza–Dirac pulses with a standing light wave (figure 1(a), beam L1) [27]. The pulses change the motional states of the matter waves but leave the internal states of the atoms unchanged [28]. Our pulse sequence and the resulting motion of the matter wave packets are illustrated in figure 2. A first pulse splits the BEC into two wave packets with opposite momenta $\pm2\hbar k_L$. Here, $k_L = 2\pi/\lambda$ is the wavenumber of the lattice beam and $\hbar$ is Planck's constant. The wave packets propagate freely for an evolution time T_1 until we apply a second pulse that inverts the direction of the wave packets and changes their momentum by $4\hbar k_L$. A third pulse is used after an evolution time T_2 to recombine the two wave packets. It is identical to the first pulse and generates three wave packets with momenta $p_0 = 0, p_\pm = \pm\ 2\hbar k_L$. The relative population of the recombined wave packets depends on the acquired phase difference $\Delta\Phi$, resulting in a probability P_0 of finding an atom in the p_0 momentum mode

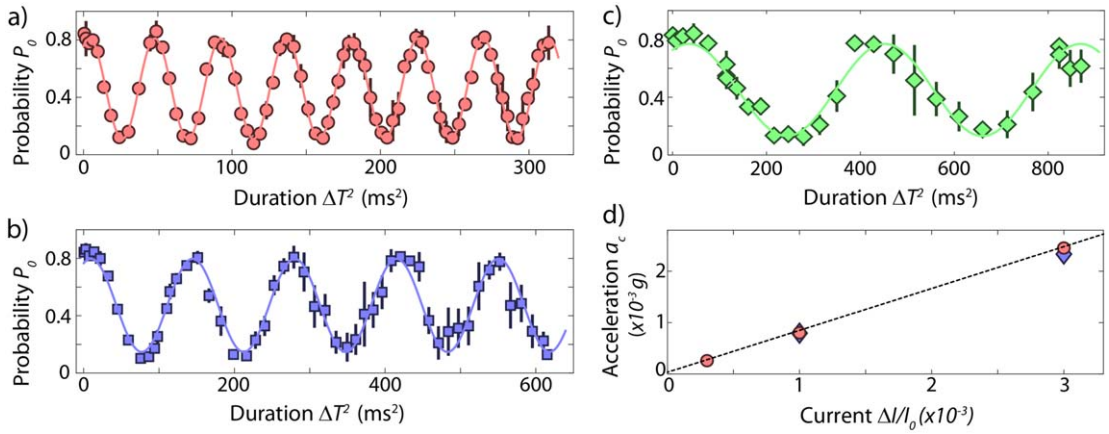

Figure 3. Interferometric measurement of milli-g accelerations. (a)–(c) Probability of observing atoms in the $0\hbar k_L$ momentum mode for increasing duration ΔT and gradient coil currents $\Delta I/I_{\mathrm{lev}}$ of (a) 0.003, (b) 0.001, (c) 0.0003. Solid lines represent fits to the data points using equations (1) and (2). (d) Comparison of the acceleration measurement with the interferometer scheme (red circles) and by the center-of-mass motion (blue diamonds). Error bars indicate one standard deviation of the data points.

$$P_0 = P_m + \frac{C}{2}\cos(\Delta\Phi). \tag{1}$$

Here, C is the interference contrast and P_m is the offset of the interference signal. We determine P_0 from the ratio of atoms in the p_0 mode to the total atom number in all momentum modes.

Several factors can contribute to the phase difference $\Delta\Phi$. For falling wave packets with spatially homogeneous acceleration a_c, the phase difference is directly proportional to the center-of-mass displacement Δz that was acquired during the total interferometer time $\Delta T = T_1 + T_2 + T_{\mathrm{pulse}}$. Here, T_{pulse} represents the total duration of the pulses. The total phase difference is given by [29]

$$\Delta\Phi = 2k_L\Delta z + \Phi_0 = 2k_L\frac{1}{2}a_c(\Delta T)^2 + \Phi_0, \tag{2}$$

with a term Φ_0 that accounts for additional phase shifts introduced during the initialization process, by noise such as lattice vibrations [15], or by interactions (see section 4.2).

The pulse sequence used in this experiment is based on previous work [20, 30, 31]. Our splitting and recombination pulses consist of three sub-pulses of lattice beam $L1$ with durations 60, 110 and 60 μs, and lattice intensities of 6.6 E_r, 0.2 E_r, and 6.6 E_r. Here, $E_r = \hbar^2k_L^2/(2m)$ is the recoil energy for cesium at a lattice wavelength of 1064 nm. Our inversion pulse has a Gaussian intensity distribution with a maximum of 17 E_r and a $1/e$-duration of 35 μs. The sub-pulse scheme allows us to reach a splitting efficiency of 96% of the atoms in the $\pm 2k_L$ modes, and we speculate that the limit of the efficiency is given by the thermal component of our BEC. The efficiency of the inversion pulse is lower, 83%, and residual atoms are clearly visible in figure 2 in the 0 and $\pm 2\hbar k_L$ modes. We suspect that this is due to the velocity selectivity of the inversion pulse and the velocity difference of the accelerated wave packets.

4. Interferometric measurements

4.1. Measuring milli-g acceleration

Our magnetic levitation scheme allows us to apply small forces to the atoms by changing the levitation current I_{lev} in the vertical coils with counter-propagating currents. We use this approach to characterize our interferometer setup for non-zero accelerations. After the preparation of the BEC we increase the current I in the coils, which create the magnetic field gradient, in 75 ms to the ratios I/I_{lev} of 1.003, 1.001, and 1.0003. The acceleration of the BEC is measured with our interferometer scheme. Figures 3(a)–(c) show the corresponding measurements of P_0 for varying evolution times ΔT^2 with $T_1 = T_2$. As expected, we observe sinusoidal oscillations of P_0, which are fitted using equations (1) and (2) (solid lines) to determine the accelerations a_c (red circles, figure 3(d)).

An independent measurement of a_c, based on the free motion of the BEC, is provided for comparison. We measure the shift of the center-of-mass position for an expansion time T_{exp} of an untrapped BEC in our magnetic field gradients, $z(T_{\mathrm{exp}}) = 1/2\, a_c\, T_{\mathrm{exp}}^2$, with a fit parameter a_c (blue diamonds, figure 3(d)). We find excellent agreement within two standard deviations between the two methods. However, the sensitivity of the free expansion measurement is limited by the observation time. Although our levitation scheme allows for very

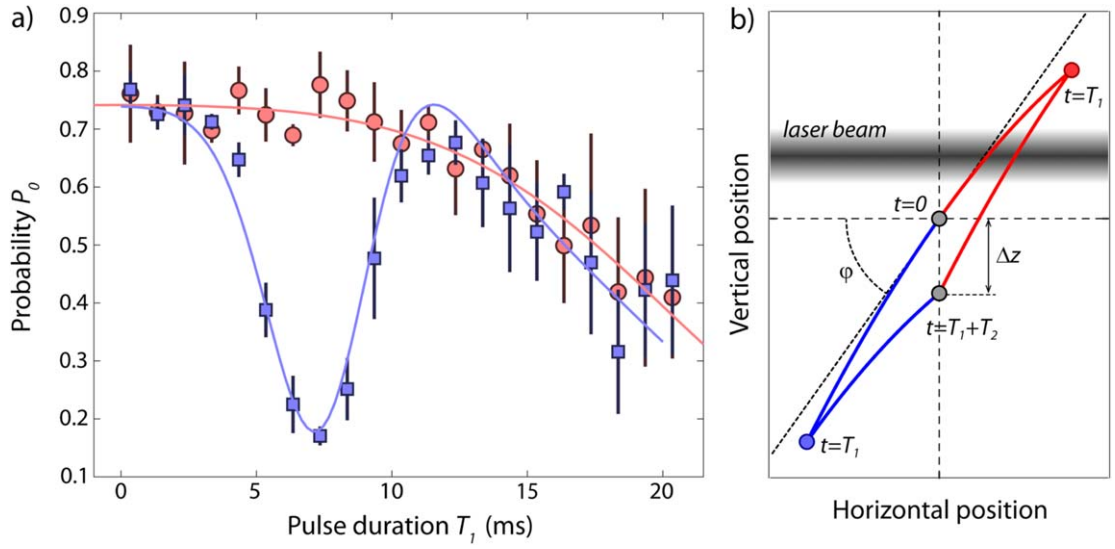

Figure 4. Interferometric measurement of micro-*g* accelerations and phase shifts due to a laser beam. (a) Probability of observing atoms in the $0\hbar k_L$ momentum mode vs T_1 for minimized acceleration of the atoms (red circles) and for an addition laser beam in the path of the upper wave packet (blue squares). Error bars indicate one standard deviation of the data points. (b) Illustration of the position of the wave packets and the additional laser beam during the pulse sequence. Angles and axes are not to scale in the illustration.

long observation times (section 6), it also induces a horizontal dispersion of the BEC in free space, which will be discussed in section 5. Here, we limit the observation time to 200 ms, which allows us to measure the acceleration for $I/I_{\mathrm{lev}} = 1.001, 1.003$, but not for 1.0003. The measurement results in figure 3(d) have relative uncertainties of approximately 4% for the free expansion measurement and 0.5% for the interferometric approach.

4.2. Measuring micro-*g* acceleration

In a second measurement, we utilize the interferometer scheme to minimize the forces on the atoms. We vary the currents in our shim coils and I_{lev} with the goal to maximize the oscillation period of P_0 (red circles figure 4). For optimal current values, we observe a slow drop of the value of P_0 from approximately 0.75 to 0.45 over $\Delta T^2 \approx 1600\ \mathrm{ms}^2$. This reduction is not necessarily caused by a residual acceleration of the wave packets, as it can also originate from dephasing mechanisms that are discussed in the next paragraph. However, fitting $P_0(t)$ with equation (1) provides an upper limit to the acceleration experienced by the atoms. We determine an upper limit for the acceleration of the atoms of $a_c = 70(10)\times10^{-6}\,g$. Atomic fountain interferometers facilitate the measurement of significantly smaller differential accelerations and reach staggering precisions of the order $\Delta g/g \sim 10^{-10}$ [3, 4, 32]. Our measurement, however, provides, to the best of our knowledge, the smallest absolute value for an acceleration that is measured directly with ultracold atom interferometry.

We estimate possible sources of measurement errors, fluctuations and dephasing mechanisms. Fluctuations of a homogeneous magnetic field will only slightly change the interaction strength of our BEC, but deviations of the magnetic field gradient can induce additional accelerations and alter the measurement result. In our setup, small deviations of the magnetic field gradient can occur as the wave packets move during an interferometer sequence away from the original position with optimized levitation. We estimate from our numerical magnetic field simulation that our coil design causes a relative increase of the field gradient of 2×10^{-6} for a vertical position shift of 50 μm. In addition, the quadratic Zeeman effect induces another deviation of the levitation force of 6×10^{-6} for the same position shift. As a result, the upper and lower wave packets experience a position-dependent acceleration, which increases the separation of the wave packets before the inversion pulse, and which reduces the convergence after the inversion pulse. Similar to our measurements in section 5, we would expect the final displacement of the wave packets to cause horizontal fringes in the absorption images, which we do not observe. As a result, we conclude that the vertical force gradients are negligible for the time scales of our interferometer.

In addition, the position-dependent magnetic field strength causes an almost linear change of the scattering length of approximately $\pm10\ a_0$ over 50 μm (see also section 6). As a result, the atoms in the upper wave packet experience a stronger interaction and faster phase evolution than atoms in the lower wave packet. Assuming constant densities and a linear change of the scattering length, we would expect the phase shift between the wave packets to increase with ΔT^2, and it would be difficult to distinguish this effect from a phase evolution due to

acceleration. However, in our setup the wave packets expand after release and the densities decrease strongly over a timescale of $1/\omega_{x,y,z} \approx 10$ ms. The position-dependent scattering length would result in a change of the oscillation frequencies within 10–15 ms in figures 3(a)–(c), which we do not observe, and we conclude that the phase shift due to a position-dependent scattering length is below our sensitivity for this measurement.

Fluctuations of the acceleration of the BEC can be caused by time-dependent changes of B_0 and $\partial_z B$, either due to external magnetic fields or due to the finite stability of the currents in our coils. We determine a current reproducibility of 1.4×10^{-6} by measuring the standard deviation of the current during the interferometer sequence over 60 consecutive cycles. For each cycle, the current measurement averages over 80 ms. We believe that the current reproducibility will eventually set the limiting precision for our interferometric measurements with levitated atoms. While it is in principle possible to increase the current reproducibility by 1–2 orders of magnitude by improving our current regulation electronics, it would be very hard to reach the precision of atomic fountain experiments. Nonetheless, we believe that magnetic levitation schemes will provide a valuable technological addition for precision measurements with ultracold atoms. Reducing gravitational acceleration to micro-g effectively removes the center-of-mass motion of the atoms, and it allows for a direct measurement of phase-shifts due to additional elements in the interferometer path. We demonstrate this approach in the next section by adding a focused laser beam in the upper path of the interferometer and by measuring its position-dependent phase shift on the atoms.

4.3. Detection of phase-shifting elements

Compared to fountain experiments, the center-of-mass motion of our wave packets is contained within a small spatial region of a few hundreds of μm, and it is straightforward to add additional phase shifting elements in the path of the wave packets. As a result, it is possible to use the levitated interferometer scheme to analyze additional potentials for the atoms with high precision. We demonstrate this approach by adding a horizontal laser beam (wavelength 1064 nm, waist 40 μm, power 29 μW) approximately 50 μm above the initial position of the atoms (figure 4(b)). This beam creates a Gaussian dipole potential with a depth of approximately 3 nK, and it introduces between the upper and lower wave packets a differential phase shift, which can be detected by the interferometer. In addition to a measurement of the AC Stark shift of the light field as in reference [33], our setup facilitates the study of the spatial dependence of the potential.

The effect of the laser beam on $P_0(t)$ is clearly visible in figure 4(a) when comparing the data sets with the beam (blue squares) and without the beam (red circles). For increasing duration T_1, the upper wave packet passes twice through the laser beam and it samples increasing spatial sections of the potential. We adjusted the power of the beam to create a single oscillation of the phase for a wave packet that fully transverses the beam, resulting in a minimum of $P_0(t)$ at an evolution time $T_1 = 7$ ms in figure 4(a).

Constant propagation velocities of the wave packets during the evolution times T_1 and T_2 make it easy to relate the time to the position of the atoms. We use a numerical model to integrate the phase shift of the upper wave packet in the dipole potential of the laser beam over the interferometer path $z(t)$ and include the unperturbed phase shift as measured in section 4.2. Fitting the model parameters to our data set (blue line figure 4(a)), we determine a beam position of 45(1) μm, a waist of 37(4) μm and a beam power of 25(3) μW, which are in excellent agreement with the independently measured values.

Our model neglects the spatial extent of the wave packets and we determine the phase shift at the center-of-mass position, whereas our experimental sequence averages over local phase shifts within the upper matter wave packet. Local phase shifts result in density variations in the profiles of the momentum modes in our absorption images, but measuring the total atom number in the momentum modes provides only the average phase shift of the wave packet.

5. Spatial curvature of the force field

Our magnetic field configuration does not only provide a vertical magnetic field gradient to levitate the atoms, but it also generates a weak, horizontal anti-trapping potential. This potential is a result of the spatial curvature of our quadrupole-like distribution of the magnetic field (see figure 1(b)). In this section, we demonstrate that the anti-trapping potential causes an additional interference pattern, which can be employed to measure the anti-trapping frequency or the angle between the lattice beam and the vertical field axis.

Within the quadrupole approximation it is possible to derive simple equations for the magnetic field and for the forces along the dashed horizontal line in figure 1(b) [19, 25, 34]

$$B_{\mathrm{horz}}(r) = B_0 + \frac{2}{9}\frac{m^2}{\mu_B}\frac{g^2}{B_0}r^2, \quad F_{\mathrm{horz}}(r) = m\alpha^2 r \quad \text{with} \quad \alpha = g\sqrt{\frac{m}{3\mu_B B_0}}. \tag{3}$$

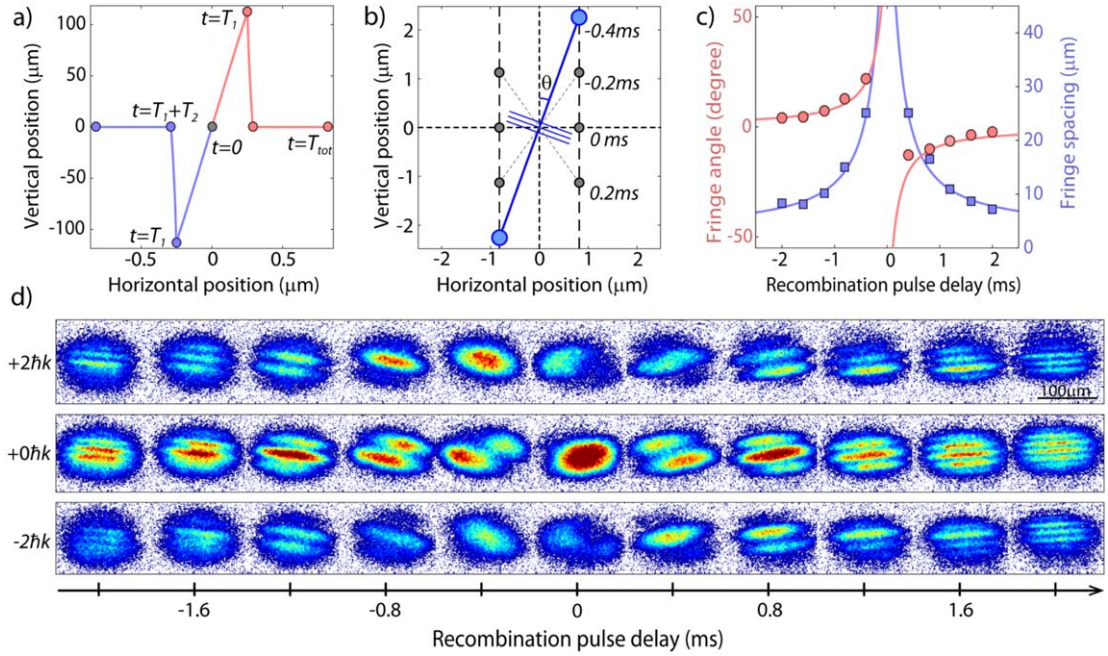

Figure 5. Effect of the force field curvature on the interference pattern. (a) Calculated interferometer path of the center-of-mass positions of the levitated wave packets with $\delta t = 0$ ms. (b) Center-of-mass positions of the two wave packets for $\delta t = -0.4$ ms (blue), $-0.2, 0, +0.2$ ms (grey). Blue parallel lines indicate the orientation of the interference pattern. (c) Fringe angles (red circles) and fringe spacings (blue squares) versus the delay δt of the recombination pulse, inferred from the data in *d*. Solid lines show our fit results for equation (6). (d) Absorption images for varying δt between -2.0 and 2.0 ms in steps of 0.4 ms. Common parameters are $\alpha = 2\pi\times 3.29$ Hz, $\varphi = 0.108°$, $T_1 = 20$ ms , $T_{\rm exp} = 30$ ms.

Here, $r = \sqrt{x^2 + y^2}$ is the horizontal displacement of the atoms from the origin. The quadratic scaling of $B_{\rm horz}(r)$ with r results in a weak, outwards-directed force in the horizontal plane. This anti-trapping effect can be associated with frequency α, and it causes a weak, position-dependent acceleration with a time-dependent horizontal position $r(t)$ and horizontal velocity $v_r(t)$ [35]:

$$\begin{aligned} r(t) &= r(0)\cosh(\alpha t) + \alpha^{-1} v_r(0)\sinh(\alpha t) \\ v_r(t) &= v_r(0)\cosh(\alpha t) + \alpha r_0 \sinh(\alpha t) \\ z(t) &= v_z(0)t + z(0). \end{aligned} \tag{4}$$

For this calculation we assume perfect levitation and linear vertical motion $z(t)$ during the interferometer sequence.

In an experimental setup there will always be a small angle φ between the lattice beam L1 and the vertical axis of the magnetic field, and a splitting pulse will always imprint a small velocity component $v_r(0) = (\hbar k_L/m)\sin(\varphi)$ along the horizontal direction. Consequently, a small horizontal displacement due to $v_r(0)$ results in an outwards-directed force on the wave packets in the anti-trapping potential, and in a finite horizontal displacement at the end of the interferometer sequence as illustrated in figure 5(a). The horizontal distance between the wave packets is typically two orders of magnitude smaller than the vertical displacement during the interferometer sequence, and both distances become comparable only in the proximity of the recombination pulse and during the expansion time. We illustrate the positions of the wave packets in figure 5(b) for small delay times of the recombination pulse $\delta t = T_2 - \mathrm{T}_1$ with $T_1 = 20$ ms. Depending on δt, the orientation of the blue line connecting the wave packets changes from almost vertical for $\delta t = \pm$ 0.4 ms to horizontal for $\delta t = 0$ ms. We define an angle θ, which is chosen to be positive clockwise and in the interval $[-90°, 90°]$, to indicate the orientation of the line, and we define $d(\delta t)$ to be the distance between the two wave packets.

In analogy to Young's double slit experiment [13, 36], the interference pattern of two wave packets at distance $d(\delta t)$ shows a fringe spacing $d_{\rm F}$ of

$$d_{\rm F} = \pi\hbar t/(md) + d_0. \tag{5}$$

Here, t is the total duration of the interferometer sequence with $t = T_1 + T_2 + T_{\rm pulse} - \delta\mathrm{t} + \mathrm{T}_{\rm exp}$, and $d_0 \geqslant 0$ is a constant phase shift that depends on the initial conditions such as the density distribution [37–39]. In our absorption images of the interfering wave packets for constant times T_1, $T_{\rm exp}$ and varying delay δt (figure 5(d)), interference fringes with varying separation $d_{\rm F}$ and angle θ are clearly visible for all momentum modes p_0, $p_\pm$.

From the evolution of the fringes as a function of time delay δt, we infer properties of the curvature α and the angle φ. We simultaneously fit the fringe spacing in equation (5) and the fringe angle θ with $\theta(\delta t) = \arctan(z(\delta t)/r(\delta t))$. Here $z(\delta t)$ and $r(\delta t)$ are the vertical and horizontal positions of the wave packets for varying δt. We integrate the center-of-mass motion of the wave packets in equation (4) with starting conditions $r(0) = z(0) = 0$ over all steps of the interferometer sequence to determine $z(\delta t)$ and $r(\delta t)$

$$\begin{aligned} z(\delta t) &= -v_z(0)\,\delta t \\ r(\delta t) &= \frac{v_r(0)}{\alpha}\cosh(\alpha T_{\mathrm{exp}})[\sinh(\alpha T_1)\cosh(\alpha(T_1+\delta t)) \\ &\quad + (\cosh(\alpha T_1) - 1)\sinh(\alpha(T_1+\delta t))] \\ &\quad + \frac{v_r(0)}{\alpha}\sinh(\alpha T_{\mathrm{exp}})([\sinh(\alpha T_1)\sinh(\alpha(T_1+\delta t)) \\ &\quad + (\cosh(\alpha T_1) - 1)\cosh(\alpha(T_1+\delta t))] + 1). \end{aligned} \tag{6}$$

Equations (6) contain two free parameters, the anti-trapping frequency α and the lattice angle φ, which can both be used to fit our data points in figure 5(c). We choose to constrain α and vary φ during the fitting procedure, as it is experimentally difficult to determine the laser beam angle with milliradian precision, and we independently measured α by observing center-of-mass oscillations of BECs in optical dipole traps. The fit results, represented by solid lines in figure 5(c), show good agreement with our data points, and we measure a lattice angle of $\varphi = 0.108(7)^\circ$ for $\alpha = 2\pi\times 3.29(5)$Hz.

Note that α scales with $1/\sqrt{B_0}$ in equation (3), and we can use larger values for B_0 to reduce the anti-trapping effect, e.g. by tuning the interaction strength with a broad magnetic Feshbach resonance at 800 G [40]. However, it will be difficult to reduce α significantly due to its square-root dependence on B_0. Instead, it is easier to compensate the anti-trapping effect with an additional dipole trap, as demonstrated in the next section.

6. Long expansion times

The sensitivity of an interferometric measurement increases with the evolution time of the wave packets [12], but even without the implementation of an interferometer scheme, long observation times of an expanding BEC facilitate a sensitive acceleration measurement. In this section, we demonstrate that magnetic levitation allows us to extend the expansion time of a BEC to 1 s, and we evaluate advantages and limitations of this scheme for precision measurements.

Typical expansion times for falling BECs are on the order of tens of milliseconds, often limited by the detection area of the imaging system, by the gravitational acceleration and by the expansion velocity of the gas. Usually, the expansion velocity of a quantum gas is not caused by the temperature of the gas but by repulsive interaction during the initial spreading. The current record for long observation times under milli-g acceleration is 1 s [12] with an expansion energy of 9 nK. The experiment was performed in a drop tower, and ballistic expansion was observed over approximately 500 ms, limited by stray magnetic fields.

In our experiment, we can reduce the interaction energy of the BEC by tuning the scattering length close to 0 a_0 by means of a magnetic Feshbach resonance (figure 1(c)). Further reduction of the expansion energy has been demonstrated by rapidly changing the scattering length from a positive value to 0 a_0 during trap release [25], but we refrain from using this trick to avoid excitations of the BEC during release. Our horizontal magnetic field curvature (section 5) introduces another limitation. During long observation times, the BEC expands horizontally into regions with a lower magnetic field gradient, causing a position-dependent sag of the density profile. In addition, small fluctuations of the horizontal magnetic field can break the symmetry and introduce slow horizontal drifts. We suppress both effects by keeping a vertical laser beam (H3 in figure 1(a)) on during the expansion time, thus observing free expansion only in the vertical direction.

In detail, we reduce the trap frequency by slowly transferring the atoms from a crossed dipole trap of beams S1, S2 to a crossed dipole trap of beams H1, H2, and H3 with final trap frequencies of $\omega_{x,y,z} = 2\pi\times(3.2, 3.4, 2.1)$ Hz, a scattering length of 15 a_0 and atom numbers of approximately 1.1×10^4. Excitations of the BEC during the transfer are suppressed by smooth changes of the potential with a total transfer duration of 4 s. After an additional settling time of 1 s we switch off the horizontal beams H1 and H2 and study the expansion of the BEC in the vertical beam H3. The vertical trapping frequency of the laser beam H3 is approximately 25 mHz, and the resulting fractional reduction of the expansion width after 1 s is 6×10^{-4}, which is far below our measurement sensitivity for the width of the BEC.

The expansion of the BEC in the vertical direction is clearly visible on absorption images (figure 6(a)) for expansion times 0–1000 ms, and horizontally-integrated 1D density profiles for expansion times of 400 ms and 600 ms are given in figures 6(c) and (d). Although the trapped BEC is initially only weakly confined with almost

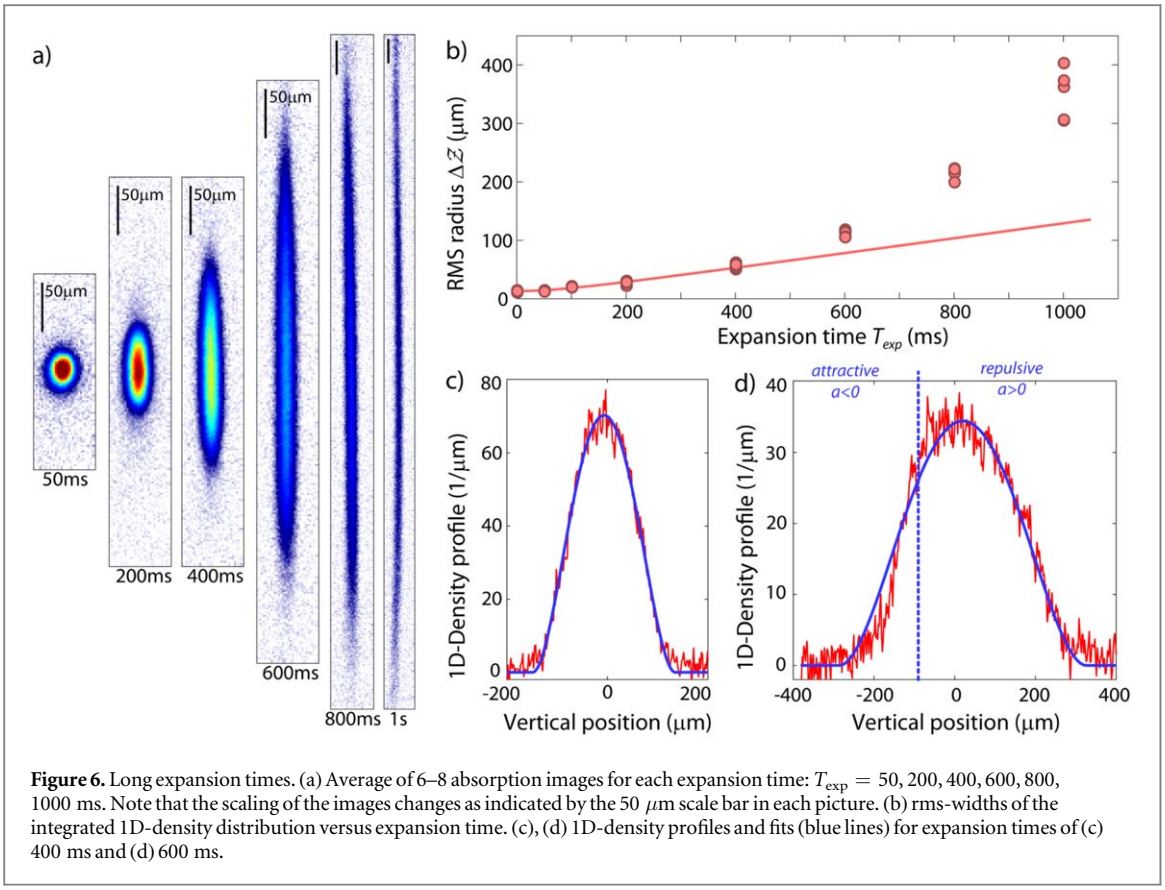

Figure 6. Long expansion times. (a) Average of 6–8 absorption images for each expansion time: $T_{\rm exp} = 50, 200, 400, 600, 800, 1000$ ms. Note that the scaling of the images changes as indicated by the 50 μm scale bar in each picture. (b) rms-widths of the integrated 1D-density distribution versus expansion time. (c), (d) 1D-density profiles and fits (blue lines) for expansion times of (c) 400 ms and (d) 600 ms.

symmetric trap frequencies, it changes dimensionality during the expansion process in the vertical beam. The density of the BEC decreases strongly during the vertical expansion, and the chemical potential becomes smaller than the transversal harmonic oscillator energy $\hbar\omega_{x,y}$ as required for a quasi-1D description [41]. As a result, we do not expect a shape-preserving spreading of the density distribution for a 1D expansion because the BEC passes through various interaction regimes as its density decreases [42, 43]. For illustration, we show a fit to the upper 80% of the 1D-density profiles $n(z)$ for the '3D cigar'-regime [44] (figure 6(c)), but we refrain from a complete analysis of the density profiles, which is beyond the scope of this article. Instead, we quantify the width of the expanding BEC with the root-mean-square (rms) radius $\Delta\mathcal{Z} = \left(\frac{1}{N}\int n(z)(z-\bar{z})^2\right)^{1/2}$ to provide an estimate of the expansion velocity (red circles figure 6(b)). Here, $\bar{z}$ is the center-of-mass position of the atoms. We observe an initial interaction driven expansion and a ballistic flight for $T_{\rm exp} \leqslant 400$ ms with an rms expansion velocity of $v_{\rm rms} = 0.128(5)$ mm s^{-1} and a corresponding kinetic energy of $mv_{\rm rms}^2/2 = 1/2\ k_B \times 260(20)$ pK. We note that this is the expansion energy of the BEC component, but not the initial temperature of the trapped quantum gas.

Similar to reference [12], we find an accelerated expansion for longer expansion times, $T_{\rm exp} > 500$ ms. We expect that the dominant source of the accelerated expansion is the curvature of our levitation gradient due to the quadratic Zeeman effect and due to our coil design, as discussed in section 4.2. However, the density profiles of the atoms on the absorption images indicate two other contributions. We observe small radial oscillations for long expansion times after release from the trap in the guiding beam H3 (see image $T_{\rm exp} = 1$ s in figure 6(a)). Those oscillations can couple to the vertical motion or they can distort the radially integrated density distribution. In addition, we observe asymmetric 1D density profiles $n(z)$ for $T_{\rm exp} > 500$ ms (figure 6(d)). The profiles show a slower expansion velocity for the lower part of the cloud than for the upper part. We assume that this effect is caused by the position-dependent scattering length due to our magnetic field gradient. The zero-crossing of a is indicated in figure 6(d) by a dashed blue line. This asymmetric expansion of a BEC with position-dependent scattering length requires further investigation that is beyond the scope of this article. We find small position fluctuations for long expansion times $T_{\rm exp} > 400$ ms of the BEC due to the finite current stability for the magnetic field gradient (section 4.2). For illustration, we re-centered the center-of-mass position in the absorption images for the averaging process in figure 6(a), but all other data in figures 6(b)–(c) results from the analysis of individual absorption images.

7. Conclusion

In conclusion, we experimentally studied the benefits and challenges of the use of magnetic levitation schemes for interferometric precision measurements with ultracold atoms. We employed a Michelson-type interferometer setup with BECs with tuneable interaction and magnetic levitation to demonstrate absolute acceleration measurements in the micro-*g* regime and we used the negligible center-of-mass motion of levitated atoms to study the position-dependent phase shift of the dipole potential of a focused laser beam. Moreover, we demonstrated expansion times of 1 s for a BEC, which is comparable to current drop tower experiments, and we used an extrapolation method for the fringe patterns to study the curvature of a force field that acts perpendicularly to our interferometer setup.

In our setup, limitations of the sensitivity arise from magnetic field fluctuations due to the current regulation, and from position-dependent interactions and magnetic field gradients. Although the sensitivity in our setup is significantly lower than the sensitivity of atomic fountain experiments, we believe that levitation schemes provide interesting features with the prospect of technical applications. Cancelling gravitational acceleration offers the possibility to combine long observation times with compact interferometer setups. Interesting applications are the measurement of local variations of electric and magnetic fields, and of mean field effects due to atomic interactions.

Acknowledgments

The authors would like to thank E Riis and PF Griffin for helpful discussions. We acknowledge financial support by the EU through the Collaborative Project QuProCS (Grant Agreement 641277). AdC acknowledges financial support by EPSRC and SFC via the International Max-Planck Partnership. The work was also supported in part by the EPSRC Programme Grant DesOEQ (Grant No EP/P009565/1).

References

[1] Gustavson T L, Bouyer P and Kasevich M A 1997 *Phys. Rev. Lett.* **78** 2046
[2] Dutta I, Savoie D, Fang B, Venon B, Garrido Alzar C L, Geiger R and Landragin A 2016 *Phys. Rev. Lett.* **116** 183003
[3] Peters A, Chung K Y and Chu S 1999 *Nature* **400** 849
[4] Hardman K S, Everitt P J, McDonald G D, Manju P, Wigley P B, Sooriyabandara M A, Kuhn C C N, Debs J E, Close J D and Robins N P 2016 *Phys. Rev. Lett.* **117** 138501
[5] Bouchendira R, Cladé P, Guellati-Khélifa S, Nez F and Biraben F 2011 *Phys. Rev. Lett.* **106** 080801
[6] Rosi G, Sorrentino F, Cacciapuoti L, Prevedelli M and Tino G M 2014 *Nature* **510** 518
[7] Prevedelli M, Cacciapuoti L, Rosi G, Sorrentino F and Tino G M 2014 *Phil. Trans. R. Soc.* A **372** 20140030
[8] Hamilton P, Jaffe M, Haslinger P, Simmons Q, Müller H and Khoury J 2015 *Science* **349** 849
[9] Cronin A D, Schmiedmayer J and Pritchard D E 2009 *Rev. Mod. Phys.* **81** 1051
[10] Debs J E, Altin P A, Barter T H, Döring D, Dennis G R, McDonald G, Anderson R P, Close J D and Robins N P 2011 *Phys. Rev.* A **84** 033610
[11] Chiow S-W, Kovachy T, Chien H-C and Kasevich M A 2011 *Phys. Rev. Lett.* **107** 130403
[12] van Zoest T *et al* 2010 *Science* **329** 1540
[13] Müntinga H 2013 *Phys. Rev. Lett.* **110** 093602
[14] Geiger R *et al* 2011 *Nat. Commun.* **2** 474
[15] Barrett B, Antoni-Micollier L, Chichet L, Battelier B, Lévèque T, Landragin A and Bouyer P 2016 *Nat. Commun.* **7** 13786
[16] Becker D *et al* 2018 *Nature* **562** 391
[17] Anderson M H, Ensher J R, Matthews M R, Wieman C E and Cornell E A 1995 *Science* **269** 198
[18] Han D J, DePue M T and Weiss D S 2001 *Phys. Rev.* A **63** 023405
[19] Weber T, Herbig J, Mark M, Nägerl H-C and Grimm R 2003 *Science* **299** 232
[20] Wang Y-J, Anderson D Z, Bright V M, Cornell E A, Diot Q, Kishimoto T, Prentiss M, Saravanan R A, Segal S R and Wu S 2005 *Phys. Rev. Lett.* **94** 090405
[21] Garcia O, Deissler B, Hughes K J, Reeves J M and Sackett C A 2006 *Phys. Rev.* A **74** 031601(R)
[22] McDonald G D, Kuhn C C N, Bennetts S, Debs J E, Hardman K S, Johnsson M, Close J D and Robins N P 2013 *Phys. Rev.* A **88** 053620
[23] Marti G E, Olf R and Stamper-Kurn D M 2015 *Phys. Rev.* A **91** 013602
[24] Burke J H T, Deissler B, Hughes K J and Sackett C A 2008 *Phys. Rev.* A **78** 023619
[25] Kraemer T, Herbig J, Mark M, Weber T, Chin C, Nägerl H-C and Grimm R 2004 *Appl. Phys.* B **79** 1013
[26] Kerman A J, Vuletic V, Chin C and Chu S 2000 *Phys. Rev. Lett.* **84** 439
[27] Gould P L, Ruff G A and Pritchard D E 1986 *Phys. Rev. Lett.* **56** 827
[28] Rasel E M, Oberthaler M K, Batelaan H, Schmiedmayer J and Zeilinger A 1995 *Phys. Rev. Lett.* **75** 2633
[29] Storey P and Cohen-Tannoudji C 1994 *J. Phys. II* **4** 1999
[30] Wu S, Wang Y-J, Diot Q and Prentiss M 2005 *Phys. Rev.* A **71** 043602
[31] Robertson B I, MacKellar A R, Halket J, Gribbon A, Pritchard J D, Arnold A S, Riis E and Griffin P F 2017 *Phys. Rev.* A **96** 053622
[32] Asenbaum P, Overstreet C, Kovachy T, Brown D D, Hogan J M and Kasevich M A 2017 *Phys. Rev. Lett.* **118** 183602
[33] Deissler B, Hughes K J, Burke J H T and Sackett C A 2008 *Phys. Rev.* A **77** 031604
[34] Sackett C A 2006 *Phys. Rev.* A **73** 013626
[35] Herbig J, Kraemer T, Mark M, Weber T, Chin C, Nägerl H-C and Grimm R 2003 *Science* **301** 1510
[36] Andrews M R, Townsend C G, Miesner H-J, Durfee D S, Kurn D M and Ketterle W 1997 *Science* **275** 637

[37] Wallis H, Röhrl A, Naraschewski M and Schenzle A 1997 *Phys. Rev.* A **55** 2109
[38] Röhrl A, Naraschewski M, Schenzle A and Wallis H 1997 *Phys. Rev. Lett.* **78** 4143
[39] Simsarian J E, Denschlag J, Edwards M, Clark C W, Deng L, Hagley E W, Helmerson K, Rolston S L and Phillips W D 2000 *Phys. Rev. Lett.* **85** 2040
[40] Berninger M, Zenesini A, Huang B, Harm W, Nägerl H-C, Ferlaino F, Grimm R, Julienne P S and Hutson J M 2013 *Phys. Rev.* A **87** 032517
[41] Petrov D S, Gangardt D M and Shlyapnikov G V 2004 *J. Phys. IV* **116** 5
[42] Öhberg P and Santos L 2002 *Phys. Rev. Lett.* **89** 240402
[43] Pedri P, Santos L, Öhberg P and Stringari S 2003 *Phys. Rev.* A **68** 043601
[44] Menotti C and Stringari S 2002 *Phys. Rev.* A **66** 043610

Appendix D

Publication: Excitation modes of bright matter-wave solitons

Editors' Suggestion

Excitation Modes of Bright Matter-Wave Solitons

Andrea Di Carli, Craig D. Colquhoun, Grant Henderson, Stuart Flannigan, Gian-Luca Oppo, Andrew J. Daley, Stefan Kuhr, and Elmar Haller

Department of Physics and SUPA, University of Strathclyde, Glasgow G4 0NG, United Kingdom

(Received 2 May 2019; revised manuscript received 18 July 2019; published 17 September 2019)

We experimentally study the excitation modes of bright matter-wave solitons in a quasi-one-dimensional geometry. The solitons are created by quenching the interactions of a Bose-Einstein condensate of cesium atoms from repulsive to attractive in combination with a rapid reduction of the longitudinal confinement. A deliberate mismatch of quench parameters allows for the excitation of breathing modes of the emerging soliton and for the determination of its breathing frequency as a function of atom number and confinement. In addition, we observe signatures of higher-order solitons and the splitting of the wave packet after the quench. Our experimental results are compared to analytical predictions and to numerical simulations of the one-dimensional Gross-Pitaevskii equation.

DOI: 10.1103/PhysRevLett.123.123602

The dispersionless propagation of solitary waves is one of the most striking features of nonlinear dynamics, with multiple applications in hydrodynamics, nonlinear optics, and broadband long-distance communications [1]. In fiber optics, one-dimensional (1D) "bright" solitons, i.e., solitons presenting a local electric field maximum with one-dimensional propagation, have been observed [2]. They exhibit a dispersionless flow and excitation modes such as breathing or higher-order modes [2–4]. Matter waves can also display solitary dispersion properties. Typically, bright matter-wave solitons are created in quasi-1D systems by quenching the particle interaction in a Bose-Einstein condensate (BEC) from repulsive to attractive [5]. Recent experiments demonstrated the collapse [6], collisions [7], reflection from a barrier [8], and the formation of trains [9–11] of bright solitons.

In this Letter, we experimentally study the excitation modes of a single bright matter-wave soliton. In previous studies, other dynamical properties have been observed, such as the center-of-mass oscillation of solitons in an external trap [7] and excitations following the collapse of attractive BECs [6,12]. Here, we probe the fundamental breathing mode of a single soliton by measuring its oscillation frequency and the time evolution of its density profile. In addition, we observe signatures of higher-order matter-wave solitons, which can be interpreted as stable excitations with periodic oscillations of the density profile and phase, or as a bound state of overlapping modes [3,13].

The shape-preserving evolution of a matter-wave soliton is due to a balancing of dispersive and attractive terms in the underlying 3D Gross-Pitaevskii equation (GPE) [14]. For quasi-1D systems with tight radial confinement, we can approximate the matter wave in the 3D GPE by the product of a Gaussian wave function for the radial direction and a function $f(z)$ for the longitudinal direction (see Ref. [15]). Depending on the ansatz for the Gaussian with either constant or varying radial sizes, $f(z)$ satisfies either the 1D GPE or the nonpolynomial Schrödinger equation [18]. We make reference to the analytical solutions of the 1D GPE in the Letter, but use both equations in our numerical simulations [15].

For the 1D GPE, an ansatz for the normalized longitudinal wave function $f(z)$ is of the form

$$f(z) = \frac{1}{\sqrt{2l_z}}\operatorname{sech}\left(\frac{z}{l_z}\right), \tag{1}$$

with a single parameter l_z that determines both the longitudinal size and the amplitude of the soliton. Solitons form with a value of l_z that minimizes the total energy and that provides a compromise between the kinetic and the interaction energies. This is illustrated in Fig. 1(b), which shows the energy of the wave packet for varying sizes l_z [19]. The kinetic energy provides a potential barrier for small l_z that prevents the collapse of the soliton, while its spreading is inhibited by the interaction energy, which increases for large l_z.

Even without an external longitudinal potential, the soliton is stable against small perturbations of l_z. In a way, a bright matter-wave soliton creates its own trapping potential, which defines its size and excitation modes. Variational methods provide accurate predictions of its size

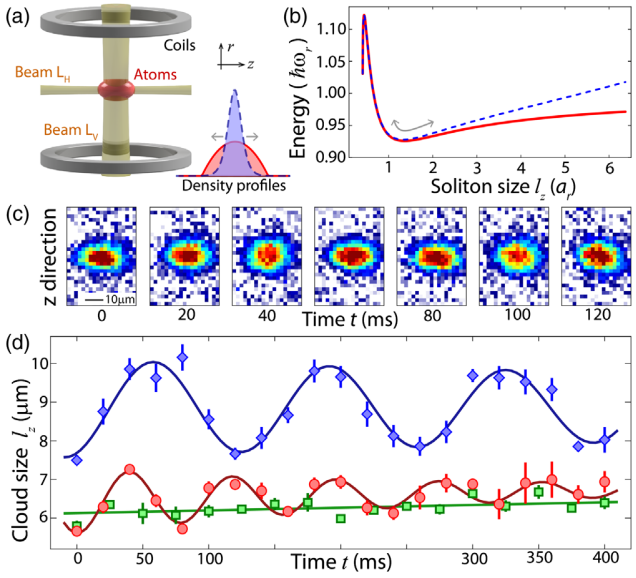

FIG. 1. Experimental setup and oscillation measurements. (a) Sketch of the experimental setup. Inset: Density profiles for a BEC (solid red line) and for a soliton (dashed blue line). (b) Total energy of a soliton, $a = -5.2a_0$, $\omega_r = 2\pi \times 95$ Hz, $N = 2000$, with an external trap, $\omega_z = 2\pi \times 5$ Hz (dashed blue line), and without external trap, $\omega_z = 0$ Hz (solid red line). (c) Absorption images after a free-expansion time of 16 ms [from dataset with circles in (d)], integrated density profile for $t =$ 60 ms (blue line) and fit (dashed red line). (d) Oscillations of a quantum gas after the quench procedure. Blue diamonds, quench of only ω_z for a BEC ($Q1$); red circles, additional interaction quench to create soliton ($Q3$); green squares, optimized quench parameters to minimize breathing of the soliton ($Q2$). Uncertainty intervals indicate ± 1 standard error.

at the energy minimum which can be calculated analytically [13,20] or numerically [19]. For the fundamental solution (order $n = 1$) of the 1D GPE with an atom number N, s-wave scattering length a, and radial trapping frequency ω_r, the size l_z corresponds to the healing length at the peak density of the soliton, i.e., $l_z^{(n=1)} = a_r^2/(N|a|)$ [13,19]. Here, $a_r = \sqrt{\hbar/(m\omega_r)}$ is the radial harmonic oscillator length. Small deviations of l_z close to the energy minimum lead to oscillations of the soliton size. We use those oscillations resulting from an initial mismatch of l_z to experimentally measure the self-trapping frequency of the soliton potential.

Our experimental starting point is a Bose-Einstein condensate of 500–2000 cesium (Cs) atoms in the state $|F = 3, m_F = 3\rangle$ at scattering length of $a = +7a_0$, where a_0 is Bohr's radius. The BEC is levitated by a magnetic field gradient, and it is confined by an optical dipole trap formed by the horizontal and vertical laser beams L_H and L_V [Fig. 1(a)]. An additional magnetic offset field allows us to tune the scattering length by means of a broad magnetic Feshbach resonance [21]. Details about our experimental setup, the levitation scheme, and the removal of atoms can be found in Refs. [15,22].

Our matter-wave solitons are confined to a quasi-1D geometry with almost free propagation along the horizontal direction and strong radial confinement of $\omega_r = 2\pi \times 95$ Hz provided by laser beam L_H. They are generated with a quench of the scattering length towards attractive interaction ($a_i \to a_f$), and by a reduction of the longitudinal trap frequency ($\omega_{z,i} \to \omega_{z,f}$). When changing a and ω_z independently, the quenches excite inward and outward motions, respectively. Usually, it is desirable to minimize the excitations of the soliton by matching the initial Thomas-Fermi density profile of the BEC closely to the density profile of the soliton [inset of Fig. 1(a)]. However, we deliberately mismatch the quench parameters to create breathing oscillations of the soliton in order to study its self-trapping potential. Quenches with different parameters are labeled by the symbols $Q1$–$Q7$ (see Ref. [15]). Following an evolution time t in quasi-1D and after a short period of 16 ms of expansion in free space, we take absorption images to determine the density profile of the atoms [Fig. 1(c)]. The cloud size $l_z(t)$ is determined by fitting the function $A(\mathrm{sech}(z/B))^2$ to the integrated 1D-density profiles with fit parameters A and B [15].

The response of the atomic cloud to the different quenches is presented in Fig. 1(d). We first quench only the longitudinal confinement by 25% to $\omega_{z,f} = 2\pi \times 4.3(2)$ Hz (quench $Q1$ in Ref. [15]) while keeping the repulsive interaction strength constant [Fig. 1(d), diamonds]. The BEC starts an outwards motion with an oscillation frequency of $2\pi \times 7.5(1)$ Hz $\approx \sqrt{3}\omega_{z,f}$ as expected for a BEC in the Thomas-Fermi regime [23,24]. In a second measurement, we additionally quench the interaction strength a_f to $-5.4a_0$ and increase $\omega_{z,i}$ to match the initial size of the BEC to the expected size of the soliton [$Q2$, Fig. 1(d), squares]. As a result, we observe almost dispersionless solitons with a linear increase of the cloud size of $0.7(3)$ μm/s [Fig. 1(d), green line]. Finally, we deliberately mismatch the initial size of the BEC by reducing $\omega_{z,i}$ ($Q3$), and generate small-amplitude oscillations of the soliton with a frequency ω_{sol} of $2\pi \times 12.8(4)$ Hz [Fig. 1(d), circles]. This breathing frequency of the soliton is significantly larger than any breathing frequency of a BEC or of noninteracting atoms, $2\omega_{z,f} = 2\pi \times 8.6(3)$ Hz. We observe no discernible oscillation in the radial direction after the quenches.

In a second experiment, we demonstrate that the breathing frequency ω_{sol} depends on the interaction term Na in the 1D GPE, a property typical of the nonlinear character of the soliton. We choose to change N, since the initial removal process is independent of the interaction quench, and we can study ω_{sol} without changing the quench protocol [$Q4$, Fig. 2(a), circles]. The measured values of ω_{sol} decrease for lower N, and they approach the breathing frequency $2\omega_{z,f}$ for noninteracting atoms in a harmonic trap [Fig. 2(a), dashed line].

We compare our experimental data points to two theoretical models. In a numerical simulation of the 1D

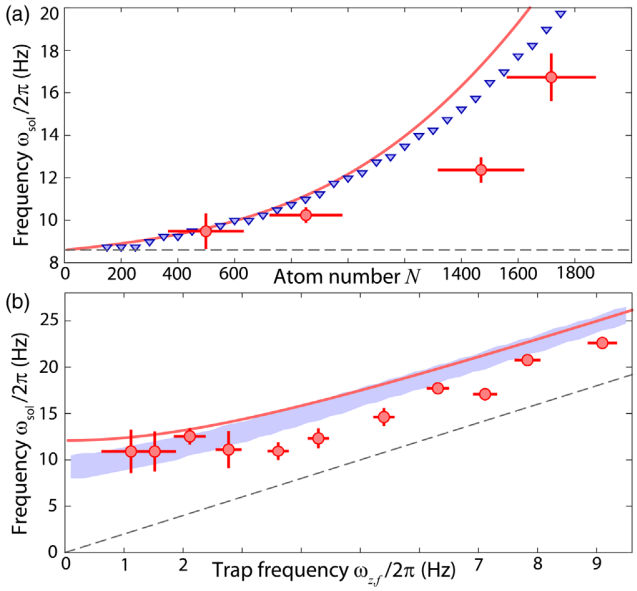

FIG. 2. Breathing frequency ω_{sol} of the soliton. (a) Atom number dependence ($Q4$). Red circles, experimental data; the uncertainty bars for the atom number indicate the standard deviation of N over the first 100 ms of each frequency measurement. Blue triangles, simulation of the 1D GPE [15]. Red line, analytical approximation [13,15]. Dashed gray line, oscillation frequency of a noninteracting gas, $2\omega_{z,f}$. (b) Dependence of ω_{sol} on the trap frequency ($Q5$). Red circles, experimental data points for $N \approx 1450$. Blue area, simulation of the 1D GPE for $N = 1300$–1500. Red line, analytical approximation. Dashed gray line, $2\omega_{z,f}$.

GPE, we use the ansatz in Eq. (1) to set the starting conditions, and we determine the breathing frequency from a spectral analysis of the time evolution of the wave function [15] [Fig. 2(a), triangles]. In addition, we use an analytical approximation for the breathing frequency (red line) calculated with a Lagrangian variational analysis at the energy minimum of the 3D GPE [13,15]. We find that both models agree well with the trend of the measurements of ω_{sol}, although our experimental data points are systematically lower for large N than our theoretical predictions. We speculate that this is due to nonharmonic contributions to the energy of the soliton on the breathing oscillations for finite oscillation amplitudes [Fig. 1(b)].

To determine the influence of the trapping potential, we measure the variation of ω_{sol} as we reduce the longitudinal trapping frequency $\omega_{z,f}$ ($Q5$). Two regimes of ω_{sol} can be identified in Fig. 2(b) for varying the values of $\omega_{z,f}$. For large values of $\omega_{z,f}$, the trap dominates the breathing of the soliton and ω_{sol} increases like $2\omega_{z,f}$. For small values of $\omega_{z,f}$, interactions dominate the breathing of the soliton and ω_{sol} reaches a constant value. This offset of the breathing frequency is a result of the "self-trapping" potential of a free soliton.

Again, we compare the experimental results with our theoretical model [Fig. 2(b), red line] and the numerical simulations of the 1D GPE. The blue band in Fig. 2(b) indicates the simulated frequencies for $N = 1300$ to $N = 1500$. The simulation predicts a lower breathing frequency for the free soliton than the analytical approximation, but all curves are within the uncertainly range of the experimental data.

External trapping potentials can in principle alter the soliton dynamics [7,25,26], causing, e.g., modulations of the soliton's tails due to residual nonautonomous terms of the 1D GPE in a harmonic potential [27]. For the following experiments, however, we employ trap frequencies that are significantly smaller than the observed oscillation frequencies of the soliton ($2\omega_z < \omega_{\mathrm{sol}}$) to decouple the influence of the trapping potential. In summary, for small-amplitude oscillations we find good agreement of ω_{sol} between our experimental results and analytical and numerical predictions based on the 1D GPE (and nonpolynomial Schrödinger equation [15]).

Breathing oscillations of l_z close to the equilibrium size are not the only possible excitation modes of solitons. The existence of higher-order solitons has been predicted in the nonlinear Schrödinger equation [3], and has been observed for optical solitons in silica-glass fibers [2,4]. A soliton of order n can be interpreted as a bound state of n strongly overlapping solitons [13]. By exploiting the equivalence of the nonlinear Schrödinger equation and 1D GPE, similar effects were later proposed for bright matter-wave solitons [13,28], where it was suggested that nth-order solitons can be generated by a rapid increase of the attractive interaction strength by a factor n^2. Similarly, our simulations of the 1D GPE show that higher-order solitons can be created for an increased initial size of the wave packet. An nth-order soliton forms for a sech-shaped wave function with an initial size $l_z^{(n)}$ that is the n^2 multiple of the healing length $l_z^{(1)}$, i.e., $l_z^{(n)} = n^2 l_z^{(1)}$ [15].

Within the 1D GPE theory, both creation methods result in the periodic development of multipeaked structures for higher-order solitons [3,29]; e.g., they create a sharp central peak with side wings for a second-order soliton [Fig. 3(a)] and a double peak for a third-order soliton [15]. Sizes and interaction quenches that do not fulfil the previous conditions lead to a "shedding" of the atomic density in the z direction. The wave packet oscillates and loses particles until its size and shape match the next (lower n) higher-order soliton [3]. For a second-order soliton, the predicted oscillation period $T^{(2)}$ is [13]

$$T^{(2)} = \frac{8\pi}{\hbar} m \left(\frac{a_r^2}{N|a_f|} \right)^2. \tag{2}$$

Recently, excitation modes of higher order have also been used as a test bed for various theoretical models beyond GP theory. The fragmentation of solitons with an increased initial width was predicted within the multiconfigurational time-dependent Hartree method for bosons

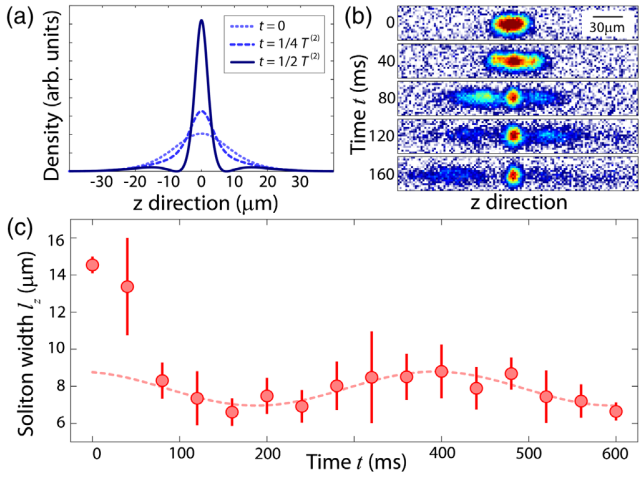

FIG. 3. Time evolution after a strong quench of interactions and trap frequency ($Q6$). (a) 1D GPE simulation of the density profiles for a second-order soliton with 1100 atoms, $a_f = -5.3a_0$, and with an oscillation period $T^{(2)}$ of 432 ms. (b) Absorption images at time t after the quench and after 11 ms of free expansion. (c) Time evolution of the measured width l_z of the central wave packet (red circles), sinusoidal fit with period 420(30) ms (dashed red line). The uncertainty intervals indicate ± 1 standard deviation.

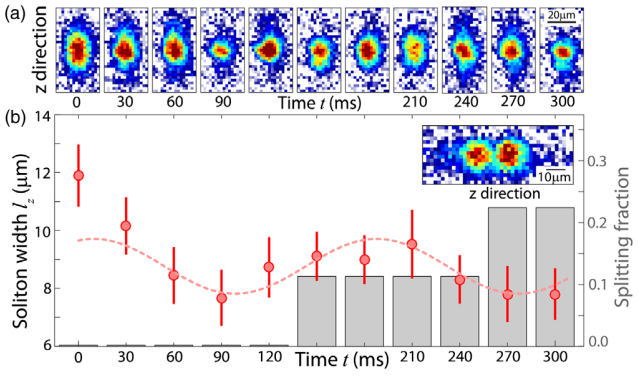

FIG. 4. Second-order soliton and splitting after the double quench $Q7$. (a) Absorption images at time t after the quench and after 7 ms of free expansion. (b) Time evolution of the measured width l_z of the central wave packet (red circles), sinusoidal fit with period 180(20) ms (dashed red line). The expected period from the 1D GPE simulations is 192 ms. The histogram counts the fraction of images showing a splitting of the wave function (9 repetitions per time step). Inset: Absorption image of a split matter wave for $t = 210$ ms.

[30] and critically discussed [31], and the influence of quantum effects on the dissociation process was investigated [32–34].

Here, we apply two different quench protocols to study the evolution of strongly excited solitons. Depending on the initial size and the quench parameters, we observe shedding and fragmentation of the wave packet, and we measure oscillation frequencies that indicate the creation of higher-order solitons. To demonstrate the effect of a strong quench of an elongated BEC, we increase a_i and reduce $\omega_{z,i}$ before ramping a and ω_z to $-5.3a_0$ and $2\pi \times 0.0(6)$ Hz in 13 ms ($Q6$). Our quench induces an initial spreading of the wave packet, followed first by a strong shedding of atoms, and then by the formation of a soliton that contains approximately $1/3$ of the initial atom number [Fig. 3(b)]. We determine the soliton width and find a slow oscillation of $l_z(t)$ with a frequency of $2\pi \times 2.4(2)$ Hz [Fig. 3(c)]. This frequency is significantly smaller than the expected breathing frequency of first-order solitons, $2\pi \times 6.0$ Hz, and it matches well to the expected frequency of $2\pi \times 2.3$ Hz for second-order solitons in Eq. (2).

Observing shedding and oscillations agrees with the predictions for higher-order solitons within the 1D GPE [3]; however, we find a strong dependence on details of the quench protocol and on the dynamical evolution during the quench. For a closer match to theoretical works [13], we implement a double-quench protocol, with a first quench to generate a soliton with weak attractive interaction, $a_f = -0.8a_0$, $\omega_f = 2\pi \times 1.4(2)$ Hz, and, after a settling time of 25 ms, a second quench of only the interaction strength, $a_f = -4.6a_0$ ($Q7$). Starting with approximately 2200 atoms, we observe no shedding but a small loss of 300 atoms during the first 60 ms. The vertical density profiles in our absorption images [Fig. 4(a)] resemble the expected profiles of a second-order soliton [Fig. 3(a)], and the vertical width of the wave packet oscillates with a frequency of $2\pi \times 5.6(6)$ Hz [Fig. 4(b)], which matches the expected frequency of $2\pi \times 5.2$ Hz for second-order solitons ($2\pi \times 13.2$ Hz for the first-order solitons).

For both measurements [Figs. 3(c) and 4(b)], a small percentage of absorption images show a splitting of the soliton into two fragments [inset of Fig. 4(b)], and they are omitted from the fitting procedure. Because of the destructive nature of our absorption images it is difficult to conclude on the evolution and on the cause of the splitting process. A double-peak structure in the density profile can indicate the generation of a third-order soliton, fragmentation due to quantum effects, or simply an insufficient technical control of our quench parameters. For our setup, the control of horizontal magnetic field gradients to avoid longitudinal accelerations is especially challenging [22]. The percentage of images that show a splitting of the wave packet increases for longer evolution times, and we indicate their fraction in Fig. 4(b) with a histogram.

In conclusion, we experimentally studied the creation and the excitation of breathing modes of bright matter-waves solitons in a quasi-one-dimensional geometry after a quench of interaction and longitudinal confinement. We measured the "self-trapping" frequency ω_{sol} for first-order solitons and its dependence on N and ω_z. For stronger excitations and for a double-quench protocol, we observed signatures of second-order solitons and the shedding and splitting of the wave function. Further measurements of the

splitting process and the damping of the oscillations due to shedding are necessary to distinguish technical fluctuations from higher-order solitons and fragmentation due to quantum effects [32–34].

The data used in this publication are openly available at the University of Strathclyde KnowledgeBase [35].

We thank L. D. Carr for helpful initial discussions during his visit. We acknowledge support by the EU through "QuProCS" (GA 641277) and the ETN "ColOpt" (GA 721465), and by the EPSRC Programme Grant "DesOEQ" (EP/P009565/1). A. D. C. acknowledges financial support by EPSRC and SFC via the IMPP. G. H. acknowledges support from a Carnegie Undergraduate Vacation Scholarship.

[1] M. P. T. Dauxois, *Physics of Solitons* (Cambridge University Press, Cambridge, England, 2006).
[2] L. F. Mollenauer, R. H. Stolen, and J. P. Gordon, Phys. Rev. Lett. **45**, 1095 (1980).
[3] J. Satsuma and N. Yajima, Prog. Theor. Phys. Suppl. **55**, 284 (1974).
[4] R. H. Stolen, W. J. Tomlinson, and L. F. Mollenauer, Opt. Lett. **8**, 186 (1983).
[5] L. Khaykovich, F. Schreck, G. Ferrari, T. Bourdel, J. Cubizolles, L. D. Carr, Y. Castin, and C. Salomon, Science **296**, 1290 (2002).
[6] E. A. Donley, N. R. Claussen, S. L. Cornish, J. L. Roberts, E. A. Cornell, and C. E. Wieman, Nature (London) **412**, 295 (2001).
[7] J. H. V. Nguyen, P. Dyke, D. Luo, B. A. Malomed, and R. G. Hulet, Nat. Phys. **10**, 918 (2014).
[8] A. L. Marchant, T. P. Billam, T. P. Wiles, M. M. H. Yu, S. A. Gardiner, and S. L. Cornish, Nat. Commun. **4**, 1865 (2013).
[9] K. E. Strecker, G. B. Partridge, A. G. Truscott, and R. G. Hulet, Nature (London) **417**, 150 (2002).
[10] J. H. V. Nguyen, D. Luo, and R. G. Hulet, Science **356**, 422 (2017).
[11] T. Mežnaršič, T. Arh, J. Brence, J. Pišljar, K. Gosar, Ž. Gosar, R. Žitko, E. Zupanič, and P. Jeglič, Phys. Rev. A **99**, 033625 (2019).
[12] S. L. Cornish, S. T. Thompson, and C. E. Wieman, Phys. Rev. Lett. **96**, 170401 (2006).
[13] L. D. Carr and Y. Castin, Phys. Rev. A **66**, 063602 (2002).
[14] F. Dalfovo, S. Giorgini, L. P. Pitaevskii, and S. Stringari, Rev. Mod. Phys. **71**, 463 (1999).
[15] See Supplemental Material at http://link.aps.org/supplemental/10.1103/PhysRevLett.123.123602 for additional information, which includes Refs. [16,17].
[16] S. Cowell, H. Heiselberg, I. E. Mazets, J. Morales, V. R. Pandharipande, and C. J. Pethick, Phys. Rev. Lett. **88**, 210403 (2002).
[17] P. J. Everitt, M. A. Sooriyabandara, M. Guasoni, P. B. Wigley, C. H. Wei, G. D. McDonald, K. S. Hardman, P. Manju, J. D. Close, C. C. N. Kuhn, S. S. Szigeti, Y. S. Kivshar, and N. P. Robins, Phys. Rev. A **96**, 041601(R) (2017).
[18] L. Salasnich, A. Parola, and L. Reatto, Phys. Rev. A **65**, 043614 (2002).
[19] N. G. Parker, S. L. Cornish, C. S. Adams, and A. M. Martin, J. Phys. B **40**, 3127 (2007).
[20] D. Longenecker and E. J. Mueller, Phys. Rev. A **99**, 053618 (2019).
[21] M. Berninger, A. Zenesini, B. Huang, W. Harm, H.-C. Nägerl, F. Ferlaino, R. Grimm, P. S. Julienne, and J. M. Hutson, Phys. Rev. A **87**, 032517 (2013).
[22] A. D. Carli, C. D. Colquhoun, S. Kuhr, and E. Haller, New J. Phys. **21**, 053028 (2019).
[23] C. Menotti and S. Stringari, Phys. Rev. A **66**, 043610 (2002).
[24] E. Haller, M. Gustavsson, M. J. Mark, J. G. Danzl, R. Hart, G. Pupillo, and H.-C. Nägerl, Science **325**, 1224 (2009).
[25] V. Serkin, A. Hasegawa, and T. Belyaeva, in *Odyssey of Light in Nonlinear Optical Fibers: Theory and Applications*, edited by K. Porsezian and R. Ganapathy (CRC Press, Boca Raton, FL, 2015), pp. 145–187.
[26] V. Serkin and T. Belyaeva, Optik (Stuttgart) **176**, 38 (2019).
[27] C. H. Tenorio, E. V. Vargas, V. N. Serkin, M. A. Granados, T. L. Belyaeva, R. P. Moreno, and L. M. Lara, Quantum Electron. **35**, 929 (2005).
[28] J. Golde, J. Ruhl, M. Olshanii, V. Dunjko, S. Datta, and B. A. Malomed, Phys. Rev. A **97**, 053604 (2018).
[29] O. Gamayun and M. Semenyakin, J. Phys. A **49**, 335201 (2016).
[30] A. I. Streltsov, O. E. Alon, and L. S. Cederbaum, Phys. Rev. Lett. **100**, 130401 (2008).
[31] J. G. Cosme, C. Weiss, and J. Brand, Phys. Rev. A **94**, 043603 (2016).
[32] C. Weiss and L. D. Carr, arXiv:1612.05545.
[33] V. A. Yurovsky, B. A. Malomed, R. G. Hulet, and M. Olshanii, Phys. Rev. Lett. **119**, 220401 (2017).
[34] K. L. Ng, B. Opanchuk, M. D. Reid, and P. D. Drummond, Phys. Rev. Lett. **122**, 203604 (2019).
[35] A. Di Carli, C. D. Colquhoun, G. Henderson, S. Flannigan, G.-L. Oppo, A. J. Daley, S. Kuhr, and E. Haller, Data for 'Excitation Modes of Bright Matter-Wave Solitons', University of Strathclyde KnowledgeBase, https://doi.org/10.15129/699a004b-fbf3-4f37-b2f3-9c1c97f44f0f.

Supplemental Material
"Excitation modes of bright matter-wave solitons"

Andrea Di Carli, Craig D. Colquhoun, Grant Henderson, Stuart Flannigan,
Gian-Luca Oppo, Andrew J. Daley, Stefan Kuhr, Elmar Haller
Department of Physics and SUPA, University of Strathclyde, Glasgow G4 0NG, Scotland, United Kingdom

I. EXPERIMENTAL METHODS

A. Controlling the atom number in the BEC

The solitons are confined to a quasi-1D geometry with almost free propagation along the horizontal direction and strong radial confinement of $\omega_r = 2\pi \times 95\,\mathrm{Hz}$ provided by laser beam L_H. In quasi-1D geometry, bright matter-wave solitons collapse for large densities and interactions [1], which for our typical experimental scattering length of approximately $-5\,a_0$ corresponds to a critical atom number of 2500 [2]. As a result, we need to strongly reduce the atom number to avoid collapse, modulation instabilities [3] and three-body loss [4] for a deterministic and reproducible creation of the soliton. We remove atoms with a small additional magnetic field gradient, which pushes the atoms over the edge of the optical dipole trap. Our precise control of magnetic field strengths allows us to reduce the atom number down to 200 atoms, with a reproducibility of ± 100 for 600 atoms and ± 350 for 4500 atoms, measured as the standard deviation of the atom number in 50 consecutive runs. A removal period of 4 s and smooth ramps of the magnetic field strength are necessary to minimize excitations of the BEC. Following the removal procedure we measure residual fluctuations of the width of the BEC below 3.5%.

B. Quench parameters

Several different quench protocols are employed for the measurements. The quenches are labeled by the symbols Q1-Q7 in the main article:

Q1 We quench only the trap frequency from $\omega_{z,i} = 2\pi \times 5.8(2)\,\mathrm{Hz}$ to $\omega_{z,f} = 2\pi \times 4.3(2)\,\mathrm{Hz}$ with a linear ramp of the laser power of beam L_V over 4 ms. Atom number $N \approx 1800$, constant interaction strength $a_i = +7\,a_0$, $\omega_r = 2\pi \times 95\,\mathrm{Hz}$.

Q2 In addition to the quench Q1 of the trap frequency, we also quench the interaction strength from $a_i = +7\,a_0$ to $a_f = -5.4\,a_0$ in 4 ms. We minimize oscillations of the width of the soliton by reducing the initial size of the BEC with $\omega_{z,i} = 2\pi \times 11.2(2)\,\mathrm{Hz}$. Atom number $N \approx 1800$, $\omega_{z,f} = 2\pi \times 4.3(2)\,\mathrm{Hz}$, $\omega_r = 2\pi \times 95\,\mathrm{Hz}$.

Q3 We mismatch the initial size of the BEC before the quench with $\omega_{z,i} = 2\pi \times 12.8(4)\,\mathrm{Hz}$ to generate small amplitude oscillations of the width of the soliton. Atom number $N \approx 1700$, $\omega_{z,f} = 2\pi \times 4.3(2)\,\mathrm{Hz}$, $\omega_r = 2\pi \times 95\,\mathrm{Hz}$.

Q4 Quench to determine the atom-number dependence of ω_{sol}. We vary the atom number N from 500 to 1700 for the measurement. $\omega_{z,f} = 2\pi \times 4.3(2)\,\mathrm{Hz}$, $a_i = +7\,a_0$, $a_f = -5.4\,a_0$, ramp duration 4 ms, $\omega_r = 2\pi \times 95\,\mathrm{Hz}$.

Q5 Quench to determine the dependence of ω_{sol} on the trap frequency $\omega_{z,f}$. We vary $\omega_{z,f}$ from approximately 1 Hz to 9 Hz. Smaller values of $\omega_{z,f}$ result in larger equilibrium sizes of the soliton, and we need to reduce the initial trap frequencies $\omega_{z,i}$ to keep the oscillation amplitudes comparable during the measurements. The typical difference between $\omega_{z,i}$ and $\omega_{z,f}$ is approximately 3 Hz. $N \approx 1500$, $a_f = -5.4\,a_0$, $\omega_r = 2\pi \times 95\,\mathrm{Hz}$.

Q6 Strong quench starting from an elongated BEC to excite higher-order oscillations and shedding. The ratio between the calculated initial Thomas-Fermi radius of the BEC and the expected width l_z of the soliton is 24. $a_i = 56\,a_0$, $a_f = -5.3\,a_0$, $\omega_{z,i} = 2\pi \times 4.9(2)\,\mathrm{Hz}$, $\omega_{z,f} = 2\pi \times 0.0(6)\,\mathrm{Hz}$, initial atom number $N \approx 3000$ drops to 1100 after shedding of atoms, quench duration 13 ms, $\omega_r = 2\pi \times 86\,\mathrm{Hz}$.

Q7 Double quench to create a stable soliton in step 1 and quench the scattering length by approximately a factor of 4 in step 2. Step 1: $\omega_{z,i} = 2\pi \times 4.9(2)\,\mathrm{Hz}$, $\omega_{z,f} = 2\pi \times 1.4(2)\,\mathrm{Hz}$, $a_i = 29\,a_0$, $a_f = -0.8\,a_0$, $\omega_r = 2\pi \times 86\,\mathrm{Hz}$, quench duration 15 ms, $N \approx 2200$. Settling delay of 25 ms between quenches. Step 2: reduce interaction strength in 2 ms to $a_f = -4.6\,a_0$, no change of other parameters.

C. Fit of density profiles

We employ absorption imaging to measure the 2D-density profile of the soliton, and we integrate over one radial axis to determine the 1D-density profile (red line in Fig. 5). The width l_z of the soliton in Eq. 1 of the main article, is determined by fitting the function $A(\mathrm{sech}(z/B))^2$, with fit-parameters A and B, to the integrated 1D-density profiles (dotted blue line in Fig. 5).

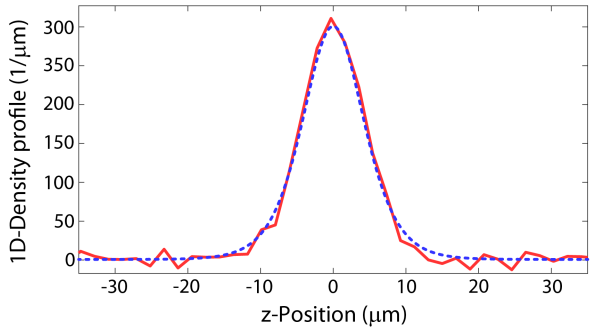

FIG. 5. 1D-density profile of a soliton. Red line: integrated density profile of the absorption image for $t = 60\,\mathrm{ms}$ in Fig. 1c (main article). Dotted blue line: fitted profile according to Eq. 1 in the main article.

II. THEORETICAL METHODS

A. The Model

The time evolution of the collective wave function of N atoms in an external potential with the 3D Gross-Pitaevski equation (GPE) for a time and space-dependent collective atomic wave-function, $\psi(\mathbf{r},t)$, is given by,

$$i\hbar\frac{\partial}{\partial t}\psi(\mathbf{r},t) = \left[-\frac{\hbar^2}{2m}\nabla^2 + V(\mathbf{r}) + gN\left|\psi(\mathbf{r},t)\right|^2\right]\psi(\mathbf{r},t), \tag{1}$$

where $g = 4\pi\hbar^2 a/m$, m is the atomic mass, and a is the two-body s-wave scattering length. This semi-classical field equation can be seen as a mean-field computation, and describes the dynamics of many weakly interacting particles at low temperatures when the condition $n|a|^3 \ll 1$ is satisfied [5], where n is the particle density. Our external potential $V(\mathbf{r})$ is given by a 3D (anisotropic) harmonic trap.

For tight radial trapping potentials, $\omega_r \gg \omega_z$, we can approximate the 3D wave function with a Gaussian solution in the radial directions and an arbitrary component, $f(z,t)$, in the longitudinal direction,

$$\psi(\mathbf{r},t) = f(z,t)\frac{1}{\sqrt{\pi}a_r\sigma(z,t)}\exp\left[-\frac{(x^2+y^2)}{2a_r^2\sigma(z,t)^2}\right], \tag{2}$$

where a_r is the harmonic oscillator length in the radial direction and $\sigma(z,t)$ is a free parameter that dictates the width of the radial wavefunction. Substituting this ansatz into the 3D-GPE, and integrating over the radial directions, we arrive at the so called non-polynomial Schödinger equation (NPSE) [6]

$$\begin{aligned} i\hbar\frac{\partial}{\partial t}f(z,t) = \Bigg[&-\frac{\hbar^2}{2m}\frac{\partial^2}{\partial z^2} + V(z) \\ &+ \frac{gN}{2\pi a_r^2\sigma(z,t)^2}\left|f(z,t)\right|^2 \\ &+ \frac{\hbar\omega_r}{2}\left(\sigma(z,t)^2 + \frac{1}{\sigma(z,t)^2}\right)\Bigg] f(z,t), \end{aligned} \tag{3}$$

where $\omega_r = \hbar/ma_r^2$. The condition for $\sigma(z,t)$ that minimizes the action functional integrated along the trajectories in phase space is [6],

$$\sigma(z,t)^2 = \sqrt{1 + 2aN|f(z,t)|^2}. \tag{4}$$

For $\sigma(z,t) = 1$, we obtain the ground state of a harmonic oscillator in the radial directions, and we recover the usual 1D-GPE

$$\begin{aligned} i\hbar\frac{\partial}{\partial t}f(z,t) = \Bigg[&-\frac{\hbar^2}{2m}\frac{\partial^2}{\partial z^2} + V(z) \\ &+ \frac{gN}{2\pi a_r^2}\left|f(z,t)\right|^2 + \hbar\omega_r\Bigg] f(z,t). \end{aligned} \tag{5}$$

We have numerically integrated Eqs 3 and 5 using the split-step Fourier transform method [7], where we exploit the fact that the kinetic and potential terms in the Hamiltonian are diagonal in momentum and real space, respectively.

III. SOLITON BREATHING FREQUENCY

In this section we explain how the numerical calculations of the soliton breathing frequencies shown in Fig. 2 of the main text were carried out. We begin with the order 1 soliton solution,

$$f(z,0) = \frac{1}{\sqrt{2l_z}}\,\mathrm{sech}\left(\frac{z}{l_z}\right) \tag{6}$$

where $l_z = a_r^2/(N|a_i|)$, and we have used $a_i = 7\,a_0$. We then evolve this initial state either with the 1D-GPE or NPSE to a simulation time of 4000 ms and evaluate the frequency spectrum of the oscillation of the soliton's centre ($z = 0$). In Fig. 6 we present the frequency spectrum for the GPE and a longitudinal frequency of $\omega_z = 2\pi \times 5\,\mathrm{Hz}$ and atom number $N = 1300$, which is characteristic of the behaviour for all other ω_z data points. We observe several prominent frequency modes in the signal, but we select the lowest frequency peak to compare to the experimental measurements, because the resolution in the experiment is restricted to low frequency components.

Fig. 6b also shows the results of the simulation using both the 1D-GPE and the NPSE (compare with Fig. 2 of the main text). We can see that for these atom numbers there are differences between the predictions of the 1D-GPE and NPSE. However these differences are small compared to the uncertainty in the experimental results.

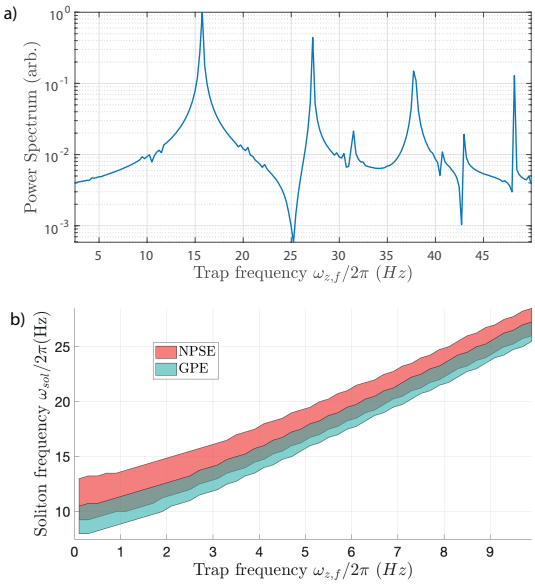

FIG. 6. Simulation results for the soliton breathing frequency, for comparison with Fig. 2 in the main text. (a) Frequency spectrum calculated using the 1D-GPE with a longitudinal frequency of $\omega_z = 2\pi \times 5\,\mathrm{Hz}$ and atom number $N = 1300$. (b) Breathing frequency (first peak in the spectrum as in a)) vs. trap frequency. $N \approx 1300 - 1500$ atoms, $a_f = -5.4\ a_0$ for the NPSE (red) and the GPE (green). The simulations were evolved in time to 4000 ms.

IV. HIGHER ORDER SOLITONS

Figure 7 shows numerical simulations of the 1D-GPE for the time evolution of second- and third-order solitons with initial sizes $l_z^{(2)}$ and $l_z^{(3)}$. Large initial soliton sizes lead to the periodic formation of local maxima and minima of the density profile. Striking characteristics of the time evolution are the periodic development of a sharp central peak with side wings for the second-order soliton (Fig. 7a,b), and the periodic formation of a broad double-peak structure for the third-order soliton (Fig. 7c,d).

We also simulate the time evolution of solitons with the same start conditions using the NPSE and analyse the results using the root mean square width of the wave packet for a quantitative comparison (Fig. 8)

$$z_{rms}(t) = \left(\frac{1}{N}\int n(z,t)(z-\bar{z})^2 dz\right)^{1/2}. \qquad (7)$$

Here, $\bar{z}$ is the mean position of the wave packet and $n(z,t)$ is the 1D-density. We observe small quantitative differences between the two equations but the overall behaviour is very similar.

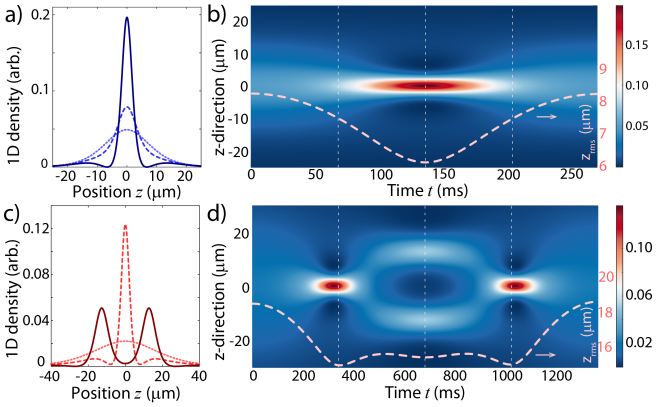

FIG. 7. Simulation of higher-order solitons in the 1D-GPE. Temporal snapshots (a) and temporal evolution (b) of the atomic density profile of an $n = 2$ soliton for $N = 1800$, $a = -3.7\,a_0$, $l_z^{(2)} = 10.2\ \mu\mathrm{m} = 4l_z^{(1)}$, and an oscillation period of $T_2 = 271\,\mathrm{ms}$. Temporal snapshots (c) and temporal evolution (d) of the atomic density profile of an $n = 3$ soliton for the same values of N, a, but with $l_z^{(3)} = 22.8\ \mu\mathrm{m} = 9l_z^{(1)}$, and with a period $T_3 = 1373\,\mathrm{ms}$. The density profiles in (a) and (c) are plotted at $t = 0$ (dotted lines), $t = 1/4T$ (dashed lines), $t = 1/2T$ (solid lines). The dashed lines in (b) and (d) display the temporal evolution of the size of the soliton wavepacket z_{rms} (right scale).

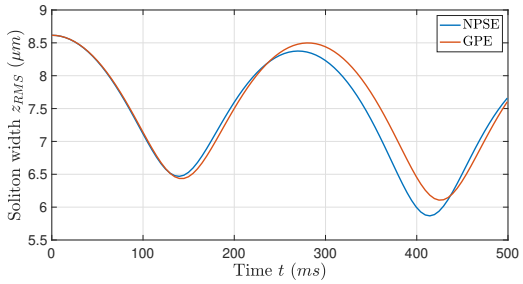

FIG. 8. Simulation results for the root mean square width of the soliton as it undergoes second order solitary behaviour, for the NPSE (blue) and the 1D-GPE (red). Here, $\omega_z = 0\,\mathrm{Hz}$, with an atom number $N = 1800$ and a scattering length $a = -3.7\ a_0$.

V. VARIATIONAL APPROACH FOR THE BREATHING FREQUENCY

In this section, we show how the longitudinal breathing frequency plotted in Fig. 2 of the main article can be determined from the variational ansatz for the soliton. For a cylindrical cigar-shaped potential the energy functional of Eq. 1 is given by [2, 8]

$$E[\psi] = \int d^3\mathbf{r}\left[\frac{\hbar^2}{2m}|\nabla\psi(\mathbf{r})|^2 + \frac{1}{2}m(\omega_r^2 r^2 + \omega_z^2 z^2)|\psi(\mathbf{r})|^2 + \frac{gN}{2}|\psi(\mathbf{r})|^4\right] \qquad (8)$$

The energy of a soliton can be determined with a variational method using the following ansatz for the wave function

$$\psi(r,z) = \frac{1}{\sqrt{2l_z}}\,\mathrm{sech}\left(\frac{z}{l_z}\right)\cdot\frac{1}{\sqrt{\pi l_r}}\exp\left(-\frac{r^2}{2l_r^2}\right), \quad (9)$$

where the transverse width l_r and longitudinal width l_z are the variational parameters [2, 8]. Combining Eqs. 8 and 9, and rescaling the variables by the transverse frequency ω_r, provides an equation for the normalized energy of the soliton [2]

$$\varepsilon_{GP} = \frac{1}{2\gamma_r^2} + \frac{\gamma_r^2}{2} + \frac{1}{6\gamma_z^2} + \frac{\pi^2}{24}\lambda^2\gamma_z^2 + \frac{\alpha}{3\gamma_r^2\gamma_z}, \quad (10)$$

with $\varepsilon_{GP} = E/\hbar\omega_r$, $\gamma_r = l_r/\sigma_r$, $\gamma_z = l_z/\sigma_r$, $\lambda = \omega_z/\omega_r$, $\alpha = Na/\sigma_r$, and $\sigma_r = \sqrt{\hbar/m\omega_r}$. We can simplify Eq. 10 for our system with weak interactions and strong transverse confinement by neglecting variations of the radial soliton size, i.e. $\gamma_r = 1$. The energy minimum is found by calculating the zero-crossing of the first derivative of Eq. 10 with respect to γ_z

$$\frac{\pi^2}{4}\lambda^2\gamma_z^4 + \sqrt{\zeta}\gamma_z - 1 = 0, \quad (11)$$

where $\alpha = -|\alpha| = -\sqrt{\zeta}$. Eq. 11 has been solved for an expulsive potential with $\omega_z^2 < 0$ [2]. Here, we provide the solution for a trapping potential with $\omega_z^2 > 0$. The longitudinal size of the soliton γ_z^* at the energy minimum is

$$\gamma_z^* = \frac{F}{\sqrt{\zeta}}, \quad (12)$$

with

$$F = -\sqrt{\frac{G}{2}} + \frac{1}{2}\sqrt{-2G + \frac{4\sqrt{2}}{\pi^2\sqrt{G}}\left(\frac{\zeta}{\lambda}\right)^2}, \quad (13)$$

where

$$G = \frac{\Delta}{\pi^{\frac{4}{3}}}\left(\frac{\zeta}{\lambda}\right)^{\frac{4}{3}} - \frac{4}{3\pi^{\frac{2}{3}}}\frac{1}{\Delta}\left(\frac{\zeta}{\lambda}\right)^{\frac{2}{3}}, \quad (14)$$

with

$$\Delta = \sqrt[3]{1 + \sqrt{1 + \frac{64\pi^2}{27}\left(\frac{\lambda}{\zeta}\right)^2}}. \quad (15)$$

In order to find the oscillation frequency ω_z of the soliton, the equations of motion for the variational parameters are determined with a Lagrangian variational analysis [2]

$$\left(\frac{\pi^2}{12}\right)\ddot{\gamma}_z = \frac{\gamma_z^{-3}}{3} - \frac{\pi^2}{12}\lambda^2\gamma_z + \frac{\alpha}{3}\gamma_z^{-2}, \quad (16)$$

where the time derivative is calculated with respect to the normalised time $\tau = \omega_r t$. Again, we have assumed that the radial size of the soliton is constant, i.e. $\gamma_r = 1$.

For small deviations of the soliton size from its equilibrium value, we can write the solution as $\gamma_z = \gamma_z^* + \delta\gamma_z$, where γ_z^* is the minimum given by Eq. 12 and $\delta\gamma_z$ is a small deviation. A linear expansion of Eq. 16 leads to the expression for the longitudinal breathing frequency

$$\omega_z = \omega_r\sqrt{\frac{12}{\pi^2}\left(\gamma_z^{*-4} + \frac{\pi^2}{12}\lambda^2 + \frac{2\alpha}{3}\gamma_z^{*-3}\right)}. \quad (17)$$

We compare our experimental measurements of the breathing frequency of the soliton to the predictions of Eq. 17 in Fig. 2 of the main article (red line).

[1] E. A. Donley, N. R. Claussen, S. L. Cornish, J. L. Roberts, E. A. Cornell, and C. E. Wieman, Nature **412**, 295 (2001).
[2] L. D. Carr and Y. Castin, Phys. Rev. A **66**, 063602 (2002).
[3] K. E. Strecker, G. B. Partridge, A. G. Truscott, and R. G. Hulet, Nature **417**, 150 (2002).
[4] P. J. Everitt, M. A. Sooriyabandara, M. Guasoni, P. B. Wigley, C. H. Wei, G. D. McDonald, K. S. Hardman, P. Manju, J. D. Close, C. C. N. Kuhn, S. S. Szigeti, Y. S. Kivshar, and N. P. Robins, Phys. Rev. A **96**, 041601 (2017).
[5] S. Cowell, H. Heiselberg, I. E. Mazets, J. Morales, V. R. Pandharipande, and C. J. Pethick, Phys. Rev. Lett. **88**, 210403 (2002).
[6] L. Salasnich, A. Parola, and L. Reatto, Phys. Rev. A **65**, 043614 (2002).
[7] P. Suarez, "An introduction to the split step fourier method using matlab." (2015).
[8] N. G. Parker, S. L. Cornish, C. S. Adams, and A. M. Martin, J. Phys. B At. Mol. Opt. Phys. **40**, 3127 (2007).

Bibliography

[1] S. Bose, "*Plancks Gesetz und Lichtquantenhypothese*", Z. Phys. **26**, 178 (1924).

[2] A. Einstein, "*Quantentheorie des einatomigen idealen Gases. II*". Sitzungber. Preuss. Akad. Wiss. **1**, 3 (1925).

[3] W. Ketterle, "*Twenty years of Atomic Quantum Gases: 1995-2015*", in "Universal Themes of Bose-Einstein Condensation", Cambridge University Press (2017).

[4] F. London, "*The λ-phenomenon of liquid helium and the Bose-Einstein degeneracy*", Nature **141**, 643 (1938).

[5] P. Kapitza, "*Viscosity of Liquid Helium Below the λ-Point*", Nature **141**, 3558 (1938).

[6] J. F. Allen, A. D. Misener, "*Flow of Liquid Helium II*", Nature **142**, 3597 (1938).

[7] N. Bogoliubov, "*On the Theory of Superfluidity*", J. Phys. **11**, 23 (1947).

[8] V. L. Ginzburg, and L. D. Landau, "*On the Theory of superconductivity*", Zh. Eksp. Teor. Fiz. **20**, 1064 (1950).

[9] O. Penrose, "*On the quantum mechanics of helium II*", Philos. Mag. **42**, 1373 (1951).

[10] O. Penrose, and L. Onsager, "*Bose-Einstein Condensation and Liquid Helium*", Phys. Rev. **104**, 576 (1956).

[11] T. Hänsch and A. Schawlow, "*Cooling of gases by laser radiation*", Optics Communications **13**, 68 (1975).

[12] S. Chu, L. W. Hollberg, J. E. Bjorkholm, A. Cable, and A. Ashkin, "*Three-dimensional viscous confinement and cooling of atoms by resonance radiation pressure*", Phys. Rev. Lett. **55**, 48 (1985).

[13] N. Masuhara, J. M. Doyle, J. C. Sandberg, D. Kleppner, T. J. Greytak, H. F. Hess, and G. P. Kochanski, "*Evaporative Cooling of Spin-Polarized Atomic Hydrogen*", Phys. Rev. Lett. **61**, 935 (1988).

[14] M. H. Anderson, J. R. Ensher, M. R. Matthews, C. E. Wieman, and E. A. Cornell, "*Observation of Bose-Einstein Condensation in a Dilute Atomic Vapor*", Science **269**, 198 (1995).

[15] K. B. Davis, M. O. Mewes, M. R. Andrews, N. J. van Druten, D. S. Durfee, D. M. Kurn, and W. Ketterle, "*Bose-Einstein Condensation in a Gas of Sodium Atoms*", Phys. Rev. Lett. **75**, 3969 (1995).

[16] C. C. Bradley, C. A. Sackett, J. J. Tollett, and R. G. Hulet, "*Evidence of Bose-Einstein condensation in an atomic gas with attractive interactions*", Phys. Rev. Lett. **75**, 1687 (1995).

[17] M. R. Andrews, C. G. Townsend, H.-J. Miesner, D. S. Durfee, D. M. Kurn and W. Ketterle, "*Observation of Interference Between Two Bose Condensates*", Science **275**, 637 (1997).

[18] I. Bloch, T. W. Hänsch, and T. Esslinger, "*Measurement of the spatial coherence of a trapped Bose gas at the phase transition*", Nature **403**, 166 (2000).

[19] M.-O. Mewes, M. R. Andrews, D. M. Kurn, D. S. Durfee, C. G. Townsend, and W. Ketterle, "*Output Coupler for Bose-Einstein Condensed Atoms*", Phys. Rev. Lett. **78**, 582 (1997).

[20] I. Bloch, T. Esslinger and T. W. Hänsch, "*Atom Laser with a cw Output Coupler*", Phys. Rev. Lett. **82**, 3008 (1999).

[21] M. Albiez, R. Gati, J. Fölling, S. Hunsmann, M. Cristiani, and M. K. Oberthaler, "*Direct Observation of Tunneling and Nonlinear Self-Trapping in a Single Bosonic Josephson Junction*", Phys. Rev. Lett. **95**, 010402 (2005).

[22] S. Levy, E. Lahoud, I. Shomroni and J. Steinhauer, "*The a.c. and d.c. Josephson effects in a Bose–Einstein condensate*", Nature **449**, 579 (2007).

[23] L. Deng, E. W. Hagley, J. Wen, M. Trippenbach, Y. Band, P. S. Julienne, J. E. Simsarian, K. Helmerson, L.Rolston, and W. D. Phillips, "*Four-wave mixing with matter waves*", Nature **398**, 218 (1999).

[24] M. R. Matthews, B. P. Anderson, P. C. Haljan, D. S. Hall, C. E. Wieman, and E. A. Cornell, "*Vortices in a Bose-Einstein Condensate*", Phys. Rev. Lett. **83**, 2498 (1999).

[25] K. W. Madison, F. Chevy, W. Wohlleben, and J. Dalibard, "*Vortex Formation in a Stirred Bose-Einstein Condensate*", Phys. Rev. Lett. **84**, 806 (2000).

[26] J. R. Abo-Shaeer, C. Raman, J. M. Vogels, and W. Ketterle, "*Observation of Vortex Lattices in Bose-Einstein Condensates*", Science **292**, 476 (2001).

[27] C. Raman, J. R. Abo-Shaeer, J. M. Vogels, K. Xu, and W. Ketterle, "*Vortex Nucleation in a Stirred Bose-Einstein Condensate*", Phys. Rev. Lett. **87**, 210402 (2001).

[28] S. Burger, K. Bongs, S. Dettmer, W. Ertmer, K. Sengstock, A. Sanpera, G. V. Shlyapnikov, and M. Lewenstein, "*Dark Solitons in Bose-Einstein Condensates*", Phys. Rev. Lett. **83**, 5198 (1999).

[29] J. Denschlag, J. E. Simsarian, D. L. Feder, C. W. Clark, L. A. Collins, J. Cubizolles, L. Deng, E. W. Hagley, K. Helmerson, W. P. Reinhardt, S. L. Rolston, B. I. Schneider, W. D. Phillips, "*Generating Solitons by Phase Engineering of a Bose-Einstein Condensate*", Science **287**, 97 (2000).

[30] K. E. Strecker, G. B. Partridge, A. G. Truscott, and R. G. Hulet, "*Formation and propagation of matter-wave soliton trains*", Nature **417**, 150 (2002).

[31] L. Khaykovich, F. Schreck, G. Ferrari, T. Bourdel, J. Cubizolles, L. D. Carr, Y. Castin, and C. Salomon, "*Formation of a Matter-Wave Bright Soliton*", Science **296**, 1290 (2002).

[32] I. Bloch, J. Dalibard, and W. Zwerger, "*Many-body physics with ultracold gases*", Rev. Mod. Phys. **80**, 885 (2008).

[33] M. Lewenstein, A. Sanpera, and V. Ahufinger, "*Ultracold Atoms in Optical Lattices. Simulating quantum many-body systems*", Oxford University Press, (2012).

[34] C. Chin, V. Vuletić, A. J. Kerman, S. Chu, E. Tiesinga, P. J. Leo, and C. J. Williams, "*Precision Feshbach spectroscopy of ultracold* Cs_2", Phys. Rev. A **70**, 032701 (2004).

[35] M. Berninger, A. Zenesini, B. Huang, W. Harm, H.-C. Nägerl, F. Ferlaino, R. Grimm, P. S. Julienne and J M. Hutson, "*Feshbach resonances, weakly bound molecular states, and coupled channel potentials for cesium at high magnetic fields*", Phys. Rev. A **87**, 032517 (2013).

[36] S. Inouye, M. R. Andrews, J. Stenger, H.-J. Miesner, D. M. Stamper-Kurn, and W. Ketterle, "*Observation of Feshbach resonances in a Bose-Einstein condensate*", Nature **392**, 151 (1998).

[37] J. L. Roberts, N. R. Clausen, J. P. Burke, C. H. Greene, E. A. Cornell, and C. E. Wieman, "*Resonant magnetic field control of elastic scattering in cold* ^{85}Rb", Phys. Rev. Lett. **81**, 5109 (1998).

[38] A. Marte, T. Volz, J. Schuster, S. Dürr, G. Rempe, E. G. M. van Kempen, and B. J. Verhaar, "*Feshbach resonances in rubidium 87: Precision measurement and analysis*", Phys. Rev. Lett. **89**, 283202 (2002).

[39] C. D'Errico, M. Zaccanti, M. Fattori, G. Roati, M. Inguscio, G. Modugno, and A. Simoni, "*Feshbach resonances in ultracold* ^{39}K", New J. Phys. **9**, 223 (2007).

[40] T. Kishimoto, J. Kobayashi, K. Noda, K. Aikawa, M. Ueda, and S. Inouye, "*Direct evaporative cooling of ^{41}K into a Bose-Einstein condensate*", Phys. Rev. A **79**, 031602 (2009).

[41] T. Weber, J. Herbig, M. Mark, H.-C. Nägerl and R. Grimm, "*Bose-Einstein Condensation of Cesium*", Science **299**, 232 (2003).

[42] T. Kraemer, M. Mark, P. Waldburger, J. G. Danzl, C. Chin, B. Engeser, A. D. Lange, K. Pilch, A. Jaakkola, H.-C. Nägerl, and R. Grimm, "*Evidence for Efimov quantum states in an ultracold gas of caesium atoms*", Nature **440**, 315 (2006).

[43] M. Gustavsson, E. Haller, M. J. Mark, J. G. Danzl, G. Rojas-Kopeinig, and H.-C. Nägerl, "*Control of Interaction-Induced Dephasing of Bloch Oscillations*", Phys. Rev. Lett. **100**, 080404 (2008).

[44] E. Haller, M. Gustavsson, M. J. Mark, J. G. Danzl, R. Hart, Guido Pupillo, H.-C. Nägerl, "*Realization of an Excited, Strongly Correlated Quantum Gas Phase*", Science **325**, 1224 (2009).

[45] M. J. Mark, E. Haller, K. Lauber, J. G. Danzl, A. Janisch, H. P. Büchler, A. J. Daley, and H.-C. Nägerl, "*Preparation and Spectroscopy of a Metastable Mott-Insulator State with Attractive Interactions*", Phys. Rev. Lett. **108**, 215302 (2012).

[46] A. Kastberg, W. D. Phillips, S. L. Rolston, R. J. C. Spreeuw, and P. S. Jessen, "*Adiabatic Cooling of Cesium to 700 nK in an Optical Lattice*", Phys. Rev. Lett. **74**, 1542 (1995).

[47] D. Boiron, A. Michaud, P. Lemonde, Y. Castin, and C. Salomon, "*Laser cooling of cesium atoms in gray optical molasses down to 1.1 μK*", Phys. Rev. A **53**, R3734(R) (1996).

[48] A. J. Kerman, V. Vuletić, C. Chin, and S. Chu, "*Beyond Optical Molasses: 3D Raman Sideband Cooling of Atomic Cesium to High Phase-Space Density*", Phys. Rev. Lett. **84**, 439 (2000).

[49] D. Guéry-Odelin, J. Söding, P. Desbiolles, and J. Dalibard, "*Is Bose-Einstein condensation of atomic cesium possible?*", Europhys. Lett. **44**, 25 (1998).

[50] J. Arlt, P. Bance, S. Hopkins, J. Martin, S. Webster, A. Wilson, K. Zetie, and C. J. Foot, "*Suppression of collisional loss from a magnetic trap*", J. Phys. B **31**, L321 (1998).

[51] D. J. Han, M. T. DePue, and D. S. Weiss, "*Loading and compressing Cs atoms in a very far-off-resonant light trap*", Phys. Rev. A **63**, 023405 (2001).

[52] J. Söding, D. Guéry-Odelin, P. Desbiolles, G. Ferrari, and J. Dalibard, "*Giant Spin Relaxation of an Ultracold Cesium Gas*", Phys. Rev. Lett. **80**, 1869 (1998).

[53] S. A. Hopkins, S. Webster, J. Arlt, P. Bance, S. Cornish, O. Maragó, and C. J. Foot, "*Measurement of elastic cross section for cold cesium collisions*", Phys. Rev. A **61**, 03270 (2000).

[54] T. Weber, J. Herbig, M. Mark, H.-C. Nägerl, and R. Grimm, "*Three-Body Recombination at Large Scattering Lengths in an Ultracold Atomic Gas*", Phys. Rev. Lett. **91**, 123201 (2003).

[55] A. M. Thomas, S. Hopkins, S. L. Cornish, and C. J. Foot, "*Strong evaporative cooling towards Bose-Einstein condensation of a magnetically trapped caesium gas*", J. Opt. B **5**, S107 (2003).

[56] A. Di Carli, C. D. Colquhoun, S. Kuhr, and E. Haller, "*Interferometric measurement of micro-g acceleration with levitated atoms*", New J. of Phys. **21**, 053028 (2019).

[57] A. Di Carli, C. D. Colquhoun, G. Henderson, S. Flannigan, G.-L. Oppo, A. J. Daley, S. Kuhr, E. Haller, "*Excitation Modes of Bright Matter-Wave Solitons*", Phys. Rev. Lett. **123**, 123602 (2019).

[58] A. Messiah, "*Quantum Mechanics*", Wiley, New York (1966).

[59] L. D. Landau and E. M. Lifshitz, "*Quantum Mechanics*", Pergamon Press, Oxford (1977).

[60] C. J. Joachain, "*Quantum Collision Theory, North Holland*", Amsterdam (1983).

[61] C. Cohen-Tannoudji and D. Guéry-Odelin, "*Advances in Atomic Physics. An Overview*", Singapore: World Scientific (2011).

[62] J. Dalibard, "*Collisional dynamics of ultra-cold atomic gases*", in: M. Inguscio, S. Stringari, and C. E.Wieman (Eds.), Proceedings of the International School of Physics - Enrico Fermi, 321, IOS Press (1999).

[63] A. J. Daley, "*Theoretical aspects of analogue quantum simulation with cold atoms*", in: T. Calarco, R. Fazio, and P. Mataloni (Eds.), Proceedings of the International School of Physics - Enrico Fermi, 55, IOS Press (2018).

[64] J. Weiner, V. S. Bagnato, S. Zilio, and P. S. Julienne, "*Experiments and theory in cold and ultracold collisions*", Rev. Mod. Phys. **71**, 1 (1999).

[65] J. Herbig, "*Quantum-Degenerate Cesium: Atoms and Molecules*", PhD thesis, Universität Innsbruck (2005).

[66] H. Feshbach, "*Unified theory of nuclear reactions*", Ann. Phys. AN.Y.B **5**, 357 (1958).

[67] H. Feshbach, "*Unified theory of nuclear reactions II*", Ann. Phys. AN.Y.B **19**, 287 (1962).

[68] U. Fano, "*Effects of configuration interaction on intensities and phase shifts*", Phys. Rev. **124**, 1866 (1961).

[69] W. C. Stwalley, "*Stability of spin-aligned hydrogen at low temperatures and high magnetic fields: New field dependent scattering resonances and predissociations*", Phys. Rev. Lett. **37**, 1628 (1976).

[70] E. Tiesinga, B. J. Verhaar, and H. T. C. Stoof, "*Threshold and resonance phenomena in ultracold ground-state collisions*", Phys. Rev. A **47**, 4114 (1993).

[71] J. M. Gerton, D. Strekalov, I. Prodan, and R. G. Hulet "*Direct observation of growth and collapse of a Bose-Einstein condesate with attractive interactions*", Nature **408**, 692 (2000).

[72] J. L. Roberts, N. R. Claussen, S. L. Cornish, E. A. Donley, E. A. Cornell, and C. E. Wieman, "*Controlled Collapse of a Bose-Einstein Condensate*", Phys. Rev. Lett. **86**, 4211 (2001).

[73] E. A. Donley, N, R. Claussen, S. L. Cornish, J. L. Roberts, E. A. Cornell, and C. E. Wieman, "*Dynamics of collapsing and exploding Bose-Einstein condensates*", Nature **412**, 295 (2001).

[74] C. A. Regal, C. Ticknor, J. L. Bohn, and D. S. Jin, "*Creation of ultracold molecules from a Fermi gas of atoms*", Nature **424**, 47 (2003).

[75] J. Herbig, T. Kraemer, M. Mark, T. Weber, C. Chin, H.-C. Nägerl, R. Grimm, "*Preparation of a Pure Molecular Quantum Gas*", Science **301**, 1510 (2003).

[76] M. Bartenstein, A. Altmeyer, S. Riedl, S. Jochim, C. Chin, J. H. Denschlag, and R. Grimm, "*Crossover from a Molecular Bose-Einstein Condensate to a Degenerate Fermi Gas*", Phys. Rev. Lett. **92**, 120401 (2004).

[77] C. A. Regal, M. Greiner, and D. S. Jin, "*Observation of Resonance Condensation of Fermionic Atom Pairs*", Phys. Rev. Lett. **92**, 040403 (2004).

[78] M. Zwierlein, C. A. Stan, C. H. Schunck, S. M. F. Raupach, A. J. Kerman, and W. Ketterle, "*Condensation of Pairs of Fermionic Atoms near a Feshbach Resonance*", Phys. Rev. Lett. **92**, 120403 (2004).

[79] N. B. Jørgensen, L. Wacker, K. T. Skalmstang, M. M. Parish, J. Levinsen, R. S. Christensen, G. M. Bruun, and J. J. Arlt, "*Observation of Attractive and Repulsive Polarons in a Bose-Einstein Condensate*", Phys. Rev. Lett. **117**, 055302 (2016).

[80] C. Chin, R. Grimm, P. S. Julienne, and E. Tiesinga, "*Feshbach resonances in ultracold gases*", Rev. Mod. Phys. **82**, 1225 (2010).

[81] A. J. Moerdijk, B. J. Verhaar, and A. Axelsson, "*Resonances in ultracold collisions of ^{6}Li, ^{7}Li, and ^{23}Na*", Phys. Rev. A **51**, 4852 (1995).

[82] V. Vuletić, A. J. Kerman, C. Chin, and S. Chu, "*Observation of low-field Feshbach resonances in collisions of cesium atoms*", Phys. Rev. Lett. **82**, 1406 (1999).

[83] C. Chin, V. Vuletić, A. J. Kerman, and S. Chu, "*High resolution Feshbach spectroscopy of cesium*", Phys. Rev. Lett. **85**, 2717 (2000).

[84] P. J. Leo, C. J. Williams, and P. S. Julienne, "*Collision Properties of Ultracold ^{133}Cs Atoms*", Phys. Rev. Lett. **85**, 2721 (2000).

[85] P. J. Leo, P. S. Julienne, F. H. Mies, and C. J. Williams, "*Collisional Frequency Shifts in ^{133}Cs Fountain Clocks*", Phys. Rev. Lett. **86**, 3743 (2001).

[86] M. Mark, F. Ferlaino, S. Knoop, J. G. Danzl, T. Kraemer, C. Chin, H.-C. Nägerl, and R. Grimm, "*Spectroscopy of ultracold trapped cesium Feshbach molecules*", Phys. Rev. A **76**, 042514 (2007).

[87] S. Knoop, M. Mark, F. Ferlaino, J. G. Danzl, T. Kraemer, H.-C. Nägerl, and R. Grimm, "*Metastable Feshbach Molecules in High Rotational States*", Phys. Rev. Lett. **100**, 083002 (2008).

[88] A. D. Lange, K. Pilch, A. Prantner, F. Ferlaino, B. Engeser, H.-C. Nägerl, R. Grimm, and C. Chin, "*Determination of atomic scattering lengths from measurements of molecular binding energies near Feshbach resonances*", Phys. Rev. A **79**, 013622 (2009).

[89] A. J. Leggett, "*Bose-Einstein condensation in the alkali gases: Some fundamental concepts*", Rev. Mod. Phys. **73**, 307 (2001).

[90] A. J. Leggett, "*Quantum Liquids: Bose Condensation and Cooper Pairing in Condensed-Matter Systems*", Oxford Graduate Texts (2006).

[91] C. N. Yang, "*Concept of Off-Diagonal Long-Range Order and the Quantum Phases of Liquid He and of Superconductors*", Rev. Mod. Phys. **34**, 694 (1962).

[92] D. W. Snoke and A. J. Daley, "*The Question of Spontaneous Symmetry Breaking in Condensates*", in Universal Themes of Bose-Einstein Condensation, Cambridge University Press (2017).

[93] E. A. Burt, R. W. Ghrist, C. J. Myatt, M. J. Holland, E. A. Cornell, and C. E. Wieman, "*Coherence, Correlations, and Collisions: What One Learns about Bose-Einstein Condensates from Their Decay*", Phys. Rev. Lett. **79**, 337 (1997).

[94] B. P. Anderson and M. A. Kasevich, "*Macroscopic Quantum Interference from Atomic Tunnel Arrays*", Science **282**, 1686 (1998).

[95] E. W. Hagley et al., "*Measurement of the Coherence of a Bose-Einstein Condensate*", Phys. Rev. Lett. **83**, 3112 (1999).

[96] C. J. Pethick and H. Smith, "*Bose-Einstein Condensation in Dilute Gases*", Cambridge University Press (2008).

[97] L. Pitaevskii and S. Stringari, "*Bose-Einstein Condensation and Superfluidity*", Oxford University Press (2016).

[98] F. Dalfovo, S. Giorgini, L. P. Pitaevskii, and S. Stringari, "*Theory of Bose-Einstein condensation in trapped gases*", Rev. Mod. Phys. **71**, 463 (1999).

[99] E. Gross, "*Structure of a quantized vortex in boson systems*", Nuovo Cimento **20**, 454 (1961).

[100] L. Pitaevskii, "*Vortex lines in an imperfect Bose gas*", Sov. Phys. JETP **13**, 451 (1961).

[101] C. D. Colquhoun, "*A New Apparatus for Experiments with Caesium Bose-Einstein Condensates*", PhD thesis, University of Strathclyde (2019).

[102] C. Wieman and T. W. Hänsch, "*Doppler-Free Laser Polarization Spectroscopy*", Phys. Rev. Lett. **36**, 1170 (1976).

[103] M. L. Harris, C. S. Adams, S. L. Cornish, I. C. McLeod, E. Tarleton, and I. G. Hughes, "*Polarization spectroscopy in rubidium and cesium*", Phys. Rev. A **73**, 062509 (2006).

[104] D. A. Steck, "*Cesium D line data*", Available online at https://steck.us/alkalidata/, (1998).

[105] A. S. Arnold, J. S. Wilson, and M. G. Boshier, "*A simple extended-cavity diode laser*", Rev. Sci. Instrum. **69**, 1236 (1998).

[106] W. Ketterle, D. S. Durfee, and D. M. Stamper-Kurn, "*Making, probing and understanding Bose-Einstein condensates*", in Proceedings of the International School of Physics Enrico Fermi Course CXL, IOS Press, Amsterdam, (1999).

[107] M. Greiner, "*Ultracold quantum gases in three-dimensional optical lattice potentials*", PhD thesis, Ludwig-Maximilians-Universität München (2003).

[108] T. Weber, "*Bose-Einstein Condensation of Optically Trapped Cesium*", PhD thesis, Universität Innsbruck (2003).

[109] H. J. Metcalf and P. van der Straten, "*Laser cooling and trapping*", Springer-Verlag (1999).

[110] C. J. Foot, "*Atomic Physics*", Oxford University Press, (2005).

[111] K. Dieckmann, R. J. C. Spreeuw, M. Weidemüller, and J. T. M. Walraven, "*Two-dimensional magneto-optical trap as a source of slow atoms*", Phys. Rev. A **58**, 3891 (1998).

[112] D.-J. Han, S. Wolf, S. Oliver, C. McCormick, M. T. DePue, and D. S.Weiss, "*3D Raman sideband cooling of cesium atoms at high density*", Phys. Rev. Lett. **85**, 724 (2000).

[113] P. Treutlein, K. Y. Chung, and S. Chu, "*High-brightness atom source for atomic fountains*", Phys. Rev. A **63**, 051401 (2001).

[114] J. Hu, A. Urvoy, Z. Vendeiro, V. Crépel, W. Chen, and V. Vuletić, "*Creation of a Bose-condensed gas of* ^{87}*Rb by laser cooling*", Science **358**, 1078 (2017).

[115] R. Grimm, M. Weidemüller, and Y. B. Ovchinnikov, "*Optical dipole traps for neutral atoms*", Adv. At. Mol. Opt. Phys. **42**, 95 (2000).

[116] P. W. H. Pinkse, A. Mosk, M. Weidemüller, M. W. Reynolds, T. W. Hijmans, and J. T. M. Walraven, "*Adiabatically changing the phase-space density of a trapped Bose gas*", Phys. Rev. Lett. **78**, (1997).

[117] D. M. Stamper-Kurn, H.-J. Miesner, A. P. Chikkatur, S. Inouye, J. Stenger, and W. Ketterle, "*Reversible Formation of a Bose-Einstein Condensate*", Phys. Rev. Lett. **81**, 2194 (1998).

[118] M. Kasevich, and S. Chu, "*Measurement of the gravitational acceleration of an atom with a light-pulse interferometer*", Appl. Phys. B **54**, 321 (1992).

[119] A. Peters, K. Y. Chung, and S. Chu, "*Measurement of gravitational acceleration by dropping atoms*", Nature **400**, 849 (1999).

[120] T. L. Gustavson, P. Bouyer and M. A. Kasevich, "*Precision Rotation Measurements with an Atom Interferometer Gyroscope*", Phys. Rev. Lett. **78**, 2046 (1997).

[121] A. Lenef, T. D. Hammond, E. T. Smith, M. S. Chapman, R. A. Rubenstein, and D. E. Pritchard, "*Rotation Sensing with an Atom Interferometer*", Phys. Rev. Lett. **78**, 760 (1997).

[122] D. S. Durfee, Y. K. Shaham, and M. A. Kasevich, "*Long-term stability of an Area-Reversible Atom-Interferometer Sagnac gyroscope*", Phys. Rev. Lett. **97**, 240801 (2006).

[123] B. Canuel, F. Leduc, D. Holleville, A. Gauguet, J. Fils, A. Virdis, A. Clairon, N. Dimarcq, C. J. Bordé, A. Landragin, and P. Bouyer, "*Six-Axis Inertial Sensor Using Cold-Atom Interferometry*", Phys. Rev. Lett. **97**, 010402 (2006).

[124] S. M. Dickerson, J. M. Hogan, A. Sugarbaker, D. M. S. Johnson, and M. A. Kasevich, "*Multiaxis Inertial Sensing with Long-Time Point Source Atom Interferometry*", Phys. Rev. Lett. **111**, 083001 (2013).

[125] I. Dutta, D. Savoie, B. Fang, B. Venon, C. L. Garrido Alzar, R. Geiger and A. Landragin, "*Continuous Cold-Atom Inertial Sensor with 1 nrad/sec Rotation Stability*", Phys. Rev. Lett. **116**, 183003 (2016).

[126] Y. Bidel, N. Zahzam, C. Blanchard, A. Bonnin, M. Cadoret, A. Bresson, D. Rouxel and M. F. Lequentrec-Lalancette, "*Absolute marine gravimetry with matter-wave interferometry*", Nat. Commun. **9**, 627 (2018).

[127] J. M. McGuirk, G. T. Foster, J. B. Fixler, M. J. Snadden, and M. A. Kasevich, "*Sensitive absolute-gravity gradiometry using atom interferometry*", Phys. Rev. A **65**, 033608(2002).

[128] G. Rosi, L. Cacciapuoti, F. Sorrentino, M. Menchetti, M. Prevedelli, and G. M. Tino, "*Measurement of the Gravity-Field Curvature by Atom Interferometry*", Phys. Rev. Lett. **114**, 013001 (2015).

[129] M. Horikoshi and K. Nakagawa, "*Dephasing due to atom-atom interaction in a waveguide interferometer using a Bose-Einstein condensate*", Phys. Rev. A **74**, 031602(R) (2006).

[130] F. Baumgärtner, R. J. Sewell, S. Eriksson, I. Llorente-Garcia, J. Dingjan, J. P. Cotter, and E. A. Hinds, "*Measuring Energy Differences by BEC Interferometry on a Chip*", Phys. Rev. Lett. **105**, 243003 (2010).

[131] S. Gupta, K. Dieckmann, Z. Hadzibabic, and D. E. Pritchard, "*Contrast Interferometry using Bose-Einstein Condensates to Measure h/m and α*", Phys. Rev. Lett. **89**, 140401 (2002).

[132] R. Bouchendira, P. Cladé, S. Guellati-Khélifa, F. Nez and F. Biraben, "*New Determination of the Fine Structure Constant and Test of the Quantum Electrodynamics*", Phys. Rev. Lett. **106**, 080801 (2011).

[133] J. B. Fixler, G. T. Foster, J. M. McGuirk, and M. Kasevich, "*Atom Interferometer Measurement of the Newtonian Constant of Gravity*", Science **315**, 74 (2007).

[134] G. Lamporesi, A. Bertoldi, L. Cacciapuoti, M. Prevedelli, and G. M. Tino, "*Determination of the Newtonian Gravitational Constant Using Atom Interferometry*", Phys. Rev. Lett. **100**, 050801 (2008).

[135] G. Rosi, F. Sorrentino, L. Cacciapuoti, M. Prevedelli, and G. M. Tino, "*Precision measurement of the Newtonian gravitational constant using cold atoms*", Nature **510**, 518 (2014).

[136] P. Hamilton, M. Jaffe, P. Haslinger, Q. Simmons, H. Müller and J. Khoury, "*Atom-interferometry constraints on dark energy*", Science **349**, 849 (2015).

[137] P. Haslinger, M. Jaffe, V. Xu, O. Schwartz, M. Sonnleitner, M. Ritsch-Marte, H. Ritsch and H. Müller, "*Attractive force on atoms due to blackbody radiation*", Nat. Phys. **14**, 257 (2018).

[138] D. W. Keith, M. L. Schattenburg, H. I. Smith, and D. E. Pritchard, "*Diffraction of atoms by a transmission grating*", Phys. Rev. Lett. **61**, 1580 (1988).

[139] O. Carnal, and J. Mlynek, "*Young's double slit experiment with atoms: A simple atom interferometer*", Phys. Rev. Lett. **66**, 2689 (1991).

[140] J. Fujita, M. Morinaga, T. Kishimoto, M. Yasuda, S. Matsui, and F. Shimizu, "*Manipulation of an atomic beam by a computer-generated hologram*", Nature **380**, 691 (1996).

[141] C. J. Bordé, "*Atomic interferometry with internal state labelling*", Phys. Lett. A **140**, 10 (1989).

[142] M. Kasevich, and S. Chu, "*Atomic interferometry using stimulated Raman transitions*", Phys. Rev. Lett. **67**, 181 (1991).

[143] P. E. Moskowitz, P. L. Gould, S. R. Atlas, and D. E. Pritchard, "*Diffraction of an atomic-beam by standing-wave radiation*", Phys. Rev. Lett. **51**, 370 (1983).

[144] P. L. Gould, G. A. Ruff, and D. E. Pritchard, "*Diffraction of atoms by light—The near-resonant Kaptiza-Dirac effect*", Phys. Rev. Lett. **56**, 827 (1986).

[145] P. J. Martin, B. G. Oldaker, A. H. Miklich, and D. E. Pritchard, "*Bragg scattering of atoms from a standing light wave*", Phys. Rev. Lett. **60**, 515 (1988).

[146] Y.-J. Wang, D. Z. Anderson, V. M. Bright, E. A. Cornell, Q. Diot, T. Kishimoto, M. Prentiss, R. A. Saravanan, S. R. Segal, and S. Wu, "*Atom Michelson Interferometer on a Chip Using a Bose-Einstein Condensate*", Phys. Rev. Lett. **94**, 090405 (2005).

[147] M. Fattori, C. D'Errico, G. Roati, M. Zaccanti, M. Jona-Lasinio, M. Modugno, M. Inguscio, and G. Modugno, "*Atom Interferometry with a Weakly Interacting Bose-Einstein Condensate*", Phys. Rev. Lett. **100**, 080405 (2008).

[148] J. E. Debs, P. A. Altin, T. H. Barter, D. Döring, G. R. Dennis, G. McDonald, R. P. Anderson, J. D. Close, and N. P. Robins, "*Cold-atom gravimetry with a Bose-Einstein condensate*", Phys. Rev. A **84**, 033610 (2011).

[149] B. I. Robertson, A. R. MacKellar, J. Halket, A. Gribbon, J. D. Pritchard, A. S. Arnold, E. Riis, and P F. Griffin, "*Detection of applied and ambient forces with a matter-wave magnetic gradiometer*", Phys. Rev. A **96**, 053622 (2017).

[150] S. Abend, M. Gebbe, M. Gersemann, H. Ahlers, H. Müntinga, E. Giese, N. Gaaloul, C. Schubert, C. Lämmerzahl, W. Ertmer, W. P. Schleich, and E. M. Rasel, "*Atom-Chip Fountain Gravimeter*", Phys. Rev. Lett. **117**, 203003 (2016).

[151] Y. Torii, Y. Suzuki, M. Kozuma, T. Sugiura, T. Kuga, L. Deng, and E. W. Hagley, "*Mach-Zehnder Bragg interferometer for a Bose-Einstein condensate*", Phys. Rev. A **61**, 041602(R) (2000).

[152] Y. Castin and J. Dalibard, "*Relative phase of two Bose-Einstein condensates*", Phys. Rev. A **55**, 4330 (1997).

[153] A. O. Jamison J. N. Kutz, and S. Gupta, "*Atomic interactions in precision interferometry using Bose-Einstein condensates*", Phys. Rev. A **84**, 043643 (2011).

[154] R. Jannin, P Cladé, and Guellati-Khélifa, "*Phase shift due to atom-atom interactions in a light-pulse atom interferometer*", Phys. Rev. A **92**, 013616 (2015).

[155] J. Close and N. Robins, "*Precision Measurement with Cold Atoms*", Physics **5**, 26 (2012).

[156] A. D. Cronin, J. Schmiedmayer and D. E. Pritchard, "*Optics and interferometry with atoms and molecules*", Rev. Mod. Phys. **81**, 1051 (2009).

[157] J. H. Denschlag, J. E. Simsarian, H. Häffner, C. McKenzie, A. Browaeys, D. Cho, K. Helmerson, S. L. Rolston and W. D. Phillips, "*A Bose-Einstein condensate in an optical lattice*", J. Phys. B **35**, 3095 (2002).

[158] H. Müller, S.-W. Chiow, S. Herrmann, and S. Chu, "*Atom Interferometers with Scalable Enclosed Area*", Phys. Rev. Lett. **102**, 240403 (2009).

[159] P. Cladé, S. Guellati-Khélifa, F. Nez, and F. Biraben, "*Large Momentum Beam Splitter Using Bloch Oscillations*", Phys. Rev. Lett. **102**, 240402 (2009).

[160] S.-W. Chiow, T. Kovachy, H.-C. Chien and M. A. Kasevich, "*102ℏk Large Area Atom Interferometers*", Phys. Rev. Lett. **107**, 130403 (2011).

[161] T. van Zoest et al., "*Bose-Einstein condensation in microgravity*", Science **329**, 1540 (2010).

[162] H. Müntinga et al., "*Interferometry with Bose-Einstein Condensates in Microgravity*", Phys. Rev. Lett. **110**, 093602 (2013).

[163] R. Geiger et al., "*Detecting inertial effects with airborne matter-wave interferometry*", Nat. Commun. **2**, 474 (2011).

[164] B. Barrett, L. Antoni-Micollier, L. Chichet, B. Battelier, T. Lévèque, A. Landragin and P. Bouyer, "*Dual matter-wave inertial sensors in weightlessness*", Nat. Commun. **7**, 13786 (2016).

[165] A. Cho, "*Trapped in orbit*", Science **357**, 986 (2017).

[166] D. Becker et al., "*Space-borne Bose–Einstein condensation for precision interferometry*", Nature **562**, 391 (2018).

[167] S. Gupta, A. Leanhardt, A. Cronin, and D. E. Pritchard, "*Coherent manipulation of atoms with standing light waves*", C. R. Acad. Sci. **2**, 479 (2001).

[168] P. L. Kapitza and P. A. M. Dirac, "*The reflection of electrons from standing light waves*", Mathematical Proceedings of the Cambridge Philosophical Society **29**, 297 (1933).

[169] Y. B. Ovchinnikov, J. H. Müller, M. R. Doery, E. J. D. Vredenbregt, K. Helmerson, S. L. Rolston, and W. D. Phillips, "*Diffraction of a released Bose-Einstein condensate by a pulsed standing light wave*", Phys. Rev. Lett. **83**, 284 (1999).

[170] B. Gadway, D. Pertot, M. G. Cohen, and D. Schneble, "*Analysis of Kapitza-Dirac diffraction patterns beyond the Raman-Nath regime*", Optics Express **17**, 19173 (2009).

[171] S. Wu, Y.-J. Wang, Q. Diot, and M. Prentiss, "*Splitting matter waves using an optimised standing-wave light-pulse sequence*", Phys. Rev. A **71**, 043602 (2005).

[172] K. J. Hughes, B. Deissler, J. H. T. Burke, and C. A. Sackett, "*High-fidelity manipulation of a Bose-Einstein condensate using an optical standing wave*", Phys. Rev. A **76**, 035601 (2007).

[173] K. J. Hughes, "*Optical manipulation of atomic motion for a compact gravitational sensor with a Bose-Einstein condensate interferometer*", PhD thesis, University of Virginia (2008).

[174] B. I. Robertson, "*High Contrast Measurements with a Bose-Einstein Condensate Atom Interferometer*", PhD thesis, University of Strathclyde (2017).

[175] A. R. MacKellar, "*Single-Shot Holographic Readout of an Atom Interferometer*", PhD thesis, University of Strathclyde (2017).

[176] P. Storey and C. Cohen-Tannoudji, "*The Feynman path integral approach to atomic interferometry. A tutorial*", J. Phys. II **4**, 1999 (1994).

[177] B. Deissler, K. J. Hughes, J. H. T. Burke, and C. A. Sackett, "*Measurement of the ac Stark shift with a guided matter-wave interferometer*", Phys. Rev. A **77**, 031604(R) (2008).

[178] T. Kraemer, J. Herbig, M. Mark, T. Weber, C. Chin, H.-C. Nägerl and R. Grimm, "*Optimized production of a cesium Bose-Einstein condensate*", Appl. Phys. B **79**, 1013 (2004).

[179] C. A. Sackett, "*Limits on weak magnetic confinement of neutral atoms*", Phys. Rev. A **73**, 013626 (2006).

[180] H. Wallis, A. Röhrl, M. Naraschewski and A. Schenzle, "*Phase-space dynamics of Bose condensates: Interference versus interaction*", Phys. Rev. A **55**, 2109 (1997).

[181] A. Röhrl, M. Naraschewski, A. Schenzle and H. Wallis, "*Transition from Phase Locking to the Interference of Independent Bose Condensates: Theory versus Experiment*", Phys. Rev. Lett. **78**, 4143 (1997).

[182] J. E. Simsarian, J. Denschlag, M. Edwards, C. W. Clark, L. Deng, E. W. Hagley, K. Helmerson, S. L. Rolston and W. D. Phillips, "*Imaging the Phase of an Evolving Bose-Einstein Condensate Wave Function*", Phys. Rev. Lett. **85**, 2040 (2000).

[183] P. Öhberg and L. Santos, "*Dynamical Transition from a Quasi-One-Dimensional Bose-Einstein Condensate to a Tonks-Girardeau Gas*", Phys. Rev. Lett. **89**, 240402 (2002).

[184] P. Pedri, L. Santos, P. Öhberg and S. Stringari, "*Violation of self-similarity in the expansion of a one-dimensional Bose gas*", Phys. Rev. A **68**, 043601 (2003).

[185] C. Menotti and S. Stringari, "*Collective oscillations of a one-dimensional trapped Bose-Einstein gas*", Phys. Rev. A **66**, 043610 (2002).

[186] D. S. Petrov, D. M. Gangardt, and G. V. Shlyapnikov, "*Low-dimensional trapped gases*", in Quantum Gases in Low Dimensions, edited by M. Olshanii, H. Perrin, and L. Pricoupenko, Proceedings of the Les Houches Summer School of Theoretical Physics [J. Phys. (France) IV **116**, 5 (2004)].

[187] T. Dauxois and M. Peyrard, "*Physics of Solitons*", Cambridge University Press (2006).

[188] L. F. Mollenauer, R. H. Stolen, and J. P. Gordon, "*Experimental Observation of Picosecond Pulse Narrowing and Solitons in Optical Fibers*", Phys. Rev. Lett. **45**, 1095 (1980).

[189] H. A. Haus and W. S. Wong, "*Solitons in optical communications*", Rev. Mod. Phys. **68**, 423 (1996).

[190] G. Soliani, C. Rebbi, "*Solitons And Particles*", World Scientific (1984).

[191] J. S. Russell, "*Report on waves*", in Report of the 14th meeting of the British Association for the Advancement of Science, 311 (1844).

[192] R. H. J. Grimshaw, "*Solitary Waves in Fluids*", WIT Press, Southampton, (2007).

[193] F. Lund, "*Interpretation of the precursor to the 1960 Great Chilean Earthquake as a seismic solitary wave*", Pure Appl. Geophys. **121**, 17 (1983).

[194] V. L. Patel, B. Dasgupta, "*Theory and observations of Alfven solitons in the finite beta magnetospheric plasma*", Physica D **27**, 387 (1987).

[195] A. Scott, "*Davydov's soliton*", Phys. Rep. **217**, 1 (1992).

[196] T. Heimburg and A. D. Jackson, "*On soliton propagation in biomembranes and nerves*", Proc. Natl. Acad. Sci. U.S.A. **102**, 9790 (2005).

[197] P. G. Kevrekidis, D. J. Frantzeskakis, R. Carretero-Gonzalez, "*Emergent Nonlinear Phenomena in Bose–Einstein Condensates*", Springer (2008).

[198] C. A. Sackett, J. M. Gerton, M. Welling, and R. G. Hulet, "*Measurements of Collective Collapse in a Bose-Einstein Condensate with Attractive Interactions*", Phys. Rev. Lett. **82**, 876 (1999).

[199] P. A. Altin, G. R. Dennis, G. D. McDonald, D. Döring, J. E. Debs, J. D. Close, C. M. Savage, and N. P. Robins, "*Collapse and three-body loss in a ^{85}Rb Bose-Einstein condensate*", Phys. Rev. A **84**, 033632 (2011).

[200] R. L. Compton, Y.-J. Lin, K. Jiménez-García, J. V. Porto, and I. B. Spielman, "*Dynamically slowed collapse of a Bose-Einstein condensate with attractive interactions*", Phys. Rev. A **86**, 063601 (2012).

[201] C. Eigen, A. L. Gaunt, A. Suleymanzade, N. Navon, Z. Hadzibabic, and R. P. Smith, "*Observation of Weak Collapse in a Bose-Einstein Condensate*", Phys. Rev. X **6**, 041058 (2016).

[202] P. A. Ruprecht, M. J. Holland, K. Burnett, and M. Edwards, "*Time-dependent solution of the nonlinear Schroedinger equation for Bose-condensed trapped neutral atoms*", Phys. Rev. A **51**, 4704 (1995).

[203] A. Gammal, T. Frederico, and L. Tomio, "*Critical number of atoms for attractive Bose-Einstein condensates with cylindrically symmetrical traps*", Phys. Rev. A **64**, 055602 (2001).

[204] A. Gammal, L. Tomio, and T. Frederico, "*Critical numbers of attractive Bose-Einstein condensed atoms in asymmetric traps*", Phys. Rev. A **66**, 043619 (2002).

[205] N. G. Parker, S. L. Cornish, C. S. Adams, and A. M. Martin, "*Bright solitary waves and trapped solutions in Bose-Einstein condensates with attractive interactions*", J. Phys. B **40**, 3127 (2007).

[206] V. M. Pérez-García, H. Michinel, J. I. Cirac, M. Lewenstein, and P. Zoller, "*Low Energy Excitations of a Bose-Einstein Condensate: A Time-Dependent Variational Analysis*", Phys. Rev. Lett. **77**, 5320 (1996).

[207] V. M. Pérez-García, H. Michinel, J. I. Cirac, M. Lewenstein, and P. Zoller, "*Dynamics of Bose-Einstein condensates: Variational solutions of the Gross-Pitaevskii equations*", Phys. Rev. A **56**, 1424 (1997).

[208] L. D. Carr and Y. Castin, "*Dynamics of a matter-wave bright soliton in an expulsive potential*", Phys. Rev. A **66**, 063602 (2002).

[209] D. S. Petrov, G. V. Shlyapnikov, and J. T. M. Walraven, "*Regimes of Quantum Degeneracy in Trapped 1D Gases*", Phys. Rev. Lett. **85**, 3745 (2000).

[210] Y. Castin, "*Simple theoretical tools for low dimension Bose gases*", in Quantum Gases in Low Dimensions, edited by M. Olshanii, H. Perrin, and L. Pricoupenko, Proceedings of the Les Houches Summer School of Theoretical Physics [J. Phys. (France) IV **116**, 89 (2004)].

[211] A. L. Gaunt, T. F. Schmidutz, I. Gotlibovych, R. P. Smith, and Z. Hadzibabic, "*Bose-Einstein Condensation of Atoms in a Uniform Potential*", Phys. Rev. Lett. **110**, 200406 (2013).

[212] A. D. Martin, C. S. Adams, and S. A. Gardiner, "*Bright Matter-Wave Soliton Collisions in a Harmonic Trap: Regular and Chaotic Dynamics*", Phys. Rev. Lett. **98**, 020402 (2007).

[213] A. D. Martin, C. S. Adams, and S. A. Gardiner, "*Bright solitary-matter-wave collisions in a harmonic trap: Regimes of solitonlike behavior*", Phys. Rev. A **77**, 013620 (2008).

[214] B. J. Dąbrowska-Wüster, S. Wüster, and M. J. Davis, "*Dynamical formation and interaction of bright solitary waves and solitons in the collapse of Bose-Einstein condensates with attractive interactions*", New J. Phys. **11**, 053017 (2009).

[215] T. P. Billam, S. A. Wrathmall, and S. A. Gardiner, "*Variational determination of approximate bright matter-wave soliton solutions in anisotropic traps*", Phys. Rev. A **85**, 013627 (2012).

[216] S. L. Cornish, S. T. Thompson, and C. E. Wieman, "*Formation of Bright Matter-Wave Solitons during the Collapse of Attractive Bose-Einstein Condensates*", Phys. Rev. Lett. **96**, 170401 (2006).

[217] S. Lepoutre, L. Fouché, A. Boissé, G. Berthet, G. Salomon, A. Aspect, and T. Bourdel, "*Production of strongly bound ^{39}K bright solitons*", Phys. Rev. A **94**, 053626 (2016).

[218] T. Mežnaršič, T. Arh, J. Brence, J. Pišljar, K. Gosar, Ž. Gosar, R. Žitko, E. Zupanič, and P. Jeglič, "*Cesium bright matter-wave solitons and soliton trains*", Phys. Rev. A **99**, 033625 (2019).

[219] J. H. V. Nguyen, D. Luo, and R. G. Hulet, "*Formation of matter-wave soliton trains by modulational instability*", Science **356**, 422 (2017).

[220] P. J. Everitt, M. A. Sooriyabandara, M. Guasoni, P. B. Wigley, C. H. Wei, G. D. McDonald, K. S. Hardman, P. Manju, J. D. Close, C. C. N. Kuhn, S. S. Szigeti, Y. S. Kivshar, N. P. Robins, "*Observation of a modulational instability in Bose-Einstein condensates*", Phys. Rev. A **96**, 041601(R) (2017).

[221] J. H. V. Nguyen, P. Dyke, D. Luo, B. A. Malomed, and R. G. Hulet, "*Collisions of matter-wave solitons*", Nat. Phys. **10**, 918 (2014).

[222] A. L. Marchant, T. P. Billam, T. P. Wiles, M. M. H. Yu, S. A. Gardiner, and S. L. Cornish, "*Controlled formation and reflection of a bright solitary matter-wave*", Nat. Commun. **4**, 1865 (2013).

[223] P. J. Everitt, M. A. Sooriyabandara, G. D. McDonald, K. S. Hardman, C. Quinlivan, M. Perumbil, P. Wigley, J. E. Debs, J. D. Close, C. C. N. Kuhn, N. P. Robins, "*Observation of Breathers in an Attractive Bose Gas*", arXiv:1509.06844 (2015).

[224] A. Negretti and C. Henkel, "*Enhanced phase sensitivity and soliton formation in an integrated BEC interferometer*", J. Phys. B **37**, L385 (2004).

[225] J. Polo and V. Ahufinger, "*Soliton-based matter-wave interferometer*", Phys. Rev. A **88**, 053628 (2013).

[226] G. D. McDonald, C. C. N. Kuhn, K. S. Hardman, S. Bennetts, P. J. Everitt, P. A. Altin, J. E. Debs, J. D. Close, and N. P. Robins, "*Bright Solitonic Matter-Wave Interferometer*", Phys. Rev. Lett. **113**, 013002 (2014).

[227] M. L. Chiofalo, M.P. Tosi, "*Output from Bose condensates in tunnel arrays: the role of mean-field interactions and of transverse confinement*", Phys. Lett. A **268**, 406 (2000).

[228] L. Salasnich, A. Parola, L. Reatto, "*Effective wave equations for the dynamics of cigar-shaped and diskshaped Bose condensates*", Phys. Rev. A **65**, 043614 (2002).

[229] L. Salasnich, "*Dynamics of a BEC bright soliton in an expulsive potential*", Phys. Rev. A **70**, 053617 (2005)

[230] C. F. Barenghi, N. G. Parker, "*A Primer on Quantum Fluids*", Springer (2016).

[231] V. Zakharov and A. Shabat, "*Exact theory of two-dimensional self-focusing and onedimensional self-modulation of waves in nonlinear media*", Sov. Phys. JETP **34**, 62 (1972), [Zh. Eksp. Teor. Fiz. **61**, 118 (1971)].

[232] J. Satsuma and N. Yajima, "*Initial Value Problems of One-Dimensional Self-Modulation of Nonlinear Waves in Dispersive Media*", Prog. Theor. Phys. Suppl. **55**, 284 (1974).

[233] J. Golde, J. Ruhl, M. Olshanii, V. Dunjko, S. Datta, and B. A. Malomed, "*Metastability versus collapse following a quench in attractive Bose-Einstein condensates*", Phys. Rev. A **97**, 053604 (2018).

[234] R. H. Stolen, L. F. Mollenauer, and W. J. Tomlinson, "*Observation of pulse restoration at the soliton period in optical fibers*", Opt. Lett. **8**, 186 (1983).

[235] G. Theocharis, P. Schmelcher, P. G. Kevrekidis, and D. J. Frantzeskakis, "*Matter-wave solitons of collisionally inhomogeneous condensates*", Phys. Rev. A **72**, 033614 (2005).

[236] F. Kh. Abdullaev and M. Salerno, "*Adiabatic compression of soliton matter waves*", J. Phys. B **36**, 2851 (2003).

[237] G. Theocharis, P. Schmelcher, P. G. Kevrekidis, and D. J. Frantzeskakis, "*Dynamical trapping and transmission of matter-wave solitons in a collisionally inhomogeneous environment*", Phys. Rev. A **74**, 053614 (2006).

[238] M. I. Rodas-Verde, H. Michinel, and V. M. Pérez-García, "*Controllable Soliton Emission from a Bose-Einstein Condensate*", Phys. Rev. Lett. **95**, 153903 (2005).

[239] A. V. Carpentier, H. Michinel, M. I. Rodas-Verde, and V. M. Pérez-García, "*Analysis of an atom laser based on the spatial control of the scattering length*", Phys. Rev. A **74**, 013619 (2006).

[240] Y. V. Bludov, V. A. Brazhnyi, and V. V. Konotop, "*Delocalizing transition in one-dimensional condensates in optical lattices due to inhomogeneous interactions*", Phys. Rev. A **76**, 023603 (2007).

[241] A. S. Rodrigues, P. G. Kevrekidis, M. A. Porter, D. J. Frantzeskakis, P. Schmelcher, and A. R. Bishop, "*Matter-wave solitons with a periodic, piecewise-constant scattering length*", Phys. Rev. A. **78**, 013611 (2008).

[242] R. Yamazaki, S. Taie S. Sugawa and Y. Takahashi, "*Submicron Spatial Modulation of an Interatomic Interaction in a Bose-Einstein Condensate*", Phys. Rev. Lett. **105**, 050405 (2010).

[243] L. W. Clark, L.-C. Ha, Chen-Yu Xu, and C. Chin, "*Quantum Dynamics with Spatiotemporal Control of Interactions in a Stable Bose-Einstein Condensate*", Phys. Rev. Lett. **115**, 155301 (2015).

[244] A. I. Streltsov, O. E. Alon, and L. S. Cederbaum, "*Formation and Dynamics of Many-Boson Fragmented States in One-Dimensional Attractive Ultracold Gases*", Phys. Rev. Lett. **100**, 130401 (2008).

[245] J. G. Cosme, C. Weiss, and J. Brand, "*Center-of-mass motion as a sensitive convergence test for variational multimode quantum dynamics*", Phys. Rev. A **94**, 043603 (2016).

[246] B. Opanchuk and P. D. Drummond, "*One-dimensional Bose gas dynamics: Breather relaxation*", Phys. Rev. A **96**, 053628 (2017).

[247] K. L. Ng, B. Opanchuk, M. D. Reid, and P. D. Drummond, "*Nonlocal Pair Correlations in a Higher-Order Bose Gas Soliton*", Phys. Rev. Lett. **122**, 203604 (2019).

[248] V. A. Yurovsky, B. A. Malomed, R. G. Hulet, and M. Olshanii, "*Dissociation of One-Dimensional Matter-Wave Breathers due to Quantum Many-Body Effects*", Phys. Rev. Lett. **119**, 220401 (2017).

[249] C. Weiss and L. D. Carr, "*Higher-order quantum bright solitons in Bose-Einstein condensates show truly quantum emergent behavior*", arXiv:1612.05545.